Cover Page

Universiteit Leiden

Leiden University
Repository

The handle http://hdl.handle.net/1887/138674 holds various files of this Leiden University dissertation.

Author: Vlieg, R.C.
Title: Two-photon multifocal microscopy for in vivo single-molecule and single-particle imaging
Issue Date: 2020-12-14

Two-photon multifocal microscopy for *in vivo* single-molecule and single-particle imaging

Proefschrift

ter verkrijging van
de graad van Doctor aan de Universiteit Leiden,
op gezag van Rector Magnificus prof.mr. C.J.J.M. Stolker,
volgens besluit van het College voor Promoties
te verdedigen op maandag 14 december 2020
klokke 11.15 uur

door

Redmar Cornelis Vlieg

geboren te Blaricum
in 1992

The cover shows the diffraction pattern of a diffractive optical element used to achieve multifocal microscopy.

Voor mijn ouders.

It takes something more than intelligence to act intelligently.

Fyodor Dostoyevsky

TABLE OF CONTENTS

Chapter 1

Introduction

The ability to image single molecules in live cells and organisms, for understanding cellular processes, has opened new possibilities over traditional averaging techniques. Fundamental to the quality of any microscopy experiment in biology is the temporal and spatial resolution. Directly related to resolution are the integration time, duration and at which signal-to-noise ratio these observations can take place. Numerous microscopy techniques have been developed to optimize abovementioned properties.

In this thesis we investigate the ability of two-photon multifocal microscopy for single-molecule microscopy in live cells and organisms. Two-photon excitation combined with multifocal scanning has the potential to achieve, high (temporal) resolution imaging at a low background. These characteristics are indeed beneficial for single-molecule experiments and any live cell imaging assay. However, two photon excitation generally requires high excitation powers, which may limit photon stability and cell integrity.

This chapter introduces the challenges of light microscopy for *in vivo* imaging and explains the main principles behind our used imaging technique. We also compare two-photon multifocal scanning with the increasingly popular microscopy technique of light-sheet microscopy.

1.1   *IN VIVO* MICROSCOPY

By looking at any tissue it becomes apparent that the propagation of light is strongly influenced by it. Also, the lack of contrast in the complex (extra)cellular environment requires highly specific markers to resolve a molecule or structure of interest. For this, a great variety of fluorescent, luminescent and/or scattering labels are available. Here we highlight some of the main physics that describes the boundaries of *in vivo* imaging.

1.1.1   SCATTERING AND ABSORPTION OF LIGHT IN CELL TISSUE

Cells, extracellular structures (collagen fibers, elastin, etc.) and fluids all combine into a complex optical system. Light needs to penetrate the tissue, travel towards the structure of interest and travel back to the objective for optical detection. During this process, light is subject to scattering and absorption, which hinders imaging and impairs image quality. The optical properties of a tissue can be described in terms of its absorption coefficient, μ_a (cm^{-1}), scattering coefficient, μ_s (cm^{-1}) and anisotropy g[1].

μ_s is defined as the probability that light is scattered per unit path length. Optical scattering can occur by particles that have a refractive index different to their surrounding medium, or due to a medium which has a continuous but fluctuating refractive index[2]. As light is scattered when travelling towards the focal spot, or back to the objective to be collected for detection, it loses its spatial coherence. In other words, a focused light beam is transformed to a diffuse bundle, resulting in dim and blurred images.

Mie theory describes the scattering of light from a sphere in a homogenous medium[3]. Scattering depends on particle diameter and the refractive index and wavelength of the incident light. Cell tissue contains a variety of particles and differences in refractive indices, making it much harder to grasp theoretically. Different tissues have different scattering characteristics which also depends on wavelength, see Figure 1.1a[4]. A common approximation for μ_s is given by:

$$\mu_s = \frac{a}{1-g}\left(\frac{\lambda}{500}\right)^{-b} \tag{1.1}$$

where g denotes the anisotropy and a and b are experimentally determined factors which can vary greatly between tissue[5]. Anisotropy g denotes the scattering direction at upon encountering a particle. For g = -1 and g = 1 light is scattered completely in backwards or forward direction, respectively. $g = 0$ indicates that scattering is evenly distributed in all directions. As such, g has a large influence on the scattering characteristics of tissue. In most biological tissues light is

predominantly scattered in a forward direction $(g > 0.9)$[1], resulting in an exponential loss of power with the thickness of the sample.
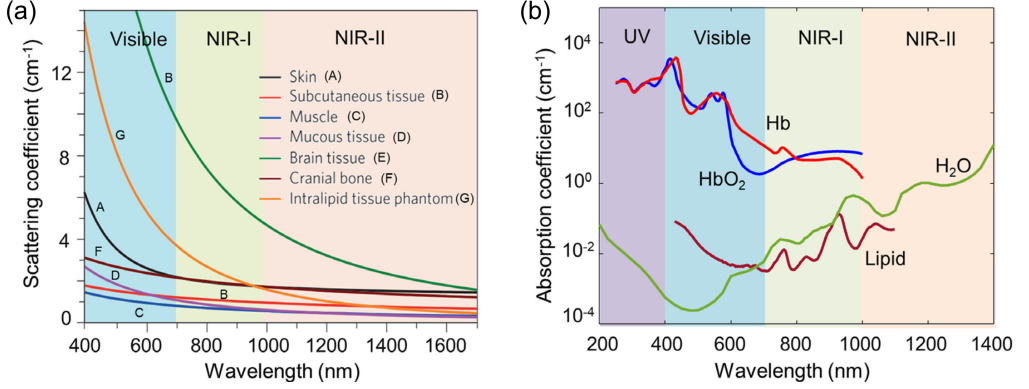
Figure 1.1: The main sources of light attenuation in microscopy are absorption and scattering. (a) The scattering coefficient as a function of wavelength varies in different types of tissue. Scattering decreases exponentially as the wavelength increases. (b) The absorption coefficient of a selection of biological materials as a function of wavelength. Absorption by hemoglobin (Hb) is significantly reduced for NIR wavelengths. In tissue where blood is absent, absorption is dominated by water and lipids. Adapted from [4].

Besides scattering, light can be absorbed by any molecule it encounters, resulting in a similar exponential decay. μ_a is defined as the probability of a photon being absorbed in a medium per unit path length. Similar to scattering, the absorption of light is wavelength dependent, see Figure 1.1b. Pigmented biological tissues feature much higher μ_a and impede high quality imaging.

The combination of scattering and absorption limits the number of photons that contribute to the signal that is collected by the detector. The number of photons (I) of wavelength (λ) at depth (z) inside a medium can be modelled as:

$$I(\lambda) = e^{-z(\mu_a(\lambda)+\mu_s(\lambda))} \tag{1.2}$$

This combination of scattering and absorption limits the imaging depth for most traditional microscopy techniques to ± 100 µm. For studying larger organisms like mice, this often means that tissue needs to be removed and imaged *ex vivo*. High absorption can be further mitigated by studying organisms or tissue that lack pigment. Additionally, the μ_a and μ_s can be significantly reduced by optical clearing techniques, which minimize refractive index mismatches or break down highly opaque structures [6–8]. For live imaging such harsh chemical preparation steps cannot be applied. However, recent developments in optical engineering like wavefront shaping, can be used to focus the light in highly turbid media[9]. Circumventing high absorption and scattering all together may also be an option. Small transparent model organisms, like round worms (*Caenorhabditis elegans*)[10] and zebrafish embryos (*Danio rerio*)[11], have for

this reason become popular in microscopy assays. The abovementioned examples form only a limited part of methods that are available on tackling the problems that optical microscopy has with opaque tissues. Dealing with absorption and scattering is therefore, arguably one of the most important challenges in *in vivo* microscopy.

1.1.2 CONTRAST LABELING

Because scattering and absorption impede microscopy imaging, alternative methods to achieve optical contrast are desirable. Self-luminescent structures, for example using fluorescence, relieve this constraint. Most biological structures feature a small amount of autofluorescence. Autofluorescence is the natural emission of light by biological structures as they absorb light, which increases the background signal of the image, see Figure 1.2[12]. So in order to resolve a specific structure of interest it is necessary to tag it with a light-emitting marker. These markers must be bright enough to be resolved in optical dense tissue and above the autofluorescent background. Roughly, contrast markers can be subdivided into three categories: fluorescent proteins, organic dyes and nanoparticles.

Fluorescent proteins (FPs) are widely used in microscopy. By cloning the genetic code of a FP into a gene, a specific protein is fluorescently tagged. Different color FPs are available and their specificity, versatility, convenience and minimal steric and biological interference has made FPs the most popular method for bio-imaging[13]. A drawback of FPs is their relatively small absorption cross section, which reduces the efficiency of excitation. Also, FPs have a limited photo-stability. When excited, they are prone to changes in conformation, oxidation, or react with free radicals in the environment and lose fluorescence, referred to as photobleaching. In long time-lapse measurements, photobleaching limits the duration of the experiment as there is a maximum to the number of times a fluorophore can cycle between the ground and the excited state and emit a photon[14].

Organic dyes offer a larger absorption cross section and quantum efficiency than FPs and span a wide spectral range of excitation wavelength[15]. This makes organic dyes versatile and bright markers. Multiple organic dyes can be attached to a single target, which can increase brightness even further. For this reason, dyes are often applied as markers for single-particle tracking microscopy. Microinjected liposomes for example, have been are tracked inside whole organisms[16].

The labelling of proteins with organic dyes cannot be done directly via genetic encoding. Therefore, one of the main challenges is attaching dye-labels to a specific target biomolecule. Several strategies are available for tagging, like enzyme-catalyzed labeling via post-translational modifications. For example, biotin and biotin acceptor peptides have been used for tagging membrane surface proteins[15]. An increasingly popular strategy is to genetically encode a HaloTag, which is a peptide designed to bind to synthetic ligands. These synthetic ligands can be attached to an organic dye for imaging of targeted proteins[17]. Delivery of organic dyes inside

of the cells can be done via: acetomethoxymethyl (AM)-ester derivatization, microinjection, gene guns, cationic liposomes, cell membrane manipulation and endocytosis [18,19]. Most of these biomolecule tagging strategies are effective on single cell experiments but not for whole organisms. Photobleaching is also still an issue for organic dyes similar to FPs.
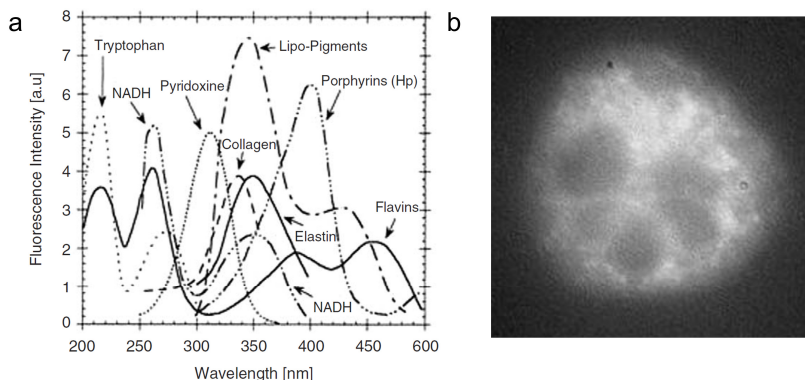
Figure 1.2: **Naturally occurring proteins fluoresce when excited at appropriate wavelengths.** (a) Excitation spectra of a selection of proteins that can be found in nearly every cell. (b) Autofluorescence of a leukocyte when excited at 365 nm. At these wavelengths autofluorescence can impair the SNR of the contrast labels. Adapted from [12].

Nanoparticles such as quantum dots (QDs) are unencumbered by photobleaching. QDs also feature an absorption cross section a factor 4 to 40 higher than fluorescent dyes and exhibit narrow excitation spectra which can extend further into the near-infrared (NIR) wavelengths[20]. These properties make QDs attractive for high-resolution single particle tracking microscopy and can be effectively used with NIR excitation sources[21]. QDs do however, blink, which entails temporary loss of signal for up to tens of seconds. This hampers their use for single particle tracking[22].

Noble metallic nanoparticles, like gold or silver nanospheres or nanorods, do not feature any blinking or bleaching and exhibit even brighter luminescence than QDs[23]. The conducting electrons of a metallic nanoparticle can couple with light, which greatly enhances both the absorption and emission of light. The oscillation frequency of this localized surface plasmon resonance (LSPR) is dependent on the material of the particle, its aspect ratio and the refractive index of the surrounding medium. Gold spherical particles have a LSPR of ±532 nm, elongated gold nanorods (GNRs) have a slower oscillation frequency and the absorption peak is therefore red-shifted, ranging to infrared wavelengths. The excitation spectrum can be tailored to the measurement setup. Moreover, relatively easy surface bio-functionalization makes GNRs compelling contrast markers for high accuracy 3D single particle tracking[24]. The high sensitivity of the LPSR to the surrounding refractive index has been exploited for highly specific detection of single molecules[25]. Similar to organic dyes, transport of QDs and GNRs to their target

biomolecules in live cells or organisms is one of the main challenges. Also the large size (1-50 nm) may induce steric hinder when attached to the smaller target proteins [20].

Comparing the three presented labeling methods, there is a trade-off between brightness, biocompatibility and steric hinder. The brightness of organic dyes and nanoparticles for example, makes them especially useful for single particle tracking in larger or more optical dense tissue but specific labeling in live tissue remains challenging. The simple, highly specific and well established labeling method for FPs make them the main method for fluorescent labeling of biological samples. Therefore, when developing novel microscopy modalities for *in vivo* imaging, special attention should be directed towards compatibility with FPs.

1.1.3 PHOTOTOXICITY

A high photon emission rate is especially necessary for resolving fast cellular processes with a good spatial resolution. The high excitation power that is required is potentially damaging for the sample[26,27]. Phototoxicity can lead to extreme damage like cell death, which is often preceded by morphological changes such as: membrane blebbing, vacuole formation, mitotic arrest and nuclear fragmentation[26,28,29]. However, adverse effects of illumination that are less apparently manifested may still impair the function of the biological system. Less noticeable effects of phototoxicity include: slowdown of cellular growth processes[30], impaired neuronal function[31], and loss of the mitochondrial membrane potential[32]. Awareness of the more subtle phototoxic effects can result in more reliable and reproducible data and is important to consider for any *in vivo* experiment.

Phototoxicity can be caused via different pathways. The presence of reactive oxygen species (ROS) is the most prevalent[33]. A natural variety of organic molecules absorb visible light and subsequently get degraded when they react with oxygen. During this process ROS are produced including superoxide radicals, hydroxyl radicals and hydrogen peroxide[34]. ROS can oxidize DNA, causing mutations, or proteins and unsaturated fatty acids in lipids, rendering them non-functional. ROS have been shown to impede the function of enzymes or change the global state of the cell cytoplasm or mitochondria[35]. Similar to naturally occurring light-absorbing proteins, the excitation of fluorophores can produce ROS[36]. Hence, the location of a fluorophore inside a cell has a large effect on the photosensitivity of that cell[37]. Excited nanoparticles can also create ROS as the energized electron can react to neighboring oxygen molecules[38]. Photobleaching and phototoxicity are closely connected to each other, although they are distinctly different phenomena. An absence of photobleaching is a good indicator of illuminating at a safe level. However, in many live samples FPs are continuously produced and hence make photobleaching an unreliable method for assessing phototoxicity[28].

ROS scavenging mechanisms, like antioxidants, have developed through evolution to remove ROS from cells. Every organism or tissue has, different resistance to phototoxic effects shaped by their living environment[33]. For example, *Drosophila* (fruit fly) and *C. elegans*

(ringworm) appear to be more resistant to laser illumination than zebrafish embryos[39]. However, the additional production of ROS during light exposure can rapidly overwhelm the natural defenses of a biological system. Once this happens the health of an organism quickly deteriorates, see Figure 1.3a/b.

The phototoxicity threshold for an organism or cell can be determined by measuring phototoxic effects at different light doses[40]. The threshold can be moved to higher light intensities by adding ROS scavengers, like antioxidants [41], ascorbic acids[42] and flavonoid rutin[43] to the imaging medium. These methods are more effective for single-cell experiments than for whole organisms due to the endothelial cell barrier that restricts access to the internal cells. To reduce phototoxic effects in larger samples, strategies like temporally pulsed illumination[44,45] or spatially selective illumination (e.g. TIRF[46], two-photon[47] and light-sheet[48] microscopy), have been explored, as well as longer excitation wavelengths and reduced peak powers.
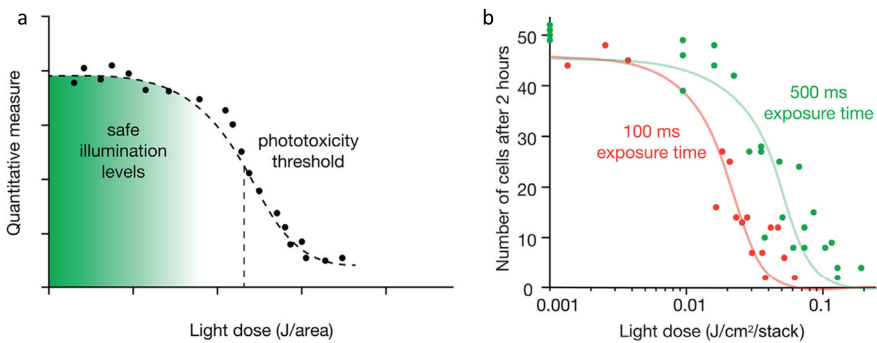
Figure 1.3: High intensity light irradiation can impair cellular mechanisms and lead to cell apoptosis. (a) Typical shape of a phototoxicity curve. When the dose exceeds a threshold, the natural oxygen scavenging defense mechanisms of a cell are overwhelmed and the rate at which cells perish increases drastically. (b) Experimental data on cell death as a function of light dose with two different illumination times. Adapted from [28].

In addition of reactive pathways, absorption of light by tissue can cause local heating and lead to cavitation and heat-induced morphological changes. Absorption scales with laser power. Most microscopy schemes use low enough illumination powers that heating of the sample does not have a major influence on the cellular metabolism. The non-linear excitation methods that we describe in this thesis are more likely to cause heating due to the substantially higher laser power [49,50]. Imaging of transparent and non-pigmented samples should generally prevent most heat-related phototoxic effects by reducing scattering and absorption.

In any *in vivo* imaging application the right balance between sample health, signal-to-noise ratio and spatial and temporal resolution needs to be found, see Figure 1.4. The highest signal to noise results in the best quality images. However, the necessary higher illumination intensity impairs sample health and increases photobleaching. A related factor is the desired temporal resolution. Reducing the acquisition time reduces the amount of signal proportionally. The

spatial resolution of an image is important for resolving the smallest details. Distribution of light over a larger area reduces signal intensity per pixel and can be rescued by longer integration times. Hence, one of these parameters cannot be optimized without compromising the others. Novel developments in optical microscopy are bound by these constraints and the challenge is to find a clever method to push the physical limits set by spatial resolution, temporal resolution, signal-to-noise ration and minimal biological damage.
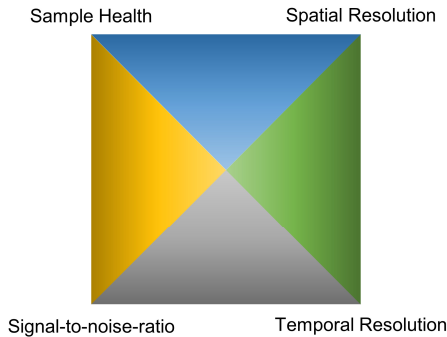
Figure 1.4: **The main condendrum for live imaging.** One parameter cannot be optimized without compromising the others.

1.2 MICROSCOPY TECHNIQUES

Wide-field epi-illumination is arguably fluorescence microscopy in its most simplistic form. A collimated excitation beam homogeneously illuminates the sample at a straight angle (i.e. epi-fluorescence) and the whole field-of-view (FOV) is illuminated in a single instance. Images are acquired rapidly by a CCD or sCMOS camera. Although wide field illumination is straightforward and high temporal resolutions are easily realized, out-of-focus fluorescence contributes to a large background signal and limits observations to two dimensions.

The background signal is greatly suppressed by implementing techniques which reduce the illumination volume such as total internal reflection fluorescence (TIRF) microscopy[51] and highly inclined and laminated optical sheet (HILO) microscopy[52]. In practice, the reduction in excitation volume limits these techniques to smaller samples and imaging is also limited in two dimensions (2D). By introducing a rasterized illumination pattern, referred to as structured illumination microscopy (SIM), background can also be computationally eliminated[53]. SIM effectively separates signal inside the focal plane from outside the focal-plane and allows to computationally dissect a sample in three-dimensions (3D)[54].

Another way of reducing background signal and improve 3D sectioning is to focus the laser beam into a single point and collect signal from this focal volume that is confined in 3D.

In laser scanning confocal microscopy (LSCM) out-of-focus fluorescence is spatially blocked by a pin-hole positioned in the emission path, an image is then reconstructed for serial measurements in which the focus is raster scanned through the sample. The sample is thus optically sectioned into thin slices and signal is collected with a low-noise, high sensitivity photomultiplier tube or photo-avalanche diode. The focused laser beam in combination with the pinhole enables deeper imaging than epi-fluorescence illumination at lower illumination power[28]. The ability to image a sample in 3D with relative ease has made LSCM a standard for live microscopy imaging. However, the serial acquisition impedes temporal resolution and life cell imaging is limited to slow processes. Despite that the light is focused, in-focus and out-of-focus fluorophores are still being bleached which limits the duration of the measurement.

1.3   TWO-PHOTON MICROSCOPY

In this thesis we use two-photon excitation (TPE) to mitigate some of the challenges *in vivo* environments impose on light microscopy. One of the ultimate goals is to reach single molecule sensitivity, which is the basis for the recent super-resolution revolution, that has boosted the performance of modern microscopy techniques. Though the combination of TPE and single molecule imaging has so far been heavily limited by photobleaching, the development of ultra-sensitive scientific CMOS cameras, in combination with advanced structural illumination schemes and better control over NIR lasers warrants a fresh effort in this direction.
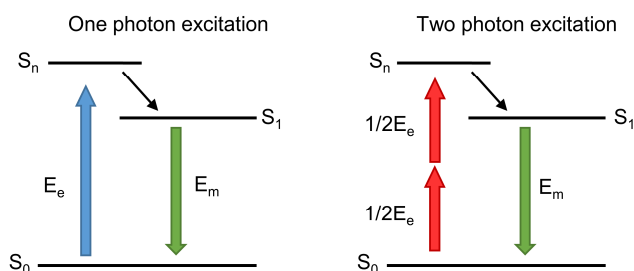
Figure 1.5: **Jablonski diagram for the excitation of a fluorophore using one photon and two photon excitation.** Half the energy per excitation photon is necessary for 2 photon excitation, which extends the excitation wavelengths to NIR. Once excited, the relaxation of the fluorophore follows the same pathway.

Invented in 1990, two-photon microscopy (TPM) is based on the excitation of a chromophore with two-photons instead of the more conventional one-photon excitation (OPE), see an illustration in Figure 1.5. Conventional OPE techniques use excitation light in the UV or visible light range to excite the chromophores of interest. For TPE, the use of two-photons

means that roughly half the energy per photon is required to excite a molecule, extending the excitation source to near-infrared (NIR) wavelengths. The absorption of two photons needs to occur within the relaxation time of a fluorophore (10^{-9} sec) which means that TPE is only effective at very high light intensities[55]. To achieve this, TPE is implemented using a focused beam in combination with femtosecond pulsed lasers[56]. Pulsed laser sources generate high peak intensities (kW-GW) necessary for TPE, while the average laser power remains relatively low (2-5 W), reducing linear absorption and thus heating and phototoxic damage to the sample. For a more quantitative understanding of the parameters involved for TPE, the probability (p) of two-photon absorption per laser pulse can be described as[57]:

$$p = \frac{P^2 \delta}{\tau_p f_p^2} \left(\frac{NA^2}{2hc\lambda} \right)^2 \tag{1.3}$$

with P the average laser intensity (W cm^{-2}), δ the two-photon absorption cross section of the chromophore (typically 10^{-50} cm^4 s) at the excitation wavelength λ (typically 650 – 1300 nm), τ_p the pulse width (typically 80 – 200 fs), f_p the repletion rate (typically 60 – 160 MHz), NA the numerical aperture, h Planck's constant, and c the speed of light. The quadratic dependence of signal to laser power characterizes TPE as a non-linear excitation mechanism. From equation 1.3 it is clear that not only the light intensity affects p, but also the chosen objective, as p scales with NA^4. With a higher NA the focal volume is decreased, concentrating the light more efficiently. After saturation of the fluorophore is reached (p=1), the signal is limited by the repetition rate of the laser. However, previous reports show that photobleaching is severe at these excitation powers and drastically impair measurement times[58].

Most TPMs use femtosecond pulsed laser sources, benefiting from the increase in p as a result of shorter pulse width, combined with the relative wide availability of Ti:Sa lasers. A typical Ti:Sa laser can produce 100 fs pulses at a rate of around 80 MHz with a tuning range between 700-1000 nm. However, TPM has also been done with picosecond and continuous wave (CW) lasers[59,60]. A CW laser necessitated around 200 times the average laser power compared to a standard Ti:Sa laser to achieve similar signal, illustrating the advantage of using pulsed lasers to reduce average laser power. The real advantage of using CW lasers is to reduce system costs as diode CW IR lasers with sufficient power are available for <€1000, whereas a typical Ti:Sa laser costs €100k>.

A major advantage of TPE is that biological tissue features less scattering and absorption at NIR than visible wavelengths. This so-called NIR-window, as plotted in Figure 1.1, makes TPM a powerful technique for deep-tissue imaging. Typically, TPM extends imaging depth in rodent brains from ±100 µm in confocal OPE to ±500 µm[5]. The deeper imaging depth has made TPM able to perform live imaging of transient neuronal Ca^{2+} fluxes in rodent brains, where one-photon excitation (OPE) failed[61]. Another interesting application for TPM is fluorescent correlation spectroscopy (FCS). FCS is based on the autocorrelation of the diffusion of a small

number of molecules through the focus. Inside live cells TPE made it possible to do FCS, where background signal would be too high for OPE to resolve single fluorophores[62].
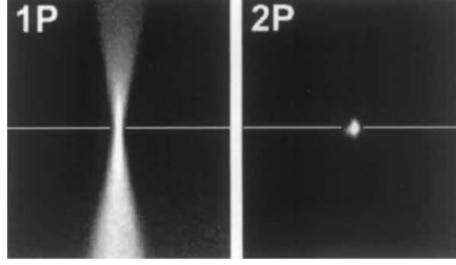
Figure 1.6: With one-photon excitation fluorophores outside the focal volume are excited. In contrast, the low probability of two-photon excitation confines fluorescence to the focal volume of the objective. Adapted from [56].

The intrinsic optical sectioning of TPE means that background fluorescence is eliminated without the need for a pin-hole, see Figure 1.6. Background is further reduced by the exceptionally large anti-Stokes spectral difference between excitation and emission photons, facilitating spectral separation of the two.

There are many theoretical methods on how to estimate the resolution of a microscope. A relatively straightforward and common approach is by calculating the full width at half maximum (FWHM) of the PSF according to Rayleigh's criterion. For LSCM, the lateral ($\omega_{r,OP}$) and axial ($\omega_{z,TP}$) resolution based on Rayleigh's criterion is[64]:

$$\omega_{r,OP} = \frac{0.51\lambda}{NA} \tag{1.4}$$

$$\omega_{z,OP} = \frac{0.88\,\lambda}{(n - \sqrt{n^2 - NA^2}} \tag{1.5}$$

with *n* the refractive index of the medium. Please note that equation 1.4 and 1.5 slightly deviate from the standard Rayleighs' criterion of $\omega_{r,OP} = 0.61\lambda/NA$ and $\omega_{z,OP} = 2\lambda n/NA^2$ due to the inclusion of the pin-hole aperture.

For a standard TPM the resolution of the microscope is purely defined by the size of the point spread function[65]. As TPE roughly uses twice the wavelength to excite the same fluorophore as OPE the resolution intuitively should be worse. However, the quadratic dependence of signal on laser power confines the excitation to a narrower volume. An estimation of the resolution of TPM could be the square root of equations 1.4 and 1.5. A more common definition however, is by the numerical estimation for $\omega_{r,TP}$ and $\omega_{z,TP}$ based on fitting quadratic

Gaussians to the intensity distribution model of Richards and Wolf, which results in a slightly different values:[63]

$$\omega_{r,TP} = \frac{0.541\lambda}{\sqrt{2}NA^{0.91}} \tag{1.5}$$

$$\omega_{z,TP} = \frac{1}{\sqrt{2}}\left(\frac{0.886\lambda}{n - \sqrt{n^2 - NA^2}}\right) \tag{1.6}$$

assuming NA > 0.7 and the detector meets the Nyquist criteria. Equations 1.5 and 1.6 do not take any side-lobes of the Airy rings into account, which will be negligible for a standard TPM. However, when the excited fluorophore approaches saturation ($p = 1$), the main lobe would flatten and the side lobes become more prominent. When this happens the optical resolution of a TPM starts to deviate from equation 1.5 and 1.6. For super-resolution, the localization accuracy can be determined by accounting for shot-noise, which reduces the uncertainty in positioning by $\sqrt{N}$, with N photons. Therefore, brighter fluorophores and thus higher excitation intensities are desirable. For normal biological imaging however, the photon flux necessary to reach fluorophore saturation would result in high photobleaching and phototoxicity, impairing sample integrity. In practice, saturation effects are only relevant for highly efficient two-photon labels, such as QDs and metallic nanoparticles[66,67].

The difference in resolution between linear and non-linear excitation can be compared using equations 1.4-1.6. For example, exciting a fluorophore at 400 nm with an NA=1.1 yields $\omega_{r,OP} = 0.19$ µm and $\omega_{z,OP} = 0.60$ µm. For exciting the same fluorophore with TPE at 800 nm results in $\omega_{r,TP} = 0.28$ µm and $\omega_{z,TP} = 0.86$ µm. As such, the theoretical resolution of a TPM is only moderately worse compared to a confocal microscope. However, in practice the higher scatter coefficient of visible light inside tissue and the lower background fluorescence of TPM generally results in resolution similar or better than that of a LSCM, especially at larger imaging depths[68]. Therefore, the consensus is that confocal and TPM have similar image resolution which shifts in favor of TPM at larger imaging depths.

Photobleaching and phototoxicity with TPE is more elusive and less well understood than with OPE. Fluorophores outside the focal volume are not excited, which confines the phototoxicity and photobleaching. Inside the focal volume however, the large flux of photons can promote already excited fluorophores to higher energy states, which increases their reactivity with surrounding molecules. This results in faster bleaching inside the focus than with OPE [69–72] and therefore makes TPM more beneficial for the imaging large volumes of bigger samples where more fluorophores are available. The two-photon photobleaching rate (τ) scales with laser power (P) as:

$$\tau = A * P^c \tag{1.7}$$

empirically, with amplitude *A* and exponent *C*. Values for *C* between 2.1 – 5.1 have been dependent on: type of fluorophore[58,73], laser pulse width [74,75], laser repetition rate[76] and surrounding temperature[58]. Using low NA objectives for illumination has also shown a strong decrease in photobleaching, suggesting that reduced peak intensities have a significant role in bleach rates[77]. The >2 exponential dependence indicates a sensitive relationship between bleach rate and excitation power. Thus reduction of the laser power should be paramount in any TPM measurement in order to keep phototoxicity minimal.

1.3.2 Multifocal scanning

Abovementioned advantages have made TPM an excellent technique for the imaging of large volumes in opaque larger organisms. However, the temporal resolution of faster scanning the laser in a serial fashion remains limited. The more so, because most commonly used fluorophores feature a poor two-photon absorption cross section which requires extended integration times[78]. Increasing laser power offers a limited solution due to the exponential dependence of bleach rate and phototoxicity (eq. 1.7). Conventional TPM does not have sufficient temporal resolution for imaging fast cellular processes or to capture single particles or molecules traveling inside living organisms.

Higher framerates can be achieved while keeping phototoxicity low by splitting the laser beam into multiple beamlets. By multiplexing the excitation volume and increasing the total laser power proportionally, the peak power per focus remains unchanged. Collection of the signal from the multiple foci requires array detectors such as sCMOS or EM-CCD cameras. The use of wide-field detectors means that the lateral resolution differs from a conventional TPM, defined by equation 1.5. The lateral resolution is now simply defined by the emission light and thus can be expressed by the standard Rayleigh criterion of 0.61λ/NA, which would not discriminate between OPE and TPE.

Two-photon multifocal microscopy (TPMM) has been done with microlens arrays (MA), microlens discs[79], cascade beam splitters[80], spatial light modulators (SLM) or diffractive optical elements (DOE). Setups using MAs, beam splitters or DOEs split the laser beam in multiple beamlets, after which they are scanned by scanning mirrors. SLMs on the other hand do not require any mechanical scanning; by applying a computer generated hologram, any arbitrary number of foci, their position and intensity can be defined accordingly[81]. Previous studies show a significant increase in imaging speed with TPMM compared to single point scanning. For example, using a SLM creating an 8 x 8 array of foci, fluorescence lifetime of fluorophores in cells was imaged 64 times faster compared to single-point imaging[82]. The imaging of Ca^{2+} transients in neurons can be extended from one to tens of neurons by positioning the foci to

different points-of-interest using a SLIM[83]. An example of multiplexed monitoring of neurons in mouse brain is depicted in Figure 1.7.
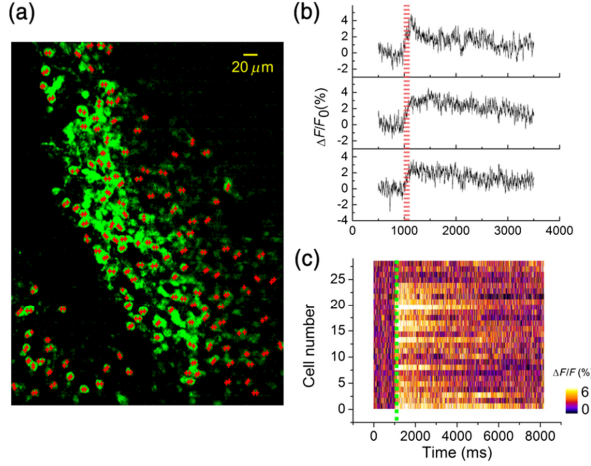
Figure 1.7: **Multiplexing the laser beam allows to measure Ca²⁺ transients in multiple neurons simultaneously at high temporal resolution. (**a) Image of stained neuron cells inside a mouse brain. The red dots annotate the locations of the foci. (b) Three selected time traces showing different kinetics upon stimulation (red dashed line). (c) All 27 time traces of neuron cells which responded to a stimulus. Adopted from [83].

1.3.3 EXPERIMENTAL SETUP

In this thesis we use a TPMM based on a DOE for rapid scanning of the focal plane and a schematic of the setup is shown in Figure 2.1. Per Chapter the details of the used configuration of the setup are described. In short, the DOE diffracts the light into 25 x 25 beamlets oriented in a hexagonal structure. The zeroth-order of the diffraction pattern is blocked by a droplet of soldering tin deposited on a glass slide. The first-order diffraction pattern is collected by a lens and further transmitted to a fast-scanning mirror which spiral-scans the array of foci across the focal plane. For most of the experiments we scanned the array of foci in an Archimedean spiral based on previous work by Van den Broek, et al[24], see Figure 1.8, which can be described in spatial coordinates x and y at time t by:

$$x = A\tau \ \sin(2\pi n\tau) \tag{1.8}$$

$$y = A\tau \ \cos(2\pi n\tau) \tag{1.9}$$

$$\tau = \sqrt{\frac{t}{T}\exp\left(\frac{(t/T)^2}{2\sigma^2}\right)} \tag{1.10}$$

with A the amplitude of the spiral, n the number of spirals, T the total exposure time of the camera and σ the width of the Gaussian profile that results from the scanning. Archimedean spiral scanning results in a homogeneous distribution of the light intensity during a single camera exposure, see Figure 1.8. The resulting smooth Gaussian curve minimizes variations in illumination, which is important for a homogeneous illumination of the sample.
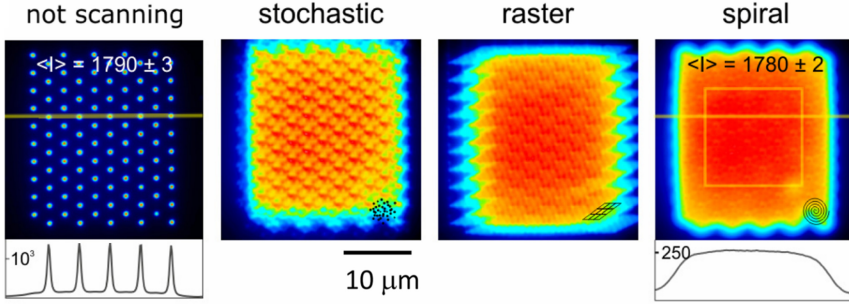
Figure 1.8: **Scanning a grid of foci following an Archimedean spiral generates a homogenous field for wide field two-photon microscopy.** This is the standard method of illumination in this thesis. Adopted from [24].

1.4 LIGHT SHEET MICROSCOPY

Arguably, one of the more recent and exciting microscopy techniques is light-sheet microscopy (LSM). Similar to TPMM, LSM improves image acquisition rates and photobleaching over single-point scanning microscopy. To help understand the advantages and disadvantages of both methods we compare LSM and TPMM. As this thesis is generally focused on TPM, we explicitly discuss two-photon light-sheet microscopy (TPLSM), which due to the non-linear excitation boasts different light-sheet characteristics as compared to single-photon LSM.

In conventional LSM the illumination beam is formed as a static sheet of light, commonly referred to as selective plane illumination microscopy (SPIM)[84]. SPIM utilizes a sheet of light to selectively optically dissect the sample. The light sheet is created by using a cylindrical lens in front of the objective. A second objective is positioned orthogonally to the axis of the illumination objective to collect the signal originating from the light-sheet, see Figure 1.9b. By uncoupling the illumination and the excitation paths, SPIM can rapidly optically dissect a sample with a large field-of-view (FOV), and preventing out-of-focus illumination. The selective illumination not only limits background, it also reduces photobleaching outside the sample and therefore limits the overall phototoxic effects normally associated with OPE methods.
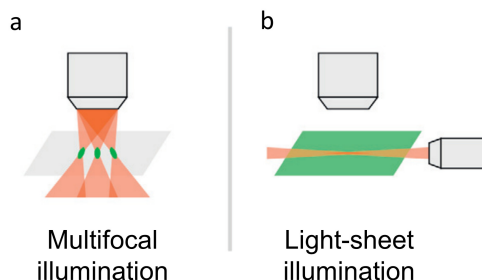
Figure 1.9: **Both multifocal scanning and illumination by a sheet of light allows for deep, fast and gentle optical dissection.** (a) Standard configuration of a multifocal scanning two-photon microscope. Multiple beamlets are focused to increase imaging speed. Illumination and detection are done with the same objective. (b) Standard configuration of a light-sheet microscope. One objective weakly focusses a laser beam to generate a sheet of light. A second orthogonally placed objective collects the fluorescence originating from excited fluorophores. Adopted from [91].

Still, the sheet of light is subject to scattering and broadening when imaging inside tissue. Two-photon SPIM was introduced in 2010 to improve upon SPIM[85–87]. The NIR light is less prone to scattering and allows for deeper imaging depth and less linear absorption[88]. Also, due to the non-linear excitation, scattered illumination photons are less likely to excite out-of-focus molecules which greatly reduces background. However, excitation efficiency decreases drastically in two-photon SPIM compared to single-point TPM due to the quadratic dependence of excitation with laser power. For more efficient two-photon LSM, the cylindrical lens is replaced by a traditional circular one and the illumination beam is focused near the back-focal plane of the objective. By doing so a Gaussian-shaped beam is created which significantly increases light intensity in the excitation volume. Subsequently, the FOV has to be sampled by scanning the illumination beam across the detection focal plane – commonly referred to as two-photon scanned light sheet microscopy (TPSLM). Despite the necessity to scan the sample, TPSLM still results in higher framerates frame rates due a 100-fold increase in signal rate (signal count per unit of average excitation power) compared to two-photon SPIM[77]. The penetration depth of TPSLM can be further improved by a factor of 6 up to 12 when using a Bessel-shaped illumination beam[87,89].

1.4.2 RESOLUTION

In TPSLM, the lateral and axial resolution are decoupled from one another. The lateral resolution is determined by the detection optics, similar to non-SPIM, whereas the axial resolution is determined by a combination of the detection optics and the thickness of the light-sheet itself, see Figure 1.10a. With a thicker light-sheet, SPIM would approach wide-field illumination and lose its ability to optical dissect a sample as out-of-focus fluorescence would become dominant. Hence, reducing the waist of the beam profile is advantageous to increase

SNR and axial resolution. However, to achieve a slimmer waist, a higher focus angle (NA) is necessary which decreases the penetration depth of the beam. Referring to Figure 1.10a, the radius of a Gaussian shaped beam at its thinnest point (ω_0) is described by[90]:

$$\omega_0 = \frac{\lambda}{\pi\,NA} \tag{1.11}$$

The axial resolution as the FWHM of the beam profile ($\omega_{z,LS}$) is then defined as:

$$\omega_{z,LS} = \omega_0\,\sqrt{\ln 2} \tag{1.12}$$

The FOV of a DSLM is determined by the propagation of the illumination beam (l_{LS}) while maintaining a certain thickness. Setting the thickness threshold at $\sqrt{2}\,\omega_0$ yields a l_{LS} of[77]:

$$l_{ls} = \frac{2n\lambda}{\pi\,NA^2} \tag{1.13}$$

From these equations the sensitive relationship between the FOV and the axial resolution can be better appreciated. For example, exciting a sample at 800 nm using a NA = 0.1 objective gives $\omega_{LS} = 2.12$ µm and $l_{ls} = 67.7$ µm. Increasing the NA to 0.2 results in a higher resolution of $\omega_{LS} = 1.06$ µm at a significantly reduced $l_{ls} = 16.9$ µm. Interestingly, considering an illumination NA of 0.1, TPMM would need a NA of 0.83 (equation 1.6) for the same axial resolution as TPSLM. For higher axial resolution however the FOV would reduce drastically, impairing the imaging of larger samples, see Figure 1.10b/c. Therefore, the illumination NA has to remain low which results in a relative poor axial resolution. See Figure 1.10b/c for a comparison between both imaging modalities in terms of axial resolution and FOV.

TPMM can use much higher NA objectives for both illumination and detection. As such, the excitation volume can stay more confined than TPSLM and would therefore have higher axial resolution and SNR. However, axial resolution inside scattering tissue is not as trivial to define, especially at larger depths. The higher angle at which light enters the sample could result in more scattering events as the path-length through tissue is longer compared to lower NA illumination. Imaging in larger samples like zebrafish embryos (*Danio rerio*), indicated that the lower incident angle of the illumination beam of a TPSLM retained its resolution at deeper imaging depths better compared to single-focus TPM[77]. TPMM would use similar NA as TPSM and therefore would likely be suffering from similar aberrations in its PSF.

The lateral resolution is solely determined by the NA of the detection objective which is not constrained in NA, in contrast to the illumination objective. Hence, the lateral resolution of LSM should be comparable to TPMM and any other microscope which utilizes a wide-field detector.
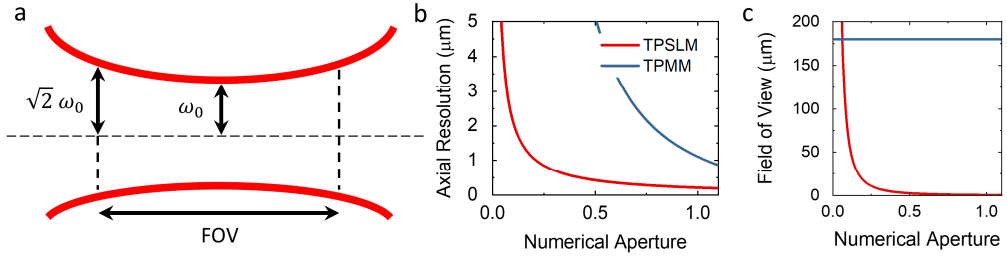
Figure 1.10: The strong correlation between axial resolution and field-of-view limits the axial resolution in two-photon light-sheet microscopy. (a) Schematic of some parameters which dictate the field-of-view and the axial resolution in a TPLSM. (b) Comparison between the axial resolution of TPLSM and TPMM. TPSLM allows to reach the same axial resolutions with lower NA as TPMM. (c) For a useful field-of-view the numerical aperture is generally NA<0.2. Hence also limiting axial resolution. The field-of-view in TPMM is dependent on the emission path optics and detector size, hence more elusive to define. Here we use the width of the excitation plane of our microscope in combination with a 25X NA=1.1 objective.

1.4.3 PHOTOTOXICITY

LSM is often referred to as a gentle way of illuminating a sample. Why LSM is considered more gentle than point scanning microscopes originates from the way the incident light of the illumination beam is being used all the way as it travels through the sample. Intuitively, the difference between TPMM and TPSLM in terms of average laser power can be understood as follows. TPMM focusses the light beam after which is disperses again and does not generate signal. In TPSLM the light being send into the sample can continuously excite fluorophores and generate signal, as long as the excitation light is intense enough. For a N times increase in acquisition rate, TPMM would need N^2 more average power, whereas a TPSLM would need $\sqrt{N}$ more power[91]. Therefore, the average excitation power to achieve the same amount of fluorescence in TPSLM is lower. Moreover the lower illumination NA reduces peak intensities which is believed to reduce higher-order bleaching effects[92]. A more thorough explanation on how TPSLM achieves higher signal-rates at similar excitation power can be found in the discussion of Chapter 4 of this thesis.

1.4.4 COMPLEXITY AND SAMPLE MOUNTING

TPMM provides potentially higher resolution, while TPSLM allows for more gentle, deeper and faster imaging. Arguably, the major challenge of TPSLM lies in the complexity of the setup and the elaborate sample mounting procedures. With only few commercial systems available for one-photon SPIM systems, a TPSLM has to be built in-house[93]. TPMM has not been commercialized yet, and therefore it would also be necessary to it from separate components.

The excitation path of a TPMM however, is quite similar to that of a conventional TPM. Multiple beamlets can be generated by placing either a micro lens array or DOE in laser beam after which a scanning mirror scans the beamlets across the focal plane. The transformation from a TP-SM to a TPMM would be roughly complete by replacing the detector (i.e. photomultiplier tube) by a camera. For TPSLM, the orthogonal orientation of multiple objectives makes it structurally more complex. Also, sample mounting is constrained as samples have to be placed in agarose capillaries to be properly aligned with the objectives[94]. Designs are available where conventional sample mounting is possible by making use of AFM cantilevers[95], or highly inclined illumination [96,97], however, this does make the microscope itself more complex or limits the imaging to smaller samples.

At the cost of more complexity, both microscope modalities can be improved in terms of: resolution, imaging depth, image speed and image quality. For example, multiple illumination objectives can be placed opposite of each other for a larger FOV in TPSLM[77,98]. In TPMM, most of the advances can be made by reducing the blurring effect of diffuse emission photons hitting wrong pixels and thereby reducing SNR. This can be done by the likes of operating the microscope in a de-scanned configuration[80,99], pin-hole rejection[100,101] or structured illumination[102,103].

Eventually, the choice between TPMM and TPSLM should be made based on the type of measurements one wants to conduct. If the advantages of TPSLM over TPMM do not add significant information, the extra costs and complexity would likely not justify the investment.

1.5 THESIS OVERVIEW

In this thesis we explore the capabilities of a multifocal two-photon microscope for *in vitro* and *in vivo* experiments down to the smallest scale of single molecules.

We start by exploring the spectroscopy capabilities of the setup in **Chapter 2** for the detection of single molecules using GNRs. The automatic tuning of the laser allowed us to measure the two-photon absorption spectra of GNRs. The quadratic dependence of signal on excitation power yields narrow SPR-bands, which could be used for highly sensitive single-molecule bio-sensing applications. We verified the ability of the setup to resolve single GNRs via: correlation with electron microscope images, light polarization and spectroscopy. The two-photon absorption spectra indeed feature narrower peaks compared to linear contrast methods. By lowering the laser power, GNRs were imaged for extended periods of time without noticeable reshaping, which in general is a major issue for illumination of metallic nanoparticles with high intensity femto pulsed lasers. By changing the refractive index of the media we observed a shift in the LSPR, confirming that spectral measurements can be used for sensing applications. We initiated measurements for single-molecule sensing but stability issues hampered the detection of binding of single molecules to GNRs by two-photon spectroscopy.

In **Chapter 3** we evaluate the performance of the setup for *in vivo* applications and focus on the imaging of single particles. Multifocal scanning allowed for rapid imaging, while the TPE confined excitation to a thin section of the sample. These properties could be valuable for many studies which need high temporal resolution with high SNR. We used GNRs for determining the PSF of the setup. GNRs were also micro injected in zebrafish embryos and tracked as they travelled inside the bloodstream of the embryos. We noticed during measurements in zebrafish embryos that the signal originating from FP expressing endothelial cells was not noticeably reduced by loss in fluorescence due to photobleaching. This led to measuring embryos expressing different FPs and confirmed negligible photobleaching. Pollen embryos were imaged to measure expression of a particular growth factor (LEC1). TPMM revealed highly localized expression of LEC1 which was not observed by one-photon confocal microscopy. Finally, we introduced multi-color imaging for nanometric localization of liposomes in respect to the blood vessel wall in the brain of zebrafish embryos. The combination of low photobleaching, high contrast, high (temporal) resolution, and also in combination with multi-color imaging makes TPMM a very interesting method for high-speed *in vivo* imaging.

Chapter 4 focusses on imaging down to the level of single FPs. The lack of photobleaching and low background of TPMM would make it a promising imaging method for single molecules in live tissue. Two-photon single molecule studies reported however significantly higher bleaching rates compared to single-photon excitation. We did not observe major photobleaching in Chapter 3, which suggests that TPMM provides sufficient fluorescent longevity for single molecule imaging. We validated the ability to measure single FPs *in vitro*

by observing discrete bleaching steps in the acquired time traces and the average measured bleaching times were sufficient for single molecule tracking.

Still, one of the key issues with wide-field detection is blurring of the image by scattered emission photons. Suppressing this phenomenon would allow for higher SNR and provide an opportunity to lower excitation power for even longer bleaching times and less background signal. We subsequently used structured illumination to suppress scatted photons, which indeed worked to increase contrast when imaging inside zebrafish embryos. However, simulations and experiments indicated that structured illumination introduces additional camera read-noise which comes from the necessity to acquire multiple images. We consequently improved the structured illumination method which resulted in superior images compared to spiral illumination.

Finally, we measured single eGFP molecules *in vivo* for extended periods of time. These results showed the novelty of TPMM as a live single molecule tracking technique, and how it provides the opportunity to study cellular processes at very long time scales.

In **Chapter 5 and 6** we highlight two studies which used our setup for measuring single particles in live zebrafish embryos. Zebrafish embryos are widely used model organisms due to their small size, transparency and easy cultivation while still being vertebrates. This makes them popular among toxicology and pathology studies. One study looked into the toxic effects when fish were exposed to, or injected with, metallic nanoparticles. We established in previous chapters that the TPMM is capable of imaging GNRs at high SNR. Combined with the high temporal resolution we could image injected GNRs as they were travelling inside embryo. We managed to image macrophages taking up GNRs, which strengthened the hypotheses that GNRs are not inert and that the immune system does respond to GNRs. The second study investigated the distribution of liposomes which switch their surface charge to negative as they are illuminated by ultraviolet (UV) light. These liposomes have the potential to improve the efficiency and specificity of drug carriers. Negatively charged particles were shown to stick to surrounding endothelial cells and were subsequently endocytosed. An UV diode was placed above the mounted embryo and UV illumination was timed with the two-photon imaging to induce charge reversal. This allowed us to monitor the transition from free flowing to immobile liposomes in real-time. We quantified information on the transition speed from neutral to cationic particles, which is normally obscured in confocal microscopy techniques.

Overall, we enhanced the capabilities of TPM, leading to improved spectral imaging, fast light-sheet imaging, multi-color *in vivo* imaging and single particle and -molecule TPM. The shown biological applications demonstrate that despite physical boundaries there is ample opportunity to improve optical microscopy and explore new applications in biology.

1.6 BIBLIOGRAPHY

1.   Jacques, S. L. Optical properties of biological tissues: A review. *Phys. Med. Biol.* **58**, (2013).

2.   Jacques, S. L. & Pogue, B. W. Tutorial on diffuse light transport. *J. Biomed. Opt.* **13**, 041302 (2008).

3.   Hergert, W. & Wriedt, T. The Mie Theory. *Mie Theory Basics Appl.* 53–71 (2012). doi:10.1007/978-3-642-28738-1

4.   Upputuri, P. K. & Pramanik, M. Photoacoustic imaging in the second near-infrared window: a review. *J. Biomed. Opt.* **24**, 1 (2019).

5.   Miller, D. R., Jarrett, J. W., Hassan, A. M. & Dunn, A. K. Deep tissue imaging with multiphoton fluorescence microscopy. *Curr. Opin. Biomed. Eng.* **4**, 32–39 (2017).

6.   Musielak, T. J., Slane, D., Liebig, C. & Bayer, M. A versatile optical clearing protocol for deep tissue imaging of fluorescent proteins in Arabidopsis thaliana. *PLoS One* **11**, 1–17 (2016).

7.   Kurihara, D., Mizuta, Y., Sato, Y. & Higashiyama, T. ClearSee: A rapid optical clearing reagent for whole-plant fluorescence imaging. *Dev.* **142**, 4168–4179 (2015).

8.   Warner, C. A. *et al.* An optical clearing technique for plant tissues allowing deep imaging and compatible with fluorescence microscopy. *Plant Physiol.* **166**, 1684–1687 (2014).

9.   Vellekoop, I. M. & Mosk, A. P. Focusing coherent light through opaque strongly scattering media. *Opt. Lett.* **32**, 2309 (2007).

10.   Corsi, A. K., Wightman, B. & Chalfie, M. A transparent window into biology: A primer on Caenorhabditis elegans. *Genetics* **200**, 387–407 (2015).

11.   Kaufmann, A., Mickoleit, M., Weber, M. & Huisken, J. Multilayer mounting enables long-term imaging of zebrafish development in a light sheet microscope. *Dev.* **139**, 3242–3247 (2012).

12.   Monici, M. Cell and tissue autofluorescence research and diagnostic applications. *Biotechnol. Annu. Rev.* **11**, 227–256 (2005).

13.   Piyaraj, P. The Green Fluorescent Protein (GFP). *Bangkok Med. J.* **05**, 101–102 (2013).

14.   Lippincott-Schwartz, J., Altan-Bonnet, N. & Patterson, G. H. Photobleaching and photoactivation: Following protein dynamics in living cells. *Nat. Rev. Mol. Cell Biol.* **4**, (2003).

15.   Sameiro, M. & Gonçalves, T. Fluorescent labeling of biomolecules with organic probes. *Chem. Rev.* **109**, 190–212 (2009).

16.   Manzo, C. & Garcia-Parajo, M. F. A review of progress in single particle tracking: From methods to biophysical insights. *Reports Prog. Phys.* **78**, (2015).

17.   Los, G. V. *et al.* HaloTag: A novel protein labeling technology for cell imaging and protein analysis. *ACS Chem. Biol.* **3**, 373–382 (2008).

18.   Torchilin, V. P. *et al.* Cell transfection in vitro and in vivo with nontoxic TAT peptide-liposome-DNA complexes. *Proc. Natl. Acad. Sci. U. S. A.* **100**, 1972–1977 (2003).

19.   Waggoner, A. Fluorescent labels for proteomics and genomics. *Curr. Opin. Chem. Biol.* **10**, 62–66 (2006).

20.   Resch-Genger, U., Grabolle, M., Cavaliere-Jaricot, S., Nitschke, R. & Nann, T. Quantum dots versus organic dyes as fluorescent labels. *Nat. Methods* **5**, 763–775

(2008).

21. Xu, C., Zipfel, W., Shear, J. B., Williams, R. M. & Webb, W. W. Multiphoton fluorescence excitation: New spectral windows for biological nonlinear microscopy. *Proc. Natl. Acad. Sci. U. S. A.* **93**, 10763–10768 (1996).

22. Efros, A. L. & Nesbitt, D. J. Origin and control of blinking in quantum dots. *Nat. Nanotechnol.* **11**, 661–671 (2016).

23. Hutter, E. & Maysinger, D. Gold nanoparticles and quantum dots for bioimaging. *Microsc. Res. Tech.* **74**, 592–604 (2011).

24. Van den Broek, B., Oosterkamp, T. H. & van Noort, J. A Multifocal Two-Photon Microscopy Setup for Parallel 3D Tracking of Gold Nanorods. *Biophys. J.* **98**, 178a (2010).

25. Zijlstra, P., Paulo, P. M. R. & Orrit, M. Optical detection of single non-absorbing molecules using the surface plasmon resonance of a gold nanorod. *Nat. Nanotechnol.* **7**, 379–382 (2012).

26. Dixit, R. & Cyr, R. Cell damage and reactive oxygen species production induced by fluorescence microscopy: Effect on mitosis and guidelines for non-invasive fluorescence microscopy. *Plant J.* **36**, 280–290 (2003).

27. Knight, M. M., Roberts, S. R., Lee, D. A. & Bader, D. L. Live cell imaging using confocal microscopy induces intracellular calcium transients and cell death. *Am. J. Physiol. - Cell Physiol.* **284**, 1083–1089 (2003).

28. Icha, J., Weber, M., Waters, J. C. & Norden, C. Phototoxicity in live fluorescence microscopy, and how to avoid it. *BioEssays* **39**, 1–15 (2017).

29. Magidson, V. & Khodjakov, A. Circumventing photodamage in live-cell microscopy. *Methods Cell Biol.* **114**, 545–560 (2013).

30. Knobel, K. M., Jorgensen, E. M. & Bastiani, M. J. Growth cones stall and collapse during axon outgrowth in Caenorhabditis elegans. *Development* **126**, 4489–4498 (1999).

31. Maravall, M., Mainen, Z. F., Sabatini, B. L. & Svoboda, K. Estimating intracellular calcium concentrations and buffering without wavelength ratioing. *Biophys. J.* **78**, 2655–2667 (2000).

32. Roechlecke, C., Schaller, A., Knels, L. & Funk, R. H. W. The influence of sublethal blue light exposure on human RPE cells. *Mol. Vis.* **15**, 1929–1938 (2009).

33. Laissue, P. P., Alghamdi, R. A., Tomancak, P., Reynaud, E. G. & Shroff, H. Assessing phototoxicity in live fluorescence imaging. *Nat. Methods* **14**, 657–661 (2017).

34. Schneckenburger, H. *et al.* Light exposure and cell viability in fluorescence microscopy. *J. Microsc.* **245**, 311–318 (2012).

35. Spikes, J. Photosensitization in Mammalian Cells. in *Photoimmunology* 23–49 (Springer US, 1983).

36. Wagner, M. *et al.* Light dose is a limiting factor to maintain cell viability in fluorescence microscopy and single molecule detection. *Int. J. Mol. Sci.* **11**, 956–966 (2010).

37. Liu, X. *et al.* A genetically encoded photosensitizer protein facilitates the rational design of a miniature photocatalytic CO 2 -reducing enzyme. *Nat. Chem.* **10**, 1201–1206 (2018).

38. Bar-Ilan, O. *et al.* Titanium dioxide nanoparticles produce phototoxicity in the developing zebrafish. *Nanotoxicology* **6**, 670–679 (2012).

39. Bianchi, J. I., Stockert, J. C., Buzz, L. I., Blázquez-Castro, A. & Hernán Simonetta, S.

Reliable screening of dye phototoxicity by using a Caenorhabditis elegans fast bioassay. *PLoS One* **10**, 1–15 (2015).

40. Tinevez, J. Y. *et al. A quantitative method for measuring phototoxicity of a live cell imaging microscope. Methods in Enzymology* **506**, (Elsevier Inc., 2012).

41. Stockley, J. H. *et al.* Surpassing light-induced cell damage in vitro with novel cell culture media. *Sci. Rep.* **7**, 1–11 (2017).

42. Waldchen, S., Lehmann, J., Klein, T., Van De Linde, S. & Sauer, M. Light-induced cell damage in live-cell super-resolution microscopy. *Sci. Rep.* **5**, 1–12 (2015).

43. Bogdanov, A. M., Kudryavtseva, E. I. & Lukyanov, K. A. Anti-Fading Media for Live Cell GFP Imaging. *PLoS One* **7**, 1–4 (2012).

44. Nishigaki, T., Wood, C. D., Shiba, K., Baba, S. A. & Darszon, A. Stroboscopic illumination usine light-emitting diodes reduces phototoxicity in fluorescence cell imaging. *Biotechniques* **41**, 191–197 (2006).

45. Penjweini, R., Loew, H. G., Hamblin, M. R. & Kratky, K. W. Long-term monitoring of live cell proliferation in presence of PVP-Hypericin: A new strategy using ms pulses of LED and the fluorescent dye CFSE. *J. Microsc.* **245**, 100–108 (2012).

46. Mattheyses, A. L., Simon, S. M. & Rappoport, J. Z. Imaging with total internal reflection fluorescence microscopy for the cell biologist. *J. Cell Sci.* **123**, 3621–3628 (2010).

47. Denk, W., Strickler, J. H. & Webb, W. W. Two-Photon Laser Scanning Fluorescence Microscopy. *Sci. New Ser.* **248**, 73–76 (1990).

48. Chen, B.-C. *et al.* Lattice light-sheet microscopy: Imaging molecules to embryos at high spatiotemporal resolution. *Science (80-.).* **346**, 1257998 (2014).

49. Masters, B. R. *et al.* Mitigating thermal mechanical damage potential during two-photon dermal imaging. *J. Biomed. Opt.* **9**, 1265 (2004).

50. Bixler, J. *et al.* Assessment of tissue heating undertunable near-infrared radiation. *J. Biomed. Opt.* 22.1-22.37 (2009). doi:10.1117/1.JBO.19.7

51. Rockhold, S. A., Quinn, R. D., Wagenen, R. A. V. A. N., Andrade, J. D. & Reichert, M. Total Internal Reflection Fluorescence (TIRF) as a quantitative probe of protein absorption. **150**, 261–275 (1983).

52. Tokunaga, M., Imamoto, N. & Sakata-sogawa, K. Highly inclined thin illumination enables clear single-molecule imaging in cells. *Nature* **5**, 159–161 (2008).

53. Gustafsson, M. G. L. Surpassing the lateral resolution limit by a factor of two using structured illumination microscopy. *J. Microsc.* **198**, 82–87 (2000).

54. Shao, L., Kner, P., Rego, E. H. & Gustafsson, M. G. L. Super-resolution 3D microscopy of live whole cells using structured illumination. *Nat. Methods* **8**, 1044–1048 (2011).

55. Benninger, R. K. P. & Piston, D. W. Two-Photon Excitation Microscopy for the Study of Living Cellsand Tissues. *Curr. Protoc. cell Biol.* **June**, 1–36 (2014).

56. Soeller, C. & Cannell, M. B. Two-Photon Microscopy : Imaging in Scattering Samples and Three-Dimensionally Resolved Flash Photolysis. *Microsc. Res. Tech.* **195**, 182–195 (1999).

57. So, P. T. C., Dong, C. Y., Masters, B. R. & Berland, K. M. Two-Photon Excitation Fluorescence Microscopy. *Annu. Rev. Biomed. Eng.* 399–429 (2000).

58. Chirico, G., Cannone, F., Baldini, G. & Diaspro, A. Two-Photon Thermal Bleaching of Single Fluorescent Molecules. *Biophys. J.* **84**, 588–598 (2003).

59. Bewersdorf, J. & Hell, S. W. Picosecond pulsed two-photon imaging with repetition

rates of 200 and 400 MHz. *J. Microsc.* **191**, 28–38 (1998).

60.   Hell, S. W. *et al.* Two-photon near- and far-field fluorescence microscopy with continuous-wave excitation. *Opt. Lett.* **23**, 1238 (1998).

61.   Stosiek, C., Garaschuk, O., Holthoff, K. & Konnerth, A. In vivo two-photon calcium imaging of neuronal networks. *Proc. Natl. Acad. Sci. U. S. A.* **100**, 7319–7324 (2003).

62.   Schwille, P., Haupts, U., Maiti, S. & Webb, W. W. Molecular dynamics in living cells observed by fluorescence correlation spectroscopy with one- and two-photon excitation. *Biophys. J.* **77**, 2251–2265 (1999).

63.   Cole, R. W., Jinadasa, T. & Brown, C. M. Measuring and interpreting point spread functions to determine confocal microscope resolution and ensure quality control. *Nat. Protoc.* **6**, 1929–1941 (2011).

64.   Sheppard, C. Image formation in two-photon fluorescence microcopy. *Optik (Stuttg).* 1–4 (1990).

65.   Zipfel, W. R., Williams, R. M. & Webb, W. W. Nonlinear magic: Multiphoton microscopy in the biosciences. *Nat. Biotechnol.* **21**, 1369–1377 (2003).

66.   Wang, T., Halaney, D., Ho, D., Feldman, M. D. & Milner, T. E. Two-photon luminescence properties of gold nanorods. *Biomed. Opt. Express* **4**, 584–95 (2013).

67.   Larson, D. R. *et al.* Water-soluble quantum dots for multiphoton fluorescence imaging in vivo. *Science (80-.).* **300**, 1434–1436 (2003).

68.   Gu, M., Gan, X., Kisteman, A. & Xu, M. G. Comparison of penetration depth between two-photon excitation and single-photon excitation in imaging through turbid tissue media. *Appl. Phys. Lett.* **77**, 1551–1553 (2000).

69.   Dittrich, P. S. & Schwille, P. Photobleaching and stabilization of fluorophores used for single-molecule analysis with one- and two-photon excitation. *Appl. Phys. B Lasers Opt.* **73**, 829–837 (2001).

70.   Eggeling, C., Volkmer, A. & Seidel, C. A. M. Molecular photobleaching kinetics of Rhodamine 6G by one- and two-photon induced confocal fluorescence microscopy. *ChemPhysChem* **6**, 791–804 (2005).

71.   Chen, T.-S., Zeng, S.-Q., Luo, Q.-M., Zhang, Z.-H. & Zhou, W. High-Order Photobleaching of Green Fluorescent Protein inside Live Cells in Two-Photon Excitation Microscopy. *Biochem. Biophys. Res. Commun.* **291**, 1272–1275 (2002).

72.   Sanchez, E. J., Novotny, L., Holtom, G. R. & Xie, X. S. Room-temperature fluorescence imaging and spectroscopy of single molecules by two-photon excitation. *J. Phys. Chem. A* **101**, 7019–7023 (1997).

73.   Patterson, G. H. & Piston, D. W. Photobleaching in Two-Photon Excitation Microscopy. *Biophys. J.* **78**, 2159–2162 (2000).

74.   Xi, P., Andegeko, Y., Weisel, L. R., Lozovoy, V. V. & Dantus, M. Greater signal, increased depth, and less photobleaching in two-photon microscopy with 10 fs pulses. *Opt. Commun.* **281**, 1841–1849 (2008).

75.   Graham, D. J. L., Tseng, S., Chen, J. H. D. J. & Alexandrakis, G. Dependence of Two-Photon eGFP Bleaching on Femtosecond Pulse Spectral Amplitude and Phase. *J. Fluoresc.* 1775–1785 (2015). doi:10.1007/s10895-015-1667-1

76.   Niu, F. *et al.* Photobleaching of ultrashort pulses with different repetition rates in two-photon excitation microscopy. *Laser Phys.* **29**, 046001 (2019).

77.   Truong, T. V, Supatto, W., Koos, D. S., Choi, J. M. & Fraser, S. E. Deep and fast live imaging with two-photon scanned light-sheet microscopy. *Nat. Methods 2011 89* **8**, 757

(2011).

78.   Drobizhev, M., Makarov, N. S., Tillo, S. E., Hughes, T. E. & Rebane, A. Two-photon absorption properties of fluorescent proteins. *Nat. Methods* **8**, 393–399 (2011).

79.   Bewersdorf, J., Pick, R. & Hell, S. W. Multifocal multiphoton microscopy. *Opt. Lett.* **23**, 655 (1998).

80.   Fittinghoff, D. N., Wiseman, P. W. & Squier, J. A. Widefield multiphoton and temporally decorrelated multifocal multiphoton microscopy. *Opt. Express* **7**, 273 (2000).

81.   Matsumoto, N. *et al.* An adaptive approach for uniform scanning in multifocal multiphoton microscopy with a spatial light modulator. *Opt. Express* **22**, 633 (2014).

82.   Poland, S. P. *et al.* Time-resolved multifocal multiphoton microscope for high speed FRET imaging in vivo. *Opt. Lett.* **39**, 6013 (2014).

83.   Pozzi, P. *et al.* High-throughput spatial light modulation two-photon microscopy for fast functional imaging. *Neurophotonics* **2**, 015005 (2015).

84.   Huisken, J., Swoger, J., Bene, F. Del, Wittbrodt, J. & Stelzer, E. H. K. Optical Sectioning Deep Inside Live Embryos by Selective Plane Illumination Microscopy.

85.   Palero, J., Santos, S. I. C. O., Artigas, D. & Loza-Alvarez, P. A simple scanless two-photon fluorescence microscope using selective plane illumination. *Opt. Express* **18**, 8491 (2010).

86.   Maruyama, A. *et al.* Wide field intravital imaging by two-photon- excitation digital-scanned light-sheet microscopy (2p-DSLM) with a high-pulse energy laser. *C)* **5**, (2014).

87.   Zong, W. *et al.* Large-field high-resolution two-photon digital scanned light-sheet microscopy. *Cell Res.* **25**, 254–257 (2015).

88.   Lavagnino, Z., Cella Zanacchi, F., Ronzitti, E. & Diaspro, A. Two-photon excitation selective plane illumination microscopy (2PE-SPIM) of highly scattering samples: characterization and application. *Opt. Express* **21**, 5998 (2013).

89.   Zhao, M. *et al.* Cellular imaging of deep organ using two-photon Bessel light-sheet nonlinear structured illumination microscopy. *Biomed. Opt. Express* **5**, 1296 (2014).

90.   Hedde, P. N. & Gratton, E. Selective Plane Illumination Microscopy with a Light Sheet of Uniform Thickness Formed by an Electrically Tunable Lens. *Microsc. Res. Tech.* **176**, 139–148 (2018).

91.   Supatto, W., Truong, T. V, Débarre, D. & Beaurepaire, E. Advances in multiphoton microscopy for imaging embryos. *Curr. Opin. Genet. Dev.* **21**, 538–548 (2011).

92.   Ji, N., Magee, J. C. & Betzig, E. High-speed, low-photodamage nonlinear imaging using passive pulse splitters. *Nat. Methods* **5**, 197–202 (2008).

93.   Girkin, J. M. & Carvalho, M. T. The light-sheet microscopy revolution. *J. Opt.* **20**, (2018).

94.   Girstmair, J. *et al.* Light-sheet microscopy for everyone? Experience of building an OpenSPIM to study flatworm development. *BMC Dev. Biol.* **16**, (2016).

95.   Ponjavic, A., Ye, Y., Laue, E., Lee, S. F. & Klenerman, D. Sensitive light-sheet microscopy in multiwell plates using an AFM cantilever. *Biomed. Opt. Express* **9**, 5863 (2018).

96.   McGorty, R. *et al.* Open-top selective plane illumination microscope for conventionally mounted specimens. *Opt. Express* **23**, 16142–53 (2015).

97.   Meddens, M. B. M. *et al.* Single objective light-sheet microscopy for high-speed whole-

cell 3D super-resolution. *Biomed. Opt. Express* **7**, 2219 (2016).

98.   Mahou, P., Vermot, J., Beaurepaire, E. & Supatto, W. Multicolor two-photon light-sheet microscopy. *Nat. Methods* **11**, 600–601 (2014).

99.   Kim, K. H. *et al.* Multifocal multiphoton microscopy based on multianode photomultiplier tubes. *Opt. Express* **15**, 11658 (2007).

100.   Martini, J., Andresen, V. & Anselmetti, D. Scattering suppression and confocal detection in multifocal multiphoton microscopy. *J. Biomed. Opt.* **12**, 034010 (2007).

101.   Rakotoson, I. *et al.* Fast 3-D Imaging of Brain Organoids With a New Single-Objective Planar-Illumination Two-Photon Microscope. *Front. Neuroanat.* **13**, 1–14 (2019).

102.   Quicke, P. *et al.* High speed functional imaging with source localized multifocal two-photon microscopy. *Biomed. Opt. Express* **9**, 3678 (2018).

103.   Ingaramo, M. *et al.* Two-photon excitation improves multifocal structured illumination microscopy in thick scattering tissue. *Proc. Natl. Acad. Sci.* **111**, 5254–5259 (2014).

Chapter 2

Multiplexed two-photon excitation spectroscopy of single gold nanorods

Plasmonic metallic nanoparticles are commonly used in (bio-)sensing applications because their localized surface plasmon resonance (SPR) is highly sensitive to changes in the environment. Although optical detection of scattered light from single particles provides a straightforward means of detection, the two-photon luminescence (TPL) of single gold nanorods (GNRs) has the potential to increase the sensitivity due to the large anti-Stokes shift and the non-linear excitation mechanism. However, two-photon microscopy and spectroscopy are restricted in bandwidth and have been limited by the thermal stability of GNRs. Here we used a scanning multifocal microscope to simultaneously measure the two-photon excitation spectra of hundreds of individual GNRs with sub-nanometer accuracy. By keeping the excitation power under the melting threshold, we show that GNRs were stable in intensity and spectrum for more than 30 min, demonstrating absence of thermal reshaping. Spectra featured a signal-to-noise ratio > 10 and a reduced plasmon peak width of typically 30 nm. Changes in the refractive index of the medium of less than 0.04, corresponding to a change in surface plasmon resonance of 8 nm, could be readily measured and over longer periods. We used this enhanced spectral sensitivity to measure the presence of neutravidin, demonstrating the potential of TPL spectroscopy of single GNRs for enhanced plasmonic sensing.

2.1 INTRODUCTION

The unique optical properties gold nanorods (GNRs) have raised interest of multiple fields of research and industry. A weak plasmon-induced optical luminescence signal of bulk gold was first reported by Mooradian[1]. Mohamed et al. later observed that the luminescence of gold could be enhanced by $>10^6$ when exciting rod-shaped gold nanoparticles in resonance with their surface plasmon wavelength, typically in the near-infrared (NIR) part of the spectrum, increasing the quantum yield to $\sim 10^{-4}$ [2]. This field enhancement yields a signal intensity similar to that of quantum dots[3], being bright enough for straight-forward detection of individual particles. GNRs however, do not blink and gold provides excellent biocompatibility, making them more appealing for biological applications. In combination with the reduced absorbance and scattering of NIR light *in vivo*, GNRs form attractive labels for *in vivo* imaging[3,4], but GNRs are also used in cancer therapy, fluorescence enhancement and bio-sensing[5–12].

The longitudinal SPR wavelength of a GNR is almost independent of the rod diameter for diameters < 50 nm, but scales linearly with its aspect ratio[13], yielding resonances between 600 and 1000 nm for aspect ratios between 2 and 5. Because the electric field of the GNR is confined to several 10's of nanometers from the tips of the GNR[14], it creates a very local excitation volume, down to several zeptoliter, which can be readily exploited for single-molecule bio-sensors, even in high concentration solutions [8,15–17]. The distinctive merits of single-molecule detection, i.e. avoiding population and temporal averaging, provide an attractive new range of applications of GNRs, but have to date mainly been demonstrated as proof-of-principle studies, lacking sufficient throughput and bandwidth for widespread exploitation.

Metallic nanoparticles can be used for (bio-)sensing in two manners, as reviewed by Taylor, et al.[18]. First, the intensity of fluorescently labeled analytes is highly enhanced when entering the proximity of the nanoparticle by increases of both the excitation rate and the quantum yield of the fluorophore. This fluorescence enhancement requires sufficient spectral overlap between the plasmon and the spectrum of the label. Various examples of single-molecule detection have been reported[15,19]. When labeling of analytes is not desired, GNRs can also be used as label-free detectors. In this mode, a change in the dielectric properties of the surroundings, as analytes enter the proximity of a GNR[20–22], induces a shift in the plasmon resonance. This plasmon shift can amount up to several nanometers, but is highly dependent on the nanoparticle geometry, binding position and size of the analyte.

Fluorescence enhancement and SPR shifts can readily be measured in bulk[23]. However, bulk analysis yields the average properties of a potentially complex solution and the kinetics can only be extracted indirectly. In the case of GNRs, the measured signal is further convoluted by the poly-dispersity of the particles. Though GNRs can be synthesized with fairly small poly-dispersity[13], the strong geometry-dependence of the SPR compared to its linewidth typically broadens the bulk spectrum as compared to single GNRs. Optimal sensitivity therefore requires analysis of individual GNRs, rather than bulk-averaged signals.

Microscopic techniques provide access to spectroscopic properties of individual GNRs, sparsely distributed on a transparent substrate. Optical signals from GNRs can be divided into

scattering, one-photon luminescence, photo-thermal scattering, and two-photon luminescence. GNRs have a high-scattering cross-section and detection can straightforwardly be multiplexed by wide-field imaging using dark-field excitation[19]. Scattering from other sources than GNRs may be difficult to discriminate in complex environments, limiting the sensing applications to relatively clean samples. Confocal imaging provides better rejection of undesired scattering, at the cost of lower throughput. Because the illumination beam focusses on a single GNR at a time, spectrometric analysis can easily be introduced in the emission path of the microscope, resolving both the transversal SPR at ~500 nm and the longitudinal SPR at NIR wavelengths[24,25]. As particles get smaller, the absorption cross-section becomes dominant over the scattering cross-section. One-photon luminescence is based on detecting the photons that are emitted after radiative relaxation of optically excited GNRs[25,26]. The associated Stokes shift of the emitted light allows for spectral filtering of luminescence from scattering. Next to radiative relaxation there is non-radiative relaxation which results in heating of the GNR. This is exploited in photo-thermal imaging, in which the increased scattering induced by the elevated refraction index of the medium surrounding the GNR, is detected through second non-resonant laser beam[15]. In this chapter we will focus however on two-photon luminescence of single GNRs, which will be further discussed below. Next to detailed insight into their geometry and fundamental photo-physical properties, spectroscopic analysis of single GNRs also is key to design sensors with desired sensitivity and kinetic response[18].

The potential of spectroscopy two-photon luminescence (TPL) of GNRs for sensing applications has yet to be explored. TPL results from successive absorption of two photons, and subsequent rapid radiative decay, which is strongly enhanced in nano particles relative to bulk gold. The quadratic dependence of the TPL signal on excitation power produces sharper plasmon resonance peaks compared to single-photon microscopy. Wang et al. for example measured TPL intensity of single GNRs with a fixed excitation wavelength of 820 nm, which indeed resulted in a narrower linewidth of the SPR compared to the bulk absorption spectrum[3]. Zijlstra et al. and Molinaro et al. also showed TPL excitation spectra of a single GNR[27,28]. However, these spectral measurements were rather limited in both sample size and spectral resolution, due to manual laser tuning and the confocal nature of typical two-photon setups.

Another major obstruction for using TPL of GNRs in sensing applications is their limited thermal stability[29–34]. As exploited by photo-thermal imaging, on-resonance excitation leads to heating of GNRs, which can result in temperature increases of 10s to 100s of degrees[29]. Thermally induced diffusion of surface atoms, which happens at temperatures far below the bulk meting temperature of gold, reduces the aspect ratio of GNRs and therefore drastically changes the longitudinal plasmon resonance[34]. The high-intensity pulsed laser excitation required for TPL results in reshaping at powers of several mJ/cm^2. Next-to stability of the optical signal, elevated temperatures are also detrimental for the stability of the biomolecules, so reduction of photothermal effects in TPL is crucial for biological applications.

Here we present wide-field two-photon spectroscopy of single GNRs, using an automated tunable Ti:Sa laser in combination with a multifocal microscope. Scanning an area of 60 by 60 μm with 625 focused laser beams at framerate of several frames per second yielded rapid, high signal-to-noise, multiplexed optical detection of hundreds of GNRs. By tuning the excitation wavelength, we measured individual TPL excitation spectra and showed that these were stable

for 10s of minutes. Finally, we resolved changes in the refractive index of the surrounding medium similar to those expected from single-molecules to illustrate the potential of TPL of GNRs for bio-sensing applications.

2.2 MATERIALS AND METHODS

Microscopy setup. A tunable near-IR Ti:Sa laser (Coherent, Chameleon Ultra) was coupled into a home-build two-photon multifocal microscope, depicted in Figure 2.1a. A diffractive optical element (DOE, custom made by Holo-eye) diffracted the laser beam into an array of 25x25 foci. A fast-scanning mirror (Newport, FSM-300-1) driven by an Archimedean spiral rapidly scanned the beams yielding a fairly homogeneous wide-field illumination, as characterized before[4]. The laser beams were focused using a 60X NA 1.49 TIRF objective (Nikon, CFI Apochromat TIRF 60XC Oil), illuminating area of 60x60 µm^2, shown in Figure 2.1b. A single period of the spiral scan took 100 ms and was synchronized with the image integration time. Based on the scan pattern and point spread function, we estimate the duty cycle for illumination of a single location in the sample to be around 2%. The wavelength for excitation was automatically tuned over the range of 720 - 950 nm. Polarization of the excitation light was controlled by inserting a half wave plate (Thorlabs, AHWP05M-980) mounted stepper-motor stage. For circularly polarized light the quarter wave plate was removed and only a quarter wave plate (Thorlabs, AQWP05M-980) was included. TPL was collected by the same objective, filtered with a dichroic mirror (Semrock, 700dcxr) and a 720 nm short pass filter (Semrock, FF01-720-SP) and focused on a 512x512 pixel EM-CCD camera (Photometrics, QuantEM 512SC). Using self-written LabVIEW (National Instruments) software, the laser, scanning mirror, stepper motor and camera were controlled in synchrony, to record time traces in which either polarization or wavelength were scanned, see Figure 2.1c. For measurements in which the refractive index of the medium was varied and for neutravidin-sensing, we used a 25X NA 1.1 water dipping objective (Nikon, CFI75 Apochromat 25XC W) and a back-illuminated 2048x2048 sCMOS camera (Photometrics, PRIME BSI), resulting in a 145x145 µm^2 field of view.
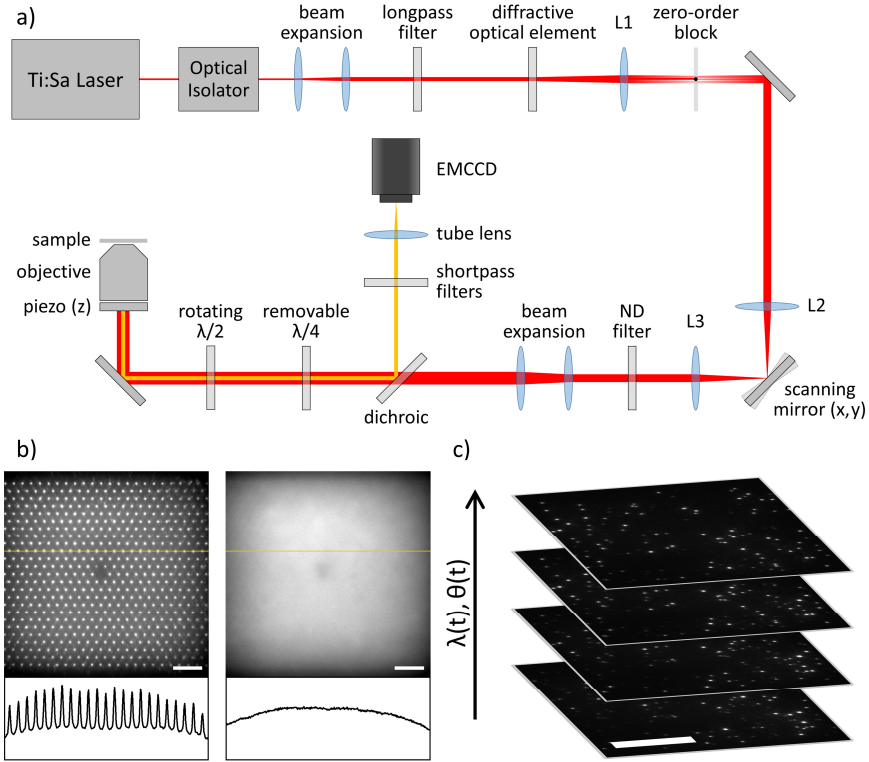
Figure 2.1: Multifocal two-photon laser scanning microscopy setup for high-throughput microscopy and spectroscopy. (a) Schematic overview of the setup. The laser beam is diffracted in an array of 25x25 foci by a diffractive optical element (DOE). (b) A wide-field excitation pattern is generated by spiral scanning the DOE pattern within the exposure time of the camera. (c) A stack of 2D images of GNRs dispersed on a glass slide. The polarization (θ) and wavelength (λ) are changed per slice, resulting in spectral characterization of the GNRs. Scale bar = 30 μm.

Sample preparation. Glass coverslips were rinsed with ethanol and dried in a stream of nitrogen. 10 μm microliter of GNRs (Nanopartz, A12-10-808) diluted in 100 μl of distilled water and were spin-coated in three steps: 200 rpm for 5 seconds, 600 rpm for 15 seconds and 1000 rpm for 60 seconds. After deposition, the samples were treated in an UV-cleaner (model No. 42A-220, Jelight company) for 30 minutes.

Data analysis. High intensity peaks in the images were attributed to single (clusters of) GNRs. Regions of interest of 5x5 pixels around each peak were summed and background subtracted, yielding TPL signal I. TPL intensity as a function of the excitation wavelength $λ$ was fitted to a squared Lorentzian:

$$I(λ) = \frac{I_0}{\left(1 + 4(\sqrt{2} - 1)\left(\frac{λ - λ_{SPR}}{ω}\right)^2\right)^2} + C$$

(2.1)

where λ_{SPR} is the SPR, ω the Full Width at Half Maximum of the SPR, I_0 the maximum intensity, and C an offset corresponding to residual background signal.

TPL signal as a function of the polarization angle of the excitation light θ was fitted to:

$$I(\theta) = I_0 \cos^4(\theta + \theta_0) + C \qquad (2.2)$$

with θ_0 being the orientation of the GNR relative to the polarization angle of the laser.

Scanning Electron Microscopy. For scanning electron microscopy (SEM) measurements, GNRs were spin-coated on an indium tin oxide (ITO) coated cover glass (SPI Supplies, 06480-AB), following the same cleaning and deposition procedure as for regular slides. Using a diamond tipped pen, a cross was scratched in the glass surface to provide a reference point for correlating the two microscopy modalities. The sample was first imaged in the two-photon microscope, after which it was placed in the SEM (FEI, Nova NanoSEM).

Sucrose solutions. Sucrose solutions in HPLC grade water were used to control the refractive index of the medium. The refractive index of each sucrose solution was measured using a refractometer (Carl-Zeiss). To facilitate exchange of solutions, measurements were performed in flow cells made from two glass coverslips that sandwiched a piece of double sided tape with cut out flow channels into which fluids were pipetted.

Neutravidin detection. Neutravidin sensing measurements were performed in similar flow cells as the sucrose experiments. One-step passivation of the glass coverslip was performed, following the protocol of Gidi et al. with a few modifications[35]. Glass coverslips were cleaned with an UVO cleaner for 10 minutes. After UVO treatment, coverslips were put in a petri dish containing desiccant (i.e. calcium chloride) and pre-heated in an oven at 90 ^{0}C for 5-10 minutes to further ensure water-free conditions. To graft the silane PEG azide (SPA) on the coverslip's surface, 1 ml of 0.1% SPA in anhydrous DMSO solution was evenly spread on the coverslip's surface and heated at 90 ºC for 30 minutes. Coverslips were rinsed with 1 ml HPLC grade water and dried under a continuous stream of N_2 to remove excess SPA. After which the flow cells were assembled.

Four oligo sequences were purchased (Intergrated DNA Technologies, USA), of which the specific sequences can be found in Table 2.1. All oligo's were prepared in Tris buffer (pH =7.2).

Oligo sequence #	Sequence & base pair (bp) length
OS1	/5DBCOTEG/AAATTATAACTATTCCTA (18 bp)
OS2	TAGGAATAGTTATAAAAA/3DTPA/ (18 bp)
OS3	GGTGGTGGTGGTTGTGGTGGTGGTGGAAAAAAAAA/3DTPA/ (35 bp)
OS4	ACCACCACCACCAAA/3Bio/ (15 bp)

Table 2.1: The sequences of the oligo's used for the neutravidin sensing experiments.

GNRs (Nanopartz, A12-10-808) were conjugated with OS2 and OS3, following a conjugation protocol from J. Li, et al.[36]. In short, GNRs were mixed with 0.02% sodium dodecyl sulfonate (SDS), 1x tris-borate-EDTA (TBE) and 500 mM NaCl (pH=3.5). Oligo OS2 and OS3 were added with a 1:1000 GNRs-oligo ratio and the whole mixture was incubated for 30 minutes mounted on a rotator at room temperature. SDS screens the positive charge of the CTAB and assist in the functionalization of the GNRs with the thiolated oligo's. The GNR-oligo pellets were separated from the supernatant by centrifuging at 8000 rpm for 30 minutes. The GNR-oligo was reconstituted in the Tris buffer and stored at 4 °C for future use.

50 µl of oligo OS1 [3.33 µM] was incubated in the channels of the flow cells for 1 hour at the room temperature to allow the copper free Click Chemistry of DBCO and azide. The DBCO at 5' end of the oligo covalently binds to the azide of the SPA grafted on the coverslip's surface. Next, the flow cells were incubated with 50 µl of the GNR-oligo OS2, OS3 solution for further 15-30 minutes to allow the annealing of oligo OS1 and OS2. After that, the flow cells were rinsed with 200 µl Tris buffer. The flow cells were either subsequently used or stored at 4 °C for future experiments.

Neutravidin was mixed with oligo OS4 at a ratio of 1:4 in Tris buffer (pH=7.2). Oligo OS4 was annealed with oligo OS 3 on the GNRs and the biotin at 3' end of the oligo was conjugated with the neutravidin (a final concertation of 25 nM). The samples were ready for the measurement.

The average of the selected time traces was normalized (I_{norm}) and weighted according to:

$$I_{norm}(t) = \frac{\sum_n (I_n(t) * s_n)}{\sum_n |s_n|} \tag{2.3}$$

where $I_n(t)$ is the signal intensity at time t for trace n and s_n the sensitivity of trace n at the excitation wavelength as measured from the excitation spectra prior to the time trace measurement.

The standard deviation of the normalized intensity SD_{norm} was defined according to:

$$SD_{norm}(t) = \frac{\sum_n \left((I_n(t)^2 - \bar{I}(t)^2) * s_n\right)}{\sum_n s_n{}^2} \tag{2.4}$$

where the signal per trace I_n at time t is subtracted by the average signal of all selected traces $\bar{I}$ at time t.

2.3 RESULTS

To identify and characterize the TPL signal of single GNRs, we first compared TPL imaging with scanning electron microscopy (SEM) images. SEM readily showed the location, geometry and orientation of single GNRs. Figures 2.2a and 2.2b show that the positions of the GNRs as identified by SEM and TPL imaging are highly correlated. The orientation of individual rods was confirmed by TLS imaging as a function of the polarization angle of the excitation beams. The corresponding polarization spectra, an example is shown in Figure 2.2c, follow eq. 2.2 and readily resolve the orientation of each rod with a standard error of fit of less than 1 degree. Differences between the orientation as obtained by TPL and from the SEM images were within 10 degrees and may originate from optical aberrations in the excitation and/or imaging path. Nevertheless, the good agreement between the SEM and TPL imaging confirms that indeed single GNRs can be identified using TPL, and that successive wide-field two-photon imaging can accurately resolve the orientation of these.
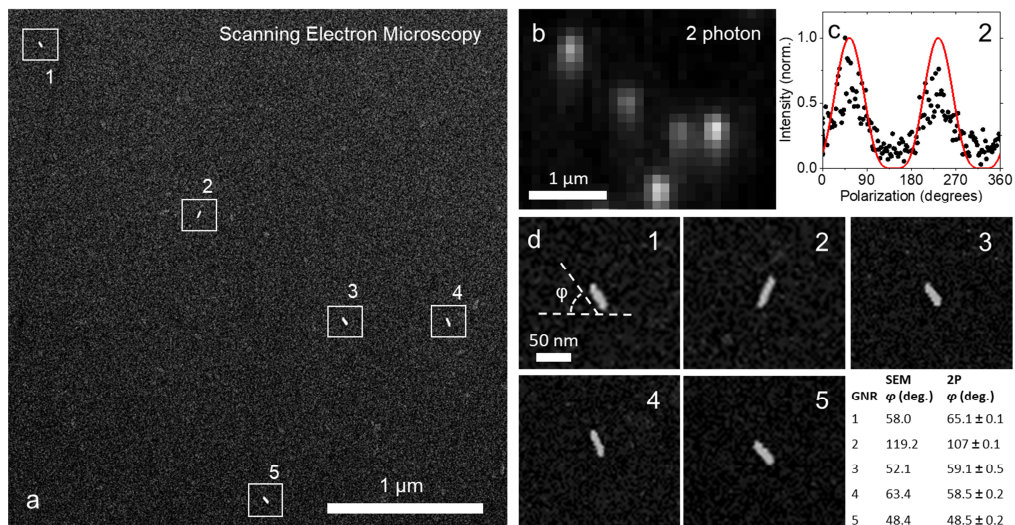
Figure 2.2: Correlated light and electron microscopy (CLEM) of single gold nanorods. (a) Scanning electron microscopy image of single GNRs dispersed on an ITO-coated glass substrate. (b) Two-photon image of the same GNRs as in (a). (c) Orientation of the rods in two-photon microscopy is measured by rotating the polarization of the linear excitation light. (d) GNR close-ups from the electron microscopy image. The orientation of the GNRs is determined by fitting an ellipsoid.

Similar to obtaining polarization spectra, we measured excitation TPL spectra of single GNRs in wide-field by scanning the excitation wavelength from 730 to 900 nm in successive images. Figure 2.3a shows the TPL image of a typical field of view of GNRs deposited on a glass coverslip and immersed in water. The background-corrected signal intensity of the GNRs varied between 9 and 140 kHz. Intensity can however not be used to identify single GNRs as differences in intensity can arise from different sizes of the GNRs or from diverse aspect ratios

which lead to different excitation efficiency when exciting at a fixed wavelength. Moreover, clusters of multiple GNRs may result in a single diffraction limited spot that cannot be differentiated from a single GNR based on size. The excitation spectra however, were more informative. The TPL excitation spectra of six GNRs are plotted in Figure 2.3b. Spectra were fitted to a squared Lorentzian (eq. 2.1) which is characteristic for two-photon excitation. The spectrum of area 4 however, showed two distinctive peaks and better matched product of two squared Lorentzians, suggesting two GNRs in a single spot. Figure 2.3c and d show the results of fitting TPE spectra of hundreds of GNRs measured in three field-of-views. All fits to eq. 2.1 with an r-squared value larger than 0.6 were included in the analysis. The distribution of SPRs in this population of GNRs varied in the range of 730-850 nm, largely resembling the bulk absorption spectrum, though SPR dropped more rapidly after 825 nm in single GNR measurements. This probably reflects the reduced intensity of our laser at larger wavelength. The power spectrum of the laser is plotted for reference in supplementary figure S2.1. Figure 2.4b shows the width of the TPE spectra of 478 single GNRs, yielded a Full-Width-at-Half-Maximum of 31 ± 1 nm (mean ± sd). The very narrow distribution not only reflects the very homogeneous optical properties of the batch of GNRs, it also demonstrates the accuracy of TPL excitation spectroscopy using scanning multifocal microscopy.

For bio-sensing applications, it is important that the SPR of single GNRs is stable over time. Absorption of intense femtosecond pulses can lead to heat-induced reshaping of the GNR, resulting in a blue-shift of the spectrum. We mapped the stability of GNRs during continuous spectral measurements by sweeping the excitation wavelength between the range of 730 and 850 nm every 25 seconds. Figure 2.4a shows the changes in excitation spectrum of a GNR with a laser power of 4.1 mW. We observed reshaping of the GNR from 780.7 nm to 755.0 nm at a rate of 2.3 nm per sweep. At a power of 1.6 mW (2.56 μW/focus) however, the spectrum was quite stable, as shown in Figure 2.4b. At the start of the measurement we fitted the SPR at 766.4 nm. The last spectrum, after 216 measurements, yielded an SPR at 766.8 nm, indicating the absence of reshaping. We estimate this laser power to be equivalent to approximately 31 fJ per pulse. Indeed, this laser power is below the reported damage threshold of 60fJ[1], demonstrating that at sufficiently low excitation power two-photon excitation does not affect the stability of a GNR.
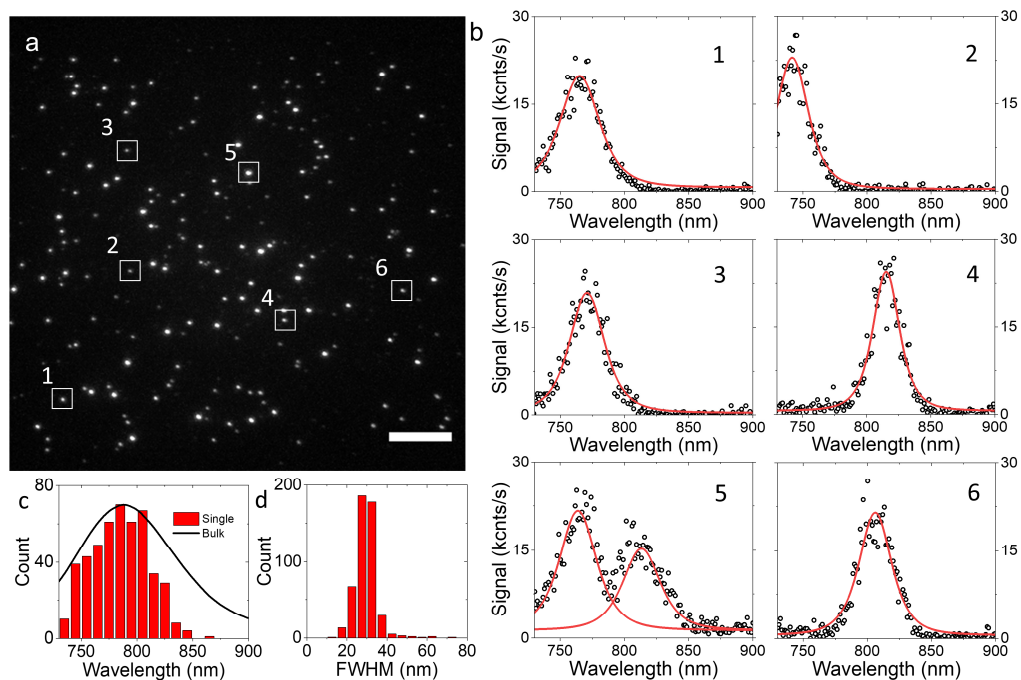
Figure 2.3: Multiplexed two-photon spectroscopy reveals excitation spectra of individual GNRs. (a) The spectra are acquired in parallel within the field of view of the camera. (b) Spectra of single rods are fitted to a squared Lorentzian (eq. 2.1). The spectrum of GNR 4 is fitted to two squared Lorentzians. (c) The distribution of SPRs measured in multiple field-of-views compared to the bulk spectrum. (d) The FWHM of the two-photon spectra shows an average width of 31 nm. Parameters are acquired from fitting eq. 2.1 to the raw data. Scale bar = 10 µm.

The trends observed in these two GNRs were representative of most GNRs. Figure 2.4c shows the spectral drift of 4 other GNRs as well as the average trend for 49 GNRs. Differences in reshaping rate probably reflect differences in GNR size, as larger GNRs will heat faster due to a larger absorption cross-section. The SPR stabilized around 725 nm. This probably reflects the reduced laser power at smaller wavelengths. At 1.6 mW, all spectra remained largely stable, as shown in Figure 2.4d. Only in the first wavelength-sweep, did we observe a small shift for some GNRs, which we tentatively attribute to laser induced changes in the immediate surrounding of the GNRs, rather than reshaping of the GNR itself. In any case, the spectrum of individual GNRs was stable for tens of minutes, opening the way for GNR based label-free sensing applications using TPL.

Figure 2.4: Gold nanorods remain stable during nearly 30 minutes of two-photon excitation. (a) Spectrogram of one GNR as the excitation wavelength is continuously swept back and forth during the measurement. The bottom graph shows the spectrum at the start of the measurement (red) and at the end (blue). (b) Spectrograph and corresponding graph of a single GNR when laser power is reduced by 40% to ±31 fJ. The SPR remains within 1 nm of the SPR measured at the start of the measurement. (c) The SPRs of mu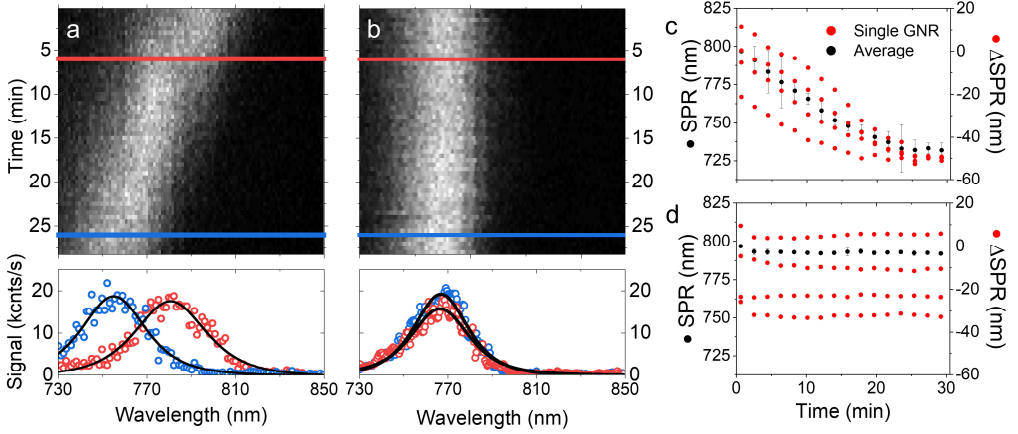ltiple rods with the laser power at ±75 fJ per pulse. Single rods are depicted in red and the average in black. (d) SPRs of multiple rods with lower excitation power.

To demonstrate the sensitivity of TPL spectroscopy on single GNRs, we measured their spectral response when changing the refractive index of the medium from that of water (n=1.333) to two different sucrose solutions. The bulk spectrum, as plotted in Figure 2.5a, red-shifted by 12 and 14 nm when the refractive index increased from 1.333 to 1.376 and subsequently to 1.432. This spectral shift corresponds to a sensitivity of 255 nm/refractive index unit (RUI) for this batch of GNRs. The TPL spectra of single GNRs showed a similar trend as plotted in Figure 2.5b and c. By only comparing the shift, we obtained a narrow distribution of changes in SPR for a large population of GNRs. A shift 8 ± 3 nm was observed when going from n = 1.333 to n = 1.376, 12 ± 7 nm when changing from n = 1.376 to n = 1.432, and 21 ± 8 nm when the medium was changed from n = 1.333 to n = 1.432. The change in SPR was reversible as changing the medium back from n = 1.432 to n = 1.333 reduced the SPR by -26 ± 9 nm. Despite that the SPR varied over more than 80 nm between GNRs, the shift of individual GNRs was very reproducible. In Figure 2.5e the SPRs for a number of GNRs are plotted as a function of the refractive index of the medium. The majority of the GNRs showed a linear increase in their SPR, though some deviated slightly from the linear trend. The slope is independent from the location of the SPR. The average change in SPR was proportional with Δn, as shown in figure 2.5d and yielded a slope 237 ± 9 nm per refractive index unit, in fair agreement with the bulk value.
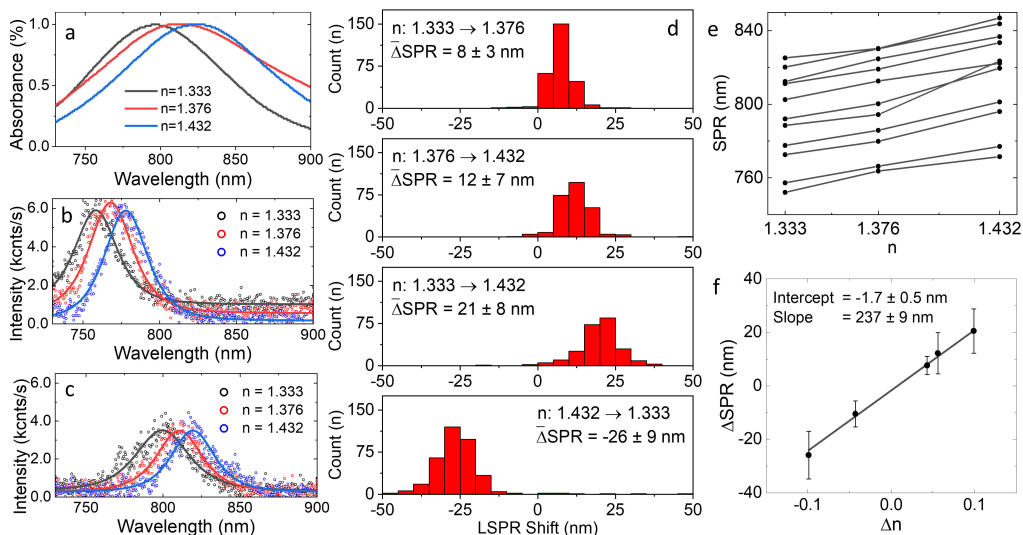
Figure 2.5: The LSPR shift of individual gold nanorods is resolved by two-photon spectroscopy. (a) UV-VIS spectra of bulk solutions of GNRs in: water, 30% sucrose and 70% sucrose solutions, respectively. (b,c) The spectrum of a GNR in water and the two different solutions of sucrose. Both rods show a red-shift when the refractive index is increased. (d) The $\overline{\Delta}$SPR of single GNRs when changing the refractive index of the medium. (e) The SPRs of individual GNRs as it shifts with different refractive indexes. (f) The $\overline{\Delta}$SPR as it is plotted against the change in refractive index. The data is fitted to a linear function.

Next we ventured towards single-molecule sensing experiments. Prior to the measurement, GNRs were functionalized with two types of oligo's. One oligo sequence (OS) for immobilization of the GNR on the glass and another for specific and long-lasting binding to analytes featuring a third complementary OS, see Figure 2.6a. After GNRs were immobilized on the glass surface, the excitation spectrum was measured by sweeping the laser from 730 nm to 900 nm while taking consecutive images. SPR peaks of the rods were fitted to a 2D Gaussian, and the corresponding amplitudes were used to produce an excitation spectrum for every rod in the FOV. The laser power was increased to 3.0 mW to improve SNR at a trade-off of rod stability. We found that most of the rods were stable and were suitable for sensing experiments. Once the excitation spectra were acquired, the wavelength was fixed at 800 nm and the luminescence of each GNR was measured continuously. A solution containing 25 nM neutravidin-oligo complex was flushed in the flow cell after 120 seconds of imaging. The complementary sequences of OS3 and OS4 allowed for specific binding of the neutravidin to the GNRs. After 380 seconds, a second excitation spectrum was taken to assess SPR shifts. The excitation spectra were fitted to a Lorentzian squared (eq. 2.1). All spectra with a FWHM larger than 35 nm were discarded from further processing to exclude GNR clusters from the data. After selection, the measurement yielded 82 traces. A control measurement, where only buffer was flushed in the flowcells, yielded 73 traces.

Figure 2.6b shows the TPL spectra of a rod before and after neutravidin was added to the medium. The SPR was red-shifted by 15 ± 1 nm, indicating an increase of the local refractive index. The initial sensitivity of the GNR is around 25 photons/sec/nm based on the derivative

of the fitted Lorentzian squared. Note that the sensitivity increases to 50 photons/sec/nm when the SPR red-shifts, as the rod is excited at a steeper part of its SPR spectrum. In Figure 2.6c, the signal intensity remained relatively stable during the first 120 seconds of the measurement. Upon flushing-in oligo-neutravidin solution, the signal intensity increased, which we attribute to a red-shift of the SPR. Discrete steps of approximately 212 photons/sec can be discerned in the time trace. Based on the sensitivity corresponds to a 15 nm red shift of the SPR. For such a large change, it is more plausible that multiple neutravidin molecules bind to the GNR. The signal intensity decreased after 320 seconds, suggesting that the rod reshaped when excited at a higher absorption cross section. However, the spectrum that was measured afterwards showed a red-shifted peak, relative to the original spectrum, suggesting that desorption mag also have happened.

A similar response was seen for the rod in Figure 2.6d and e. Initial signal intensity of the time trace is 1019 ± 227 photons/sec. It decreased instantly to 357 ± 164 photons/sec after addition of neutravidin, suggesting multiple binding events. The decrease in signal intensity is conform with the location of the SPR peak relative to the excitation wavelength. More examples of spectra and time traces resembling the ones shown here are plotted in Figure S2.2.

We flushed-in buffer absent of oligo-neutravidin to verify that the SPR perturbations are not caused by proteins and measurement artefacts like instabilities or buffer impurities. The spectra of one GNR from this control measurement, plotted in Figure 2.6f, show that the SPR shifted marginally, by 0.4 ± 0.5 nm, upon flushing in buffer. The time trace of the corresponding GNR, shown in Figure 2.6g, continues as a constant signal intensity. The spectra and time traces plotted in Figure S2.3 illustrate similar behavior of other GNRs measured in this control experiment.
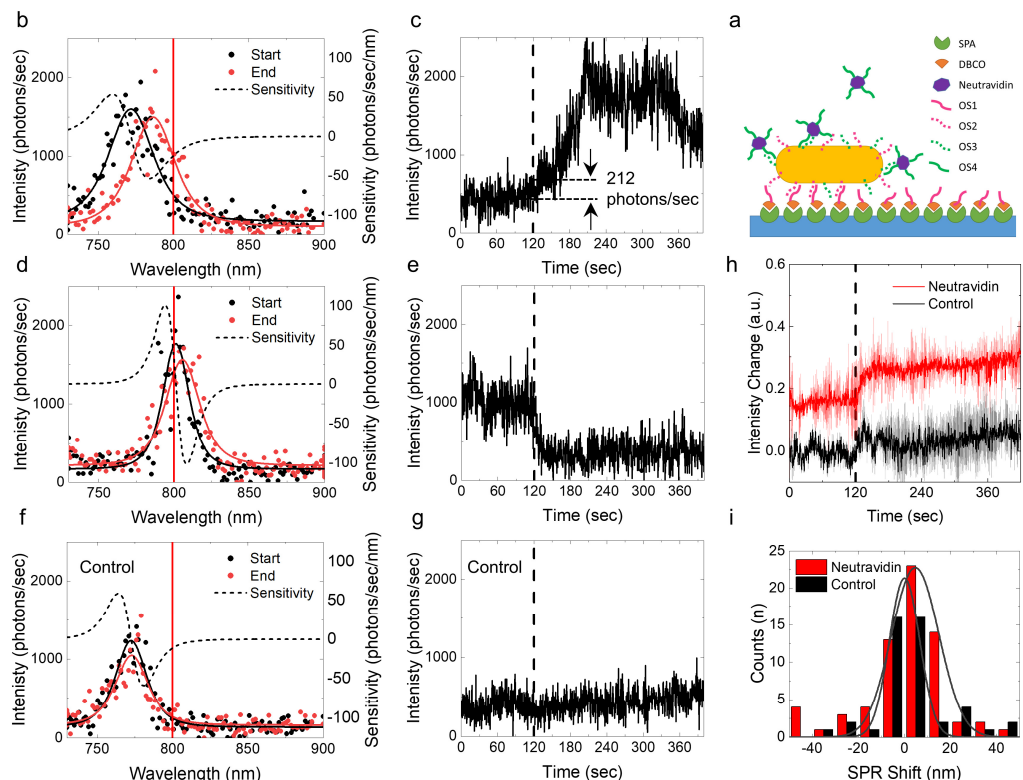
Figure 2.6: Specific binding of DNA oligo-neutravidin complexes induce a shift in the LSPR. (a) Schematic of the experiment. Inside a flow cell, GNRs are immobilized on a glass surface by binding of two complementary oligo strands (pink). A second oligo pair (green) mediates binding of neutravidin to the GNR. (b,d) Excitation spectra of two GNRs before (black) and after (red) addition of neutravidin to the medium. In both instances the LSPR is red-shifted, indicating an increase of the refractive index of the medium surrounding the rod. The data is fitted to a squared Lorentzian (solid lines) according to eq. 2.1. The derivative of the fitted curve (dotted line) indicates the expected signal change upon a shift in the LSPR. Both rods were excited at 800 nm (vertical red line). (c,e) Time traces of the GNRs corresponding to the spectra in the column of *b*. After 120 seconds of imaging (dotted black line), 25 nM neutravidin was flushed in the flowcell, resulting in signal intensity changes. (f,g) The excitation spectra and time trace of a GNR where buffer, instead of neutravidin, was flushed in after 120 seconds of imaging. No LSPR shift was observed and the time trace did not feature significant changes in signal intensity. (h) Normalized and weighted average signal intensity, according to eq. 2.3, of the ensemble of GNRs when flushing in neutravidin (red) or only buffer (black) at 120 seconds (dotted black line). The red trace is offset for clarity, and started at zero. (i) The SPR shift of the ensemble of GNRs. When neutravidin was added the LSPR features an average red shift of 5 ± 1 nm.

To quantify the response of all rods we averaged and weighted the time signals according to eq. 2.3 and plotted the results in Figure 2.6h. The average signal intensity changed 12 ± 4 % with the addition of neutravidin. Flushing-in buffer absent of neutravidin resulted in a shift of 4 ± 2 %. The larger average intensity change when adding neutravidin indicates a specific response. The standard deviation (SD), defined in eq. 2.4, of both averages also increases after 120 seconds. This could be caused by mechanical instabilities, impurities in the solution or reshaping of the GNRs, which would also explain the relative wide distribution of the SPR shift

in Figure 2.5i. By fitting a Gaussian function to the distribution of SPR shifts, we find that the SPR shifts during the control measurement on average 0.1 ± 0.8 nm, with a FWHM $= 16 \pm 3$ nm. Note that the SPR is both red- and blue –shifted without a specific direction, as is also seen in the averaged time trace and depends on the initial position of the SPR relative to the excitation wavelength. The average SPR of the GNRs with oligo-neutravidin was a red-shifted by 5 ± 1 nm, which matches the trend we saw in the average time trace in Figure 2.6h, and confirms a specific interaction of oligo-neutravidin with the GNR.

2.4 DISCUSSION AND CONCLUSION

We measured the TPE spectra of single GNRs in parallel by scanning the excitation wavelength of a multi focal two-photon microscope. The narrow peaks of the plasmon resonances follow a squared Lorentzian dependence, which confirms two photon excitation. Irradiation of rods with an energy estimated at 31 fJ per pulse allowed for stable spectra measurements for nearly 30 minutes. Whereas increasing excitation power to above the threshold level resulted in reshaping accompanied by a blue-shift of the plasmon resonance. We demonstrated that by changing the refractive index of the medium the TPE spectra shifted accordingly. We observed specific interactions of oligo-functionalized GNRs with complementary oligo-neutravidin molecules in solution.

To identify TPL from single GNRs we correlated SEM with two-photon images. Besides SEM, single GNRs were also identified by making use of light polarization and the excitation spectra. Considering the spectra measurements, as shown in Figure 2.3b, clusters of GNRs resulted in a broader SPR because the spectrum is the product of multiple individual rods combined. Previous studies also concluded that the spectrum of a cluster of rods is a combination of multiple single GNRs[37–39]. Discriminating single GNRs from clusters by using light polarization was used as an alternative method. The $\cos^4(\phi)$ dependence on polarization seen in Figure 2.1 for a single rod agrees with earlier findings H. Wang et al. and K. Imura et al., which furthermore confirms that the collected signal originates from a two-photon excitation process [3,40].

The plasmon resonance for single GNRs was determined with sub-nanometer accuracy. The average FWHM we found is $\pm 35\%$ smaller compared to reported one-photon spectra which lies approximately between 45 and 60 nm[6,17,41,42]. Moreover, the width of 24 nm for the narrowest peaks is nearly a factor of two smaller than any reported one-photon spectra we could find. Narrow peaks are preferred for sensing applications as narrower peaks translate to a larger derivative around the SPR and therefore higher sensitivity. We attribute differences in FWHM to inhomogeneity's in the ensemble of GNRs as the width of the plasmon resonance depends on the volume of the rod[43].

TPE spectra from previous studies, although limited in their bandwidth, do provide details about FHWM. Zijlstra et al. measured a reduction in FHWM of approximately 60% when comparing scattering- or one-photon luminescence- to TPE spectra[27]. C. Molinaro et al. showed

that their measured TPE spectra overlaps with the model of absorption calculated using Gans-Mie theory, which describes the scattering and absorbing of small ellipsoid shaped nanocrystals[28]. Considering the differences in SPR width between one- and two-photon excitation, the Gans-Mie model results in reduced peak widths of a factor $2\sqrt{\sqrt{2}-2} \approx 1.29$. Both the findings from Zijlstra and Molinaro fit with our own data, where the narrowest peaks are as narrow as 20 nm, and the broadest around 40 nm.

The location of the SPRs correspond to the absorption spectrum of the bulk solution. A sharp cut-off below 740 nm can be explained by the lower limit of the excitation wavelength at 730 nm, which impairs imaging of the plasmon peak. For wavelengths larger than 850 nm we also do not observe any SPR maxima's. We suspect this to originate from limitations in the DOE pattern by loss of focus caused by chromatic aberrations and lower laser power at these wavelengths (see Figure S2.1). Still, the resulting bandwidth of 120 nm in which we can image GNRs, is sufficient to measure the larger part of the distribution of rods considering the bulk spectrum.

The EM-CCD camera readout for single rods ranged between 15e3 and 20e3 kcounts/sec. Considering the EM-gain of 40 and the quantum efficiency of the camera, the readout signal translates to a photon count of approximately 340 to 450 photons/sec. The luminescence of GNRs is known to reach intensities of thousands of photons per second. However, reshaping of rods due to high laser intensities limits the excitation power and thereby lowering the photon emission from the rods. Nevertheless, SNR is excellent as the non-linear TPE results in an almost negligible background, dominated by readout noise of the camera.

By lowering excitation power under the damage threshold we measured stable TPE spectra. The majority of GNRs blue-shifted their SPR by a few nanometers upon initial irradiation. For these small shifts in wavelength, reshaping does not seem as the underlying mechanism as a change in aspect ratio would induce shifts of an order of magnitude larger[6]. Moreover, Zijlstra et al. showed that for rods with a plasmon resonance between 750 and 800 nm, which roughly corresponds to our distribution of measured rods, reshaping does not occur until 150 fJ of laser power is absorbed by a GNR. Reshaping below the melting temperature of gold was observed by A. Taylor et al.[34]. They showed that their observations fitted well with a surface diffusion model from Mullins. Diffusion around the tips of the rod changes the aspect ratio causing a shift in the plasmon resonance. However, for rods with an aspect ratio between 3.8 and 4.1 – similar to the rods we use – Taylor measured a thermal threshold of approximately 60 and 40 fJ respectively. From these results, we expect that we do not see reshaping but rather that upon initial exposure to the laser beam, sedimented particles and remaining CTAB coating (n=1.435)[44] residing around the rods are ablated from the surface. Increasing the excitation power to above the damage threshold resulted in a linear decrease of the average SPR shift per wavelength sweep between a SPR of 800 and 740 nm. From the results of O. Ekici et al., we expect that the GNRs almost instantaneously reach thermal equilibrium when illuminated in-resonance, as there is enough time for the energy to disperse in the 12.5 ns between each femtosecond pulse of the 80 MHz pulsed laser[45]. Therefore, illuminating the rods in-resonance for longer periods of time result in a linear response of the SPR shift. As the SPR is linearly dependent on the aspect ratio of the GNR, the linear decrease indicates an also linear decrease

in the aspect ratio of the rod. In the oligo-neutravidin measurements we increased laser power to slightly above the damage threshold of the GNRs, which may have resulted in a fraction of unstable rods. The difference in robustness of the GNRs to the laser illumination could arise from the uneven spatial distribution of laser intensity across the FOV or a slightly tilted excitation plane, which would reduce the absorption of a rod.

Our reference measurement for the sensitivity of the GNRs in bulk (Figure 2.5a) yielded in a sensitivity of 255 nm/RUI. This result is higher than the sensitivity of 237 ± 9 nm/RUI we measured for single GNRs in the two-photon microscope. However, differences in SPR shift between individual rods and the bulk solution are to be expected, as sensitivity to refractive index changes is highly dependent on aspect ratio and the rod-to-substrate interface[15,46]. A lower sensitivity for individual rods when compared to bulk was also found by others, and also attributed to the physical hindrance of the substrate with the GNRs. E. Martinsson et al. studied the influence of a negatively charged glass substrate on the SPR of several differently shaped metallic nanoparticles. They measured a reduction in sensitivity of 34% when comparing GNRs in bulk and distributed on glass[47]. Fortunately, we can use the multiplexed capabilities of the setup to select the most sensitive rods from the ensemble.

Additionally, our reported bulk sensitivity of 237 ± 9 nm/RUI for individual rods on a substrate, resembles the findings of other studies. M. Piliarik et al. measured a bulk sensitivity of 140 nm/RUI of GNRs with a dimension of 35 nm x 75 nm (AR = 2.14); Zijlstra et al. a bulk sensitivity of 202 ± 15 nm/RUI with an average GNR size of 37 nm x 9 nm (AR = 4.1); and Martinsson et al. found 255 nm/RUI for rods with an average size of 67 nm x 19 nm (AR = 3.5) [15,47,48]. Differences between sensitivities are attributed to the differences in the shapes of the GNRs. The AR, absolute length and diameter of a nanorod dictates the sensitivity of a GNR for changes in the bulk refractive index, where larger rods with a larger AR have higher sensitivity [49,50].

Spectral studies on gold nanoparticles have been limited to scattering and photothermal microscopy. In terms of *in vivo* environments, these type of experiments are better suited for single cells or organoids. By utilizing the deep-tissue imaging capabilities of two-photon microscopy, one could envision doing spectral studies in larger animals like zebra fish embryos and mice. Besides deeper penetration depth, the low background and sensitivity of TPE would also be of considerable benefits. Sensitivity of the measurements can also be increased by making use of bipyramid-shaped nanoparticles instead of rods. Although thermally more unstable compared to rods, the more confined electrical field around the sharper tips of bipyramids, do result in a higher sensitivity to refractive index changes[5]. For addressing the thermal stability of gold nanoparticles, Y, Chen et al. found that by coating GNRs with a silica layer they were considerable more stable to pulsed laser light as when coated with CTAB or PEG [51].

In our bio-sensing experiments we saw a relatively large shift of the SPR when oligo-neutravidin was added to the buffer solution, which we tentatively attributed to multiple binding events of neutravidin. To estimate how many neutravidin molecules can bind at the sensitive ends of the rods we take an average size of the rod of 40 x 40 x 10 nm^3. Approximately 1/4 of the area would be blocked by the substrate. Thus a rod should have around 235 nm^2 exposed area. The surface area of neutravidin is approximately 22.4 nm^2 and thus around 10 neutravidin

molecules could bind to a rod[52]. Based on streptavidin (53 kDa) experiments by Zijlstra et al., who use similar GNRs as us, we expect a SPR shift a little over 0.5 nm per neutravidin (60 kDa) binding event[53]. Note though that we used a DNA linker to mediate neutravidin-GNR interactions. This yields a larger distance to the GNR and hence a lower sensitivity. Ignoring this difference, a maximum number of ten neutravidin molecules per rod would therefore result in a SPR shift of 5 nm. However, some of our reported spectra feature a spectral shift of up to 20 nm, which could indicate that we measure a larger SPR shift per molecule, or that unspecific binding of impurities in the medium induces an additional red-shift. The average plasmon shift of 4 ± 1 nm of the ensemble of GNRs better matches the shift we expect. We did not observe steps in the time traces, see Figures 2.6e and S2.2d for examples. However, considering a GNR with a sensitivity of 100 photons/sec/nm, a single binding event would change the signal by 50 photons/sec, making it unlikely that the discrete steps we observed were caused by single molecule binding events. The noise on a signal with an intensity of 1019 ± 227 photons/sec, as potted in Figure 2.6e, suggests that detection of single neutravidin molecules would be hampered by a SNR<1. The standard deviation of the signal however, does not correspond with the expected shot-noise of 32 photons/sec. The background noise of the camera appeared to be 99 ± 5 photons/sec (data not shown), which is excessive compared to the dark- and readout-noise of an air-cooled sCMOS camera. Other explanations might be mechanical instabilities of the microscope or temporal fluctuations in the spiral-scanning pattern. Based on the expected SPR shift and the theoretical shot-noise limit, we expect that the setup should be capable of imaging single binding events once GNRs can be imaged at shot-noise limited conditions. Another strategy to improve sensitivity would entail decreasing the linker-size between target molecule and the rod. For example, by using smaller molecules instead of oligo's, neutravidin could move closer to the surface of the rod and experience a stronger field intensity and cause a larger shift in the plasmon resonance[54].

In conclusion, we measured the TPL response on the excitation wavelength of hundreds of GNRs measured in multiplex. The narrow spectra demonstrate the possible application of two-photon microscopy with GNRs to increase the sensitivity of applications based on plasmonic nanoparticles. When ultra-high sensitivity is needed, one can decrease the peak width by almost 60% when moving from one- to two-photon excitation mechanism. Furthermore, combining high sensitivity with multi focal microscopy enables the measurement of GNRs in wide-field – allowing for acquiring statistical significant data within minutes. We demonstrated the ability of the setup to measure the change of the TPL spectra when changing the refractive index of the medium and take the first steps in single molecule bio-sensing. Given the TPL response on the refractive index and the ability to measure GNRs without reshaping, we lay a framework for TPL plasmonic single-molecule sensors.

2.5   SUPPLEMENTARY FIGURES
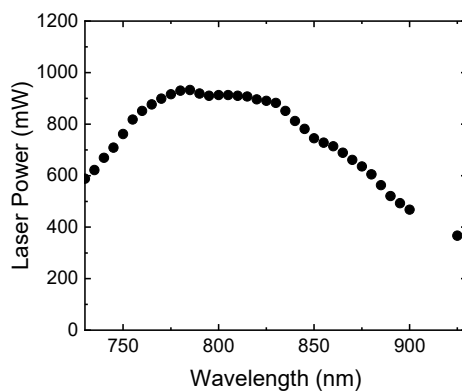
Figure S2.1: Spectrum of the maximum average laser power. Power is measured by directly placing a power meter on top of the objective.
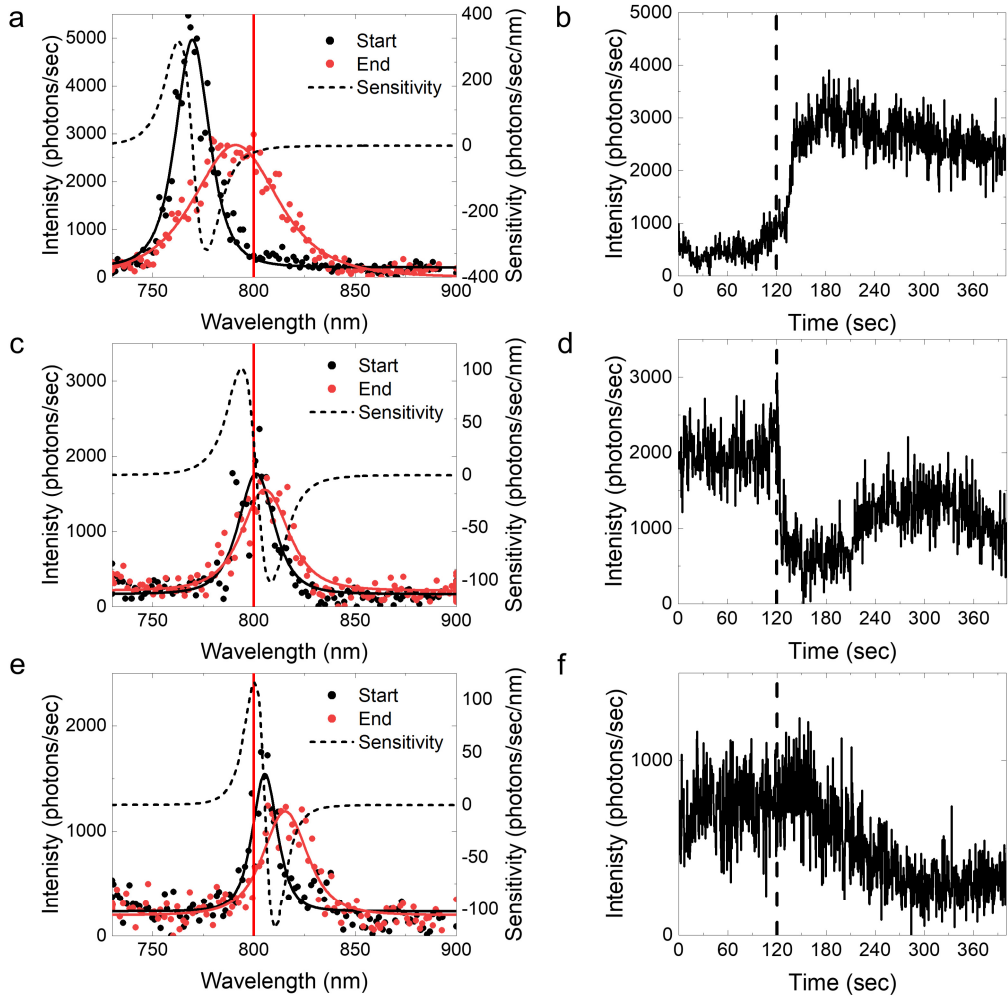
Figure S2.2: Example traces of SPR response when introducing oligo-neutravidin complexes to the surrounding medium of GNRs. (a,c,e) Excitation spectra of single gold nanorods before and after flushing in neutravidin. In all three traces there is a red-shift visible of the LSPR. (b,d,f) Time traces of the GNRs with their respective spectra on the left. Neutravidin was flushed in after 120 seconds of measuring (dotted black line), after which signal intensity starts fluctuating according to the position of the LSPR with the excitation wavelength.
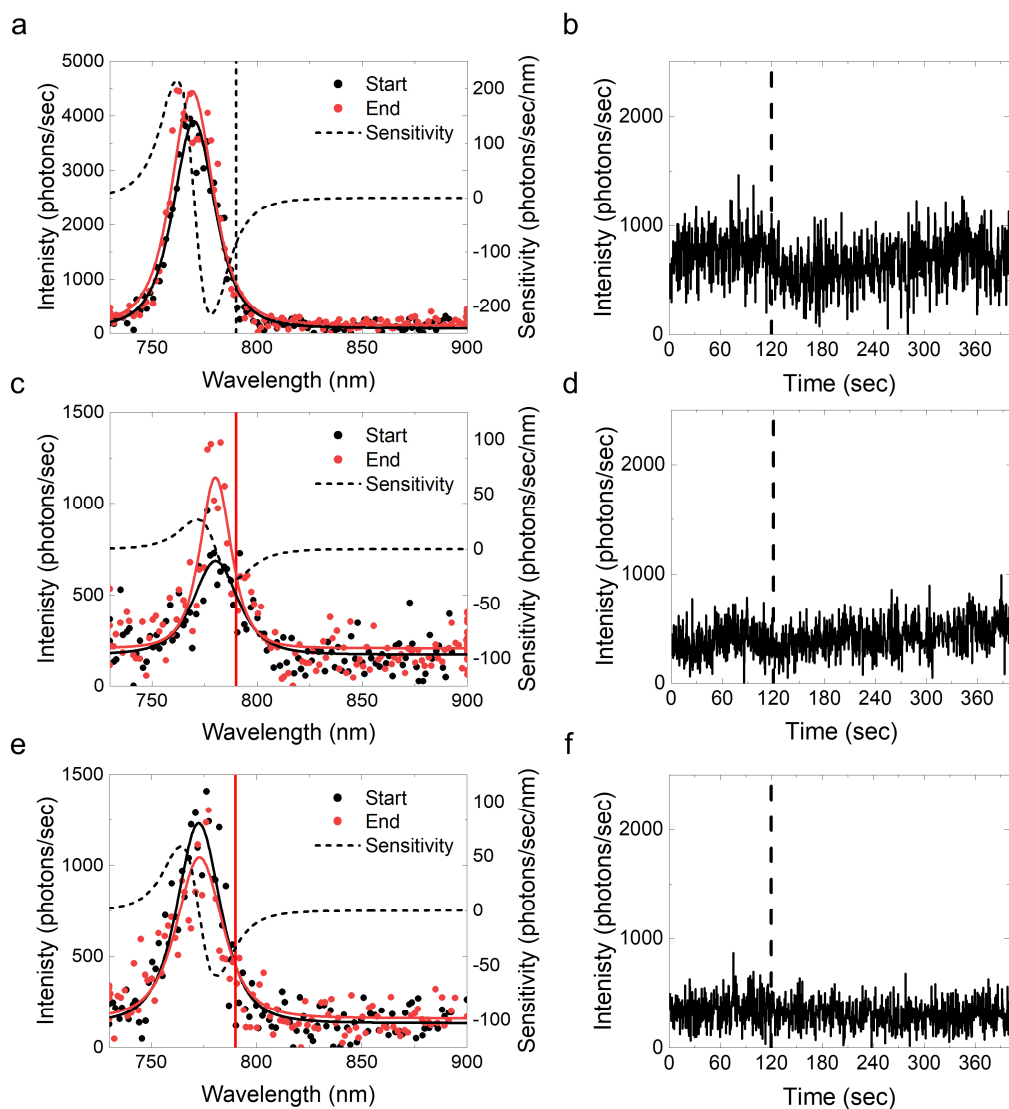
Figure S2.3: Example traces of the LSPR response of GNRs when flushing medium without oligo-neutravidin complexes in the flowcells. (a,c,e) Excitation spectra of single gold nanorods before and after the measurement. No clear LSPR shift is observed. (b,d,f) Time traces of the GNRs with their respective spectra on the left. Buffer was flushed in at 120 seconds of measuring (dotted black line), after which no significant change in signal intensity is observed.

2.6 BIBLIOGRAPHY

1.   Mooradian, A. Photoluminescence of metals. *Phys. Rev. Lett.* **22**, 185–187 (1969).

2.   Mohamed, M. B., Volkov, V., Link, S. & El-Sayed, M. A. The 'lightning' gold nanorods: Fluorescence enhancement of over a million compared to the gold metal. *Chem. Phys. Lett.* **317**, 517–523 (2000).

3.   Wang, H. *et al.* In vitro and in vivo two-photon luminescence imaging of single gold nanorods. *Proc. Natl. Acad. Sci. U. S. A.* **102**, 15752–15756 (2005).

4.   Van den Broek, B., Oosterkamp, T. H. & van Noort, J. A Multifocal Two-Photon Microscopy Setup for Parallel 3D Tracking of Gold Nanorods. *Biophys. J.* **98**, 178a (2010).

5.   Stella M. Marinakos, Sihai Chen, and & Chilkoti*, A. Plasmonic Detection of a Model Analyte in Serum by a Gold Nanorod Sensor. (2007). doi:10.1021/AC0706527

6.   Zhang, W., Caldarola, M., Pradhan, B. & Orrit, M. Gold Nanorod Enhanced Fluorescence Enables Single-Molecule Electrochemistry of Methylene Blue. *Angew. Chemie* **129**, 3620–3623 (2017).

7.   Yu, C. & Irudayaraj, J. Multiplex Biosensor Using Gold Nanorods. *Anal. Chem.* **79**, 572–579 (2007).

8.   Shajari, D., Bahari, A. & Gill, P. Fast and simple detection of bovine serum albumin concentration by studying its interaction with gold nanorods. *Colloids Surfaces A Physicochem. Eng. Asp.* **543**, 118–125 (2018).

9.   Mohammad Eghtedari, † *et al.* High Sensitivity of In Vivo Detection of Gold Nanorods Using a Laser Optoacoustic Imaging System. *Nano Lett.* **7**, 1914–1918 (2007).

10.   de la Zerda, A. *et al.* Optical coherence contrast imaging using gold nanorods in living mice eyes. *Clin. Experiment. Ophthalmol.* **43**, 358–366 (2015).

11.   Ali, M. R. K., Ali, H. R., Rankin, C. R. & El-Sayed, M. A. Targeting heat shock protein 70 using gold nanorods enhances cancer cell apoptosis in low dose plasmonic photothermal therapy. *Biomaterials* **102**, 1–8 (2016).

12.   Riley, R. S. & Day, E. S. Gold nanoparticle-mediated photothermal therapy: applications and opportunities for multimodal cancer treatment. *Wiley Interdiscip. Rev. Nanomedicine Nanobiotechnology* **9**, e1449 (2017).

13.   Ni, W., Kou, X., Yang, Z. & Wang, J. Tailoring longitudinal surface plasmon wavelengths, scattering and absorption cross sections of gold nanorods. *ACS Nano* **2**, 677–686 (2008).

14.   Nusz, G. J., Curry, A. C., Marinakos, S. M., Wax, A. & Chilkoti, A. Rational selection of gold nanorod geometry for label-free plasmonic biosensors. *ACS Nano* **3**, 795–806 (2009).

15.   Zijlstra, P., Paulo, P. M. R. & Orrit, M. Optical detection of single non-absorbing

molecules using the surface plasmon resonance of a gold nanorod. *Nat. Nanotechnol.* **7**, 379–382 (2012).

16. Ament, I., Prasad, J., Henkel, A., Schmachtel, S. & Sönnichsen, C. Single unlabeled protein detection on individual plasmonic nanoparticles. *Nano Lett.* **12**, 1092–1095 (2012).

17. Greg J. Nusz, † *et al.* Label-Free Plasmonic Detection of Biomolecular Binding by a Single Gold Nanorod. (2008). doi:10.1021/AC7017348

18. Taylor, A. B. & Zijlstra, P. Single-Molecule Plasmon Sensing: Current Status and Future Prospects. *ACS Sensors* **2**, 1103–1122 (2017).

19. Beuwer, M. A., Prins, M. W. J. & Zijlstra, P. Stochastic Protein Interactions Monitored by Hundreds of Single-Molecule Plasmonic Biosensors. *Nano Lett.* **15**, 3507–3511 (2015).

20. Olesiak-Banska, J., Waszkielewicz, M., Obstarczyk, P. & Samoc, M. Two-photon absorption and photoluminescence of colloidal gold nanoparticles and nanoclusters. *Chem. Soc. Rev.* **48**, 4087–4117 (2019).

21. Marinakos, S. M., Chen, S. & Chilkoti, A. Plasmonic detection of a model analyte in serum by a gold nanorod sensor. *Anal. Chem.* **79**, 5278–5283 (2007).

22. Ament, I., Prasad, J., Henkel, A., Schmachtel, S. & Sönnichsen, C. Single unlabeled protein detection on individual plasmonic nanoparticles. *Nano Lett.* **12**, 1092–1095 (2012).

23. Wang, D.-S., Hsu, F.-Y. & Lin, C.-W. Surface plasmon effects on two photon luminescence of gold nanorods. *Opt. Express* **17**, 11350–11359 (2009).

24. Funston, A. M., Davis, T. J., Novo, C. & Mulvaney, P. Coupling modes of gold trimer superstructures. *Phil. Trans. R. Soc. A* **369**, 3472–3482 (2011).

25. Wackenhut, F., Failla, A. V. & Meixner, A. J. Multicolor microscopy and spectroscopy reveals the physics of the one-photon luminescence in gold nanorods. *J. Phys. Chem. C* **117**, 17870–17877 (2013).

26. Tcherniak, A. *et al.* One-photon plasmon luminescence and its application to correlation spectroscopy as a probe for rotational and translational dynamics of gold nanorods. *J. Phys. Chem. C* **115**, 15938–15949 (2011).

27. Zijlstra, P., Chon, J. W. M. & Gu, M. Five-dimensional optical recording mediated by surface plasmons in gold nanorods. *Nature* **459**, 410–413 (2009).

28. Molinaro, C. *et al.* Two-Photon Luminescence of Single Colloidal Gold Nanorods: Revealing the Origin of Plasmon Relaxation in Small Nanocrystals. *J. Phys. Chem. C* **120**, 23136–23143 (2016).

29. Ekici, O. *et al.* Thermal Analysis of Gold Nanorods Heated with Femtosecond Laser Pulses. *J. Phys. D. Appl. Phys.* **41**, 185501 (2008).

30. Link, S. & El-Sayed, M. A. Spectroscopic determination of the melting energy of a gold nanorod. *J. Chem. Phys.* **114**, 2362–2368 (2001).

31.   El-Sayed, M. A. Some Interesting Properties of Metals Confined in Time and Nanometer Space of Different Shapes. doi:10.1021/ar960016n

32.   Zijlstra, P., Chon, J. W. M. & Gu, M. White light scattering spectroscopy and electron microscopy of laser induced melting in single gold nanorods. *Phys. Chem. Chem. Phys.* **11**, 5915 (2009).

33.   González-Rubio, G. *et al.* Femtosecond laser reshaping yields gold nanorods with ultranarrow surface plasmon resonances. doi:10.1192/bjp.bp.108.055459

34.   Taylor, A. B., Siddiquee, A. M. & Chon, J. W. M. Below melting point photothermal reshaping of single gold nanorods driven by surface diffusion. *ACS Nano* **8**, 12071–12079 (2014).

35.   Gidi, Y., Bayram, S., Ablenas, C. J., Blum, A. S. & Cosa, G. Efficient One-Step PEG-Silane Passivation of Glass Surfaces for Single-Molecule Fluorescence Studies. *ACS Appl. Mater. Interfaces* **10**, 39505–39511 (2018).

36.   Li, J. *et al.* Simple and Rapid Functionalization of Gold Nanorods with Oligonucleotides Using an mPEG-SH/Tween 20-Assisted Approach. doi:10.1021/acs.langmuir.5b01680

37.   Funston, A. M., Davis, T. J., Novo, C. & Mulvaney, P. Coupling modes of gold trimer superstructures. *Phil. Trans. R. Soc. A* **369**, 3472–3482 (2011).

38.   Garai, M., Zhang, T., Gao, N., Zhu, H. & Xu, Q.-H. Single Particle Studies on Two-Photon Photoluminescence of Gold Nanorod-Nanosphere Heterodimers. *J. Phys. Chem. C* **120**, 11621–11630 (2016).

39.   Wu, J. *et al.* Angle-resolved plasmonic properties of single gold nanorod dimers. *Nano-Micro Lett.* **6**, 372–380 (2014).

40.   Imura, K., Nagahara, T. & Okamoto, H. Near-field two-photon-induced photoluminescence from single gold nanorods and imaging of plasmon modes. *J. Phys. Chem. B* **109**, 13214–13220 (2005).

41.   Ruijgrok, P. V., Verhart, N. R., Zijlstra, P., Tchebotareva, A. L. & Orrit, M. Brownian Fluctuations and Heating of an Optically Aligned Gold Nanorod. *Phys. Rev. Lett.* **107**, 037401 (2011).

42.   and, K.-S. L. & El-Sayed*, M. A. Dependence of the Enhanced Optical Scattering Efficiency Relative to That of Absorption for Gold Metal Nanorods on Aspect Ratio, Size, End-Cap Shape, and Medium Refractive Index. (2005). doi:10.1021/JP054385P

43.   Henkel, A. *et al.* Narrowing the Plasmonic Sensitivity Distribution by Considering the Individual Size of Gold Nanorods. *J. Phys. Chem. C* **122**, 10133–10137 (2018).

44.   Kekicheff, P. & Spalla, O. Refractive Index of Thin Aqueous Films Confined between Two Hydrophobic Surfaces. *Langmuir* **10**, 1584–1591 (1994).

45.   Ekici, O. *et al.* Thermal analysis of gold nanorods heated with femtosecond laser pulses. *J. Phys. D. Appl. Phys.* **41**, (2008).

46.   Becker, J., Trügler, A., Jakab, A., Hohenester, U. & Sönnichsen, C. The Optimal Aspect Ratio of Gold Nanorods for Plasmonic Bio-sensing. *Plasmonics* **5**, 161–167 (2010).

47.   Martinsson, E. *et al.* Influence of Surfactant Bilayers on the Refractive Index Sensitivity and Catalytic Properties of Anisotropic Gold Nanoparticles. *Small* **12**, 330–342 (2016).

48.   Piliarik, M., Kvasnička, P., Galler, N., Krenn, J. R. & Homola, J. Local refractive index sensitivity of plasmonic nanoparticles. *Opt. Express* **19**, 9213 (2011).

49.   Nusz, G. J., Curry, A. C., Marinakos, S. M., Wax, A. & Chilkoti, A. Rational selection of gold nanorod geometry for label-free plasmonic biosensors. *ACS Nano* **3**, 795–806 (2009).

50.   Chen, H., Kou, X., Yang, Z., Ni, W. & Wang, J. Shape-and Size-Dependent Refractive Index Sensitivity of Gold Nanoparticles. doi:10.1021/la800305j

51.   Chen, Y.-S. *et al.* Enhanced thermal stability of silica-coated gold nanorods for photoacoustic imaging and image-guided therapy. *Opt. Express* **18**, 8867–78 (2010).

52.   Rosano, C., Arosio, P. & Bolognesi, M. The X-ray three-dimensional structure of avidin. *Biomol. Eng.* **16**, 5–12 (1999).

53.   Zijlstra, P. & Orrit, M. Single metal nanoparticles: optical detection, spectroscopy and applications. *Reports Prog. Phys.* **74**, 106401 (2011).

54.   Omair, Z. & Talukder, M. A. Sensitivity Analysis of Gold Nanorod Biosensors for Single Molecule Detection. *Plasmonics* **14**, 1611–1619 (2019).

Chapter 3

Two-photon multifocal microscopy for *in vivo* single particle tracking

Microscopic tracking of single particles by fluorescence microscopy is a powerful technique to study life processes at the molecular scale. Whereas single-particle, and even single-molecule, tracking in individual cultured cells has been used widely and yielded spectacular results, nanometric imaging and tracking in larger multicellular samples remains challenging, due to the increased scattering of light, increased out-of-focus fluorescence and reduced resolution in the third dimension. Using two-photon – rather than one photon – excitation relieves these constraints but requires a higher excitation power, which is commonly achieved using confocal microscopy. However, such a serial acquisition scheme severely limits the frame rate and generally can not resolve the fast dynamics of nanometric particles. Moreover, the high power that is required to obtain sufficient contrast severely reduces the photostability of commonly used fluorescent labels. Here we explore the possibilities of scanning two-photon multifocal microscopy for *in vivo* single particle tracking. We show that the combination of a modern scientific CMOS camera, which features a higher sensitivity and very low dark signal, with a reduced power per focus and a reduced duty cycle for excitation yields extraordinary low bleaching rates, framerates larger than 10 Hz and a field of view of 100's of microns while maintaining the advantages of two photon excitation. We demonstrate the use of this novel microscopy modality in zebra fish embryos and rapeseed pollen, and show that it allows for multicolor imaging, using spectral selection in either excitation or emission. Furthermore, we show that single gold nanorods in the veins of zebra fish embryos can be tracked with nanometric accuracy, resolving temporal fluctuations in bloodstream velocity. The unprecedented photostability in combination with the reduced background suggests that it should be possible to resolve single fluorescent proteins *in vivo* with two-photon multifocal microscopy.

3.1 INTRODUCTION

Single particle tracking (SPT) can uniquely reveal molecular dynamics in cells[1]. The brightness and longevity of the used chromophore is an important metric for a SPT measurement. Cellular proteins can be fluorescently labeled via genetic incorporation for highly specific tagging with minimal steric hinder[2]. Inside larger organisms however, scattering and absorption of the weak signal obstructs the detection of single fluorophores. Also, once a fluorophore is bleached the tagged structure can no longer be detected. Markers such as quantum dots[3], gold nanorods[4] (GNRs) or liposomes[5] tackle the limited signal and photostability of fluorescent proteins while bio-functionalization allows for specific labeling [6]. A protein can be tracked for much longer as signal originates from a multitude of fluorophores or luminescence. In larger organisms however, out-of-focus fluorescence and scattering lowers signal-to-noise ratio (SNR) which impedes detection and tracking of particles. Spinning-disc microscopy is able to detect particles at larger depths by rejecting photons outside the focal plane. Still, excitation of out-of-focus fluorophores is wasteful and the sample is more prone to photobleaching or phototoxicity.

Two-photon microscopy (TPM) tackles out-of-focus fluorescence by confining excitation to the focus of the objective[7,8]. With signal solely originating from the focus, depletion of out-of-focus fluorophores is eliminated while background is greatly reduced without the need for a pin-hole aperture. Moreover, the near-infrared excitation wavelength is less prone to absorption and scattering in tissue compared to visible wavelengths[9]. This further reduces photo-toxicity, autofluorescence and increases the depth at which particles can be detected[10]. These advantages make TPM a promising technique for deep and long time-lapse imaging. However, single-beam scanning and the relative weak two-photon absorption cross section of fluorophores impedes imaging acquisition times – making TPM unsuitable for SPT[11].

Two-photon multifocal microscopy (TPMM) improves acquisition speeds by multiplexing the excitation beam. Distributing a high laser power (2-3 Watt) over multiple beamlets increases scanned volume proportional to the number of foci. Multiplexing of the excitation beam can be achieved via passive components such as: beam-splitters[12,13], micro-mirrors[14], diffractive optical elements[4,15] (DOEs) and spatial light modulators[16–20] (SLMs). Kilohertz acquisition speeds are possible by under-sampling of the field-of-view (FOV) via random-access scanning using SLMs[20–23]. These high frame rates have been used for fast imaging of calcium waves in brain cells. However, the reliance on structural information from a prior scanned image makes it unsuited for capturing the unpredictable behavior of single particles. Recently, SPT was realized by two-photon tomography, which illuminates a sample using lines instead of traditional excitation points. Scanning lines of excitation across the focal plane at multiple angles allows

to rapidly reconstruct the full FOV via back-projection algorithms. Although relatively complex, this method was able to track fluorescent beads *in vitro* in a volume of 250 μm diameter and 250 μm depth at 10 Hz[24]. Another approach is target-locking a single particle based on its estimated position from the ratio of four tetrahedral positioned foci[25]. Via spatiotemporal splitting of the laser beam, temporal resolutions down to 50 μs inside opaque spheroids haven been realized. Although achieving impressive depth and (temporal) resolution, the method is limited to tracking a single particle per measurement. Arguably, most straightforward technique for SPT is to rapidly sample a full FOV by scanning a fixed beamlet-pattern. The excitation beam is split by a single element, while fast scanning (galvanometric) mirrors sample the focal plane. Signal from the multiple foci are captured via camera detectors for inherent wide-field detection. Via this method, nanometric wide-field tracking of single GNRs inside cells has been achieved by spiral scanning a 10 x 10 array of beamlets[4].

The abovementioned designs focus on maximizing framerates for highest temporal resolution and requires relative high excitation powers. However, while signal increases quadratic to laser power, bleaching increases with a power larger than $2^{26,27}$. Therefore, longer time-lapse measurements would favor minimum excitation power and consequently low count-rate per fluorophore. To compensate for a low-count rate, without impeding acquisition speeds, a larger number of foci is favorable to minimize the area a single beamlet has to sample.

Here we investigate the merits of TPMM with a relative large number of foci for high acquisition speeds combined with low photo-damage. We adopt the straightforward approach of spiral-scanning an array of 25 x 25 beamlets using a high-efficient DOE to create a homogeneous virtual-light sheet. The accessible design retains a single high-NA objective for high resolution and easy mounting of samples. Rapid refresh rates allow to gently optically dissect samples while single particles in zebrafish embryos (*Danio rerio*) and rapeseed embryos (*Brassica napus*) can be readily observed. The combination of low photobleaching, high framerates and low background make TPMM a very compelling imaging technique and our findings here show promise that it could even be used for single molecule tracking studies.

3.2   MATERIALS AND METHODS

Microscopy setup. A tunable near-IR Ti:Sa laser (Coherent, Chameleon Ultra) was coupled into a home-build two-photon multifocal microscope. A diffractive optical element (DOE, custom made by Holo-eye) diffracted the laser beam into an array of 25x25 foci. A fast-scanning mirror (Newport, FSM-300-1) driven by an Archimedean spiral rapidly scanned the beams yielding a fairly homogeneous wide-field illumination, as characterized before[4]. The laser beams were focused using a 25X NA 1.1 water dipping objective (Nikon, CFI75

Apochromat 25XC), illuminating an area of 180 μm x 180 μm. Except when stated otherwise, a single period of the spiral scan took 100 ms and was synchronized with the camera. TPL was collected by the same objective, filtered with a dichroic mirror (Semrock, 700dcxr) and two short pass filters (Semrock, FF01-720-SP & FF01-750-SP) and focused on a 2048 x 2028 pixel back-illuminated sCMOS camera (Photometrics, Prime BSI). Additional band pass filters, mounted in a motorized fast-change filter wheel (Thorlabs, FW103H/M), could be positioned in front of the camera. The excitation wavelength, scanning mirror, stepper motor and camera were controlled by self-written LabVIEW (National Instruments) software.

Gold nanorod sample. GNRs with a central plasmon resonance of 808 nm (Nanopartz, A12-10-808) were embedded in a plastisol environment and sandwiched between two glass coverslips according to previously established protocol[28]. This yielded a transparent sample with a random distribution of GNRs in three dimensions. Excitation wavelength was set at 800 nm to efficiently excite GNRs at their plasmon resonance. Diffraction limited spots were sorted based on maximum intensity and a 3D Gaussian (eq. 3.1) was fitted onto a volume of 11 x 11 x 21 pixels per spot.

$$I(x, y, z) = A \exp\left(-\left(\frac{(x - x_0)^2}{2w_x^2} + \frac{(y - y_0)^2}{2w_y^2} + \frac{(z - z_0)^2}{2w_z^2}\right)\right) + C \qquad (3.1)$$

With the amplitude A, offset C, x_0 y_0 and z_0 are the centroids of the Gaussian in x,y and z coordinates. The width of the Gaussian is defined by w_x, w_y and w_z. The sub-pixel coordinates (x_0, y_0, z_0) were used to align the measured spots onto a 6 times interpolated grid, yielding a smoothed average PSF in both longitudinal and axial plane, as shown in Figure 3.1b.

The theoretical localization uncertainty σ between consecutive z-stacks was calculated using the model of Thompson et al[29]:

$$\sigma = \sqrt{\frac{s^2}{N_p} + \frac{a^2}{12N_p} + \frac{8\pi s^2 b^2}{a^2 N_p^2}} \qquad (3.2)$$

where s is the width of the PSF, N_p the number of detected photons, a the pixel size and b the number of background photons. Note that eq. 3.2 does not account for three-dimensional data. Previous research has shown that the model matches experimental results within 1 nm error[30].

Zebrafish embryos. Zebrafish (*Danio rerio*, strain AB/TL) were maintained and handled according to the guidelines from the Zebrafish Model Organism Database (http://zfin.org) and in compliance with the directives of the local animal welfare committee of Leiden University. Fertilization was performed by natural spawning at the beginning of the light period, and eggs were raised at 28.5 °C in egg water (60 μg/ mL Instant Ocean sea salts). Previously established

Tg(kdrl:mCherry)[31], *Tg(kdrl:eGFP)*[32] and *Tg(kdrl:mTurquoise)*[33] zebrafish lines were used to label the vascular system. Rhodamine B labeled liposomes consisting of DSPC + LU3 were synthesized in-house by the SBC group of the Leiden Institute of Chemistry. A detailed description on the transfection and culturing of carcinoma cells can be found in previous published work[5]. In short, PC-3 M-Pro4 cells were labeled with mCherry and transfected with miR-221-5p 48 hours before inoculation.

The liposomes or gold nanorods [10 nM] were injected into 84 or 56 hours post fertilization (hpf) zebrafish embryos using a modified microangraphy protocol. Before injection, embryos were anesthetized in 0.01% tricaine and embedded in 0.4% agarose containing tricaine. To improve reproducibility of microangiography experiments, 1 nL volumes were calibrated and injected into the sinus venous/duct of Cuvier. After the injection needle penetrated the skin, it was gently pulled back, thereby creating a small pyramidal space in which the liposomes and gold nanorods were injected. Successfully injected embryos showed backward translocation of venous erythrocytes and absence of damage to the yolk ball. Using the same method, around 400 PC-3 M-Pro4 carcinoma cells were injected and imaged one-day post injection.

Zebrafish embryos were mounted onto the sample holder of the microscope. If micro-injections were unnecessary, zebrafish were embedded directly into the agarose-tricaine mixture and mounted onto the microscope sample holder.

Rapeseed pollen. The LEC1:LEC1-eGFP reporter line was generated according to previous established methods [34,35]. In short, a 3110 base pair (bp) DNA fragment starting 1292 bp upstream of the transcription start site was amplified by PCR and recombined into pGKGWG using the Gateway cloning system (Invitogen). This construct was consequently transformed to a *Agrobactrium tumefaciens* strain C58C1 carrying the PMP90 Ti plasmid and then to *B. napus*.

Microspores from *Brassica napus* cv DH12075 were isolated according to a previously established protocol for *B. napus*[36]. Flower buds for culture were selected on length (2.6 to 4.0 mm) and their microspores were isolated and cultured in NLN-13 medium. To induce embryogenesis, microspores were cultured in the dark at 33 °C for 20 hours, and afterwards at 25 °C. Non-induced microspore cultures were cultured at 25 °C. Once isolated, microspores were inoculated in medium containing trichostatin-a (TSA) in DMSO (Sigma-Aldrich), or solely DMSO for the control microspores, and cultured for another 20 hours at 33 °C or 25 °C. Afterwards, cultures were centrifuged at 200g for 3 minutes and re-suspended in fresh NLN-13 medium absent or TSA at 25 °C.

The SNR of regions of interests (ROIs) in the pollen images was defined as:

$$SNR = \frac{I_{signal} - I_{background}}{\mu_{background}} \quad (3.3)$$

where I_{signal} is the average signal intensity, $I_{background}$ the average background intensity, and $\mu_{background}$ the standard deviation of the background intensity.

Bleaching. The signal intensity I as a function of time for the bleaching measurements in zebrafish and pollen embryos was fitted to:

$$I = A\, e^{-t/\tau} + C \tag{3.4}$$

with amplitude A, offset C, time t and decay time τ.

Theoretical count rate. We estimated the TPE intensity from a single fluorophore based on the probability of TPE per pulse (p)[7]:

$$p \approx \frac{p_0^2 \delta}{\tau_p f_p^2}\left(\frac{(NA)^2}{2hc\lambda}\right)^2 \tag{3.5}$$

where p_0 is the average laser intensity per focus, δ the two-photon absorption cross section of the fluorophore at wavelength λ, τ_p the duration of a single pulse, f_p is the repetition rate of the laser, NA the numerical aperture of the objective, h is Planck's constant, and c is the speed of light.

From eq. 3.5 we find the expected count rate (I_{signal}) by taking the collection efficiency of the setup (η) into account, the duty cycle (DC) of a single spiral scan, and the quantum efficiency of the fluorophore (Q).

$$I_{signal} = p * f_p * \eta * DC * Q \tag{3.6}$$

η was estimated on the collection efficiency of the objective (0.20, NA=1.1), the multiple filters and optical elements in the emission path and the quantum efficiency of the camera (0.93). This results in $\eta = 0.10$. The DC was estimated as the spot size divided over the field-of-view it has to scan. At 25X magnification, the distance between two neighboring foci is 9.0 µm (data not shown) and the size of a pixel is 0.26 µm. Further, based on the results in Figure 3.1c, the PSF width is 0.4 µm. From these values we estimate a DC of 0.00425

3.3 RESULTS

3.3.1 OPTICAL SECTIONING

To characterize the resolution of the microscope and the thickness of the virtual light-sheet we measured the 3D point spread function (PSF) using gold nanorods (GNRs) embedded in a

plastisol environment. GNRs form diffraction limited, bright, non-blinking and non-bleaching point sources. 164 GNRs were detected in a volume of 180 µm x 180 µm x 100 µm, sampled in slices of 0.3 µm. The maximum intensity projection shown in Figure 3.1a shows randomly distributed GNRs as distinct spots with varying brightness. This variation in brightness is expected from the narrow TPE spectrum in combination with a somewhat poly-disperse GNR population, resulting in off-resonance excitation for some GNRs. Moreover, aggregation of rods causes some spots to appear excessively bright and non-diffraction limited. All individual spots were fitted to a 3D Gaussian (equation 3.1).

To ensure that only single GNRs were included, spots with a lateral FWHM ($FWHM_{x,y}$) > 0.75 µm axial height ($FWHM_z$) > 3.0 µm were excluded. Fits with a R-squared < 0.1 were also excluded from further processing. Using the filtered x, y and z offsets, 124 regions of interest (ROIs) were aligned and summed, yielding an averaged 3D image representing the PSF, shown in Figure 3.1b. The profiles of the average PSFs (black line) partially follow the theoretical lateral and axial minimum resolution for TPE (solid red line) of 0.400 µm and 0.863 µm[8]. In addition, the profiles have a weaker secondary component which fits to a Gaussian with $FWHM_{x,y}$ = 0.75 µm and $FWHM_z$ = 2.19 µm. These values are higher than the theoretical $FWHM_{xy}$ = 0.46 µm and $FWHM_z$ = 1.37 µm for a one-photon PSF, as would be expected for scattering by the GNR. This suggests that besides linear contrast mechanisms, averaging the 124 GNRs has broadened the peaks further. Additional emission filters will reduce scattered photons which should narrow especially the axial PSF. Still, the narrow two-photon PSF will be dominant for labels that have a smaller scattering cross-section than GNRs, and shows how TPE confines excitation compared to linear contrast mechanisms.
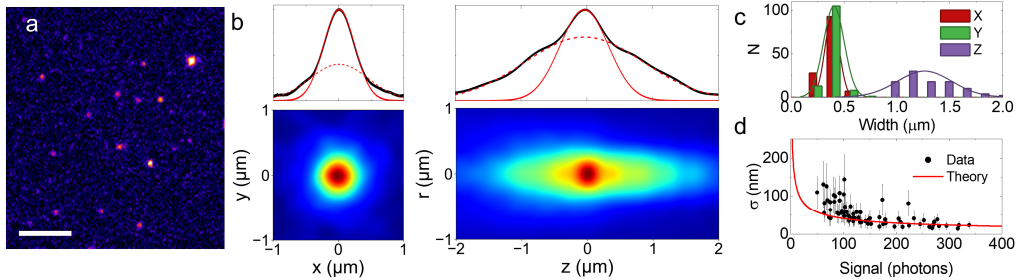
Figure 3.1: Multifocal scanning in combination with two-photon excitation allows for high resolution wide-field imaging. (a) Max intensity projection of a volume of gold nanorods imbedded in plastisol. Scale bar = 10 µm. (b) Average point-spread function in lateral and axial plane of 124 GNRs. Profiles (solid black line) are overlaid with two Gaussians. One Gaussian (solid red line) corresponds to expected theoretical profile and the second Gaussian (dashed red line) is fitted to the broader component of the profile. The theoretical Gaussians have a $FWHM_{xy}$ = 0.4 µm and $FWHM_z$ = 0.86 µm. The fitted curve yields $FWHM_{xy}$ = 0.86 µm and $FWHM_z$ = 2.2 µm. (c) The distribution of both the lateral and axial PSF from fitting a Gaussian to all detected GNRs. The average resolution in the lateral plane is 0.39 ± 0.08 µm with an axial resolution of 1.26 ± 0.26 µm. (d) Localization precision is shot-noise limited.

The distributions of the FWHM of individual GNRs in x, y and z are plotted in Figure 3.1c and nicely match the expected diffraction limit of 0.4 μm, with $FWHM_x = 0.39 \pm 0.07$ μm (mean $\pm$ SD) and $FWHM_y = 0.40 \pm 0.09$ μm, but show a small eccentricity due to optical aberrations in the emission path. $\sigma_z = 1.3 \pm 0.3$ μm is significantly larger than the expected value of 0.86 μm. The larger mean $FWHM_z$ likely originates from scattering and one-photon excitation, as previously addressed. The larger width in *z* is also seen in Figure 3.1b where the amplitude of the secondary components is approximately twice as large as in *x,y*.

Besides resolution enhancement due to the non-linear absorption, accurately localizing point sources can further improve image resolution. We quantified the reproducibility of localizing single spots by repeatedly imaging a volume of 180 μm x 180 μm x 40 μm of the fixed GNR sample. The average 3D localization differences between consecutive measurements are shown in Figure 3.1c. Experimental values follow the theoretical limit (equation 3.2) which indicates that localization precision is shot-noise limited. Localization errors due to shot noise can be reduced with increased luminescence intensity by using a high excitation power. We refrained from doing so as a higher power greatly reduces GNR stability due to melting[37]. Nevertheless, GNRs were localized in 3D with shot-noise limited super resolution accuracy.

3.3.2 PHOTOBLEACHING

Fluorescent proteins and organic dyes also feature limited stability upon optical excitation. TPM is associated with high excitation powers and consequently high in-focus photobleaching rates which may reduce biological damage and may limit the duration of fluorescence microscopy. We investigated the photobleaching rates of three different fluorescent proteins expressed in live three-day post fertilization (*dpf*) zebrafish embryos. The embryo expressed either: eGFP, mCherry or mTurquoise in endothelial cells by the fusion of fluorescent proteins to the vascular endothelial growth factor *kdrl*. After immobilization in agarose gel, images of brain blood vessels were taken continuously with an average excitation power of 1.44 mW per focus. A previously recorded wide-field transmission image, shown in Figure 3.2a, shows the orientation of the head, with the large eyes as reference structures. It also shows the large extend of light scattering, despite the transparency of the fish. The wide-field TPL images retain sharp features despite this scattering, indicating that the optical sectioning of TPE is sufficient to reject most scattering, which is achieved in confocal imaging by the pinhole.

First, we imaged blood vessels in eGFP-expressing embryos, shown in Figure 3.2b. Thin blood vessel walls are interspersed with larger spots that mark the location of nuclei of the endothelial cells. After 30 minutes of continuous imaging at 4 fps we see negligible decrease in fluorescence. Despite fixation in agarose, movement of the embryo during the measurement shifted the blood vessel 20 μm to the right. In the z-direction the blood vessel remained within the excitation plane, implying that entry of new eGFP from out-of-focus regions by a drift of the excitation plane cannot explain the absence of bleaching. In contrast to eGPF, continuous

excitation of mCherry, as shown in Figure 3.2c, resulted in much faster bleaching of fluorescence. mTurquoise, displayed in Figure 3.2d, showed similar absence of bleaching as with eGFP.
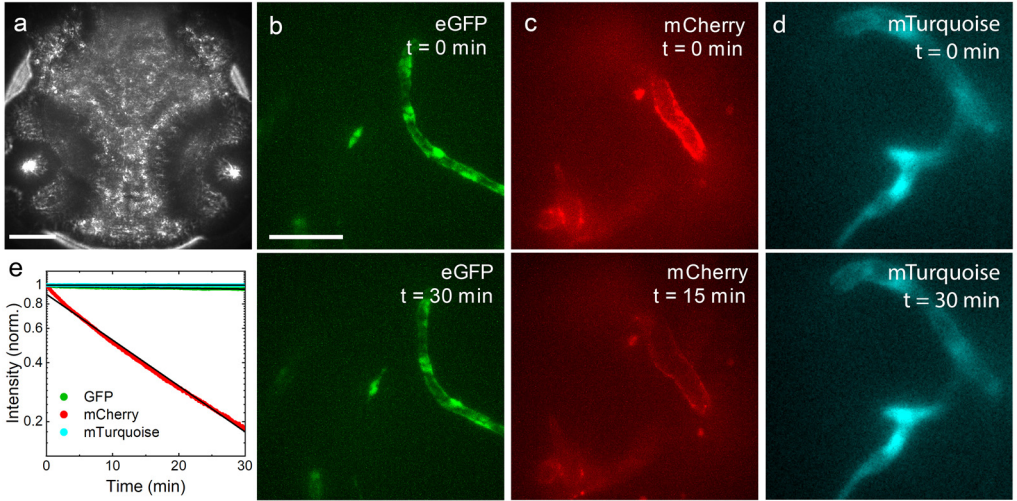

Figure 3.2: Photobleaching is reduced by averaging the excitation power over multiple foci. (a) Transmission image of the head of a zebrafish embryo. (b) eGFP stained endothelial cells of blood vessels inside a zebra fish embryo brain. Scale bar = 50 μm. (c) mCherry stained endothelial cells are almost completely depleted from fluorescence after 30 minutes of imaging. (d) mTurquoise shows similar limited bleaching as eGFP. e) Signal intensity over time fitted to eq. 3.3, yielding $\tau = 16.1 \pm 0.3$ hours for eGFP, $\tau = 310 \pm 25$ hours for mTurquoise and $\tau = 17.4 \pm 0.1$ minutes for mCherry. Scale bar = 25 μm.

To quantify the bleaching rate, we integrated the signal of a 25 μm x 25 μm ROI and plotted the intensity in time (Figure 3.2e). The intensity was fitted to an exponential decay function to extract the decay time of the fluorescence. Under continuous illumination, eGFP shows a decay time of 9.7 ± 0.2 x 10^2 minutes and mTurquoise 18.6 ± 1.5 x 10^2 minutes. The bleach rate of mCherry is significantly shorter with 17.4 ± 0.1 minutes. The initial deviation from the exponential decay may in this case be explained by small axial drift of the sample or by single-photon bleaching. Overall, eGFP and mTurquoise, with their negligible bleaching, are better suited for long-term time-lapse imaging than mCherry. Nevertheless, all fluorophores show sufficient stability to acquire >1000 frames.

3.3.3 BACKGROUND SUPPRESSION

A major advantage of TPE for *in vivo* imaging is background suppression via reduced autofluorescence and reduced scattering due to near-infrared excitation. To illustrate this, and to test whether this advantage remains for multifocal wide-field microscopy, we imaged *Brassica napus* (rapeseed) pollen embryos and compared the results with one-photon confocal

microscopy. Specific fluorescence labeling was introduced by expression of the transcription factor LEFY COTYLEDON1 (LEC1) fused with eGFP. LEC1 plays a key role in regulating seed development and is expressed from the moment a single pollen grain enters embryonic state[38]. As a transcription factor, LEC1 is expected to reside inside the nucleus. Interestingly however, it was reported to be present anywhere inside the cytoplasm, suggesting poor targeting to the nucleus after transcription[39]. We also observed this in one-photon confocal images of two-day and three-day old pollen embryos, shown in Figure 3.3a and 3.3b. eGFP signal is distributed throughout the embryos with highest signal in the nucleus. The nucleolus is distinguishable as a low intensity area residing within the nucleus (white arrows, Figure 3.3a). The left-most pollen grain in Figure 3.3b has just entered embryonic state and only traces of LEC1:eGFP are expressed. In the cytoplasm, low concentration of LEC1:eGFP contrasts with the pollen wall that is visible via autofluorescence. Overall, confocal microscopy suggests that LEC1:eGFP is relatively homogeneously distributed within the pollen embryos.
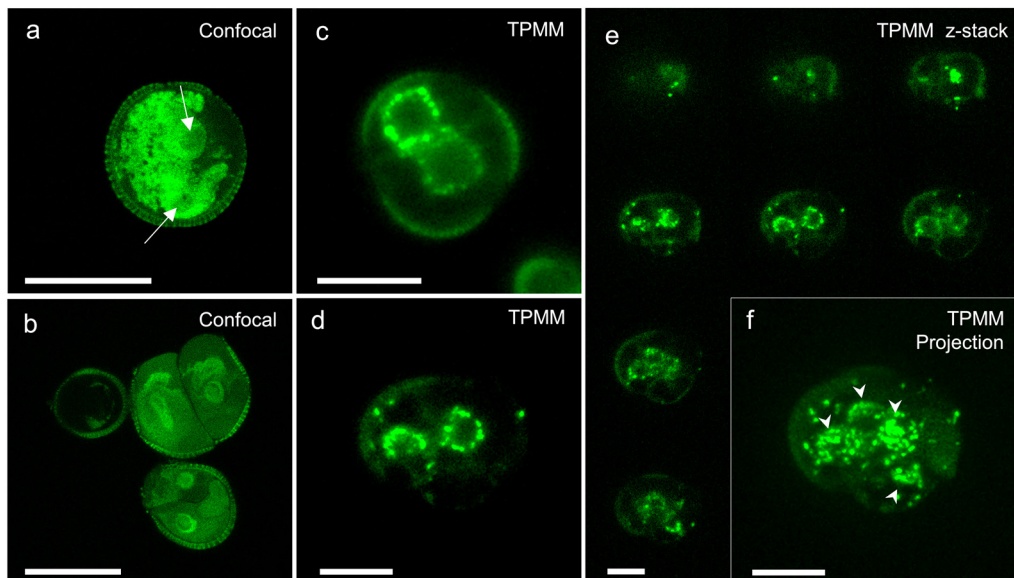
Figure 3.3: TPMM reveals localized LEC1:GFP expression at high contrast inside pollen embryos. (a) A two-day old pollen embryo imaged using one-photon confocal microscopy. LEC1:GFP shows to be homogeneously distributed throughout the pollen embryo. (b) Confocal image of four-day old pollen grains. The more developed embryo has undergone more divisions, with LEC1:GFP distribution imaged similarly as in *a*. (c) A TPMM image of a similar pollen embryo as in *a*. Where in confocal LEC1:GFP was captured dispersed throughout the embryo, here it is imaged as highly localized puncta oriented around the nucleus. (d) TPMM image of a four-day old pollen embryo, similar to *b*. Again LEC1:GFP is concentrated around the nucleus as distinct puncta. (e) Z-stack of the same pollen grain as in *d* showing an image every 2.4 µm apart. LEC1:GFP is located throughout the pollen grain, with highest concentration around the nuclei. (f) Maximum intensity projection the z-stack in *e*. Here the location of the nuclei can be clearly seen as they are surrounded by LEC:GFP puncta. Scale bars = 25 µm.

Imaging similar pollen grains with TPE reveals a different picture, as shown in Figure 3.3c. LEC1:eGFP signal is predominantly located around the nuclei in distinct puncta, in contrast to the homogeneous distribution we saw with confocal microscopy. In non-induced pollen, no accumulation of fluorescence was observed, see Figure S3.1. The pollen wall was visible in both strains, though significantly reduced in intensity as compared to LEC1:eGFP. There is the large difference in acquisition time between confocal (56 seconds) and TPMM (0.1 seconds). Similar noise levels (μ) were achieved by averaging 20 TPMM images (2 seconds), see Figure 3.2S. The SNR of the cytoplasm is similar in confocal images and the TPMM. In the TPMM measurement of the non-induced pollen, SNR in the cytoplasm was at the same level, indicating that this signal should not be attributed to eGFP. The bright puncta in TPMM have a 3.5-fold increase in SNR compared to the eGFP signal in the confocal images. The average signal of 5 LEC1:eGFP puncta was measured to be 684 ± 64 photons. Considering acquisition time of 0.1 seconds and a duty cycle of 1 ms per pixel, we estimate an average count rate of 6.8 x $10^5 \pm 6.3$ x 10^4 photons/sec per punctum. With an average excitation power per focus of 1.4 mW, we expect a count rate of 8.6 10^3 photons/sec for a single eGFP molecule (eq. 3.5). These calculations suggest that the puncta consist of about 80 LEC1:eGFP proteins. In the TPMM image of a three-day old pollen embryo, shown in Figure 3.3d, most LEC1:eGFP is again clustered in the nucleus, though LEC1:eGFP puncta also appear near the pollen wall. The intensity per punctum increased to 1.30 ± 0.03 x 10^6 photons/sec, indicating strong accumulation of hundreds LEC1 proteins per spot. So it appears that LEC1 aggregates at the periphery of the nucleus during development. From these results, confocal imaging revealed that LEC1:eGFP is homogeneously distributed in the cytoplasm. Surprisingly however, it did not capture the bright puncta observed in TPMM. TPMM did yield LEC1:eGFP in the cytoplasm.

The entire pollen grain was imaged in 150 z-slices of 0.3 μm to study LEC1:eGFP distribution in three dimensions, as shown in Figure 3.3d. A selection of the slices is displayed in Figure 3.3e. Three nuclei in the pollen grain at different heights can be clearly distinguished from the accumulation of LEC1:eGFP near the nuclear membrane. The three-dimensional image shows that LEC1:eGFP appears to be isotopically distributed over each of the nuclei. Though a small number of individual puncta appear to be scattered near the pollen wall as well. From the maximum intensity projection, shown in Figure 3.3f, we count about 20 out of 120 spots that are not located near the nuclei (white arrowheads). In summary, the thin virtual light sheet created by TPE allowed to optically dissect a pollen grain in 3D, and resolved individual puncta of LEC1:eGFP that were scattered in the nuclei. Differences in contrast between confocal and TPMM were apparent for the imaging of pollen embryos. Finally, the reduced acquisition time potentially increases the throughput and allows for rapid time lapse imaging.

3.3.4 SINGLE PARTICLE TRACKING

To test the potential for time-lapse imaging we evaluated SPT in live zebrafish embryos. GNRs were intravenously microinjected in three day old embryos, where they circulated freely in the bloodstream. Embryos were sedated with tricaine (50 µg/mL) and embedded in agarose gel for stability and imaged directly after the gel hardened. A blood vessel located in the brain, as depicted in Figure 3.4a, was continuously imaged at 10 frames per second (fps). GFP-expressing endothelial cells mark the blood vessel wall and show a T-junction just below the skin of the embryo. Tissue surrounding the blood vessel also features luminescence, which may be due to second harmonic generation (SHG) from collagen in the skin[40]. This signal was more dominant in the upper-head area. Note the slightly patterned features in the image that originate from imperfect scanning parameters. The deeper lying blood vessels featured less background. However, the concentration of GNRs was too high to accurately distinguish single GNRs.
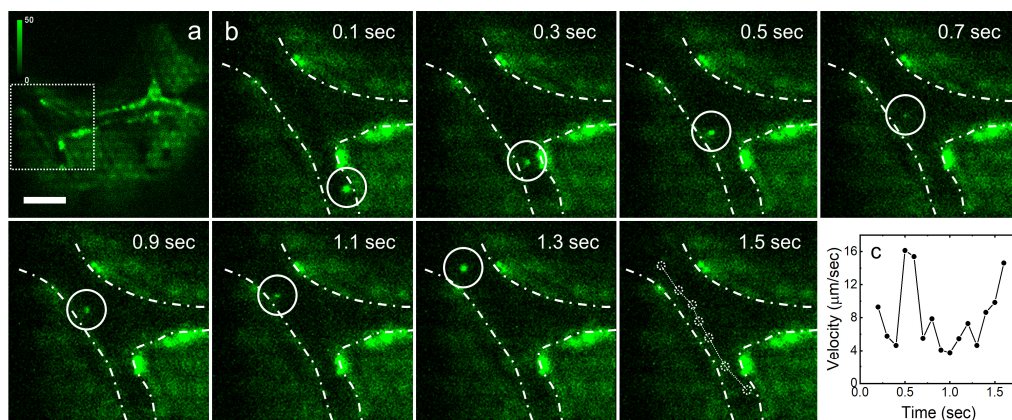
Figure 3.4: Sub-second tracking of a single gold nanorods in zebrafish embryos. (a) Image of a blood vessel surrounded by endothelial cells in the brain of an embryo. Scale bar = 25 µm. (b) Close-ups of the blood vessel (white square, a). A GNR appears on the bottom (white circle) and is captured at 10 fps as it moves along the vessel. (c) Graph with the trend in velocity of the GNR between every taken image. Speed goes up around 0.5 seconds, while also increasing 1 second later at 1.5 seconds.

During acquisition, multiple GNRs were passing through the vein, as shown in Figure 3.4b (white square). To guide the eye, the blood vessels are annotated by white dotted lines and the location of the GNR by a white circle. After the GNR enters the ROI, it travels along the direction of the blood stream. It takes approximately 1.5 seconds for the GNR to cover a distance of 22.5 µm before disappearing outside the FOV. During the time 15 images were taken and the location of the GNR in each image was extracted. The signal intensity varied somewhat due to the GNR moving in and out of focus. Nevertheless, the GNR could be tracked continuously and its velocity is plotted in Figure 3.4c. The velocity varied between 4 and 16 µm/sec in a 1 second

interval. This oscillation in speed corresponds with heart rates found in embryos sedated by similar dosage of tricaine[41]. Tracking single particles in live zebrafish embryos nicely demonstrates the ability of TPMM to visualize dynamics of nanometric structures *in vivo*.

3.3.5 MULTI-COLOR IMAGING

Like one-photon fluorescence, TPE has two ways of achieving multicolor imaging: the differences in both excitation and emission spectra can be exploited to separate orthogonal fluorophores. As TPE spectra are not commonly found in literature, we first measured the excitation spectra of three fluorescent proteins and an organic dye in our microscope. In doing so, we also characterized the spectral response of all elements in the excitation and emission path. Over a range between 730 nm and 1000 nm the laser power gradually increased and reached a maximum power of approximately 900 mW at 800 nm, plotted in Figure 3.5a, corresponding to 1.44 mW per focus. The spectrum follows laser specifications, except for a small periodic modulation, resulting in dips at 780, 845 and 875 nm. These dips are likely caused by interference of the filters in the excitation path. Due to the quadratic dependence of TPE on excitation intensity, the small dip in the excitation spectra at 785 nm would result in a ±30% fluorescent signal reduction. The dip at 815 nm would result in 11% reduced signal. Moreover, the global variation in laser power over the entire spectrum, would modulate signal by a factor of 18. Though the power spectrum of the laser could be used to correct the fluorescence emission, we refrained from doing so as we cannot exclude that part the detected signal originates from either scattering or OPE, making such corrections highly non-trivial.

Having measured the laser spectrum, we next measured the excitation spectra of rhodamine B, mCherry, mTurquoise and eGFP expressed in endothelial cells in zebrafish embryo brains. Excitation spectra were acquired by continuous imaging, while sweeping the excitation wavelength between 730 nm and 1000 nm, using a 700 nm low-pass emission filter. Signal intensities were measured by integrating over an area of 50 µm x 50 µm and the resulting normalized spectra are shown in Figure 3.5b. mTurquoise, GFP and rhodamine B all featured a maximum signal at 830 nm. As expected the modulation in excitation power spectrum is more pronounced in the TPE spectrum. mCherry has maximum excitation at 750 nm, which rapidly drops at wavelengths larger than 810 nm. This difference in excitation spectrum allows for simultaneous imaging with the other fluorophores by alternating the excitation wavelength. The difference in excitation between rhodamine B and eGFP can also be used for multi-color imaging when switching between 830 and 870 nm. Rhodamine B features a distinctive peak at 880 nm that can be exploited despite the three times lower laser power at this wavelength. However, mCherry has the most distinguishable spectrum, allowing two-color imaging with any of the other dyes.
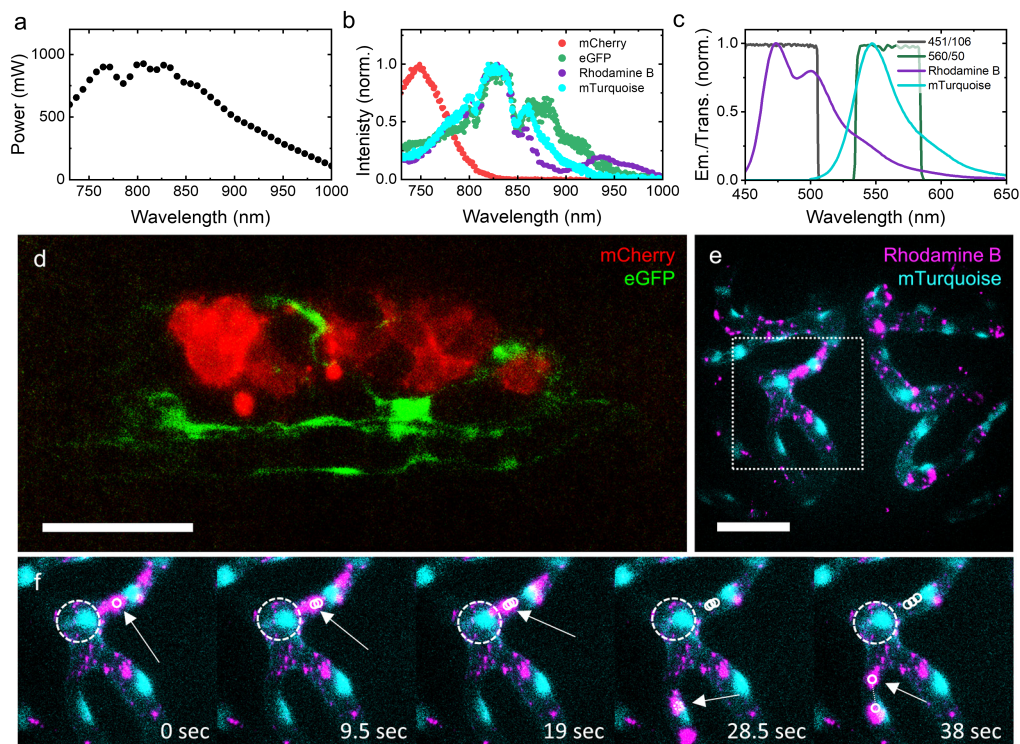
Figure 3.5: Multi-color imaging by alternating either excitation wavelength or the emission filter. (a) Power spectrum of the laser measured at the sample stage. The power unexpectedly dips at 770 nm and 820 nm due to interferences in the excitation path. (b) Excitation spectra of four commonly used dyes. c) Tailored band pass filters to spectrally separate fluorophores. (d) Carcinoma (mCherry, red), located in the tail of a zebra fish embryo, is resolved from surrounding endothelial cells (eGFP, green) by changing the excitation wavelength of the laser. (e) Liposomes (rhodamine B, magenta) line the endothelial cells (mTurquoise, cyan) inside a zebra fish embryo brain. (f) Liposome aggregates, likely endocytosed by macrophages, are imaged from *5e, inset* as they travel through the blood vessels. Scale bars = 50 μm.

To demonstrate this, we imaged human carcinoma cells injected into a 2dpf zebrafish embryo. Carcinoma cells were stained with mCherry while the endothelial cells the embryo expressed eGPF. Two images were measured at 750 nm and 830 nm and displayed in separate colors in Figure 3.5d. Again thin blood vessel walls (green) featured thicker regions that reveal the location the nuclei of the endothelial cells. Larger areas of green signal are attributed to more complex networks of endothelial cells. The mCherry channel exposes individual carcinoma cells (red) lying around the framework of blood vessels. Carcinoma cells on the left appear brighter compared to the ones on the right, which may be explained by maturity of the cells, or variations in mCherry expression. These images were recorded with an integration time of 100 ms. Overall, switching between wavelengths is a viable method for multi-color TPE imaging and can be used to study the dynamic progression of cancer metastasis in live embryos.

Though changing the excitation wavelength can be achieved with 40 nm/sec, the more common approach is to change the emission filters, which may yield faster and/or better contrast multi-color images. The shared excitation peak of rhodamine B and mTurquoise at 830 nm, in combination with a large difference in the emission spectrum, plotted in Figure 3.5c, was used to test this mode. Liposomes loaded with rhodamine B that were intravenously injected into 3dpf embryos with mTurquoise expressing endothelial cells. Two emission filters separate the emission of rhodamine B (maximum at 475 nm) and the emission of mTurquoise (maximum at 560 nm), and were alternated to capture separate channels. Due to spectral leakage we expect 25% of signal in the 451/106 channel to originate from rhodamine B, instead of mTurquoise.

The liposomes are expected to be distributed throughout the embryo, like the GNRs, while also adhering to the blood vessel walls. Each liposome was loaded with approximately 1000-3000 rhodamine B molecules. After injection, a volume of 150 μm x 150 μm x 30 μm of the brain was imaged in 9.5 seconds while automatically alternating the emission filters. The overlay of two maximum intensity projections for each channel is shown in Figure 3.5e, with mTurquoise in cyan and rhodamine B in magenta. The network of blood vessels is easily distinguished from the dark background in the mTurquoise channel. Similar to Figure 3.5d, the endothelial nuclei featured bright patches on the walls of the veins. The thin blood vessel walls appeared to be decorated with liposomes, visible as diffraction limited spots. We expect that each spot originates from a single liposome. Larger spots are tentatively attributed to aggregated liposomes.

Besides immobile spots, freely circulating liposomes were also visible. Figure 3.5f shows an example of aggregates of liposomes moving through a blood vessel. Each image is the maximum intensity projection of the two channels at the location annotated in Figure 3.5e (white dotted square). The speed at which the aggregates move suggests that the liposomes have been endocytosed by macrophage cells. The first aggregate travels along the blood vessel where it disappears after 19 seconds. It may have left the imaged volume through a blood vessel, moving upwards, indicated by the white dotted circle. The second annotated aggregate, which appears at 28.5 seconds, most likely travels via the same blood vessel out of view after 38 seconds. By overlaying the two channels, the liposome distribution could be positioned to well-defined boundaries of the blood vessels, demonstrating the use of TPMM microscopy to capture dynamic events in live zebrafish embryos with diffraction limited resolution.

3.4   DISCUSSION AND CONCLUSION

Due to its confocal set-up, TPM is generally slow, hampering rapid time-lapse imaging. Here, we characterized the abilities of TPMM for video-rate imaging of biological tissues. Confinement of excitation together with the rapid scanning of multiple foci resulted in a virtual light sheet with a thickness of 1.2 μm. The virtual light sheet allowed us to optically dissect pollen embryos in 3D and accurately resolve LEC1:eGFP distribution inside. While maintaining high resolution and low background, we could also track single GNRs and liposomes inside the brain blood vessels of zebrafish embryos. Using TPMM, we observed that common protein and organic dyes in endothelial cells of zebrafish embryos showed remarkably long fluorescent decay times of up to 310 hours. By either changing the excitation wavelength or by alternating between emission filters, different structures inside zebrafish embryos were readily imaging in 3D using multi-color imaging.

The reduced duty cycle in TPMM, combined with an improved, low-noise sCMOS camera allowed for a low excitation power of typically 1.4 mW per focus while maintaining SNR > 10. Gentle illumination resulted in a photobleaching time of 16 ± 0.3 hours for eGFP. The bleaching rate of eGFP as a function of laser power has been measured to increase with a power of 2.69 [42]. This sensitive relation between excitation power and bleaching explains the low bleaching we observe at 1.4 mW per focus. The two-photon fluorescent stability as a function of power has not been characterized for mTurquoise and mCherry. Interestingly however, for OPE, mTurquoise showed to be the most sensitive for bleaching with a power of 1.89, compared to 1.23 for eGPF[43]. Although the bleaching mechanism by OPE and TPE have been described to be different[26,44], the higher sensitivity of mTurquoise with OPE to laser power corresponds to the reduced bleaching decay of $3.1 \pm 0.1 \times 10^2$ hours in TPMM. mCherry bleached several orders of magnitude faster, despite having similar OPE bleaching characteristics to eGFP[45]. However, exciting mCherry at 750 nm may bring it in a higher energetic state than at its primary two-photon absorption peak at 1080 nm[11,46]. Previous research indicate that faster photobleaching processes can occur at these higher energetic states by formation of ion pairs[44,47]. The high fluorophore stability that we report here for the other fluorescent proteins suggests that photo-damage can be reduced by exciting the fluorophore to its lowest excited energy state.

In addition to fluorophore stability, non-fluorescent absorption causes damage in biological systems. Imaging with low photo-toxicity is therefore essential for any *in vivo* environment. Pollen embryos studies using OPE for example, have been limited to short timespans and selectively on embryos late in culture, as photodamage at earlier stages prevented long experiments[50]. Based on the extremely low bleaching rate, TPMM may extend imaging

times to allow visualization from initial embryogenesis to more developed stages, while achieving similar resolution and reduction of out-of-focus scattering.

Previous TPMM studies focused on imaging speed or image depth with higher excitation power per focus. Common TPMM designs use linear patterns of up to 64[13,50] foci, or arrays of 8 x 8[51,52] or 10 x 10[18,20] foci. At ±10 times more excitation power available per focus and more rapid scanning an order of magnitude faster imaging rates at similar FOV could be realized. However, the required higher power comes at a cost of increased bleach rate. On the other hand, decreasing power inevitably results in lower brightness, which subsequently requires longer integration time. For longer time-lapse microscopy experiments, it may therefore be favorable to maximize the number of beamlets rather than scanning a limited number of high power beamlets at a faster pace. Parallel imaging using multiple beamlets can be implemented in several ways. Although constrained in design pattern, a DOE-based TPMM provides a simple, high efficient method for increasing temporal resolution. Alternatively, SLM would be a more flexible choice to tailor the illumination pattern according to a specific sample. However, the necessary adaptation of phase-maps complicates design and associated artefacts should be tackled for proper illumination[18]. Therefore, introduction of a DOE may be better suited for practical applications in laboratories that do not want to invest in advanced optics.

A different strategy for improving contrast without increasing the excitation power, is to use brighter labels. GNRs exhibit an absorption coefficient that is two orders of magnitude larger than that of organic dyes[53]. This efficient excitation, mediated by their localized surface plasmon resonance, proved sufficient to resolve single GNRs as labels inside zebra fish embryos. Previous TPM studies using GNRs were limited to single cells[4,54–57], or could only resolve clusters of GNRs inside larger model organisms where scattering is prominent when imaging deeper into the tissue [58,59]. This exemplifies how TPMM can overcome these effects of scattering in deep tissue, without compromising on resolution or FOV. GNRs can be functionalized in a straight-forward manner to target specific proteins inside live animals[60,61]. Tracking such functionalized GNRs with nanometer accuracy in 3D will give a better insight into physiological pathways of nanoparticles, and may reveal new mechanisms of delivery that could enhance targeted delivery of nano-medicines. Alternatively, we imaged single liposomes inside zebrafish embryos. Liposomes can be loaded with large quantities of fluorophores[62] and have previously been used in zebrafish embryos as model systems for targeted drug carriers[5,63]. Here we achieved a frame rate of 10 Hz in 2D and 1 Hz in 3D, allowing for detailed time-lapse analysis. The low bleaching conditions enabled imaging of single liposomes for extended periods of time, showcasing the use of TPMM for following single particles *in vivo*.

Similarly, TPMM was able to resolve LEC1:eGFP inside vesicles located around the nucleus of pollen embryos. Interestingly, confocal OPE microscopy, revealed more homogenously distributed LEC1:eGFP in the embryo. A previous confocal study also showed a homogenous distribution of LEC1 in both the nucleus and cytoplasm, similar to our confocal observation[64]. In *Arabidopsis* embryos however, LEC1 aggregation inside the nucleus was also

observed by confocal microscopy, resembling our TPMM images of rapeseed pollen[39]. The difference in contrast that we observe may be explained by several factors. First, auto-fluorescence of other structures than LEC1:eGFP may contribute to the signal in the confocal microscope, whereas TPM may be less affected. This may be strengthened by the better optical sectioning that is achieved by TPE. Of course it could also be that the difference originated from biological variance. To test this, the same pollen should be imaged in both modalities. TPE would be advantageous for imaging more developed pollen which are bigger and will thus benefit more from the reduced scattering. Suppression of background signal in plant tissue via TPE has been shown in recent studies[65–68]. TPMM adds to these findings by the increased temporal resolution.

Multi-color imaging in TPM is well established. Here we combine it with the rapid image acquisition of multifocal scanning. Having a tunable laser, it was possible to alternate mCherry and eGFP with a lag-time of ±5 seconds. Alternatively, emission filters can be switched to separate mTurquoise and rhodamine B using the same excitation wavelength. Tri-color TPM however, has been found challenging due to overlapping emission spectra or inefficient TPE absorption and required more complex excitation strategies such as spectral mixing[69,70] or tailored higher harmonic excitation[71]. Three-color imaging could be readily achieved by combining the different excitation wavelengths and emission filters as we did here. In addition, second-harmonic generation, for example by collagen fibers could be used as a third imaging channel. Collagen is a well-documented second harmonic generating structure which is efficiently excited with IR light, while its emission at 400 nm does not interfere with fluorescent fluorophores used here [72]. By choosing any of abovementioned techniques multi-color imaging can be readily achieved with TPMM allowing for rapid co-localization of structures.

In wide-field imaging of large tissue containing opaque structures, image quality is degraded by scattering of emission photons. Recent TPMM designs address this spatial cross-talk by rejecting scattered photons or redirecting them to correct pixels. Most of these methods however, involve advanced changes to microscope design such as de-scanned detection[13,52], wide-spaced multi-anode photomultiplier tubes[73] or spinning-disc scanning[74]. For a wider use, background and scattered photons should be suppressed with minimal changes to the design of the microscope. For example, by source-localization of detected photons; Richardson-Lucy deconvolution, relocates scattered photons to their estimated correct pixel without additional optical component[75]. Structured illumination microscopy (SIM) also rejects scattered photons by reconstructing the frequency-modulated illumination pattern. SIM combined with TPMM was shown to increase SNR, imaging depth as well as resolution without changes to the setup[76,77], and may further improve image quality by changing from a spiral- to a linear illumination pattern.

In conclusion, we have shown that TPMM yields: fast, high-resolution, low background and stable *in vivo* imaging. It encompasses a favorable balance between bleaching and signal intensity, such that biological processes in cell tissue can be imaged for extended periods of

time and with high temporal resolution. These merits will be especially useful for studying rapid movements of nano-scale objects in long time-lapse studies.

3.5   SUPPLEMENTARY FIGURES
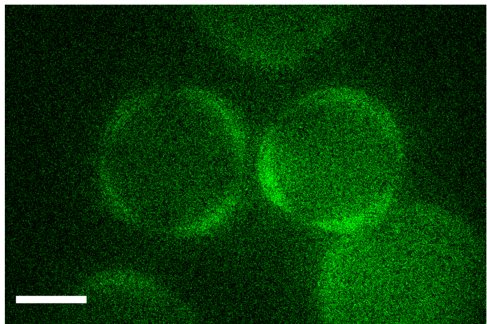
Figure S3.1: TPMM images of two-day old WT pollen grains. No localized signal was detected inside the embryos in absence of the GFP:LEC1 fusion protein. Pollen walls are visible via autofluorescence. Scale bar = 25 µm.
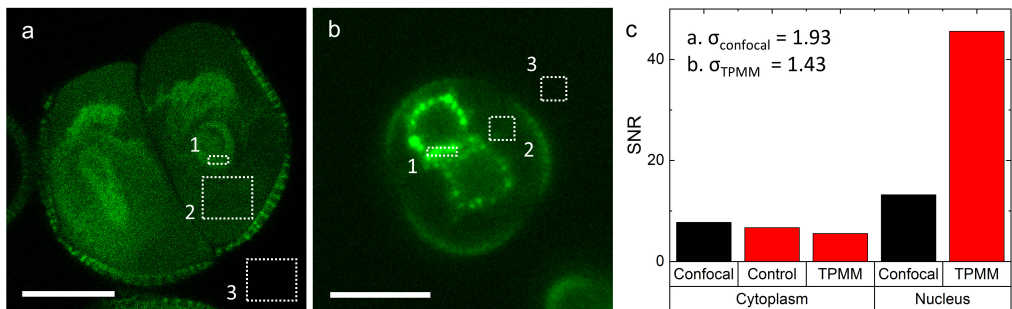
Figure S3.2: By averaging 20 TPMM images, noise (σ) is similar for confocal and TPMM. (a) Confocal image of a three-day old pollen embryo. White squares annotate the region of the nucleus (1), cytoplasm (2) and background (3). Scale bar = 10 µm. (b) Two-photon image of a three-day old pollen, annotated similarly to *a*. Scale bar = 25 µm. (c) SNRs calculated according to equation 3.3 from the mean values of the ROIs as annotated in *a* and *b*. SNR of the cytoplasm of the control measurement was calculated from the image in Figure S1.

3.6 BIBLIOGRAPHY

1.   Manzo, C. & Garcia-parajo, M. F. A review of progress in single particle tracking : from methods to biophysical insights. (2015). doi:10.1088/0034-4885/78/12/124601
2.   Piyaraj, P. The Green Fluorescent Protein (GFP). *Bangkok Med. J.* **05**, 101–102 (2013).
3.   Resch-Genger, U., Grabolle, M., Cavaliere-Jaricot, S., Nitschke, R. & Nann, T. Quantum dots versus organic dyes as fluorescent labels. *Nat. Methods* **5**, 763–775 (2008).
4.   Van den Broek, B., Oosterkamp, T. H. & van Noort, J. A Multifocal Two-Photon Microscopy Setup for Parallel 3D Tracking of Gold Nanorods. *Biophys. J.* **98**, 178a (2010).
5.   Kilin, V. N. *et al.* Counterion-enhanced cyanine dye loading into lipid nano-droplets for single-particle tracking in zebrafish. *Biomaterials* **35**, 4950–4957 (2014).
6.   Li, J. *et al.* Simple and Rapid Functionalization of Gold Nanorods with Oligonucleotides Using an mPEG-SH/Tween 20-Assisted Approach. *Langmuir* **31**, 7869–7876 (2015).
7.   So, P. T. C., Dong, C. Y., Masters, B. R. & Berland, K. M. Two-Photon Excitation Fluorescence Microscopy. *Annu. Rev. Biomed. Eng.* 399–429 (2000).
8.   Zipfel, W. R., Williams, R. M. & Webb, W. W. Nonlinear magic: Multiphoton microscopy in the biosciences. *Nat. Biotechnol.* **21**, 1369–1377 (2003).
9.   Biermann, B. *et al.* Imaging of molecular surface dynamics in brain slices using single-particle tracking. *Nat. Commun.* (2014). doi:10.1038/ncomms4024
10.   Diaspro, A., Chirico, G. & Collini, M. Two-photon fluorescence excitation and related techniques in biological microscopy. *Q. Rev. Biophys.* **38**, 97–166 (2005).
11.   Drobizhev, M., Makarov, N. S., Tillo, S. E., Hughes, T. E. & Rebane, A. Two-photon absorption properties of fluorescent proteins. *Nat. Methods* **8**, 393–399 (2011).
12.   Fittinghoff, D. N., Wiseman, P. W. & Squier, J. A. Widefield multiphoton and temporally decorrelated multifocal multiphoton microscopy. *Opt. Express* **7**, 273 (2000).
13.   Martini, J., Andresen, V. & Anselmetti, D. Scattering suppression and confocal detection in multifocal multiphoton microscopy. *J. Biomed. Opt.* **12**, 034010 (2007).
14.   Nielsen, T., Fricke, M., Hellweg, D. & Andresen, P. High efficiency beam splitter for multifocal multiphoton microscopy. *J. Microsc.* **201**, 368–376 (2001).
15.   Sacconi, L. *et al.* Multiphoton multifocal microscopy exploiting a diffractive optical element. *Opt. Lett.* **28**, 1918 (2003).
16.   Poland, S. P. *et al.* Time-resolved multifocal multiphoton microscope for high speed FRET imaging in vivo. *Opt. Lett.* **39**, 6013 (2014).
17.   Matsumoto, N. *et al.* Correction of spherical aberration in multi-focal multiphoton microscopy with spatial light modulator. *Opt. Express* **25**, 7055 (2017).
18.   Matsumoto, N. *et al.* An adaptive approach for uniform scanning in multifocal multiphoton microscopy with a spatial light modulator. *Opt. Express* **22**, 633 (2014).
19.   Nikolenko, V. *et al.* SLM Microscopy: Scanless Two-Photon Imaging and Photostimulation with Spatial Light Modulators. *Front. Neural Circuits* **2**, 5 (2008).
20.   Pozzi, P. *et al.* High-throughput spatial light modulation two-photon microscopy for fast functional imaging. *Neurophotonics* **2**, 015005 (2015).
21.   Nikolenko, V., Poskanzer, K. E. & Yuste, R. Two-photon photostimulation and imaging

of neural circuits. *Nat. Methods* **4**, 943–950 (2007).

22. Salomé, R. *et al.* Ultrafast random-access scanning in two-photon microscopy using acousto-optic deflectors. *J. Neurosci. Methods* **154**, 161–174 (2006).

23. Yang, W. *et al.* Simultaneous Multi-plane Imaging of Neural Circuits. *Neuron* **89**, 269 (2016).

24. Kazemipour, A. *et al.* Kilohertz frame-rate two-photon tomography. *Nat. Methods* **16**, (2019).

25. Perillo, E. P. *et al.* Deep and high-resolution three-dimensional tracking of single particles using nonlinear and multiplexed illumination. *Nat. Commun.* **6**, (2015).

26. Patterson, G. H. & Piston, D. W. Photobleaching in Two-Photon Excitation Microscopy. *Biophys. J.* **78**, 2159–2162 (2000).

27. Chen, T.-S., Zeng, S.-Q., Luo, Q.-M., Zhang, Z.-H. & Zhou, W. High-Order Photobleaching of Green Fluorescent Protein inside Live Cells in Two-Photon Excitation Microscopy. *Biochem. Biophys. Res. Commun.* **291**, 1272–1275 (2002).

28. Neutsch, K., Gö-ring, L. & Gerhardt, N. C. Common-path digital holographic microscopy for 3D nanoparticle localization. **1072616**, 41 (2018).

29. Thompson, R. E., Larson, D. R. & Webb, W. W. Precise nanometer localization analysis for individual fluorescent probes. *Biophys. J.* **82**, 2775–2783 (2002).

30. Carozza, S., Culkin, J. & Noort, J. Van. Accuracy of the detection of binding events using 3D single particle tracking. *BMC Biophys.* 1–13 (2017). doi:10.1186/s13628-017-0035-8

31. Proulx, K., Lu, A. & Sumanas, S. Cranial vasculature in zebrafish forms by angioblast cluster-derived angiogenesis. *Dev. Biol.* **348**, 34–46 (2010).

32. Jin, S. W., Beis, D., Mitchell, T., Chen, J. N. & Stainier, D. Y. R. Cellular and molecular analyses of vascular tube and lumen formation in zebrafish. *Development* (2005). doi:10.1242/dev.02087

33. Bussmann, J. & Schulte-Merker, S. Unpublished. (2011).

34. Soriano, M. *et al.* Plasticity in cell division patterns and auxin transport dependency during in vitro embryogenesis in Brassica napus. *Plant Cell* **26**, 2568–2581 (2014).

35. Li, H. *et al.* The histone deacetylase inhibitor trichostatin a promotes totipotency in the male gametophyte. *Plant Cell* **26**, 195–209 (2014).

36. Custers, J. B. M. Microspore culture in rapeseed (Brassica napus L.). in *Doubled Haploid Production in Crop Plants* (Springer, 2003).

37. Taylor, A. B., Siddiquee, A. M. & Chon, J. W. M. Below melting point photothermal reshaping of single gold nanorods driven by surface diffusion. *ACS Nano* **8**, 12071–12079 (2014).

38. Lotan, T. *et al.* Arabidopsis LEAFY COTYLEDON1 is sufficient to induce embryo development in vegetative cells. *Cell* **93**, 1195–1205 (1998).

39. Boulard, C. *et al.* LEC1 (NF-YB9) directly interacts with LEC2 to control gene expression in seed. *Biochim. Biophys. Acta - Gene Regul. Mech.* **1861**, 443–450 (2018).

40. Morris, J. L. *et al.* Live imaging of collagen deposition during skin development and repair in a collagen I – GFP fusion transgenic zebrafish line. *Dev. Biol.* **441**, 4–11 (2018).

41. Muntean, B. S. *et al.* A comparative study of embedded and anesthetized zebrafish in vivo on myocardiac calcium oscillation and heart muscle contraction. *Front. Pharmacol.* **DEC**, 1–9 (2010).

42.   Graham, D. J. L., Tseng, S., Chen, J. H. D. J. & Alexandrakis, G. Dependence of Two-Photon eGFP Bleaching on Femtosecond Pulse Spectral Amplitude and Phase. *J. Fluoresc.* 1775–1785 (2015). doi:10.1007/s10895-015-1667-1

43.   Cranfill, P. J. *et al.* Quantitative assessment of fluorescent proteins. *Nat. Methods* **13**, 557–562 (2016).

44.   Dittrich, P. S. & Schwille, P. Photobleaching and stabilization of fluorophores used for single-molecule analysis with one- and two-photon excitation. *Appl. Phys. B Lasers Opt.* **73**, 829–837 (2001).

45.   Shaner, N. C. *et al.* Improving the photostability of bright monomeric orange and red fluorescent proteins. **5**, 545–551 (2008).

46.   Drobizhev, M., Makarov, N. S., Hughes, T. & Rebane, A. Resonance enhancement of two-photon absorption in fluorescent proteins. *J. Phys. Chem. B* **111**, 14051–14054 (2007).

47.   Eggeling, C., Widengren, J., Rigler, R. & Seidel, C. A. M. Photobleaching of Fluorescent Dyes under Conditions Used for Single-Molecule Detection: Evidence of Two-Step Photolysis. *Anal. Chem.* **70**, 2651–2659 (1998).

48.   Truong, T. V, Supatto, W., Koos, D. S., Choi, J. M. & Fraser, S. E. Deep and fast live imaging with two-photon scanned light-sheet microscopy. *Nat. Methods 2011 89* **8**, 757 (2011).

49.   Ji, N., Magee, J. C. & Betzig, E. High-speed, low-photodamage nonlinear imaging using passive pulse splitters. *Nat. Methods* **5**, 197–202 (2008).

50.   Corral-Martínez, P. *et al.* Live Imaging of embryogenic structures in Brassica napus microspore embryo cultures highlights the developmental plasticity of induced totipotent cells. *Plant Reprod.* (2020). doi:10.1007/s00497-020-00391-z

51.   Niesner, R., Andresen, V., Neumann, J., Spiecker, H. & Gunzer, M. The power of single and multibeam two-photon microscopy for high-resolution and high-speed deep tissue and intravital imaging. *Biophys. J.* **93**, 2519–2529 (2007).

52.   Poland, S. P. *et al.* Multifocal multiphoton volumetric imaging approach for high-speed time-resolved Förster resonance energy transfer imaging in vivo. *Opt. Lett.* **43**, 6057 (2018).

53.   Kim, K. H. *et al.* Multifocal multiphoton microscopy based on multianode photomultiplier tubes. *Opt. Express* **15**, 11658 (2007).

54.   Wang, H. *et al.* In vitro and in vivo two-photon luminescence imaging of single gold nanorods. *Proc. Natl. Acad. Sci. U. S. A.* **102**, 15752–15756 (2005).

55.   Sridhar, S. *et al.* In vitro imaging of embryonic stem cells using multiphoton luminescence of gold nanoparticles. *Int. J. Nanomedicine* **2**, 813–819 (2007).

56.   Abdelrasoul, G. N. *et al.* PEGylated gold nanorods as optical trackers for biomedical applications: an *in vivo* and *in vitro* comparative study. *Nanotechnology* **27**, 255101 (2016).

57.   Durr, N. J. *et al.* Two-photon luminescence imaging of cancer cells using molecularly targeted gold nanorods. *Nano Lett.* **7**, 941–945 (2007).

58.   Li, J. L. & Gu, M. Surface plasmonic gold nanorods for enhanced two-photon microscopic imaging and apoptosis induction of cancer cells. *Biomaterials* **31**, 9492–9498 (2010).

59.   Gonzalez-Moragas, L. *et al.* In vivo testing of gold nanoparticles using the Caenorhabditis elegans model organism. *Acta Biomater.* (2017).

doi:10.1016/j.actbio.2017.01.080

60.   Li, D. *et al.* Graphene oxide nanoparticles for two-photon fluorescence imaging of zebrafish. *Opt. Quantum Electron.* **48**, (2016).

61.   Ali, M. R. K., Ali, H. R., Rankin, C. R. & El-Sayed, M. A. Targeting heat shock protein 70 using gold nanorods enhances cancer cell apoptosis in low dose plasmonic photothermal therapy. *Biomaterials* **102**, 1–8 (2016).

62.   Riley, R. S. & Day, E. S. Gold nanoparticle-mediated photothermal therapy: applications and opportunities for multimodal cancer treatment. *Wiley Interdiscip. Rev. Nanomedicine Nanobiotechnology* **9**, e1449 (2017).

63.   Molotkovsky, J. G. Fluorescent lipid probes: Properties and application. *Russ. J. Bioorganic Chem.* **25**, 759–771 (1999).

64.   Campbell, F. *et al.* Directing Nanoparticle Biodistribution through Evasion and Exploitation of Stab2-Dependent Nanoparticle Uptake. *ACS Nano* **12**, 2138–2150 (2018).

65.   Li, H. *Microspore embryogenesis: Reprogramming Cell Fate form Pollen to Embryo Development.* (2014).

66.   Cheung, A. Y., Boavida, L. C., Aggarwal, M., Wu, H. M. & Feijó, J. A. The pollen tube journey in the pistil and imaging the in vivo process by two-photon microscopy. *J. Exp. Bot.* **61**, 1907–1915 (2010).

67.   Gooh, K. *et al.* Live-Cell Imaging and Optical Manipulation of Arabidopsis Early Embryogenesis. *Dev. Cell* **34**, 242–251 (2015).

68.   Ohtsu, M. *et al.* Fluorescent Labeling of the Cyst Nematode Heterodera glycines in Deep-Tissue Live Imaging. *Cytologia (Tokyo).* **82**, 251–259 (2017).

69.   Mizuta, Y., Kurihara, D. & Higashiyama, T. Two-photon imaging with longer wavelength excitation in intact Arabidopsis tissues. *Protoplasma* **252**, 1231–1240 (2015).

70.   Mahou, P. *et al.* Multicolor two-photon tissue imaging by wavelength mixing. *Nat. Methods* **9**, 815–818 (2012).

71.   Stringari, C. *et al.* Multicolor two-photon imaging of endogenous fluorophores in living tissues by wavelength mixing. *Sci. Rep.* **7**, 1–11 (2017).

72.   Tillo, S. E., Hughes, T. E., Makarov, N. S., Rebane, A. & Drobizhev, M. A new approach to dual-color two-photon microscopy with fluorescent proteins. *BMC Biotechnol.* **10**, 2–7 (2010).

73.   Zoumi, A., Yeh, A. & Tromberg, B. J. Imaging cells and extracellular matrix in vivo by using second-harmonic generation and two-photon excited fluorescence. *Proc. Natl. Acad. Sci. U. S. A.* **99**, 11014–11019 (2002).

74.   Cha, J. W. *et al.* Non-descanned multifocal multiphoton microscopy with a multianode photomultiplier tube. *AIP Adv.* **5**, 084802 (2015).

75.   Rakotoson, I. *et al.* Fast 3-D Imaging of Brain Organoids With a New Single-Objective Planar-Illumination Two-Photon Microscope. *Front. Neuroanat.* **13**, 1–14 (2019).

76.   Quicke, P. *et al.* High speed functional imaging with source localized multifocal two-photon microscopy. *Biomed. Opt. Express* **9**, 3678 (2018).

77.   Hagen, G. M., Fliegel, K., Republic, C. & Republic, C. Comparison of image reconstruction methods for structured illumination microscopy. **9129**, 1–13 (2014).

78.   Ingaramo, M. *et al.* Two-photon excitation improves multifocal structured illumination microscopy in thick scattering tissue. *Proc. Natl. Acad. Sci.* **111**, 5254–5259 (2014).

Chapter 4

Wide-field two-photon imaging of single fluorophores by structured illumination

Single molecule microscopy is often hampered by autofluorescence and *in vivo* inelastic scattering impairs the visibility of the weak signal from single fluorophores. Two-photon microscopy decreases background fluorescence by using near-infrared light, and reduces the excitation volume due to the non-linear excitation mechanism, and limits out-of-focus photodamage and bleaching. However, the low two-photon absorption cross-section of most fluorophores requires a high light intensity. This is usually implemented by confocal scanning and yields lower frame rates and increases photobleaching. Here we build on previous efforts using multifocal excitation to increase the image speed, and compare two scanning modes that both yield a wide field light-sheet-like excitation. In live zebrafish embryos background fluorescence and photobleaching are further reduced, enabling tracking of single fluorophores for more than 30 seconds. Furthermore, we show that multifocal excitation with structured light sheet illumination suppresses background in highly scattering environments. Finally, we used single-molecule tracking to quantify diffusive behavior of single eGFP-HRas molecules and observed longer and less confined tracks, that suggest that the mobility of these proteins differs in different regions of the same cell. The experiments demonstrate for the first time that two-photon microscopy can readily be used for *in vivo* single-molecule tracking and, contrary to previous reports, it is shown to reduce photobleaching, while achieving significantly improved signal to noise ratios.

Contributing authors:
Vlieg, R. C., Gora, R., Pham, C., Schaaf, M., van Noort, J.

4.1 INTRODUCTION

Single molecule fluorescence microscopy has been fundamental for quantitative understanding on how biological systems function at the microscale. The ability to track a protein in space and time allows to study behavior normally obscured by the ensemble of molecules. To resolve the weak signal from a single fluorophore, often residing within a complex and scattering environment, efficient signal collection and background suppression is required. Total internal reflection microscopy (TIRF) reduces background signal by illuminating only in near-field, limiting the detection of fluorophores to within ±100 nm from the cover glass[1]. For three-dimensional (3D) tracking of fluorophores a larger volume needs to be illuminated, which generally necessitates a pinhole to reject out-of-focus light, as done in fluorescence correlation spectroscopy (FCS)[2], laser scanning confocal[3], and spinning-disc microscopy[4]. Although effective for reducing background, fluorophores that do not contribute to the image still suffers from photobleaching outside the focal volume.

A more preferable scenario for tracking fluorophores in 3D would be to excite only within the focal volume, thereby eliminating out-of-focus signal. Two-photon microscopy (TPM) does exactly this by confining excitation to a volume defined by a quadratic dependence on laser power[5]. Moreover, excitation by near-infrared light allows for deeper imaging into tissues[6] and reduces autofluorescence[7]. Despite these advantages single fluorophore studies with TPM have been limited mostly to *in vitro* experiments[8–16].

One major issue with two-photon excitation (TPE) is fluorophore stability. The high photon intensity in the focal volume and the promotion of a fluorophore to higher order excited states result in bleaching times that are typically a factor $3 - 5$ shorter compared to single-photon excitation[10,17,18]. Also, the low two-photon absorption cross section ($\sigma^{(2)}$) of most commonly used fluorophores diminishes fluorophore brightness, necessitating longer pixel dwell times or even higher laser power. Unfortunately, bleaching scales with laser power to an exponential power larger than 2, while fluorescence scales only quadratically[14,17,19–21]. This prevents capturing single fluorophores at a high temporal and spatial resolution for extended periods of time. For example, using quasi wide-field TPE, proteins tagged by a single fluorophore were tracked on an artificial cellular membrane[13]. Although the reported background of the membrane was drastically reduced from 400 counts pixel[-1] ms^{-1} with one-photon, to 3.4 counts pixel[-1] ms^{-1} with TPE, most fluorophores lost their fluorescence before 20 images could be taken.

The issue of photobleaching by TPE calls for an illumination method where laser power is reduced, while tracking applications require pixel acquisition rates that are sufficiently high to capture single fluorophores over a large field-of-view (FOV). To achieve a *N*-fold increase in pixel rate at the same signal-to-noise ratio (SNR), a two-photon single-focus microscope (TPSM) would need $\sqrt{N}$ higher laser intensity. Two-photon multifocal microscopy (TPMM)

improves acquisition speeds by N by splitting the excitation beam into N beamlets[22]. Unlike TPSM, the increase in speed is achieved without increasing the excitation power in each focus. This property suggests that higher frame rates can be achieved with TPMM at similar bleach rates as TPSM, or that bleaching times can be extended when imaging a similar-sized FOV. TPMM can be readily implemented by using passive optical elements to split the laser beam (e.g. diffractive optical elements (DOEs)[23,24], beam splitters[25,26]) and a camera to detect emission from the multiple foci.

A drawback of TPMM is the increase in background signal from scattered emission photons reaching incorrect camera pixels. Especially for highly scattering biological samples, low background signal is essential to resolve the weak signals of single fluorophores. A number of methods have been developed to suppress background from diffused emission light. In a de-scanned approach, the position of the emission beamlets remains stationary irrespective of the scanner motion by reflecting the emission photons back along the scanning mirror onto a multi-anode photomultiplier tube. This allows to collect more scattered photons onto the right detector and achieving higher contrast at deeper imaging depths[27,28]. Improvements were made in SNR by reducing the emission path-length in a non-descanned approach and increasing the distance between each focus[29]. Still, the low quantum efficiency ($\pm16\%$) of multianode photomultipliers and the limited imaging speeds gain impairs detection of single fluorophores. By using a Richardson-Lucy deconvolution method to correct the location of the scattered photons, no additional optics is needed for background suppression while employing a sCMOS camera with a high quantum efficiency (82%)[24]. Structured illumination microscopy (SIM) has similar benefits to deconvolution. SIM suppresses background by filtering out the low spatial frequency noise from the image signal, resulting in enhanced contrast[30–32].

Here we combine structured illumination with TPE into structured light sheet illumination microscopy (SLIM). Besides changing the scan-pattern and the image reconstruction, SLIM requires no additional optics compared to conventional TPMM. SLIM uses multiple frequency-modulated images to compute a reconstructed image. In subsequent images, illumination patterns are spatially shifted and the total set of images illuminate the full FOV. By applying a discrete Fourier transform to the stack of images, all signal with frequencies other than the modulation frequency are suppressed – thus reducing background. SLIM is compatible with high-quantum efficiency camera detectors which are required for single molecule detection[33].

In this work we explore the TPMM capability of imaging single fluorophores in wide-field. Dividing excitation power over multiple foci resulted in 5-fold higher acquisition speeds at similar bleaching rates compared to confocal TPM. We also investigated the ability of SLIM to further reduce the background intensity in zebrafish embryos (*Danio rerio*) and compare the result to previously established spiral-scanning illumination[34]. Using SLIM, background signal was reduced to below single-molecule brightness in the highly scattering zebrafish embryos environments. Subsequent measurements revealed individual eGFP tagged HRas proteins as they moved across the membrane. The limited *in vivo* photobleaching allowed us to track

molecules for hundreds of frames. The ability to measure single fluorophores for extended periods of time enables the study of protein dynamics normally obscured by photobleaching in more established microscopy techniques like total internal reflection fluorescence (TIRF) microscopy. These properties make TPMM combined with SLIM a new and promising technique for single molecule studies.

4.2 MATERIALS AND METHODS

Microscopy setup. A tunable near-IR Ti:Sa laser (Coherent, Chameleon Ultra) was coupled into a home-build two-photon multifocal microscope. A diffractive optical element (DOE, custom made by Holo-eye) diffracted the laser beam into an array of 10 x 10 beamlets. A fast-scanning mirror (FSM, Newport, FSM-300-1) scanned the beamlets across the excitation plane. The laser beams were focused using 60X NA 1.49 oil objective (Nikon, CFI60 Apochromat TIRF 60XC) mounted on a piezo-stage (PI, P-726 PIFOC), illuminating an area of 40 μm x 40 μm. Two-photon luminescence was collected by the same objective, filtered with a dichroic mirror (Semrock, 700dcxr) and two short pass filters (Semrock, FF01-720-SP & FF01-750-SP) and focused on a 2048 x 2048 pixel back-illuminated sCMOS camera (Photometrics, Prime BSI). Additional band pass filters, mounted in a motorized fast-change filter wheel (Thorlabs, FW103H/M), were positioned in front of the camera. Using self-written LabVIEW (National Instruments) software, the scanning mirror, focusing stepper motors and camera were controlled synchronously. For imaging of the zebrafish embryo the objective was replaced by a 25X NA 1.1 water objective (Nikon, CFI75 Apochromat 25XC) and the DOE was replaced by another DOE that generated a pattern of 25 x 25 beamlets (custom made by Holo-eye). This yielded an illuminated area of 180 μm x 180 μm.

Spiral illumination. For spiral scanning, the FSM was driven by an Archimedean spiral to rapidly scan the beams producing a fairly homogeneous illuminated wide-field, as characterized before[34]. A single period of the spiral scan took 200 ms and was synchronized with the camera integration time.

SLIM. For structured illumination the beamlets were scanned in four periods of a sinusoidal pattern in one direction (y). The amplitude in y-direction was 3 times the distance between neighboring foci (d), with d = 7.5 μm. The relative large amplitude resulted in more regular illumination than when the amplitude matched the spot-to-spot distance, especially at the maxima and minima of the periodic sweep. Four oscillations of the scanning beam were synchronized with integration time for one frame, which resulted in a "phase image" (g_n), as shown in Figure 4.1. Next, the beamlets were translated in x direction by $(d - \omega)/N$, with ω the

full-width at half maximum of the point spread function of the system (0.39 μm) and N the number of phase images per SLIM image. With $d/2 = 3.25$ μm, the optimal N was given by $d/\omega_{PSF} = 8.3$, which was rounded down to spatially sample the entire field-of-view (FOV). Between successive images there was a dead time of 5 ms, plus 1 ms per 128 pixel lines, which was used to empty the camera buffer into solid state storage and to reposition the FSM. The brief pauses between acquisition resulted in a total exposure duty cycle of 0.96. SLIM images were reconstructed via:

$$I(x,y) = \left| \sum_{n=1}^{N} g_n(x,y) e^{-i\varphi_n} \right| \tag{4.1}$$

with the spatial phase φ_n defined as:
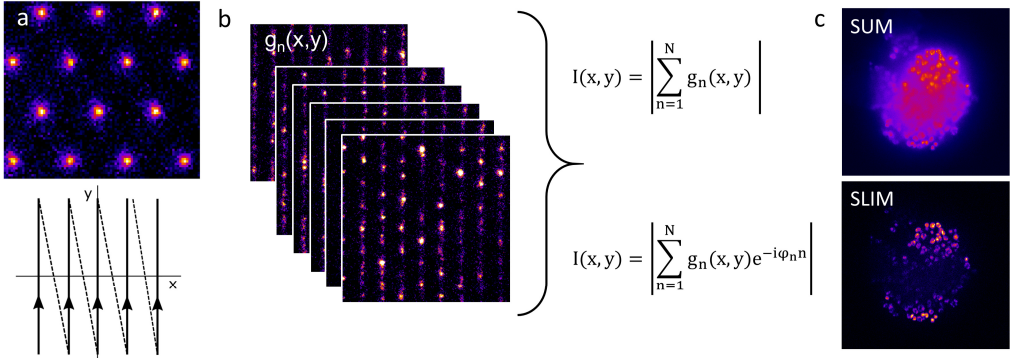
$$\varphi_n = \frac{2\pi(n-1)}{n} \tag{4.2}$$

Figure 4.1: SLIM reconstruction reduces background signal. (a) To create a single SLIM image, the foci-pattern is linearly scanned across the image plane with a small lateral shift in each image. **(b)** n phase-images (g_n) are combined to yield either a conventional image, or a frequency selected reconstructed image, by a discrete Fourier transformation. **(c)** The summated image of a spheroid cluster of cells features a high intensity with a maximum at the center of the spheroid. In the SLIM image, reduction of scattered photons makes single cells clearly visible.

Rhodamine 6G sample preparation. Glass coverslips were sonicated in ethanol for 30 minutes, dried in a stream of nitrogen and treated in a UV-cleaner for 30 minutes. After cleaning, 100 μl of rhodamine 6G solution [100 pg/μl] (Sigma-Aldrich, 83697) was pipetted onto the glass surface and gently removed after 3 minutes under a nitrogen stream.

For the bleaching experiments the concentration of rhodamine 6G was increased to 100 ng/μl to form a homogenous layer on the glass surface.

Rhodamine-labeled DNA. Rhodamine-5-dUTP (11534378910, Sigma-Aldrich) was enzymatically incorporated into DNA using polymerase chain reaction (PCR). Plasmid pUC18 DNA was used as a template. A 100 µl PCR mixture contained 2.5 units of FastStart Taq DNA polymerase (5U/µl), 10 µM of forward (5' CTC CAA GCT GGG CTG TGT 3') and 10 µM backward primers (5' GAT AAA TCT GGA GCC GGT GA 3'), 100µM of dNTPs and 50 µM of rhodamine-5-dUTP and 1X PCR reaction buffer with 10X MgCl₂. The PCR reaction was run with the following program: step 1: 240 seconds at 95 ℃; step 2: 30 seconds at 95 ℃; step 3: 30 seconds at 49 ℃; step 4: 45 seconds at 72 ℃; step 5: 300 seconds at 72 ℃. Steps 2-4 were cycled 40 times. The PCR products were purified with a Promega Wizard SV Gel & PCR cleanup kit following the manufacturers' protocol. The concentration of the DNA substrate was measured with UV/Vis spectrophotometer (BioDrop µLITE, Isogen Life Science).

Flowcell preparation. The DNA-rhodamine constructs were immobilized inside flow cells. Glass coverslips were sonicated for 30 minutes in ethanol and UV-cleaned for an additional 30 minutes. After cleaning, flow cells were constructed by sandwiching double-sided stickers between the cover slips. Rectangular holes were cut into the stickers to create channels of approximately 50 µl per channel. The flow cell was mounted onto a laser cut scaffold for stability and to facilitate for pipetting solutions into the channel. Once constructed, the channels were incubated with a 0.01% (w/v) poly-L-lysine solution (P4707, Sigma-Aldrich) for 30 minutes. After gently flushing with 150 µl HPLC-grade water, 50 µl of 100 pM DNA was injected and incubated for 3 minutes. After 3 minutes the flow cell was again gently flushed with 150 µl of HLPC-grade water and ready for imaging.

Zebrafish embryos. Zebrafish (*Danio rerio*, strain AB/TL) were maintained and handled according to the guidelines from the Zebrafish Model Organism Database (http://zfin.org) and in compliance with the directives of the local animal welfare committee of Leiden University. Fertilization was performed by natural spawning at the beginning of the light period, and eggs were raised at 28.5 °C in egg water (60 µg/ mL Instant Ocean sea salts). The previously established *Tg(kdrl:mTurquoise)* zebrafish line was used yielding fluorescence in the endothelial cells by fusion of the fluorescent protein mTurquoise to the vascular endothelial growth factor *kdrl*[35]. Three-day post fertilization (*dpf*) old embryos were anesthetized in 0.01% tricaine and placed onto a glass coverslip. Embedding the embryos in 0.4% agarose before imaging minimized movement. For the single molecule measurements, transfection of eGFP-C10H-Ras into *kdrl* line embryos and sample mounting was done according to previously described protocol[36]. In short, zebrafish eggs at the one- to two cell stage were microinjected with eGFP-C10H-Ras mRNA (30pg/egg). At three *dpf*, embryos were positioned on their side on a glass coverslip and a ±0.75 mm thick sheet of agarose was placed over the tail section of the embryo for imaging.

Simulations. Simulations of single molecule measurements by spiral illumination and SLIM were done in Pyhton 3 code. A pattern of foci was generated based on the actual distance between foci of the setup: 6.4 μm ± 0.1 μm. For each time-step, corresponding to 1 μs, the position of the pattern was translated corresponding to the voltage (V_x, V_y) of the fast-scanning mirror of the setup. V_x and V_y were converted to pixels based on an experimentally determined conversion factor. In each time step the coordinates of the foci were convoluted by the excitation point spread function (PSF$_{exc}$). *PSF$_{exc}$* was approximated by a two-dimensional (2D) Gaussian profile with width (σ_{exc}) based on the numerical model of Richards and Wolf[37] Which state that for objectives with NA>0.7, the estimate of a squared Gaussian profile best fits with a slight inverse power dependence of 0.91:

$$\sigma_{exc} = \frac{0.65\,\lambda}{NA^{0.91}} \tag{4.3}$$

A map of the effective exposure time for each pixel (M$_{exp}$) was computed by integration of the intensity of each pixel over all time steps during one exposure. This was combined with a map of randomly distributed molecules on a 2D surface (*M$_{sample}$*). A fluorescence image (*M$_{fluorescence}$*) was calculated according to:

$$M_{fluorescence} = q\,M_{sample}M_{exp}\ p\,R\,P_{focus}{}^2 \tag{4.4}$$

with power per focus *P$_{focus}$* in W/cm^2, the repetition rate of the laser *R*, *q* the quantum efficiency of rhodamine 6G (q=0.95)[14], and *p* the probability of two-photon excitation per pulse per Watt/cm^2. *p* was defined as[38]:

$$p = \frac{0.588}{2}\sigma^{(2)}\tau\left(\frac{1}{R\tau}\frac{\lambda}{hc}\right)^2 \tag{4.5}$$

with $\sigma^{(2)}$ the two-photon absorption cross-section of a fluorophore (in cm^4 s photon^{-1}), τ the pulse width (in fs), *h* Planck's constant, *c* the speed of light. At an excitation wavelength of 0.83 μm we used $\sigma^{(2)} = 100$ cm^4 s photon^{-1} for rhodamine 6G in methanol[14]. Convolution of *M$_{fluorescence}$* with the emission PSF (σ=0.4 μm) gives the 2D image with the diffraction limited signals (M$_{signal}$).

The amount of signal was corrected for the collection efficiency of the setup:

$$I_{image} = M_{fluorescence}\,\eta_{objective}\,\eta_{path}\,q_{cam} \tag{4.6}$$

where *I$_{image}$* is the actual signal detected by the camera. η_{obj} is the collection efficiency of the objective, η_{path} the transmission efficiency of the emission path, and q_{cam} the quantum efficiency of the camera. For our camera, q$_{cam}$ = 0.93, as specified by the manufacturer. The collection efficiency for a 1.49 NA objective is 0.42. η_{path} was calculated by multiplication of the

transmission coefficients of the filters in the emission path and an additional factor of 0.96 per lens surface, which results in $\eta_{path} = 0.55$. Overall, the detection efficiency was $\eta_{setup} = 0.21$, for a wavelength of 500 nm.

For the final image (I) noise factors were added:

$$I = \text{Poisson}(I_{signal}) + \sigma_{dark} + \sigma_{read} \tag{4.7}$$

where the Poisson distribution of I_{signal} accounts for shot-noise, σ_{dark} is the Poisson distributed dark-noise of the camera and σ_{read} the Poisson distributed read-noise of the camera. Simulated images were processed using the same software as the experimental data.

Spot detection. The locations of peaks in the fluorescence images were extracted iteratively, starting with the maximum intensity in the image. A circular mask of 7 pixels x 7 pixels was used to block the signal around the found pixel, after which the next pixel with the highest intensity was located. This iterative process was continued until a pixel intensity lower than the mean intensity of the image plus three times the standard deviation of the background was reached.

Signal-to-noise ratio. For each detected spot a circular shaped region of interest (ROI) of 5 pixels diameter was summed to calculate the signal-to-noise ratio (SNR):

$$\text{SNR} = \frac{I_{signal} - I_{background}}{\sigma_{background}} \tag{4.8}$$

with I_{signal} the integrated intensity of the ROI. A second doughnut shaped ROI with the same area as the first ROI was used to calculate $I_{background}$ and $\sigma_{background}$.

Bleaching curves. For extracting the bleaching times (τ_{bleach}), $I(t)$ was fitted to an exponential function:

$$I(t) = I_0 e^{-t/\tau_{bleach}} + c \tag{4.9}$$

with I_0 the initial intensity and c the offset.

Single molecule tracking and mean squared displacement (MSD). Spots from the movies of eGFP-HRas measurements were located using TrackMate software as bundled with the Fiji distribution package of ImageJ[39]. The image was median filtered and a Laplacian to Gaussian (LoG) detector was used to filter the image on blob sizes with an estimated diameter of 0.5 μm. Blobs with an intensity lower than 3 times the standard deviation of the background were discarded. A simple linear assignment problem (LAP) tracking algorithm was used to link

the detected spots. We set the maximum distance for spot-linking and the maximum gap-closing distance at 0.6 μm, the maximum frame gap between spots was set to 5 frames. After spot-linking, the shortest 10% of all traces were discarded.

The remaining time traces were exported to the open source Icy software. Using the incorporated Track Manager, trace coordinates were converted to a MSD per time-unit t_{lag}. All MSD curves were averaged over all traces, and the confinement length (L) and diffusion coefficient (D) were extracted from the data by fitting a confined displacement model:

$$\text{MSD}\left(t_{\text{lag}}\right) = \frac{L^2}{3}\left(1 - \exp\left(\frac{-12D_0 t_{\text{lag}}}{L^2}\right)\right) + A \qquad (4.10)$$

with the initial diffusion constant D_0 and a fixed offset A set at 0.005.

4.3 RESULTS

4.3.1 SINGLE MOLECULE FLUORESCENCE BY SPIRAL ILLUMINATION

First we measured single fluorophores by two-photon spiral illumination. To minimize photo-bleaching, the laser power was attenuated to 1.8 mW per focus by neutral density filters. A region of interest (ROI) from the resulting image is shown in Figure 4.2a and shows randomly distributed diffraction limited spots. To determine whether the spots originated from single fluorophores we continuously imaged at 4 Hz for 60 seconds and checked for discrete bleaching steps. Three representative time traces are plotted in Figure 4.2b. The intensity for all three traces is around 1000 Hz at the start of the measurement. Distinct single bleaching steps, indicative of single molecules, occurred during the measurement which shows that the TPE signal from single fluorophores is readily observed for tens of seconds.

Having established two-photon single molecule fluorescence, we next characterized the signal of all fluorophores. A total of 86 peaks were identified in the first image of the measurement. Bleaching was defined as when the 5 point moving average filtered signal dropped below 1.5 times the average background. The distribution of the signal intensity from these 86 traces and their background is plotted in Figure 4.2c. With a signal of $9 \pm 4 \times 10^2$ Hz (mean $\pm$ SD) and an average background of $2.4 \pm 1.1 \times 10^2$ Hz, the signal-to-noise ratio (SNR) for all traces was 4 ± 2. This indicates that the excitation power of 1.8 mW per focus in combination with 200 ms integration time, is sufficient to detect single fluorophores with sufficient SNR. We observed a larger variation ($\sigma = 4 \times 10^2$ Hz) in intensity than we would expect from a shot-noise limited signal ($\sigma = 0.5 \times 10^2$ Hz). These larger fluctuations could arise could from instability of the fluorophores. The corresponding time before bleaching is plotted in Figure 4.1d. The distribution of bleaching times was fitted to an exponential decay function (equation 4.9), yielding an average bleaching time of 17 ± 2 seconds. A large number of peaks did not bleach during 60 seconds of imaging, but these were not processed due to poor SNR. The presence of these weak fluorescent signals after 60 seconds suggests a non-homogeneous excitation pattern and that these fluorophores received less illumination than the fluorophores displayed in Figure 4.2. Though these measurements show that it is possible to image single fluorophores in wide-field with TPE *in vitro*, for biological applications *in vivo* the demands are tougher, partially due to the increased background.
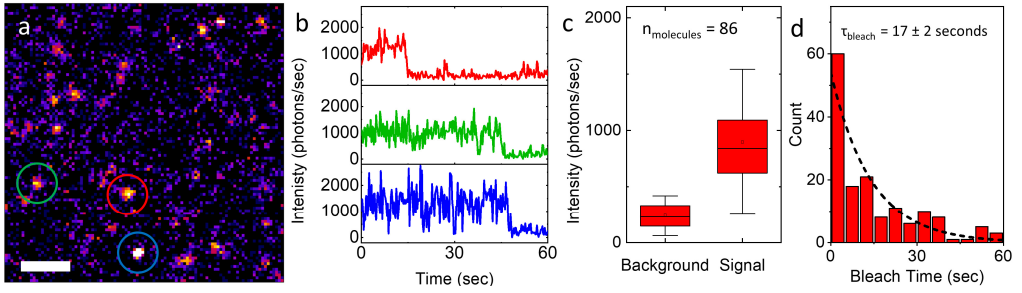
Figure 4.2: **Two photon image of single rhodamine 6G molecules imaged in wide-field.** (a) A wide-field image of individual rhodamine 6G molecules on a glass surface. Sample is illuminated by spiral-scanning of multiple foci. Scale bar = 5 µm. (b) Time traces of the fluorophores as indicated by color from *a*. Single bleaching steps indicate that signal originates from a single fluorophore. (c) Distribution of the background and signal of single molecules. Single molecules are resolved with an average SNR of 3.5. d) Distribution of the bleach times from 86 individual fluorophores. Distribution is fitted to an exponential, yielding a half-time ($t_{1/2}$) of 16.5 seconds.

4.3.2 BACKGROUND REDUCTION BY SLIM

Reducing the background signal is important for better contrast images, and indirectly for extending the bleaching time because it allows for lower excitation power. To investigate the ability of SLIM to reduce the background intensity *in vivo*, we imaged blood vessels inside the brain of three-day old zebrafish embryos. The embryos expressed mTurquoise in endothelial cells by fusion of the fluorescent protein to the vascular growth factor *kdrl*. Figure 4.3a shows a cross-section of a blood vessel approximately 40 µm inside the embryo imaged by spiral illumination. The SLIM image in Figure 4.3b is of the same location as Figure 4.3a. As opposed to the SLIM image, in the spiral scanning image there is substantial intensity in the center of the blood vessel. Also on the right of the blood vessel there is a large area which features enhanced brightness. As both image modalities optically dissect the sample via TPE, this signal cannot be attributed to out of focus excitation, and is therefore likely the result of scattered fluorescent signal. A ROI from Figure 4.3a (white square) is shown in Figure 4.3c. The image displays the higher fluorescence in the blood vessel more clearly. In the annotated ROIs (dotted white lines) the average intensity inside was 205 ± 62 Hz and outside the blood vessel it was 93 ± 29 Hz. We compared the background found here with the signal we measured for single rhodamine 6G molecules on glass using the same illumination settings. For this, we divided the average intensity of 900 Hz from Figure 4.2c by the 5 x 5 mask size from which that signal was integrated, this yields an intensity per pixel of 36 Hz. Note that the peak intensity of a spot was typically three times higher. The average intensity is lower than the background intensity of the *in vitro* measurements, suggesting that spiral illumination would hardly be able to resolve TPE single molecule fluorescence in zebrafish embryos. At the same location for the SLIM image, shown in Figure 4.2f, the background is 14 ± 26 Hz inside and 15 ± 17 Hz outside the blood

vessel. In both cases, the reduction in background suggests that it would be possible to detect single fluorophores *in vivo* using TPE.
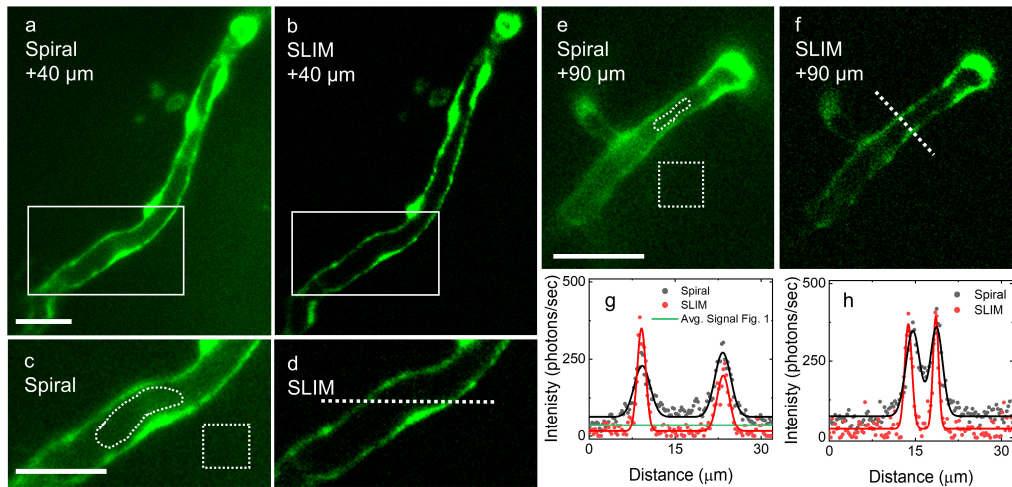

Figure 4.3: Structured illumination reduces scattered light to improve background in *in vivo* environments like the brain of zebrafish embryos. (a) A cross section of a blood vessel imaged via spiral illumination approximately 40 µm inside the embryo. The nuclei are indicated by the thicker and brighter areas of the blood vessel. Scattered light is visible even at larger distances away from the vessel. (b) Imaging the same FOV as in *a* now with SLIM yields a clear reduction in background noise across the image, while retaining signal from the blood vessel. (c) Zoom-in on a blood vessel as annotated in *a* (white square). Background is higher inside the blood vessel compared to the outside. (d) Zoom-in on the annotated ROI in *b* (white square). SLIM clearly reduces background both out- and inside the blood vessel. (e) Cross-section of a blood vessel imaged via spiral illumination located at approximately 90 µm inside the brain. Background appears brighter inside the thinner blood vessel. (f) Even at larger depths SLIM is able to reduce background to a minimum. (g) Comparison between the intensity profiles as annotated in *d* (dotted white line). The boundaries of the blood vessel are clearly visible by two peaks. SLIM reduces background in the blood vessel to the same level as outside the blood vessel. For reference, a line is drawn that indicates the average signal of single fluorophores on glass from Figure 4.2. (h) Intensity profiles from the cross section as annotated in *f* (white dotted line). Again SLIM reduces the background inside the blood vessel to similar level as outside the blood vessel. Also, the blood vessel walls are imaged much sharper in SLIM compared to spiral. Scale bars = 25 µm.

Besides the lower background, the SLIM image features thinner blood vessel walls than the spiral image, as can be seen from the profile plots in Figure 4.3g. Fitting Gaussian functions to the peaks gives a full-width-at-half maximum (FWHM) of 3.3 ± 0.2 µm for both peaks in the spiral image, and 1.8 ± 0.1 µm and 2.5 ± 0.2 µm in the SLIM image. The sharper defined boundary of the endothelial cells quantifies the better resolution due to the suppression of scattered photons. We also imaged blood vessels 90 µm inside the brain. The spiral image of this section is shown in Figure 4.3e and the SLIM image in Figure 4.3f. Similar to the images captured closer to the objective, SLIM reduces background signal significantly. From annotated ROIs (white dotted lines) we find that the background signal inside the blood vessel is reduced

from 207 ± 48 Hz to 27 ± 24 Hz when illuminating with SLIM as compared to spiral scanning. Background signal inside the blood vessel is higher compared to the more superficial vessel. Still, SLIM drastically reduced background signal at 90 µm imaging depth, with a background below single molecule intensities. The increased absorption and scattering of emission photons however, may complicate the detection of single molecules at these depths. The higher background is likely caused by the narrower blood vessel which increases the possibility of including signal of the top or bottom of the vessel. Outside the blood vessel SLIM does reduce background to 11 ± 17 Hz, which is similar to that of the superficial vessel. The intensity profiles (dotted white line, Figure 4.3f) for the spiral and SLIM images are plotted in Figure 4.3h. The profile plots clearly show that SLIM is able to image the blood vessels sharper, which translates to a reduction in background signal inside the vessel as there is no overlap between signal from the blood vessel walls. From fitting Gaussian profiles in the spiral image, we find that the FWHMs of the blood vessel walls are 2.9 ± 0.2 µm and 2.5 ± 0.1 µm. In contrast, in the SLIM image they are 1.4 ± 0.1 µm and 1.2 ± 0.1 µm – a reduction of more than two.

Besides attenuating scattered emission photons, SLIM may also help to reduce reflected excitation light from the laser. Due to the difference in wavelength, and hence the difference in PSF of the excitation and the emission light, this may be especially effective for out-of-focus reflections, for example at the interface between the bottom of the slide and the immersion liquid. The ability to suppress back-reflected light relaxes the necessity for spectral filters in the emission path which will increase the collection efficiency of the setup. To demonstrate this, we imaged rhodamine-5-molecules incorporated in a DNA construct that was immobilized on a glass surface. To facilitate detection an average of 9 rhodamine molecules were incorporated per DNA molecule. To enhance the contribution of reflected light we removed one of the band pass filters in the emission path and imaged the sample by spiral scanning and SLIM, the results are shown in Figure 4.4a and 4.4b. Without the second emission filter, the excitation area can be clearly distinguished by the increased background signal in the middle of the spiral image. Inside the excitation area, spots of higher intensity indicate the location of DNA rhodamine. Although the DNA molecules are clearly discernable, the increased background compromises the signal to background ratio. Note that the difference in intensity between the spots likely originates from variations of the number of rhodamine fluorophores per DNA molecule or perhaps even from aggregates of DNA. Switching to SLIM, the reflections from the laser are indeed significantly reduced and DNA rhodamine is clearly visible in the reduced background.

We compared the background for both illumination modalities by plotting the average intensity inside annotated ROIs (white squares). With two band pass filters, spiral and SLIM have a similar average background of 20 ± 21 Hz and 17 ± 24 Hz, respectively. The background increases around a factor of 4 to 80 ± 26 photons/second when a band pass filter is removed in spiral imaging. In contrast, the SLIM image retains a low background at 13 ± 25 photons/second. We confirmed suppression of scattered photons in simulations, see Figure S4.1. The simulations show how SLIM is less affected by an increasing background signal compared to spiral

illumination. Interestingly, the simulations suggest that in absence of reflected laser light, spiral illumination is able to resolve more single fluorophores and at a higher SNR. Still, from these results we can conclude that SLIM is effective to remove reflected of light from the laser, which allows for more efficient detection of fluorescence and could be useful for single molecule detection.
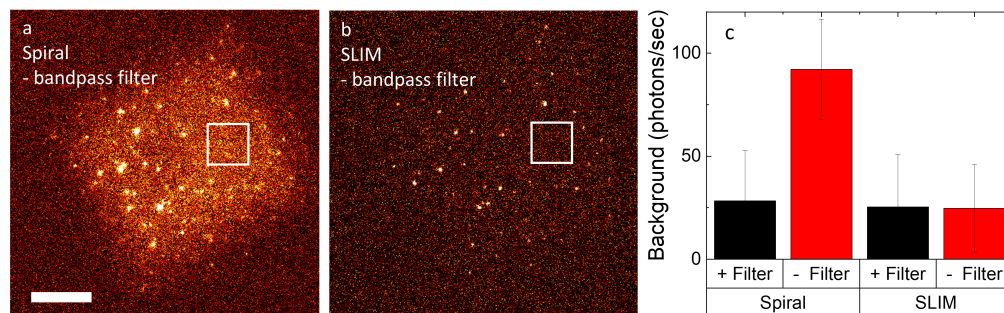

Figure 4.4: Reflected light is removed from the image by SLIM. (a) DNA tethered on glass loaded with an average of 9 rhodamine B molecules imaged via spiral scanning. By removing a band pass filter in the emission path laser light adds a high background intensity. Scale bar = 10 μm. (b) SLIM image of the same FOV and with similar imaging conditions as *a*. Background is reduced to the level outside the excitation field, while the DNA-rhodamine spots are still visible. (c) Comparison of the background of both illumination modalities with and without bandpass filter. Spiral scanning increases the average background 3.7 times while SLIM remains at similar levels.

4.3.3 SIMULATIONS

We simulated single molecule experiments for both spiral and SLIM illumination to better understand how SLIM could improve single molecule studies. First we studied the influence of the number of phase-images on single molecule detection. From the *in vivo* measurements in zebrafish embryos we noticed that SLIM results in less homogenous illumination than spiral scanning, see Figure S4.2. Due to the non-linear excitation, this may be more problematic for two-photon imaging than for one-photon imaging. In the simulations, randomly generated locations of fluorophores were convoluted with a Gaussian profile with a width of 0.4 μm to act as the ground truth image of the fluorophores, shown in Figure 4.5a. The same fluorophore coordinates were used in the spiral- and SLIM simulations for direct comparison between the images. Spiral scanning was simulated with the same parameters as used in the experiments, while for SLIM the number of phase images was varied from 1 to 9.
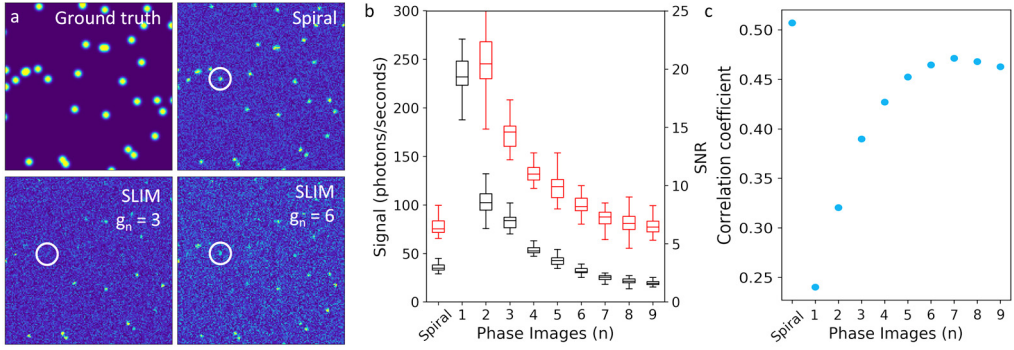
Figure 4.5: Theoretical comparison of spiral scanning and SLIM microscopy. For SLIM the number of phase-images has a large effect on the resulting image. Spiral scanning yields a better representation of all fluorophores while SLIM produces higher SNR. (a) ROI of an input image showing a distribution of fluorophores. The spiral image captures all fluorophores, whereas some fluorophores in the SLIM images are hardly visible. (b) The signal intensity (red) and SNR (black) of 150 fluorophores from each simulation. The small variation in signal intensity from spiral scanning indicates a homogeneous illumination across the image. SLIM under-samples the image which results in large variations in signal intensity. For seven phase-images or more, signal comes close to that of spiral images, but SNR decreases however. (c) Correlating the images with the ground truth provides a measure on how well the image is reconstructed. The higher correlation coefficient of spiral scanning indicates better performance of spiral scanning for imaging fluorophores. At n=7, correlation is highest in SLIM reconstruction.

In the simulations, each fluorophore was observable in the spiral image, albeit somewhat obscured by the noise. In the image reconstruction from three phase images, it is clear that SLIM spatially under-samples the FOV, such that many fluorophores were undetected. The fluorophores which were detected are however brighter due to the longer exposure time per image. With eight phase images, the FOV appears to be fully sampled as all fluorophores were detected. However, their signal appeared less bright compared to the spiral image and showed more variation in brightness between the fluorophores. For example, the fluorophore indicated by the white circles is barely visible. To quantify these observations, images were processed similarly as the experimental single-fluorophore data. The SNR of 150 fluorophores was calculated. Signal intensity was defined by the amplitude of a fitted 2D Gaussian. The distribution of the peak intensity and the background are plotted in Figure 4.5b. The intensity of the spiral illuminated photons was 76 ± 12 Hz and the corresponding SNR is 2.7 ± 0.2. The relatively small variance indicates a homogenous illumination as the fluorophores receive similar exposure during integration of the camera.

In contrast, SLIM with only a few phase-images results in inhomogeneous illumination and therefore in large variation in signal and SNR. Illumination is distributed more evenly when increasing the number of phase-images. However, doing so decreased the signal and SNR. Using 6 phase images, the SNR is lower than that of spiral illumination. The lower SNR with higher average signal of 98 ± 14 Hz, indicates that a higher variance in background impairs the SNR of the SLIM images. Next to inhomogeneous illumination, this might be explained by additional

readout noise per phase-image that would reduce the SNR of the reconstructed SLIM image. To measure the resemblance with the ground truth image, we plotted the amplitude of the cross-correlation between the ground truth image and the simulated images in Figure 4.5c. Despite the 20% higher collection efficiency of SLIM due to the absence of a band pass filter, spiral scanning had the highest correlation coefficient. SLIM had a maximum correlation at 7 phase-images.
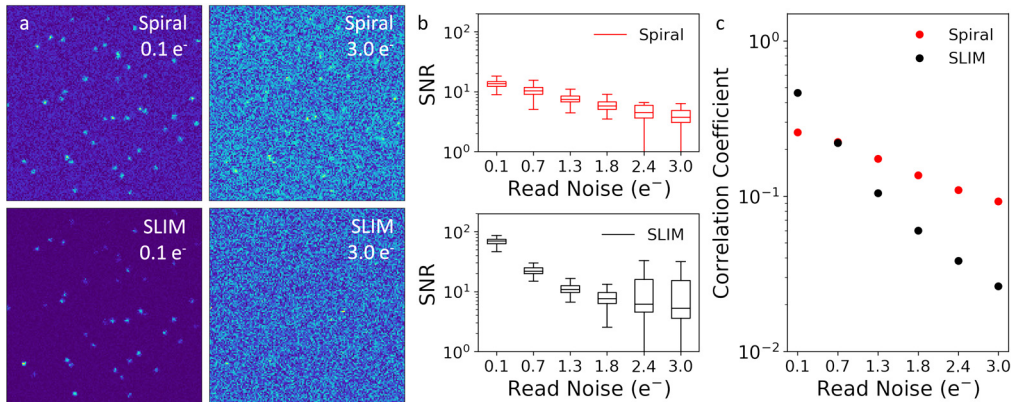

Figure 4.6: Simulations to study the influence of read noise on imaging single fluorophores for spiral scanning and SLIM. (a) Four ROIs for both illumination modalities at two different noise levels. At 0.1 e⁻ read noise spiral scanning and SLIM perform similar, while at 3.0 e⁻ fluorophores can hardly be observed in the SLIM image. (b) SNR for the spiral and the SLIM simulations. At 0.1 e⁻ the SNR of SLIM is higher, however it drops rapidly when the read noise is increased. The large standard deviation of the SNR for SLIM impedes detection of fluorophores. (c) Correlation coefficients for spiral and SLIM at different read noise levels. SLIM suffers more from a higher read noise than spiral scanning. These results show that the read-noise from multiple separate phase images result in a poorer performance of SLIM compared to spiral scanning.

The decrease in SNR when using more than 7 images for SLIM reconstruction suggests that camera read-out noise, which is a random signal that is generated each time a frame is acquired, may become the largest contributor to reduced image quality. To test this, we simulated spiral and SLIM measurements at different levels of camera readout noise. With 0.1 e⁻ readout noise both spiral and SLIM can easily discriminate fluorophores from the background, as shown in Figure 4.6a. At 3.0 e⁻ noise, no clear peaks are observed with SLIM, while in the spiral image most peaks are still above the noise floor. The trend in SNR when read noise is increased is plotted in Figure 4.6b. SLIM suffers significantly from more read noise compared to spiral. Interestingly, at 0.1 e⁻ SLIM achieves higher SNR than spiral scanning, where external scattered signal is dominant over read noise. The correlation coefficient, plotted in Figure 4.6c, shows a similar trend as the SNR. At minimal read noise SLIM is able to capture the distribution of fluorophores better than spiral illumination. However, as read noise becomes dominant, the correlation coefficient of SLIM decreases exponentially, with a rate 2.7 faster than the spiral

simulations. Why SLIM is more effected by read noise might be explained by the less signal which is collected per phase-image compared to a spiral image. With less signal and increasing noise, the SNR per phase-image decreases more rapidly compared to spiral scanning, which would translate into worse SNR of the reconstructed SLIM image. The median of the read noise of the camera used in our experiments is 1.1 e$^-$ as stated by the manufacturer. Based on these simulations with a low scattering background (0.5 e$^-$/second), spiral illumination would be the preferred illumination modality.

4.3.4 TWO PHOTON BLEACHING RATES

Suppression of background and removal of the band pass filter for higher collection efficiency, can be used to lower the excitation power while maintaining a similar SNR compared to spiral illumination. A reduction in excitation power is important for less photo-toxicity and reduced photobleaching. To clarify the relation between excitation power and bleaching, we measured the reduction in fluorescence over time when continuously imaging a dense layer of rhodamine 6G deposited on a glass coverslip. The summed intensity of a region of interest is plotted in Figure 4.7a. To extract the bleach rate (τ_{bleach}) we fitted a mono-exponential decay (equation 4.9) and plotted the bleach time as a function of excitation power on a log-log scale in figure 4.7b. At 1.8 mW excitation power the average bleaching time of 17 seconds, as found for single rhodamine molecules, is shorter than the 26 seconds found here in Figure 4.2d. We attribute this to a difference in the position of the focus relative to the fluorophore. Fitting a power law to τ_{bleach} yielded a slope of 2.5 ± 0.1. The initial intensity of the bleaching curves is also plotted in Figure 4.7b and fitted to a slope of 2.0 ± 0.1, confirming two-photon excitation.
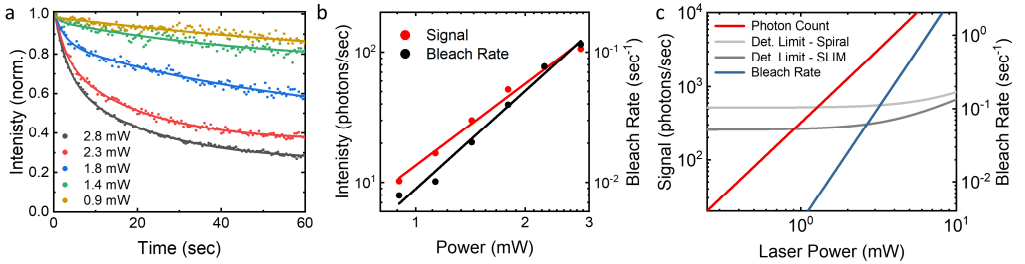
Figure 4.7: Photo-bleaching scales faster than signal intensity as functions of laser power. (a) Photobleaching of a layer of rhodamine 6G deposited on a glass coverslip. Measurements were performed at different excitation powers and fitted to an exponential function. (b) The decay times obtained from *a* plotted as a function of excitation power. The bleaching rates are fitted to a linear function yielding an exponent of 2.5. The signal intensity at the start of each scales with an exponent of 2.0, as expected for two-photon excitation. (c) Theoretical photon count, detection limit and bleach rate as a function of laser power. Bleach rate is obtained from *b*. As excitation power increases, the bleach rate scales unfavourably with laser power. Therefore, background suppression and higher detection efficiency of SLIM could potentially decrease bleach rates while maintaining similar SNR.

The higher slope of the bleaching curve suggests a multi-photon process for bleaching, possibly the absorption of another photon after two-photon excitation. In any case, longevity of a fluorophore increases more with less excitation power than the fluorescent signal decreases, suggesting that bleaching becomes less problematic when background can be reduced, allowing for lower excitation intensities. This relation between SNR and bleach time is plotted in Figure 4.7c, together with the measured bleach rate, the theoretical signal intensity of rhodamine 6G (equation 4.4) and the detection limit (equation 4.5). For spiral illumination an additional noise level of 6.0 photons/second was added to include the increased scattering in *in vivo* environments. For SLIM illumination, the transmission efficiency of the emission path was increased by 21%, which can be achieved by removal of a band pass filter.

A theoretical fluorescent signal of 1400 Hz is expected for single molecules, which slightly deviates from the measured intensities in Figure 4.2 of 897 ± 215 Hz. Inaccuracies in the estimation of the detection efficiency may be the cause for this difference. For spiral scanning, the signal only exceeds the detection limit at an excitation power of 1.05 mW, which results in a bleach time of 450 seconds. For SLIM, signal exceeds the detection limit at 0.8 mW excitation power, which corresponds to a bleach rate of 2500 seconds. Thus, a reduction of 0.69 in power extends bleaching by more than a factor of 5. From these results we expect that single fluorophore studies can benefit from TPE SLIM for both *in vitro*, by the increased transmission efficiency, and in *in vivo* environments, by suppression of scattered photons.

4.3.5   SINGLE MOLECULE FLUORESCENCE BY SLIM

To compare single molecule imaging by SLIM with spiral illumination, the same sample with single rhodamine 6G molecules was measured at an excitation power of 1.8 mW per focus. The band pass filter was removed from the emission path to improve detection efficiency. A ROI from the resulting image is shown in Figure 4.8a. Three diffraction limited spots are identified from the image and annotated by the colored circles. Single bleaching steps in the time traces, shown in Figure 4.8b, confirm that signal originates from single fluorophores. However, the density of observed fluorophores is much smaller compared to the spiral illuminated sample in Figure 4.2a.

From the entire image, a total of 16 fluorophores were detected compared to 86 with spiral illumination. Thus we overlooked 80% of the molecules. The average intensity of detected fluorophores however, is higher with 1480 ± 787 photons/second, as plotted in Figure 4.5c. When fluorescence is lost an average background signal of 509.9 ± 276 photons/second is recorded. Based on the background and average signal, fluorophores are detected with SNR = 2.9, which is slightly less than spiral illumination (SNR = 3.5). Besides SNR, the bleaching time of 14 ± 2 seconds, as plotted in Figure 4.8d, is also comparable to the bleaching time recorded in Figure 4.2d of 17.5 ± 1.7 seconds. So surprisingly, *in vitro* SLIM yields single molecule

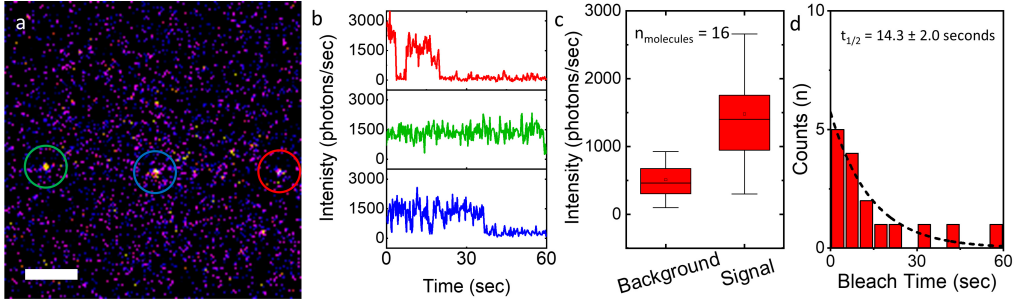measurements with similar quality as spiral scanning but a large number of fluorophores remain undetected.

Figure 4.8: Two-photon SLIM imaging single rhodamine 6G molecules. (a) ROI showing single Rhodamine B molecules deposited on a glass coverslip. Scale bar = 5 µm. (b) Time traces of the displayed fluorophores in *a*. Discrete bleaching steps indicate single fluorophores. (c) Average distribution of the background and signal of single 16 fluorophores. Based on the mean values, a single fluorophore is resolved with a SNR of 2.9. (d) The distribution of the bleach times yields a half-time of 14.3 seconds.

4.3.6   ENHANCED SLIM (SLIM+)

To tackle the high readout noise and enhance single molecule visibility we reduced the number of phase-images for one SLIM acquisition. This was achieved by scanning three lines during one phase-image, thereby broadening the resulting excitation pattern compared to conventional SLIM, see Figure 4.9a. The broader lines in the enhanced SLIM configuration reduced the number of phase images from eight to three. To assess the performance of SLIM+ we simulated single molecule measurements at different background intensities and compared SLIM+ to conventional SLIM and spiral illumination. The resulting images were cross-correlated with the ground truth to assess which illumination modality provides highest fidelity results, see Figure 4.9b.

The correlation coefficient of SLIM+ is significantly higher than SLIM and except for 0.3 photons/sec noise, is also higher than spiral illumination. This indicates that SLIM+ is superior to spiral scanning for most measurements. The slope of the correlation coefficient for SLIM+ is steeper compared to SLIM which suggests that for higher scattering media SLIM would perform better. This is likely caused by inefficient signal modulation at higher background in SLIM+ due to the broader illumination lines. Besides higher correlation, SLIM+ roughly doubles the SNR compared to spiral and SLIM illumination at a background intensity of 2 photons/sec, as shown in Figure 4.9c. Besides better quality images, the reduction in phase-images also reduced the file size of a measurement and allowed for faster imaging as less time is spent on reading-out the camera buffer. But most importantly, the higher SNR especially shows how the reduction in readout noise is beneficial for single molecule tracking. SLIM+ eliminates most of the drawbacks of SLIM.
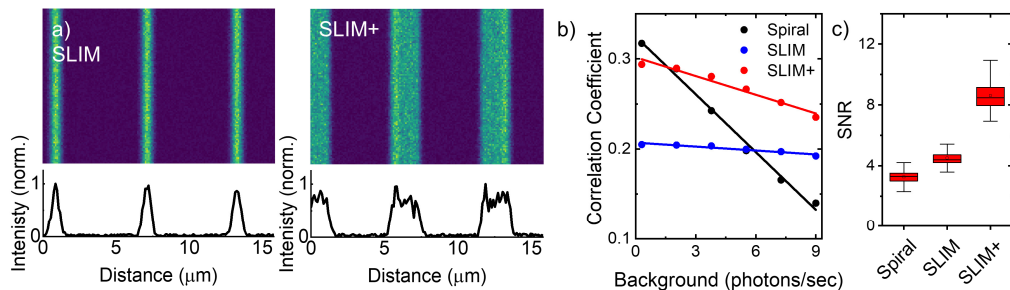
Figure 4.9: Reducing the number of phase-images improves image quality for SLIM. (a) Simulated excitation-images of SLIM and SLIM+. By scanning three lines per phase-image, the width of the resulting streak is broadened. With only three phase-images the FOV is fully sampled, reducing camera readout noise. (b) The correlation coefficient is improved by SLIM+, indicating that more fluorophores are resolved compared to SLIM. For high background images, SLIM+ performs better than spiral scanning. c) Due to the reduced readout noise the SNR is doubled by using SLIM+ compared to SLIM.

4.3.7 *IN VIVO* SINGLE MOLECULE FLUORESCENCE

Next we tested whether the improvements of SLIM+ made it possible to measure single fluorophores in live zebrafish embryos. For these measurements the membrane protein HRas was fluorescently tagged at its CAAX anchor domain with an eGFP fluorescent protein. The membrane of the skin cells in the tail of the embryo, shown in Figure 4.10a, were imaged using a spiral illumination. The boundaries of the cells can be distinguished by their distinct pentagonal shape. Homogenous intensities of the diffraction limited spots suggest single fluorophores. Note that we hardly observed photobleaching, the hallmark of single molecule fluorescence. We validated our results by comparing our SLIM+ images to measurements done with the well-established single molecule imaging technique of TIRF microscopy, see Figure S4.3. The two images both feature diffraction limited spots originating from HRas proteins. Within each image the spots feature comparable signal intensity and the similarities between both imaging modalities indicate that TPMM signal originates from single fluorophores. The background signal was greatly reduced when switching to SLIM+ as shown in Figure 4.10b. This can also be seen in the increase of SNR between the images as plotted in Figure 4.10c. The median SNR of the spiral image was 4.3 while the median of the SLIM+ image was 7.1, a factor of 1.6 improvement. Besides higher positional accuracy, a higher SNR allows to increase image speed or reduce excitation power to reduce phototoxicity and photobleaching.
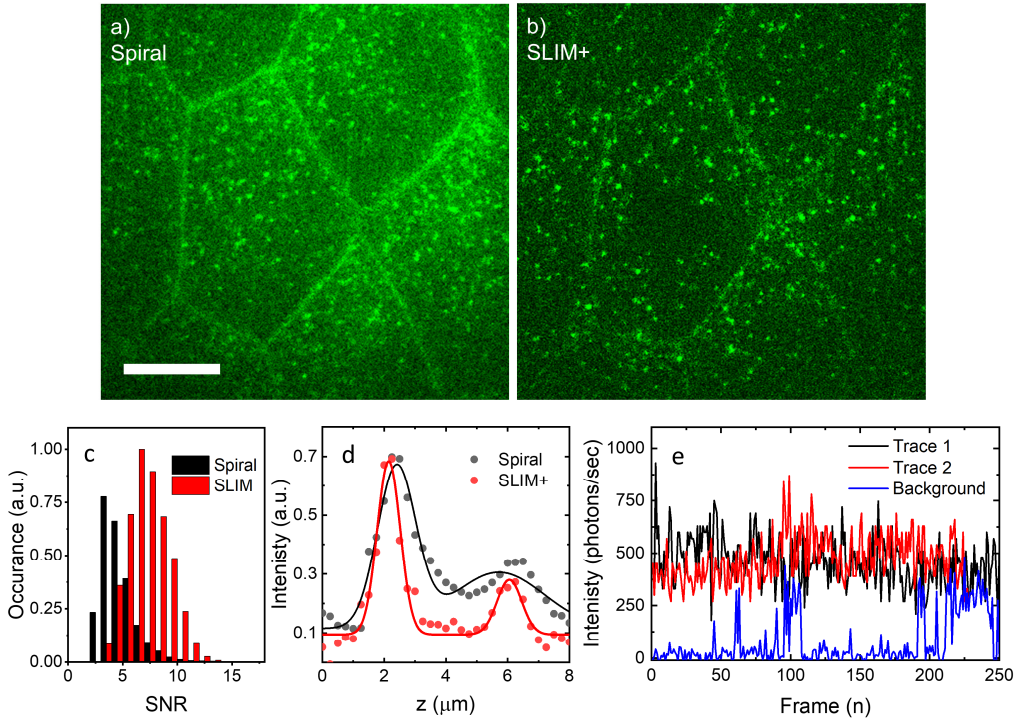
Figure 4.10: In live zebrafish embryos SLIM+ achieves higher SNR and improves the axial resolution compared to spiral scanning for imaging single molecules. (a) Spiral image of skin cells in the tail of a zebrafish embryo. eGFP labelled HRas proteins located in the cell membrane are clearly distinguishable. Scale bar = 10 µm. (b) SLIM+ image of the same location as *a*. The suppression of background improves the visualization of single eGFP-HRas proteins. (c) SNR calculated from the diffraction limited spots according to eq. 4.8. Spiral illumination reveals eGFP-Hras proteins with a median SNR of 4.3. SLIM+ improves SNR nearly 2-fold to 7.2. (d) Line profiles of a z-stack of the imaged cells. The first peak is the bottom membrane, the second peak, ±4 µm deeper, reveals the top membrane. Due to suppression of scattered photons in SLIM+, the membrane can be imaged at a higher axial resolution compared to spiral illumination. Fitting a double Gaussian yields a FHWM of 0.88 ± 0.06 µm for the first peak with SLIM+ and 0.94 ± 0.20 µm for the second peak. For the spiral z-stack: FWHM = 1.5 ± 0.1 µm and 3.5 ± 0.7 µm. (e) Intensity time trace of two tracked traces and a static region of interest. Note that the absence of photobleaching enabled tracking of the molecules for extended periods of time.

Next we assessed whether the Hras spots were confined to the membrane by measuring their position in 3D. ROIs of 69 x 79 pixels for both spiral and SLIM + images were taken from inside the center cell and the average signal of their z-profile are plotted Figure 4.10d. The two cell walls can be clearly distinguished from the two peaks, indicating that fluorescent signal is exclusively present in the membrane. Fitting a double Gaussian to the SLIM+ profile yields a FHWM = 0.88 ± 0.06 µm for the first peak and 0.94 ± 0.20 µm for the second peak. In comparison, the peaks in the spiral image feature a FWHM = 1.5 ± 0.1 µm for the first- and 3.5

± 0.7 µm for the second- peak. The suppression of background signal yields a much thinner cell membrane, and limited fluorescence degradation in axial resolution for the top membrane.

Most notably is the limited photobleaching we observed during these measurements. We set camera integration time at 100 ms and imaged for hundreds of frames using SLIM+ yielding movies lasting up to five minutes. Using TrackMate software combined with a simple linear assignment problem (LAP) tracking algorithm[39], individual spots of single molecules were tracked for hundreds of consecutive frames. Two examples of the resulting intensity traces are shown in Figure 4.10e. To compare to the background signal we also plotted the average signal from a static ROI in the middle of the cell with the same diameter (0.53 µm) as the traced spots. The spikes in intensity at the end indicate fluorophores passing through this region as HRas proteins diffuses through the membrane. We expect the detected intensity from each single molecule to be the same. Indeed, trace 1 and trace 2 both feature a similar average signal intensity of approximately 500 Hz. Also the spikes in the background signal reach similar levels of intensity. Lower intensity spikes are the result of molecules passing through the edge of the ROI. Trace 2 disappears after 225 frames which indicates that the fluorophore is bleached, the molecules moves out of focus, or the tracking algorithm is unable to link the consecutive frames. It is difficult to assess the reason behind the disappearance of a trace while they are moving in an *in vivo* environment. These results show how TPMM in combination with structured illumination enables the *in vivo* visualization of single molecules with limited photobleaching and negligible background signal.

4.3.8 ANALYSIS OF *IN VIVO* SINGLE MOLECULE DYNAMICS

Having established *in vivo* single molecule imaging with TPMM, we next investigated its functionality by tracking eGFP-HRas proteins in live zebrafish embryos. We used both spiral and SLIM+ illumination modalities to assess how they compare. To quantify this, we defined two ROIs: ROI 1 near the lateral membrane of the cell and ROI 2 at the center of the bottom membrane of the cell, shown in Figure 4.11a. The limited photobleaching allowed us to automatically track molecules by TrackMate software[39] for tens of seconds in a one minute movie. From the trajectories in ROI 2, shown in Figure 4.11b, we see that most traces are relatively short and some molecules reside for longer time periods within a confined area. These trajectories comply with out visual inspection. A large population of HRas proteins rapidly traveled across the membrane while sometimes remaining immobile for short periods of time, and a smaller second population appear to reside within a confined area for longer periods.

We studied the temporal-spatial dynamics of HRas by means of their MSD, which was calculated from the tracked coordinates. The MSD for both ROIs are plotted in Figure 4.11c and a confined diffusion model (equation 4.10) was fitted to the data. The variation in confinement between traces was very large, see Figure S4.4a for individual traces, and therefore we focus on the average MSD. The large spread in confinement may justify a more refined, multi-population

approach but here we limit the analysis to a simple single population. During the tens of seconds of tracking a molecule could also change its mobility, for example by interactions with its environment, which could also affect the MSD analysis.
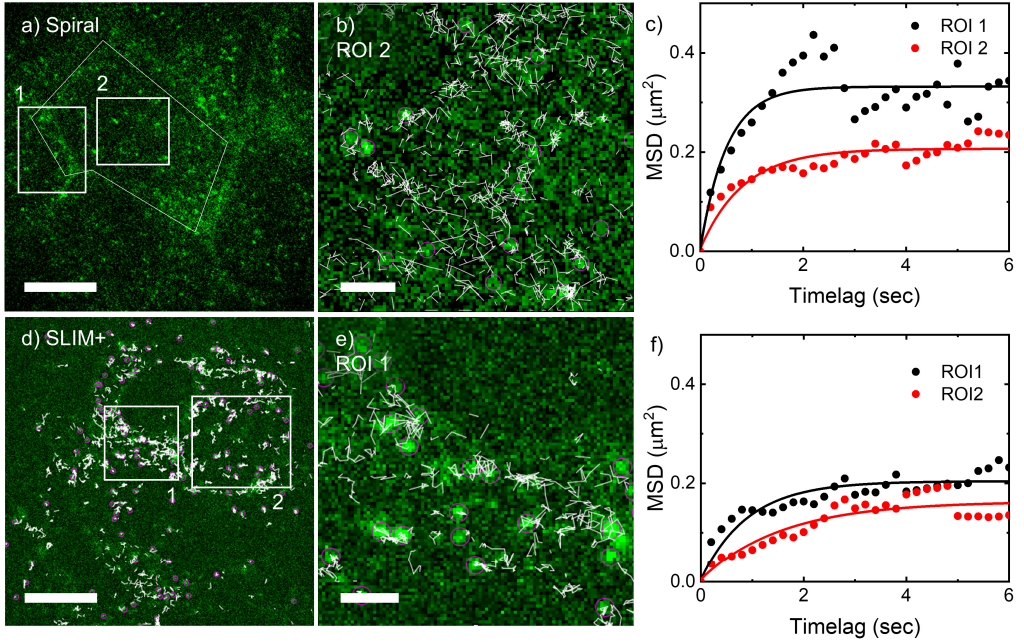

Figure 4.11: HRas proteins in the membrane of live zebrafish embryos feature different dynamics in different regions of the cell. (a) Two ROIs (white squares) annotate areas near the lateral membrane and the centre of the bottom membrane in a spiral-illuminated image. Scale bar = 10 μm. (b) Visualization of the trajectories of several eGFP-HRas proteins in ROI 2. Scale bar = 2 μm. (c) The average MSD calculated from the spatial coordinates of the tracked traces. Fitting a confined diffusion model (eq. 4.10) to the data yields a higher diffusion constant and less confinement for the traces located at the lateral membrane (L = 0.57 ± 0.17 μm) than those located in the interior of the cell (L = 0.46 ± 0.17 μm). (d) A SLIM+ image of embryo skin cells with traces from the tracked molecules overlaid in white. The regions near the lateral cell membranes feature higher eGFP-HRas mobility (ROI 1) than in the centre of the bottom membrane of the cell (ROI 2). (e) Enlarged image of ROI 1 at the lateral cell membrane. (f) Although small, the average confinement for ROI 1 with a L = 0.44 ± 0.10 μm is higher than 0.40 ± 0.14 μm at ROI 2.

Both MSD curves reach an asymptote indicating confinement. The area of confinement is larger near the lateral membrane wall, L = 0.57 ± 0.17 μm than at the bottom of the cell with a L= 0.46 ± 0.17 μm. From HRas measurements using TIRF microscopy at the bottom of the cell membrane we measured L = 0.33 ± 0.17 μm, see Figure S4.4b. The diffusion constants as measured by TPMM of 0.16 ± 0.03 μm²/sec and 0.06 ± 0.01 μm²/sec, were smaller than measured in TIRF of 1.68 ± 0.24 μm²/sec. This could be due to the lower frame rate of TPMM, which may bias our analysis to the slower fraction of molecules. The difference in confinement between the microscopy modalities could be due to the large variation in the traces in TPMM,

which would warrant a more refined analysis. However, the enhanced photobleaching of TIRF could also eliminate longer traces which may skew results towards more confinement.

At a different region in the tail of the zebrafish embryo we also used SLIM+ to track eGFP-HRas. The FOV shown in Figure 4.11d features multiple cells. By superimposing the eGFP-HRas trajectories on the image the difference in HRas activity between the different cell regions and cells can be qualitatively appreciated. For example, the area at the top of ROI 1 which features no traces is likely a cell which expresses very limited eGFP-HRas. Similar to the spiral measurement we saw more HRas mobility at a lateral cell membrane (ROI 1) than in the interior of a cell (ROI 2). Figure 4.11e provides a closer view at ROI 1 and similar to Figure 4.11b, shows how some molecules remain longer immobilized at a specific place, while other traces are shorter and/or more mobile. Although we cannot exclude photobleaching, it is unlikely that bleaching is responsible for such short traces as there is no sign of bleaching at the cell membrane nor any part of the embryo (data not shown). More likely eGFP-HRas moves out of focus or the tracking algorithm was unable to link a spot to the trace. From the MSD curves plotted in Figure 4.11f we find that the traces are confined with $L = 0.44 \pm 1.0$ µm for the lateral membrane and 0.40 ± 1.4 µm for the interior of a cell. The variation in MSD traces is again very large. Still, the average area of confinement at the lateral membrane is higher than that at the central bottom of the cell. For both regions the confinement appears to be smaller than in the spiral measurement and resembles the TIRF measurement. The apparent diffusion constant is further reduced to 0.055 ± 0.006 µm^2/sec and 0.025 ± 0.003 µm^2/sec. Differences between MSD values could be caused by biological variations between cells, or by modulations in either spiral or SLIM+ acquisitions. A more rigorous study should be conducted to assess these differences between the two scanning modalities. Besides a higher SNR, as also reported in Figure 4.10, and the slightly different diffusion behavior, we did not see major differences between movies obtained with spiral and SLIM+. Both were able to track single molecules for tens of seconds and provided insight in HRas dynamics across multiple cellular bodies.

4.4 DISCUSSION AND CONCLUSION

In this work we measured wide field two-photon fluorescence of single fluorophores both *in vitro* and *in vivo*. Individual rhodamine 6G molecules on glass were readily imaged with an average life-time of 17.5 seconds. To enhance visibility of single fluorophores and to increase SNR in images overall, we developed SLIM to suppress scattering of photons. The higher background in turbid media, such as of zebrafish embryos, was reduced to below single molecule brightness by SLIM. Moreover, we further improved SLIM to reduce the effect of the increased readout noise and make it suitable for imaging of single fluorophores. Indeed, we

imaged single eGFP-HRas proteins in live zebrafish embryos where the absence of bleaching allowed us to track single molecules for sometimes hundreds of consecutive frames.

The fluorophores immobilized on glass which were detected by spiral illumination, had an average signal of 900 Hz at a relative low excitation power of 1.8 mW. TPSM on rhodamine B[13] shows similar bleach rates as rhodamine 6G, indicating that imaging these fluorophores with TPMM would yield similar results for *in vitro* environments. When compensated for difference in illumination intensity measured by TPSM (our 410 kW/cm^2 versus 1340 kW/cm^2) and scan speed (9.4 ms/pixel versus 0.2 ms/pixel), our results closely follow the power dependence on the bleach rate of single rhodamine 6G molecules[14]. However, the frame rate of TPMM is 5.6 times higher. To achieve a similar frame rate while maintaining SNR, TPSM would need to scan 5.6 times faster and thus required approximately 2.4 times larger excitation power, which would decrease bleaching times to approximately 2 seconds. For practical imaging purposes this comparison indicates that TPMM indeed offers lower bleaching times than single point excitation.

The photobleaching times of eGFP molecules inside the zebrafish embryo were significantly different to rhodamine 6G on glass, with molecules that could be tracked for over one minute. These drastically different results were achieved at a slightly lower excitation power of 1.6 mW for *in vivo* versus 1.8 mW for the *in vitro* measurements. The small difference here in power is unlikely to cause an order of magnitude difference in bleaching times but the different fluorophores have different bleaching behavior.

The exact two-photon bleaching mechanisms of fluorescent proteins remains elusive. Fluorescent correlation spectroscopy (FCS) measurements showed that the two-photon photobleaching rates of fluorescent dyes and proteins were not influenced by the addition or removal of solvated oxygen to the imaging medium, whereas in one-photon excitation oxygen strongly increases bleach rates[40]. Moreover, TPE did not appear to induce significant triplet-state formation, which is one of the main oxygen dependent bleaching pathways of one-photon excitation. These results suggested that the two-photon photobleaching process differs significantly with one photon excitation. TPE may induce higher-order excited-states, e.g. three-photon absorption, which could lead to destruction of fluorescence by formation of an ion pair between the fluorophore and a solvated electron[41–43]. This effect can be countered by adding stabilizing agents such as ascorbic acid, which non-destructively deoxidizes the excited fluorophore[40]. Interestingly, the bleach rate of eGFP does not respond to ascorbic acid and was previously found to be remarkably stable upon TPE [40,44]. The tight cylinder of amino chain acids is believed to shield the fluorescent center from reactive agents and protects it from being bleached[45]. Previous TPSM studies on single eGFP molecules in live sup-T1 and 293T cells reported a bleach rate of 52.7 ± 5.2 seconds for a high laser power of 130.8 mW[9]. Our results are consistent with these findings, as we illuminate eGFP molecules at very low laser intensities of 1.6 mW, thereby strongly reducing the chance of being excited to higher-order excited states. Rhodamine 6G molecules do not feature a protective barrel to shield them from radical agents,

and indeed we see much faster bleaching. Importantly, the rhodamine molecules were imaged in air and hence no stabilizing agents nor oxygen scavengers were present in their surroundings. For *in vivo* measurements we did not observe photobleaching of eGFP and would recommend its use for TPM studies.

In one-photon microscopy, it has been shown that SIM can cause artefacts when the images are reconstructed from low contrast data[46]. Therefore SIM is commonly used for imaging larger assemblies and more densely packed fluorophores instead of single fluorophores[47,48]. Indeed, we found that for imaging larger and brighter structures such as blood vessels in zebrafish embryos, SLIM offers excellent reduction in background compared to spiral illumination and we did not observe artefacts.

SLIM diminishes the result of scattering of emission photons in wide-field detection without additional hardware. Due to the two-photon non-linear excitation mechanism, which yields a sharper excitation PSF, super resolution reconstruction could further improve image resolution compared to conventional SIM. This would require multiple orientation angles of the illumination pattern but would enhance the effects of read noise[49]. Future studies will need to experimentally find the optimal settings for TPMM SLIM super resolution.

In this work we focused on tracking single molecules with different TPMM modes. The disparity in number of observed fluorophores *in vitro* between spiral illumination and SLIM is likely caused by two factors. First, the increase in camera readout noise impaired fluorophore visibility. Second, incomplete spatial sampling of the image plane will result in missed fluorophores. Although hardly visible in single frames, the SLIM illumination pattern is distinguishable in the maximum intensity projection of the brain of a zebrafish embryo (Figure S4.2). Note that the width of excitation PSF is narrower than the emission PSF, so the observed gaps in the two-photon fluorescence underestimate the gaps in the illumination pattern[37]. For imaging larger cellular structures a low-pass image filtering may suffice to remove such illumination artefacts[50]. However, for imaging individual fluorophores the focal plane should be sampled with a finer mesh. No illumination artifacts were observed in the spiral illumination projection, which indicates that spiral illumination samples the image plane more homogeneously. Spatial under-sampling would also explain the higher signal intensity of SLIM for single molecules as the excitation power is distributed over a smaller area. Increasing the number of phase-images would result in higher homogeneity but also increases the read noise. Six-phase images per reconstruction proved to be the best compromise between SNR and spatial sampling.

SLIM+ reduced the degenerative effect of readout noise and sampled the focal plane more homogeneously by combining three lines per phase image. This allowed us to image single eGFP-HRas proteins without noticeable modulations in signal. However, this was difficult to assess in the fluorescently sparse samples.

When excitation power is inhomogeneously distributed across the focal plane, trace trajectories could be interrupted which would impair the tracking of a particle. The MSD from

the SLIM+ measurement was lower than that of the spiral illumination, which could be an indication of spatial modulation in excitation power. Please note that biological variations between cells could also explain the difference in MSD. Another degenerative signal modulation during SLIM acquisition could arise when a particle moves fast enough to skip an illumination line between phase images and will not be detected after reconstruction. When a particle moves along the illumination lines, its signal would also be filtered out by the Fourier transformation. The broader excitation lines in SLIM+ acquisition reduces effects of a particle movement as only three phase-images are required and the faster frame rate may also be advantageous. Despite the higher SNR of SLIM+, the abovementioned concerns suggest that spiral illumination provides the most robust method for tracking of single molecules, as was also indicated by 3D tracking of gold nanorods in live cells[34].

We measured a disparity in confinement and diffusion constant between the different traces between spiral illumination, SLIM+ and TIRF. More extensive research by TIRF microscopy on HRas proteins in live 3T3-A14 cells showed that the dynamics of HRas could be modelled to a fast, freely diffusing state and a confined state within a 0.2 μm^2 domain[51]. Likely, averaging all traces by a MSD curve is insufficient to differentiate the states of a single HRas protein from the long trajectories TPMM produces. Assessing the traces individually, or using more specific automated analysis models should further validate the potential of TPMM for single molecule tracking studies.

A different microscopy technique which combines fast acquisition speeds and low photobleaching is two photon light-sheet microscopy. Due to the lower excitation NA however, there might be concern whether two-photon light-sheet microscopy can generate enough fluorescent signal for single molecule detection. Considering a spherically focused beam, the probability for two-photon excitation in the focal volume scales with NA^4 (equation 4.5) while the volume itself scales with NA^{-4} as explained in[37]. This means that the total amount of fluorescence from the focal volume is independent on NA. Thus, a lower signal intensity per voxel is compensated with exciting a larger number of voxels. Indeed, imaging with the same resolution and average excitation power, the total signal acquisition rates of two-photon light-sheet and single-point scanning microscopy are similar to each other[52]. To match the higher count rate per voxel of a point-focused microscope, the dwell time of the excitation beam has to be increased to collect the same amount of signal. According to this logic, two-photon light-sheet microscopy should be able to image single fluorophores at similar SNR as TPSM[9,14,15], and does not perform as well as TPMM in terms of frame rate.

To increase acquisition rate by a factor N, the laser beam of TPLM would need $\sqrt{N}$ more excitation power, owing to the squared signal dependence on power. In comparison, an increase in acquisition rate with TPMM goes linear with the number of foci. So the same N times increase in frame rate is accompanied with N number of foci and N times more average excitation power. A higher average laser power increases one photon absorption and photodamage which impedes

long time-lapse studies. However, the major advantage of light-sheet microscopy comes from the reduced peak intensities. Peak intensity scales with NA^2 and the excitation NA of a light-sheet microscope is typically 4-10 times lower than TPMM or TPSM [52–55].

Lower peak intensities translate to longer bleaching times. It has been suggested that bleaching times increase as a result of a lower contribution of higher order (2>) absorption events[52,56]. This would be a significant advantage to extend single molecule time traces. Alternatively, reduced photo-damage makes higher average laser powers possible, which should enable TPLM to reach faster acquisition speeds or higher SNR compared to TPMM. TPLM has also been combined with structured illumination to reduce scattered emission photons[57]. The light-sheet thickness will however be inherently thicker in TPLM due to the lower illumination NA which would impair spatial resolution. Still, the lower phototoxicity or higher SNR suggest that TPLM is a competitive alternative to TPMM for wide-field single molecule imaging, though to the best of our knowledge, single molecule imaging has not been reported using TPLM.

In conclusion, we demonstrated *in vivo* two-photon fluorescence of single molecules by wide-field detection. Our results indicate that low excitation power distributed over multiple foci results in lower bleach rates compared to single point scanning and very limited bleaching of eGFP molecules *in vivo*. Unwanted scattering of emitted light in *in vivo* imaging applications were reduced to below single-molecule levels using SLIM and SLIM+. Besides single molecule sensitivity, lower bleach rates and higher frame rates allowed for long time-lapse studies on single eGFP-HRas fluorophores in live zebrafish embryos. This is the first time that two-photon single molecule tracking in wide field has been reported. We expect that the high quality and long time traces that can be obtained TPMM will expand the wide range of biophysical experiments and provide new insights in molecular dynamics in complex biological samples.

4.5   SUPPLEMENTARY FIGURES
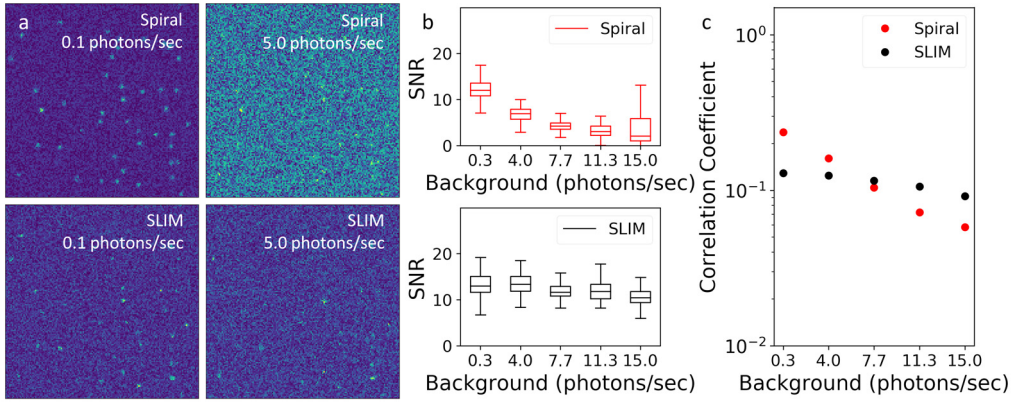
Figure S4.1: Simulations to investigate the influence on background noise for both spiral scanning and SLIM.
(a) Four ROIs for both illumination modalities at low noise conditions and high noise conditions. At 0.1 e⁻/sec, spiral scanning captures more fluorophores than SLIM. However, at 5.0 e⁻/sec the background suppression of SLIM provides a higher fidelity. (b) The distribution of the SNR of 150 fluorophores for spiral and SLIM for a range of noise levels. SNR reduces in spiral imaging due to increased background while for SLIM it remains relatively stable. (c) The correlation coefficient in respect to the ground truth. Around 2.6 e⁻/sec SLIM overtakes spiral scanning in how much the image resembles the ground truth image.
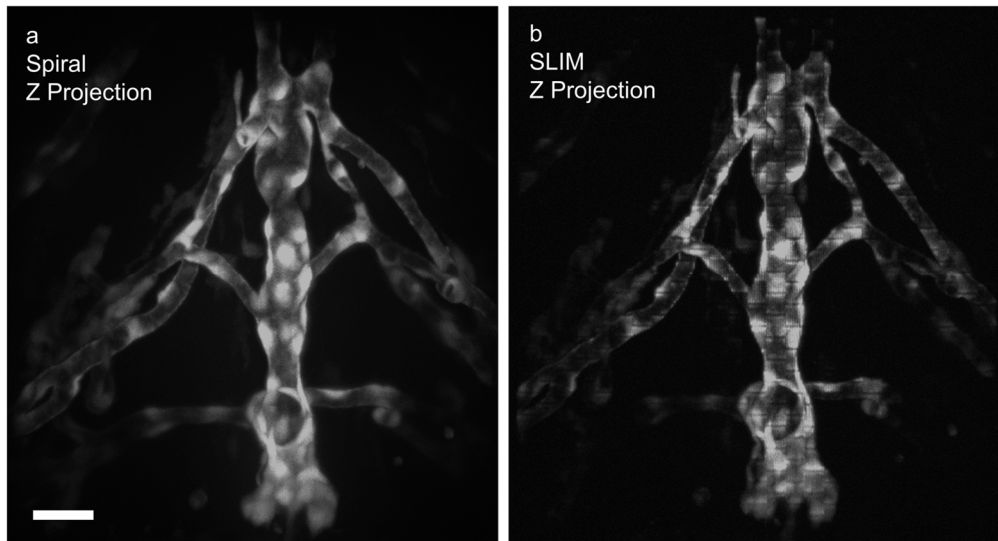
Figure S4.2. Rapid multifocal scanning combined with TPE allows for 3D imaging of blood vessels in the brain of zebrafish embryos. (a) Maximum intensity projection of a volume of 700 images taken over a depth of 350 μm from the brain of a zebrafish embryo via spiral scanning. mTurquoise fused to *kdrl* expressing endothelial cells mark the blood vessel walls. (b) Maximum z-projection of the same volume as in *a*, illuminated via SLIM. The projection features some SLIM illumination artefacts (e.g. a slightly inhomogeneous illumination). Scale bar = 25 μm.
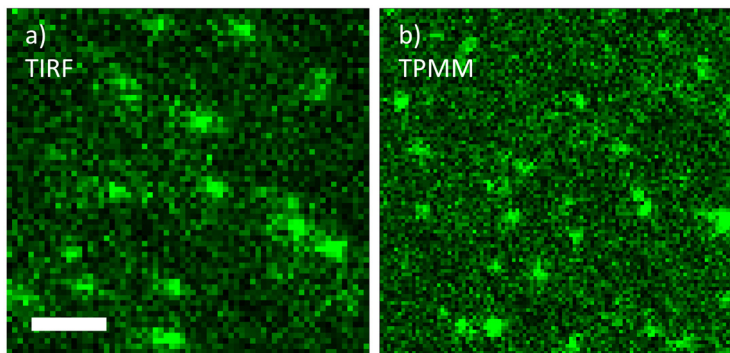
Figure S4.3: One-photon TIRF microscopy and TPMM/SLIM+ show very similar images when measuring eGFP labelled HRas proteins in live zebrafish embryos, indicating TPMM single molecule fluorescence. (a) A TIRF image of a region of a skin cell showing spots originating from single fluorescent proteins. Scale bar = 2 μm. (b) A TPMM/SLIM+ image of a different area of the same size, featuring similar diffraction limited spots.
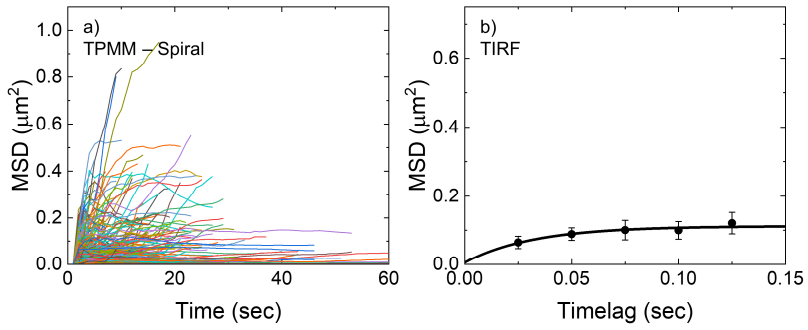
Figure S4.4: TPMM and TIRF microscopy feature different time-dependent MSD curves. (a) MSD curves of individual traces from a TPMM measurement using spiral illumination. Some traces last for tens of seconds. There is a large spread in confinement and diffusion coefficient between the molecules. (b) Typical MSD curve from a TIRF measurement on HRas molecules located in the interior membrane of the cell. The confinement of 0.33 ± 0.10 µm features a very small deviation from its mean. Note that this curve was generated using the PICS algorithm[58], which combines displacement of all peaks into a single MSD curve.

4.6   BIBLIOGRAPHY

1.   Axelrod, D. Cell-substrate contacts illuminated by total internal reflection fluorescence. *J. Cell Biol.* **89**, 141–145 (1981).

2.   Hohlbein, J. *et al.* Reports on Progress in Physics Related content Fluorescence correlation spectroscopy : the technique and its applications Fluorescence correlation spectroscopy : the technique. *Reports Prog. Phys.* **65**, 251–297 (2002).

3.   Segers-Nolten, G. M. J. Scanning confocal fluorescence microscopy for single molecule analysis of nucleotide excision repair complexes. *Nucleic Acids Res.* **30**, 4720–4727 (2002).

4.   Pierobon, P. *et al.* Velocity, processivity, and individual steps of single myosin V molecules in live cells. *Biophys. J.* **96**, 4268–4275 (2009).

5.   Denk, W., Strickler, J. H. & Webb, W. W. Two-Photon Laser Scanning Fluorescence Microscopy. *Sci. New Ser.* **248**, 73–76 (1990).

6.   Biermann, B. *et al.* Imaging of molecular surface dynamics in brain slices using single-particle tracking. *Nat. Commun.* (2014). doi:10.1038/ncomms4024

7.   Berland, K. M., So, P. T. C. & Gratton, E. Two-Photon Fluorescepce Correlation Spectroscopy : Method and Application to the Intracellular Environment. *Biophys. J.* **68**, 694–701 (1995).

8.   Farrer, R. A. *et al.* Single-molecule detection with a two-photon fluorescence microscope with fast-scanning capabilities and polarization sensitivity. *Opt. Lett.* **24**, 1832 (1999).

9.   Hou, X. & Cheng, W. Detection of single fluorescent proteins inside eukaryotic cells using two-photon fluorescence. *Biomed. Opt. Express* **3**, 340 (2012).

10. Sanchez, E. J., Novotny, L., Holtom, G. R. & Xie, X. S. Room-Temperature Fluorescence Imaging and Spectroscopy of Single Molecules by Two-Photon Excitation. **101**, 0–4 (1997).

11. Hou, X. & Cheng, W. Single-molecule detection using continuous wave excitation of two-photon fluorescence. *Opt. Lett.* **36**, 3185 (2011).

12. Lewis, M. K., Wolanin, P., Gafni, A. & Steel, D. G. Near-field scanning optical microscopy of single molecules by femtosecond two-photon excitation. *Opt. Lett.* **23**, 1111 (1998).

13. Sonnleitner, M., Schütz, G. . & Schmidt, T. Imaging individual molecules by two-photon excitation. *Chem. Phys. Lett.* **300**, 221–226 (1999).

14. Chirico, G., Cannone, F., Baldini, G. & Diaspro, A. Two-Photon Thermal Bleaching of Single Fluorescent Molecules. *Biophys. J.* **84**, 588–598 (2003).

15. Chirico, G., Cannone, F., Beretta, S., Baldini, G. & Diaspro, A. Single molecule studies by means of the two-photon fluorescence distribution. *Microsc. Res. Tech.* **55**, 359–364 (2001).

16. Mertz, J., Xu, C. & Webb, W. W. Single-molecule detection by two-photon-excited fluorescence. *Opt. Lett.* **20**, 2532 (1995).

17. Chen, T.-S., Zeng, S.-Q., Luo, Q.-M., Zhang, Z.-H. & Zhou, W. High-Order Photobleaching of Green Fluorescent Protein inside Live Cells in Two-Photon Excitation Microscopy. *Biochem. Biophys. Res. Commun.* **291**, 1272–1275 (2002).

18. Eggeling, C., Volkmer, A. & Seidel, C. A. M. Molecular photobleaching kinetics of

Rhodamine 6G by one- and two-photon induced confocal fluorescence microscopy. *ChemPhysChem* **6**, 791–804 (2005).

19. Patterson, G. H. & Piston, D. W. Photobleaching in Two-Photon Excitation Microscopy. *Biophys. J.* **78**, 2159–2162 (2000).

20. Niu, F. *et al.* Photobleaching of ultrashort pulses with different repetition rates in two-photon excitation microscopy. *Laser Phys.* **29**, 046001 (2019).

21. Sanchez, E. J., Novotny, L., Holtom, G. R. & Xie, X. S. Room-temperature fluorescence imaging and spectroscopy of single molecules by two-photon excitation. *J. Phys. Chem. A* **101**, 7019–7023 (1997).

22. Straub, M. & Hell, S. W. Multifocal multiphoton microscopy : a fast and efficient tool for 3-D fluorescence imaging. *Bioimaging* **6**, 177–185 (1998).

23. Sacconi, L. *et al.* Multiphoton multifocal microscopy exploiting a diffractive optical element. *Opt. Lett.* **28**, 1918 (2003).

24. Quicke, P. *et al.* High speed functional imaging with source localized multifocal two-photon microscopy. *Biomed. Opt. Express* **9**, 3678 (2018).

25. Fittinghoff, D. N., Wiseman, P. W. & Squier, J. A. Widefield multiphoton and temporally decorrelated multifocal multiphoton microscopy. *Opt. Express* **7**, 273 (2000).

26. Nielsen, T., Fricke, M., Hellweg, D. & Andresen, P. High efficiency beam splitter for multifocal multiphoton microscopy. *J. Microsc.* **201**, 368–376 (2001).

27. Martini, J., Andresen, V. & Anselmetti, D. Scattering suppression and confocal detection in multifocal multiphoton microscopy. *J. Biomed. Opt.* **12**, 034010 (2007).

28. Kim, K. H. *et al.* Multifocal multiphoton microscopy based on multianode photomultiplier tubes. *Opt. Express* **15**, 11658 (2007).

29. Cha, J. W. *et al.* Non-descanned multifocal multiphoton microscopy with a multianode photomultiplier tube. *AIP Adv.* **5**, 084802 (2015).

30. Ingaramo, M. *et al.* Two-photon excitation improves multifocal structured illumination microscopy in thick scattering tissue. *Proc. Natl. Acad. Sci.* **111**, 5254–5259 (2014).

31. Isobe, K. *et al.* Enhancement of lateral resolution and optical sectioning capability of two-photon fluorescence microscopy by combining temporal-focusing with structured illumination. **4**, 10565–10573 (2013).

32. Urban, B. E. & Zhang, H. F. Imaging neuronal structure dynamics using 2-photon super-resolution patterned excitation reconstruction microscopy. 1–9 (2018). doi:10.1002/jbio.201700171

33. Saumya Saurabh, Suvrajit Maji & Marcel P. Bruchez. Evaluation of sCMOS cameras for detection and localization of single Cy5 molecules. *Opt. Soc. Am.* (2012).

34. Van den Broek, B., Oosterkamp, T. H. & van Noort, J. A Multifocal Two-Photon Microscopy Setup for Parallel 3D Tracking of Gold Nanorods. *Biophys. J.* **98**, 178a (2010).

35. Bussmann, J. & Schulte-Merker, S. -. *Unpublished* (2011).

36. Schaaf, M. J. M. *et al.* Single-Molecule Microscopy Reveals Membrane Microdomain Organization of Cells in a Living Vertebrate. *Biophys. J.* **97**, 1206–1214 (2009).

37. Zipfel, W. R., Williams, R. M. & Webb, W. W. Nonlinear magic: Multiphoton microscopy in the biosciences. *Nat. Biotechnol.* **21**, 1369–1377 (2003).

38. So, P. T. C., Dong, C. Y., Masters, B. R. & Berland, K. M. Two-Photon Excitation Fluorescence Microscopy. *Annu. Rev. Biomed. Eng.* 399–429 (2000).

39. Tinevez, J. Y. *et al.* TrackMate: An open and extensible platform for single-particle tracking. *Methods* **115**, 80–90 (2017).

40. Dittrich, P. S. & Schwille, P. Photobleaching and stabilization of fluorophores used for single-molecule analysis with one- and two-photon excitation. *Appl. Phys. B Lasers Opt.* **73**, 829–837 (2001).

41. Liu, X., Rudolph, W. & Thomas, J. L. Photobleaching resistance of stimulated parametric emission in microscopy. *Opt. Lett.* **34**, 304 (2009).

42. Marian, C. M., Etinski, M. & Rai-Constapel, V. Reverse intersystem crossing in rhodamines by near-infrared laser excitation. *J. Phys. Chem. A* **118**, 6985–6990 (2014).

43. Chen, T. S., Zeng, S. Q., Zhou, W. & Luo, Q. M. A Quantitative Theory Model of a Photobleaching Mechanism. *Chinese Phys. Lett.* **20**, 1940–1943 (2003).

44. Schwille, P., Haupts, U., Maiti, S. & Webb, W. W. Molecular dynamics in living cells observed by fluorescence correlation spectroscopy with one- and two-photon excitation. *Biophys. J.* **77**, 2251–2265 (1999).

45. Brejc, K. *et al.* Structural basis for dual excitation and photoisomerization of the Aequorea victoria green fluorescent protein. *Proc. Natl. Acad. Sci. U. S. A.* **94**, 2306–2311 (1997).

46. Wegel, E. *et al.* Imaging cellular structures in super-resolution with SIM, STED and Localisation Microscopy: A practical comparison. *Sci. Rep.* **6**, 1–13 (2016).

47. Biteen, J. & Willets, K. A. Introduction: Super-Resolution and Single-Molecule Imaging. *Chem. Rev.* **117**, 7241–7243 (2017).

48. Hirano, Y., Matsuda, A. & Hiraoka, Y. Recent advancements in structured-illumination microscopy toward live-cell imaging. *Microscopy* **64**, 237–249 (2015).

49. Gustafsson, M. G. L. Nonlinear structured-illumination microscopy: Wide-field fluorescence imaging with theoretically unlimited resolution. *Proc. Natl. Acad. Sci. U. S. A.* **102**, 13081–13086 (2005).

50. Winter, P. W. *et al.* Incoherent structured illumination improves optical sectioning and contrast in multiphoton super-resolution microscopy. **23**, 260–265 (2015).

51. Lommerse, P. H. M., Snaar-Jagalska, B. E., Spaink, H. P. & Schmidt, T. Single-molecule diffusion measurements of H-Ras at the plasma membrane of live cells reveal microdomain localization upon activation. *J. Cell Sci.* **118**, 1799–1809 (2005).

52. Truong, T. V, Supatto, W., Koos, D. S., Choi, J. M. & Fraser, S. E. Deep and fast live imaging with two-photon scanned light-sheet microscopy. *Nat. Methods 2011 89* **8**, 757 (2011).

53. Fahrbach, F. O., Gurchenkov, V., Alessandri, K., Nassoy, P. & Rohrbach, A. Light-sheet microscopy in thick media using scanned Bessel beams and two-photon fluorescence excitation. *Opt. Express* **21**, 13824 (2013).

54. Lavagnino, Z., Cella Zanacchi, F., Ronzitti, E. & Diaspro, A. Two-photon excitation selective plane illumination microscopy (2PE-SPIM) of highly scattering samples: characterization and application. *Opt. Express* **21**, 5998 (2013).

55. Olarte, O. E. *et al.* Image formation by linear and nonlinear digital scanned light-sheet fluorescence microscopy with Gaussian and Bessel beam profiles. *Biomed. Opt. Express* **3**, 1492–505 (2012).

56. Ji, N., Magee, J. C. & Betzig, E. High-speed, low-photodamage nonlinear imaging using passive pulse splitters. *Nat. Methods* **5**, 197–202 (2008).

57. Zhao, M. *et al.* Cellular imaging of deep organ using two-photon Bessel light-sheet

nonlinear structured illumination microscopy. *Biomed. Opt. Express* **5**, 1296 (2014).

58.   Semrau, S., Schmidt, T. Particle image correlation spectroscopy (PICS): Retrieving nanometer-scale correlations from high-density single-molecule position data. *Biophysical Journal* **92**, 613-621 (2007)

Chapter 5

Light-triggered switching of liposomes surface charge directs delivery of membrane impermeable payloads *in vivo*

Chapter 5 highlights a study which demonstrates the capabilities of our TPMM in a real-case scenario. The study was performed in zebrafish embryos, where to two-photon excitation and the high temporal resolution enabled imaging of particle distribution in real-time.

Author contributions:

F.C. conceived the research

F.C., G.A, R.V and S.B. designed the experiments

G.A, L.K, R.V, A.R, P.P and F.C carried out the experiments

GA. L.K, R.V, A.R, P.P, M.S.M, S.B, S.V, J.v.N, A.K and F.C analyzed the data.

M.S.M performed the light actinometry.

R.V and J.v.N designed and build the microscope

F.C, G.A, R.V wrote the manuscript with feedback from all authors

A.K supervised the research

5.1 PREFACE

To demonstrate the potential of our novel two-photon multifocal microscope technique, we highlight a collaboration study on photo-switchable liposomes which become cationic upon UV irradiation. The positively charged surface of the liposomes will stick to the surface of the blood vessel walls and subsequently be endocytosed by the endothelial cells. This property has potential for targeted liposomal drug delivery where drugs would be delivered at the UV-irradiated location.

Being able to record the dynamics of the transition period between anionic and cationic while the liposomes are circulating in the blood stream is advantageous for studying the effectiveness of the liposomes as potential drug delivery systems. However, confocal microscopy typically used to study zebrafish embryos lacks the temporal resolution to capture these dynamics. Also, to study the surface-charge transition live, UV irradiation has to be rapidly alternated with image acquisition to prevent over-exposure of the detector. A limited image acquisition speed would therefore limit the duration of UV irradiation and skew the surface charge transition dynamics.

To tackle these concerns we positioned a UV LED above the sample stage of our setup. Illumination of the LED was synchronized with the scanning mirror and camera, which allowed to reach a UV irradiation duty cycle of 95% while intermittently taking images of the liposome distribution inside the blood vessels. The resulting measurements showed that directly upon UV irradiation, signal intensity of the homogeneously distributed liposomes drops linearly. After a couple of minutes, liposome uptake by macrophages indicated activation of the immune-response system.

Without the higher temporal resolution of the TPMM, the transition speed and the response time of the immune system would have remained elusive, TPMM gave valuable insight in how UV irradiation dosage affects the effectiveness of the liposomes as drug-carriers.

5.2 ABSTRACT

Surface charge plays a fundamental role in determining the fate of a nanoparticle, and any encapsulated contents, *in vivo*. Herein, we describe, and visualize in real time, light-triggered switching of liposome surface charge, from neutral to cationic, *in situ* and *in vivo* (embryonic zebrafish). Prior to light activation, intravenously administered liposomes, composed of just two lipid reagents, freely circulate and successfully evade innate immune cells present in the fish. Upon *in situ* irradiation and surface charge switching, however, liposomes rapidly adsorb to, and are taken up by, endothelial cells and/or are phagocytosed by blood resident macrophages. Coupling complete external control of nanoparticle targeting together with the intracellular delivery of encapsulated (and membrane impermeable) cargos, these compositionally simple liposomes are proof that advanced nanoparticle function *in vivo* does not require increased design complexity but rather a thorough understanding of the fundamental nano-bio interactions involved.

5.3 INTRODUCTION

Surface charge is a key determinant of nanoparticle fate *in vivo*.[1,2] Following intravenous (*i.v.*) injection, nanoparticles with high surface charge density, either anionic or cationic, are rapidly cleared from circulation by specialised cells of the reticulo-endothelial system (RES).[3–5] In mammals, RES cell types are primarily located in the liver (key hepatic RES cell types: Kupffer cells, KCs, and liver sinusoidal endothelial cells, LSECs) and spleen. These cells are responsible for clearing up to 99% of *i.v.* administered nanoparticles from circulation.[6] High nanoparticle surface charge density has a qualitative and quantitative impact on serum protein binding,[7–12] driving the opsonisation of circulating nanoparticles and subsequent recognition and clearance by the RES.[13–15] In addition, cationic nanoparticles tend to adsorb to the anionic surface of cells and are subsequently internalised,[16–20] often leading to acute cytotoxicity.[21–23] Given the adverse pharmacokinetics of charged nanoparticles in the body, most clinically approved, nanoparticle-drug formulations (nanomedicines) possess a (near) neutral surface charge to prolong circulation lifetimes and maximise drug exposure within target (vascularized) tissues in the body.[24]

We have previously shown that *i.v.* administered liposomes with (near) neutral surface charge, and optimally 100 nm in size, tend to freely circulate in embryonic zebrafish (*Danio rerio*).[25] Anionic nanoparticles (in our experience, <-20 mV measured zeta (ζ) potential) interact strongly with RES cell types, namely scavenging endothelial cells (SECs, *via* a *stabilin*-mediated clearance pathway) and blood resident macrophages.[25,26] Whereas, cationic liposomes (>20 mV measured ζ-potential) are rapidly removed from circulation through a combination of non-specific cellular interactions (*i.e.* adsorption to the anionic surface of the blood vessel walls), and/or clearance *via* the RES.[25] While usually considered detrimental to *in vivo* performance, the non-specific, cellular interactions of cationic nanoparticles/complexes (*e.g.* Lipofectamine^{TM}) have been widely exploited to deliver membrane impermeable, (genetic) material across cell membranes *in vitro*.[27–30] In these cases, a net cationic surface charge not only promotes non-specific adsorption and uptake within cultured cells but also facilitates endosomal escape and cytosolic payload release. In contrast, anionic and neutral nanoparticles are generally taken up sparingly by non-RES cell types, while those that are internalised tend to localise within lysosomes[21,31] – a chemically hostile environment in which encapsulated payloads are rapidly degraded.

The contrasting fates of differently charged nanoparticles have all the ingredients of an ideal targeted drug delivery system. On the one hand, *i.v.* administered, (near) neutral nanoparticles freely circulate, maximising exposure within any (vascularized) tissue of the body. On the other, cationic nanoparticles are non-specifically taken up by virtually all cells, delivering high intracellular concentrations of encapsulated (and membrane impermeable)

payloads. Herein, we describe the rapid switching of liposome surface charge, from neutral to cationic, *in situ* and *in vivo* using light as exclusive trigger (Figure 1). Light is chosen as trigger given the rapid and quantitative photolysis of common chemical photocages,[32] its proven clinical relevance[33] and the prospect of emerging technologies to apply light deep within patients. These include fiber-optic[34,35] and injectable microLED hardware,[36] as well as photocleavable chemical functionality sensitive to visible or near infrared (NIR) light. [37–39] Light wavelengths between 600 and 950 nm can penetrate various human tissues (skin, fat and blood) up to a depth of 2 cm.[40] As model organism, we select the small and transparent zebrafish embryo. This organism is increasingly being used as a versatile preclinical screening platform for nanoparticles[41] and offers unprecedented opportunities to image nanoparticles across whole live organisms (*i.e.* visualising total injected nanoparticle doses), at cellular resolution and in real time.[42] Moreover, the zebrafish embryo can *qualitatively* predict nanoparticle interactions with scavenging cell types of the reticuloendothelial system (RES) in mammalian models.[25,43]

In this study, following *i.v.* administration within a zebrafish embryo, photoactive liposomes, composed of just two lipids and prior to light activation, freely circulate and do not significantly interact with RES and/or other cell types of the embryo. Following *in situ* light activation, however, rapid surface charge switching results in non-specific adsorption and uptake of liposomes across the entire endothelium of the fish, as well as phagocytic uptake in blood resident macrophages. Importantly, light triggered surface charge switching does not disrupt liposome integrity and encapsulated, membrane impermeable payloads are successfully transported across cell membranes following surface charge switching.

5.4 MATERIALS AND METHODS

Materials and Reagents. 1,2-dioleoyl-*sn*-glycero-3-phosphocholine (DOPC), 1,2-dioleoyl-3-trimethylammonium-propane (DOTAP), 1,2-dioleoyl-*sn*-glycero-3-phosphoethanolamine-N-(lissamine rhodamine B sulfonyl) (Rhodamine-PE) were purchased from Avanti Polar Lipids (Alabaster, AL, US). **1,2-Dioleoyl-*sn*-glycero-3-phosphoethanolamine-Atto 633** was purchased from ATTO-TEC GmbH (Germany). Additional DOPC was purchased from Lipoid GmbH. Cholesterol and sulforhodamine B (SR-B, sodium salt) were purchased from Sigma Aldrich. pHrodo™ Red, succinimidyl ester (pHrodo™ Red, SE) was purchased from Thermo Fisher Scientific. DOPE-pHrodo was prepared through conjugation of DOPE with pHrodo succinimidyl ester under basic conditions, followed by column chromatography.[76] Fluorescein-labeled hyaluronic acid (fluoHA) was prepared through conjugation of hyaluronic acid (100 kDa) with fluorescein isothiocyanate (Isomer I, Sigma-Aldrich) under mildly basic conditions, followed by ethanol precipitation.[77] All other chemical reagents were purchased at the highest grade available from Sigma Aldrich and used without further purification. All solvents were

purchased from Biosolve Ltd. For anhydrous reactions, solvents were dried over activated molecular sieves (3 Å, 4–8 mesh). *HEPES buffer*: HEPES (10 mM) adjusted to pH 7.4 with 1 M aqueous NaOH. Ultrapure MilliQ® water, purified by a MilliQ Advantage A10 water purification system from MilliPore, was used throughout.

Chemical synthesis and characterization. TLC analysis was performed using aluminium TLC plates, coated with 0.25 mm silica gel 60 F_{254} from Merck KGaA. Plates were visualized by UV absorption at 254 nm and/or staining with $KMnO_4$ solution. Flash-column chromatography was performed using silica gel 60 (particle size of 40-63 μm) from Merck KGaA. ^1H and ^{13}C NMR spectra were acquired using an Avance DPX-300MHz or AV-400 MHz NMR spectrometer from Bruker at room temperature. Chemical shifts are given in ppm with tetramethylsilane (TMS) or residual solvent ($CDCl_3$: 7.26 ppm for ^1H NMR and 77.2 ppm for ^{13}C NMR) as internal standard. Signal multiplicity is described with common abbreviations: singlet (s), broad singlet (s_{br}), doublet (d), triplet (t), quartet (q), multiplet (m). Coupling constants are given in Hz. High-resolution mass spectrometry (HRMS) were recorded on a Thermo Scientific LTQ Orbitrap XL. UV absorption spectra were measured using a Cary 3 Bio UV-vis spectrometer (Cary WinUV software, version 3.0, Agilent), scanning from 200 nm to 550 nm at 1 nm intervals. Scan rate: 120 nm min^{-1}.

Light source and actinometry. A commercially available 375-nm LED (Maximum measured wavelength = 370 nm, FWHM = 13.4 nm; H2A1-H375-S, Roithner Lasertechnik, Vienna, Austria), driven by a custom-built LED driver (I = 350 mA), was used as UV light source in all cases. The optical power density of the LED light source was determined using an integrating sphere setup. For this, the LED was positioned precisely 5 cm above the 6.0 mm aperture of an integrating sphere (AvaSphere-30-IRRAD, Avantes, Apeldoorn, The Netherlands). This sphere was connected by an optical fiber (FC-UV600-2, Avantes) to a UV-Vis spectrometer (AvaSpec-ULS2048L StarLine CCD spectrometer, Avantes). The setup was calibrated using a NIST-traceable calibration light source (Avalight-HAL-CAL-ISP30, Avantes). The LED was switched on, and allowed to warm up for 1 min, before a spectrum was recorded. The obtained spectrum was integrated to obtain the total incident optical power density (in mW cm^{-2}). Light dosages (J per embryo) were obtained by multiplying the optical power density by the irradiation time. Average embryo surface area used was 0.03 cm^2 (0.1 x 0.3 cm). Precise irradiation setups are detailed within experimental descriptions.

Liposome preparation. All liposomes (without encapsulated payloads) were formulated in either (deionized) H_2O or 10 mM HEPES buffer at a total lipid concentration of 4 mM. Individual lipids, as stock solutions (1-10 mM) in chloroform, were combined to the desired molar ratios and dried to a film, first under a stream of N_2 then >1 h under vacuum. Large unilamellar vesicles were formed through extrusion above the T_m of all lipids (room

temperature, Mini-extruder, Avanti Polar Lipids, Alabaster, US). Hydrated lipids were passed 11 times through 2 x 400 nm polycarbonate (PC) membranes (Nucleopore Track-Etch membranes, Whatman), followed by 11 times through 2 x 100 nm PC pores. All liposome dispersions were stored at 4°C. All liposomes were stable for at least 1 month (in the dark).

Size and zeta potential measurements. Particle size and zeta potentials were measured using a Malvern Zetasizer Nano ZS (software version 7.13, Malvern Panalytical). For DLS (operating wavelength = 633 nm), measurements were carried out at room temperature in water or HEPES (10 mM) buffer at a total lipid concentration of approx. 100 μM. Zeta potentials were measured at 500 μM total lipid concentration, using a dip-cell electrode (Malvern), at room temperature. For liposomes formulated in water, aq. NaCl was added to the liposome solution to a final concentration of 10mM NaCl before zeta potential measurement. All reported DLS measurements and zeta potentials are the average of three measurements. For DLS and zeta potential experiments monitoring changes following light activation, liposomes were irradiated (370 ± 7 nm, 202 mW cm^{-2}) in quartz cuvettes with the LED mounted at a distance of 1 cm from the sample. The same liposome sample was used for time course DLS and zeta potential measurements.

Cryogenic transmission electron microscopy. Liposomes (3-6 μL, 4 mM total lipid concentration) were applied to a freshly glow-discharged carbon 200 mesh Cu grid (Lacey carbon film, Electron Microscopy Sciences, Aurion, Wageningen, The Netherlands). Grids were blotted for 1, 2 or 3 s at 99% humidity in a Vitrobot plunge-freezer (FEI Vitrobot™ Mark III, Thermo Fisher Scientific). Cryo-EM images were collected on a Talos L120C (NeCEN, Leiden University) operating at 120 kV. Images were recorded manually at a nominal magnification of 17500x or 36000x yielding a pixel size at the specimen of 5.88 or 2.90 ångström (Å), respectively. For cryoTEM images monitoring changes following light activation, liposomes were irradiated (15 mins, 370 ± 7 nm, 202 mW cm^{-2}) in quartz cuvettes with the LED mounted at a distance of 1 cm from the sample. The same liposome sample was used for before and after UV.

Sulforhodamine-B (SR-B) encapsulation and characterization. DOPC:**4** (1:1) lipid films (10 mM total lipids) were hydrated with HEPES buffer (1 mL) containing SR-B (10 mM) and formulated by extrusion, as described for empty liposomes. Un-encapsulated SR-B was removed by size exclusion chromatography (illustra™ NAP™ Sephadex™ G-25 DNA grade pre-made columns (GE Healthcare)) following the supplier's instructions. Eluted liposomes with encapsulated SR-B were diluted 2.5x during SEC (to approximately 4 mM [total lipid]) and injected without further dilution.

Contents leakage assay: SR-B leakage from DOPC:**4** (1:1) liposomes, before and after light activation, was monitored using a TECAN Infinite M1000 Fluorescence Plate Reader and

were performed in 96-well plates (PP Microplate, solid F-bottom (flat), chimney well) at room temperature. Final experimental volume in each well was 200 µL. To monitor SR-B leakage (and dye de-quenching) during photoactivation, fluorescence emission (excitation: 520 nm; emission: 580 nm) was measured every 20 s for 600 s, the sample was then irradiated (20 mins, 370 ± 7 nm, 202 mW cm^{-2}) in a quartz cuvette, with the LED mounted at a distance of 1 cm from the sample, returned to the 96-well plate and fluorescence emission measured for a further 10 mins. After this, Triton X-100 (10 µL, 1% w/v) was added to the sample well (10 s agitation) to solubilize liposomes and release any remaining encapsulated SR-B.

Zebrafish husbandry, injections and irradiation setup. Zebrafish (*Danio rerio*, strain AB/TL) were maintained and handled in accordance with guidelines from the European Convention on the protection of vertebrate animals used for experimental and other scientific purposes,[78] and in compliance with the directives of the local animal welfare committee of Leiden University. Fertilization was performed by natural spawning at the beginning of the light period, and eggs were raised at 28.5 °C in egg water (60 µg mL^{-1} Instant Ocean sea salts). The following previously established zebrafish lines were used: *Tg(kdrl:eGFP)*^{s843},[79] *Tg(mpeg1:GFP)*^{gl22},[80] *Tg(mpeg1:mCherry)*^{gl23}.[80] Liposomes were injected into 2-day old zebrafish embryos (52-56 hpf) using a modified microangiography protocol.[81] Embryos were anesthetized in 0.01% tricaine and embedded in 0.4% agarose containing tricaine before injection. To improve reproducibility of microangiography experiments, 1 nL sample volumes were calibrated and injected into the sinus venous/duct of Cuvier. A small injection space was created by penetrating the skin with the injection needle and gently pulling the needle back, thereby creating a small pyramidal space in which the liposomes were injected. Successfully injected embryos were identified through the backward translocation of venous erythrocytes and the absence of damage to the yolk ball. For embryo irradiation, the UV source (370 ± 7 nm) was positioned approximately 1.5 cm above the agar-embedded embryo (~90 mW cm^{-2}). 15 min total irradiation time (~2.4 J per embryo light dose) was used in all cases of embryo irradiation followed by confocal imaging. For experiments monitoring changes in liposome biodistribution following light triggered surface charge switching, the same embryo was imaged before and after UV irradiation.

Confocal image acquisition and quantification. Zebrafish embryos were selected according to successful injections and randomly picked from a dish of 20-60 successfully injected embryos. At least four zebrafish were visualized and the most representative zebrafish was imaged by a Leica TCS SPE or SP8 confocal microscope (Leica Application Suite X software, version 3.5.5.19976, Leica Microsystems). Confocal z-stacks were captured using a 10x air objective (HCX PL FLUOTAR), a 40x water-immersion objective (HCX APO L) or 63x water-immersion objective (HC PL APO CS). For whole-embryo views, 3 overlapping z-stacks were

captured to cover the complete embryo. Laser intensity, gain and offset settings were identical between stacks and experiments. Images were processed and quantified using the Fiji distribution of ImageJ.[82,83] For quantification of liposome circulation lifetime decay, at least three individual embryos (biological replicates) were imaged using confocal microscopy at each time point. Quantification (not blinded) was performed on 40x confocal z-stacks (optical thickness of 2-3 µm per slice) using methods and ImageJ macros previously described.[25] Median values are reported.

Two-photon setup and image acquisition. A custom-built two-photon multifocal microscope was used for simultaneous UV irradiation and two-photon fluorescent imaging. A femtosecond pulsed Ti:Sa laser set at 830 nm (Coherent, Chameleon Ultra) was used as excitation source. Multifocal illumination of the sample was achieved by a diffractive optical element (DOE, custom made by Holoeye) which splits the laser beam into an array of 25 x 25 foci. A virtual light sheet was created by spiral scanning the foci within the 50 ms exposure time of the camera using a fast-scanning mirror (Newport, FSM-300-1).[84] The virtual light sheet was focused and emission photons collected by a 25X, high-NA water-dipping objective (Nikon, CFI75 Apochromat 25XC W). The objective was positioned onto a piezo stage (P-726 PIFOC, PI) for z-stack measurements. Emission light was separated from the excitation path by a dichroic mirror (700 dcxr, Chroma). After passing through a 700 nm short pass filter, emission photons were detected with a 2048 x 2048 pixel sCMOS camera (Hamamatsu, Orca Flash 4.0 V2). Emission images were taken at the start of the experiment with a white LED. After the emission images, the UV-LED was installed at the location of the white LED. The UV LED was positioned approximately 1.5 cm (~90 mW cm^{-2}) above the sample and on/off-times were timed by the same data acquisition card (USB-6226, National Instruments) which triggered the camera. Simultaneous UV irradiation and two-photon fluorescent imaging was performed one hour post injection. To ensure stability, embryos were imaged for 15 minutes before the measurement. Once embryos were stable, images were taken every 1 second for 5 minutes. After 5 minutes the UV lamp was turned on and switched off only during camera exposure. Two-photon microscopy data was processed using custom-built LabVIEW software (version 2018 SP2, National Instruments).

Statistics and Reproducibility. All experiments presented in the main manuscript were repeated at least twice with the exception of Figures 6b,c. All replicate experiments were performed using freshly prepared liposomes. Unless clearly stated in the manuscript text (*e.g.* varying macrophage uptake prior to UV activation), all replicate experiments were successful and confirm the presented data. All experiments presented in Supplementary Information were repeated at least twice, with the exception of Supplementary Figures S5.1 and S5.6. All replicate experiments were performed using freshly prepared liposomes. For all experiments performed in embryonic zebrafish, at least four embryos were randomly selected (from a pool of >20

successfully injected embryos) and imaged (low resolution microscopy). Unless clearly stated in the manuscript text (*e.g.* varying macrophage uptake prior to UV activation), all imaged embryos showed consistent results and confirmed the presented data. From these four embryos, one was selected for high resolution, confocal microscopy. No statistical analysis is performed in this work.

Data Availability. Data supporting the findings of this paper are available from the corresponding authors upon reasonable request. Source data (raw confocal z-stacks and collated data as single Excel sheet) underpinning the data presented in Figure 4g have been deposited within the public image database, figshare.com (DOI: 10.6084/m9.figshare.12387629).

5.5 RESULTS

5.5.1 DESIGN OF PHOTOACTIVE LIPOSOMES

Photoswitching the surface charge of a liposome – from neutral to cationic – requires photoactive lipids embedded within a liposome membrane (Figure 5.1). In the absence of light and at physiological pH, photocaged lipids should carry no net charge to maintain a (near) neutral liposome surface charge (*i.e.* freely circulating). To ensure sufficient cationic surface charge density following photoactivation (in our experience, liposomes with a measured ζ-potential >20 mV), photocaged lipids should make up a significant proportion, if not all, of the overall lipid membrane composition. And, for optimal performance, photolysis and subsequent charge switching should be rapid. Finally, to achieve intracellular delivery of (membrane impermeable) drugs, encapsulated payloads should remain entrapped within liposomes, before, during and after light activation. Surface charge switching should not, therefore, involve any large-scale reorganization of the liposome membrane and with it the potential for leakage of encapsulated drugs.

To ensure the non-specific adsorption of cationic liposomes to blood vessel walls following light triggered surface charge switching, we first assessed the physicochemical properties and *in vivo* behaviour of liposomes containing cationic, cholesterylamine compounds, **1-3** (Figure 5.2a, see Materials and methods for synthesis and characterization). Cholesterol can be incorporated into a reconstituted (phospho)lipid bilayer up to approximately 50 mol%,[44] and is often included in liposomal formulations to modulate drug retention and release profiles.[45] Knowing the hydroxyl head group of cholesterol sits deeper within a lipid bilayer than neighboring phospholipid head groups,[46] a series of cholesterylamine compounds, **1-3**, were assessed, in which the spacer length between the hydrophobic cholesteryl anchor and primary

amine head group was varied. In all cases, linkers were connected to cholesterol *via* an ester bond. While spacers were primarily included to ensure effective charge presentation at the lipid-water interface, our choice of spacer chemistry was also influenced knowing the final photocaged cholesteryl compounds would be charge neutral, hydrophobic and potentially form lipid droplets within a phospholipid membrane.[47] In this scenario and upon light activation, we envisaged extensive membrane remodeling to reposition the newly revealed primary amine at the water-lipid interface and with it the potential for contents leakage. To minimize this risk and to increase the amphipathicity of the final photocaged cholesteryl compound, we focused on short glycine and polyethylene glycol (PEG) linkers as hydrophilic and/or uncharged spacers.
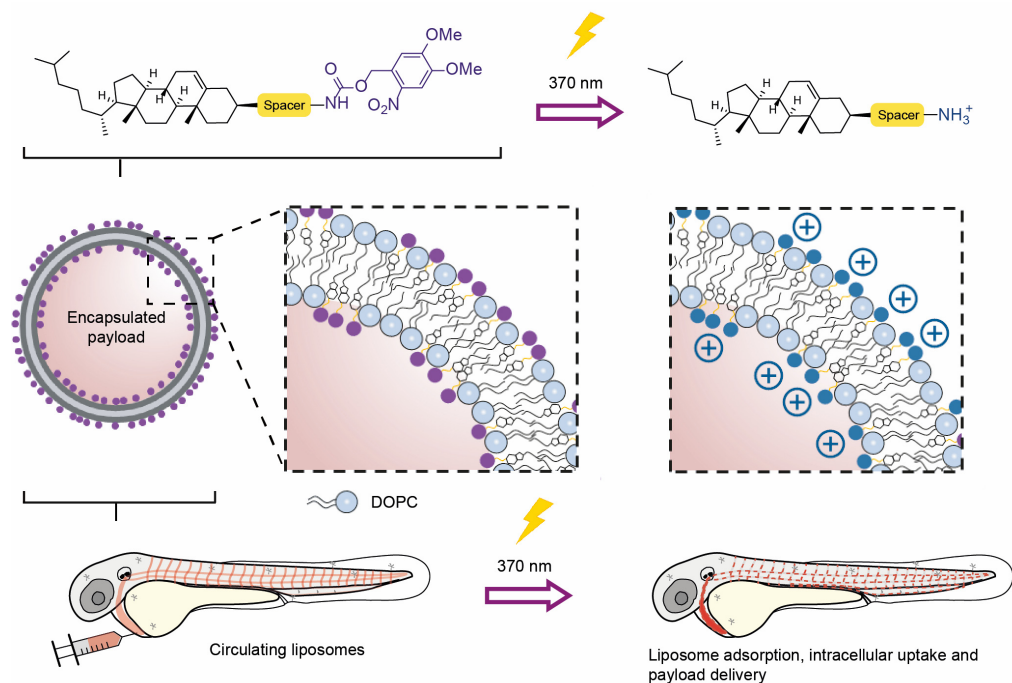

Figure 5.1. Photoswitching the surface charge of a liposome – from neutral to cationic – requires photoactive lipids embedded within a liposome membrane. Prior to light activation, charge neutral, photoactive liposomes freely circulate throughout the vasculature of a zebrafish embryo and do not interact with RES cell types, or any other cell type, of the embryonic fish. Upon light irradiation and photolysis of photocaged, cholesterylamine lipids, rapid surface charge switching, from neutral to cationic, leads to non-specific adsorption of liposomes across the endothelium of the embryo, liposome uptake and intracellular delivery of liposome-encapsulated, membrane impermeable payloads. DOPC = 1,2-dioleoyl-*sn*-glycero-3-phosphocholine.

Liposomes, containing varying amounts of 1-3, up to 50 mol%, were co-formulated with zwitterionic, 1,2-dioleoyl-*sn*-glycero-3-phosphocholine (DOPC) phospholipids. All formulated liposomes were prepared by standard extrusion techniques and were approximately 100 nm in size, with polydispersity indices (PDI) <0.2 as measured by dynamic light scattering (DLS,

Table S5.1). DOPC was chosen as co-formulant phospholipid as we have previously shown liposomes composed of 100% DOPC,[25] as well as 1:1 mixtures of DOPC and cholesterol (Figure S5.1), freely circulate throughout the vasculature of an embryonic zebrafish beyond 1 hour post-injection (hpi). As expected, increasing the amount of cholesterylamine, 1-3, within the DOPC liposome membrane resulted in greater cationic surface charge (Figure 5.2b and Table S5.1). However, at high mol% of cationic lipids, a trend emerged whereby longer spacers resulted in an increasingly cationic surface charge.
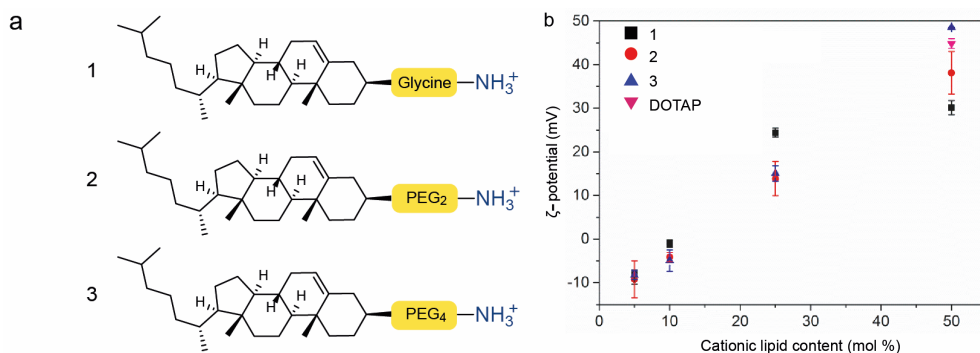

Figure 5.2. Varying cholesterylamine content within DOPC liposomes. (a) Cationic cholesterylamine analogues, **1-3**. (b) Measured surface charges (ζ-potential) of DOPC liposomes containing varying mol% **1-3**. DOPC:DOTAP (1:1) liposomes are included as a representative (commercially available) cationic liposome formulation. Measure of centre: mean; Error bars: standard deviation.

Satisfyingly, the measured surface charge of DOPC:3 (1:1) liposomes was comparable to liposomes formulated with commercially available, cationic 1,2-dioleoyl-3-trimethylammonium-propane (DOTAP) lipids (Figure 5.2b). We have previously shown that *i.v.* administered DOTAP liposomes (*e.g.* EndoTAG-1® - DOPC:DOTAP (45:55) and 100% DOTAP liposomes) non-specifically adsorb to blood vessel walls throughout the vasculature of an embryonic zebrafish.[25] Following *i.v.* microinjection in a two day old zebrafish embryo (2 days post-fertilisation, dpf), all three cationic liposome formulations – *i.e.* DOPC co-formulated with 50 mol% 1, 2 or 3 – showed comparable biodistributions to cationic DOPC:DOTAP (1:1) liposomes (Figure S5.2a). In all cases, liposomes were mainly visible as immobile punctae bound to all blood vessel walls (both arterial and venous) and largely removed from circulation at 1 hpi (Figures 5.3a-c and Figures S5.2b,c). In contrast, DOPC liposomes co-formulated with lower mol% of cholesterylamine 3 showed variable biodistributions dependent on the surface charge density of the liposome (Figure 5.3d,i). In particular, (near) neutral DOPC liposomes, containing 10 mol% 3, were extensively taken up by blood-resident macrophages within the caudal haematopoietic tissue (CHT) of the embryonic fish (Figures 5.3j,k and Figure 5.3 for whole embryo images).
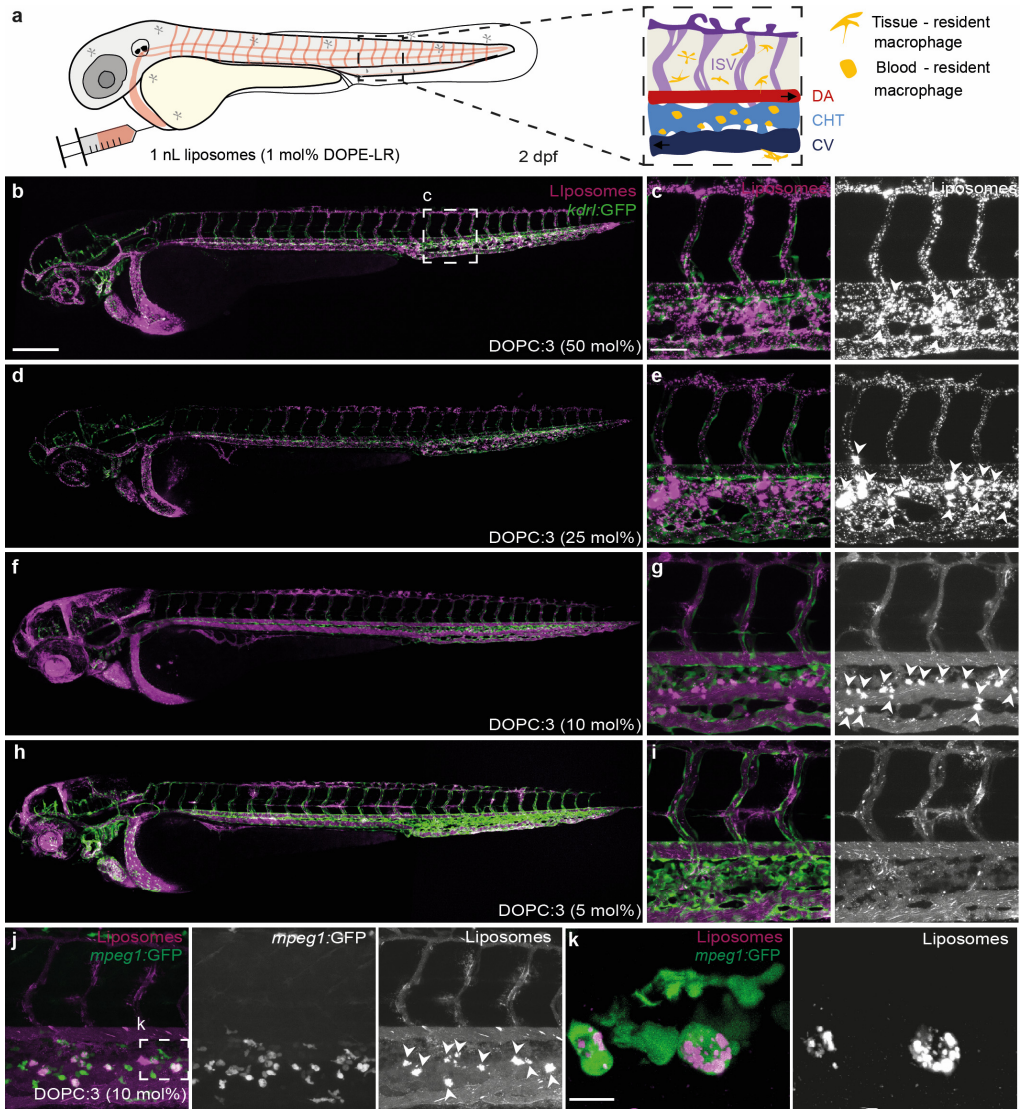
Figure 5.3. Biodistribution of cationic, DOPC:3 liposomes in embryonic zebrafish. (a) Schematic showing the site of microinjection within a zebrafish embryo, two days post-fertilization (dpf). Boxed region showing the organisation of blood vessels/macrophages within the tail of the embryo. DA: dorsal aorta; CHT: caudal hematopoietic tissue; CV: caudal vein; ISV: intersegmental vessel. Black arrows indicate direction of blood flow. (b-i) Biodistribution of DOPC liposomes containing cholesterylamine, **3**, at varying mol%. Whole embryo (10x magnification) and tissue level (40x magnification) views of liposome distribution in *kdrl:GFP* transgenic embryos, stably expressing GFP in all endothelial cells, at 1 hpi. White arrowheads indicate apparent liposome uptake within blood resident macrophages, based on location and cell morphology. (j, k) Tissue and cellular (63x magnification) level views of DOPC:**3** (10mol% **3**) liposome distribution in *mpeg1:GFP* transgenic embryos, stably expressing GFP in all macrophages, at 1hpi. Extensive fluorescence co-localization of liposomes and transgenic GFP confirmed the uptake of DOPC:**3** (10mol% **3**) liposomes

in blood resident macrophages of the zebrafish embryo. Slight variations in the positions of macrophages (between **j** and **k**) are due to macrophage migration during the time taken to change magnification settings on the confocal microscope. All liposomes (**b-k**) contained 1 mol% fluorescent lipid probe, DOPE-LR, for visualization. Scale bars: 200 μm (whole embryo); 50 μm (tissue level); 10 μm (cellular level).

5.5.2 LIGHT-TRIGGERED SWITCHING OF LIPOSOME SURFACE CHARGE *IN VITRO* AND *IN VIVO*

As DOPC:**3** (1:1) liposomes possessed the highest measured cationic surface charge, we proceeded to photocage **3**, forming the uncharged, photoactive cholesteryl compound, **4** (Figure 5.4a, see Materials and methods Information for synthesis and characterisation). Upon UV irradiation (370 ± 7 nm, 202 mW cm^{-2}), in H$_2$O/MeCN/^{t}BuOH (1:1:1), complete photolysis of **4** was achieved in less than two minutes, with clean photolysis confirmed by the appearance of two isosbestic points in the UV spectra (Figure S5.4a). Irradiation of DOPC:**4** (1:1) liposomes, formulated in 10 mM HEPES buffer (pH 7.4), resulted in comprehensive surface charge reversal – from ζ-potential -8 to +26 mV – within this same short timeframe (Figure 4b). Despite batch-to-batch variation (resulting in measured zeta potentials ranging from +20 to +35 mV ζ-potential), the cationic surface charge of irradiated DOPC:**4**→**3** (1:1) liposomes was consistently lower than that of parent DOPC:**3** (1:1) liposomes (ζ-potential +48 mV). Both formulations should, in theory, be compositionally identical and, at this point, we do not have a reasonable explanation for this discrepancy. The measured size (approx. 100 nm) and PDI (<0.1) of DOPC:**4** (1:1) liposomes was unchanged before and after irradiation (Figure S5.4b and Table S5.1). Likewise, their spherical, unilamellar morphology, as imaged by cryoTEM, generally remained unchanged before and after UV irradiation (Figure 4c, see Figure S5.5 for larger populations), although a small fraction (<10%) of irradiated DOPC:**4**→**3** liposomes did appear non-spherical (oblong) (Figures S5.5b,e). Whether this morphological change is the result of membrane reorganization upon light triggered photolysis of membrane embedded **4** is hard to conclude given we persistently observed only very small populations of DOPC:**4** liposomes (prior to light activation) by cryoTEM. Importantly, however, any potential membrane reorganization did not lead to disruption of liposome integrity and liposome encapsulated and membrane impermeable contents remained within the aqueous core of the liposome before, during and after light activation (Figure S5.6).
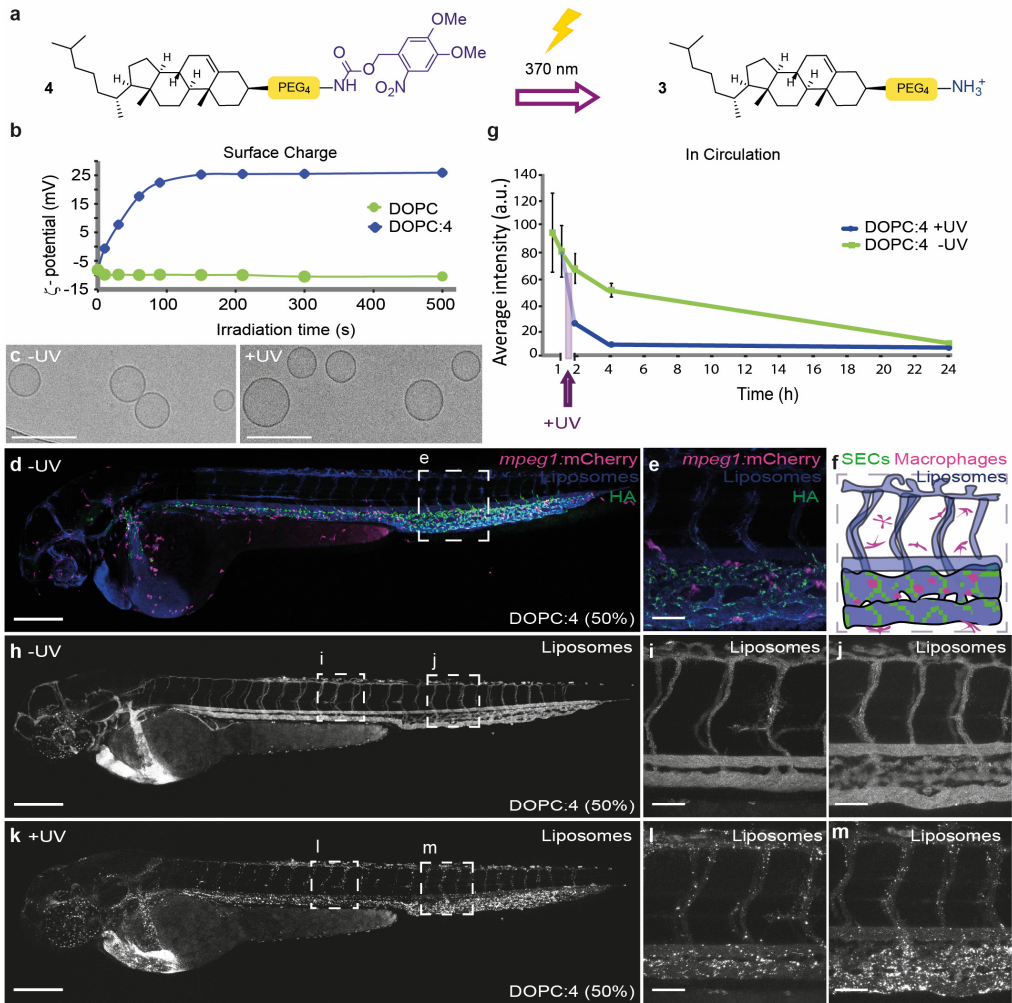
Figure 5.4. Photoswitching liposome surface charge *in vitro* and *in vivo*. (a) Chemical structure of **4** and its photolysis to **3**. (b) Evolution of measured surface charge of DOPC:**4** liposomes (1:1) as a function of UV (370 ± 7 nm, 202 mW cm^{-2}) irradiation time. Note: batch-to-batch variation resulted in measured zeta potentials of DOPC:**4**→**3** liposomes ranging from +20 to +35 mV. Data presented is representative of liposomes used in Figure 3h-m. 100% DOPC control liposomes demonstrate surface charge of liposomes without photoactive lipids is unaffected by UV irradiation. (c) Cryo-TEM images of DOPC:**4** before and after *in situ* irradiation (15 min, 370 ± 7 nm, 202 mW cm^{-2}). Scale bar: 200 nm. See Information Figure S5.5 for low magnification cryoTEM images. (d,e) Whole embryo and tissue level views of DOPC:**4** liposome biodistribution following co-injection with fluoHA in *mpeg1:mCherry* transgenic embryos (2 dpf). FluoHA is a specific *in vivo* marker of SECs and does not compete with liposome binding.[25] Liposomes (d,e) contained 1 mol% fluorescent lipid probe, DOPE-Atto633, for visualization. (f) Tissue level organization of macrophages and fluoHA-labelled SECs within the tail region of an *mpeg1:mCherry* embryo (2 dpf). (g) Quantification of DOPC:**4** liposome levels in circulation based on mean liposome fluorescence intensity in the lumen of the DA at 0.5, 1, 2, 4, and 24 hpi (measure of centre: median; error bars: standard deviation); n = 6 (0.5 and 1 hpi) and n = 3 (2, 4 and 24 hpi) individually injected embryos per formulation per time point (see **Fig. S7** for individual images). (**h-j**) Whole embryo

and tissue level views of DOPC:**4** liposome biodistribution in *kdrl:GFP* embryos, prior to UV irradiation, 1 hpi. (k-m) Whole embryo and tissue level views of DOPC: **4→3** liposome biodistribution in *kdrl:GFP* embryos, directly after *in situ* irradiation (15 min, 370 ± 7 nm, ~90 mW cm^{-2}, ~2.4 J per embryo), approx. 1.5 hpi. Liposomes (h-m) contained 1 mol% fluorescent lipid probe, DOPE-LR, for visualization. Scale bars (d-m): 200 μm (whole embryo); 50 μm (tissue level).

Following microinjection in the embryonic zebrafish (54-56 hours post fertilization, hpf) and prior to light activation, DOPC:**4** liposomes (formulated at 1:1 molar ratio in all subsequent experiments) were freely circulating and did not significantly interact with RES cell types of the embryonic fish, namely blood resident macrophages and scavenging endothelial cells (SECs), at 1 hpi (Figures **4**d-f,h-j). Indeed, the exponential circulation lifetime decay of DOPC:**4** liposomes in the embryonic fish was very similar to that previously observed for 100 nm liposomes based on the lipid composition of Myocet®.[25] Myocet® (lipid composition: POPC:cholesterol; 55:45) is a clinically approved liposomal-doxorubicin formulation designed to evade the RES, circulate freely and passively target solid tumors *via* the enhanced permeability and retention (EPR) effect.[48] In humans, the circulation half-life of Myocet® is 2.5 h.[49] In this case, like Myocet®, a significant fraction of photoactive DOPC:**4** liposomes remained in circulation >4 hpi (Figure 5.4g and Figures 7 and 8 for individual images used for quantification). Upon *in situ* irradiation (15 min, 370 ± 7 nm, ~90 mW cm^{-2}, ~2.4 J per embryo, 1 hpi) of the entire zebrafish embryo, however, a dramatic change in liposome fate was observed, whereby DOPC:**4→3** liposomes were now visible as immobile punctae associated with all blood vessel walls (Figures 4k-m) and largely removed from the circulating blood flow (Figure 5.4g). The biodistribution of DOPC:**4→3** liposomes matched that of cationic DOPC:**3** (1:1) liposomes (Figures 5.3b,c), confirming successful photoswitching of DOPC:**4** liposome surface charge – from (near) neutral to cationic – *in situ* and *in vivo*. In contrast, the biodistribution of freely circulating DOPC liposomes (100% DOPC content) was unaffected following identical irradiation procedures, confirming that the observed changes in biodistribution require the combination of both circulating DOPC:**4** liposomes as well as applied UV light (Figure S5.7). All UV irradiated embryos used in this study continued to develop normally without observable phenotypic abnormalities up to 6 dpf, confirming the suitability of this animal model for photoactivation studies.[50] Furthermore, any small potential increase in the temperature of the embryo as a result of UV irradiation will likely be counteracted by the remarkable resilience of the zebrafish embryo (from 1dpf) to heat stress.[51]
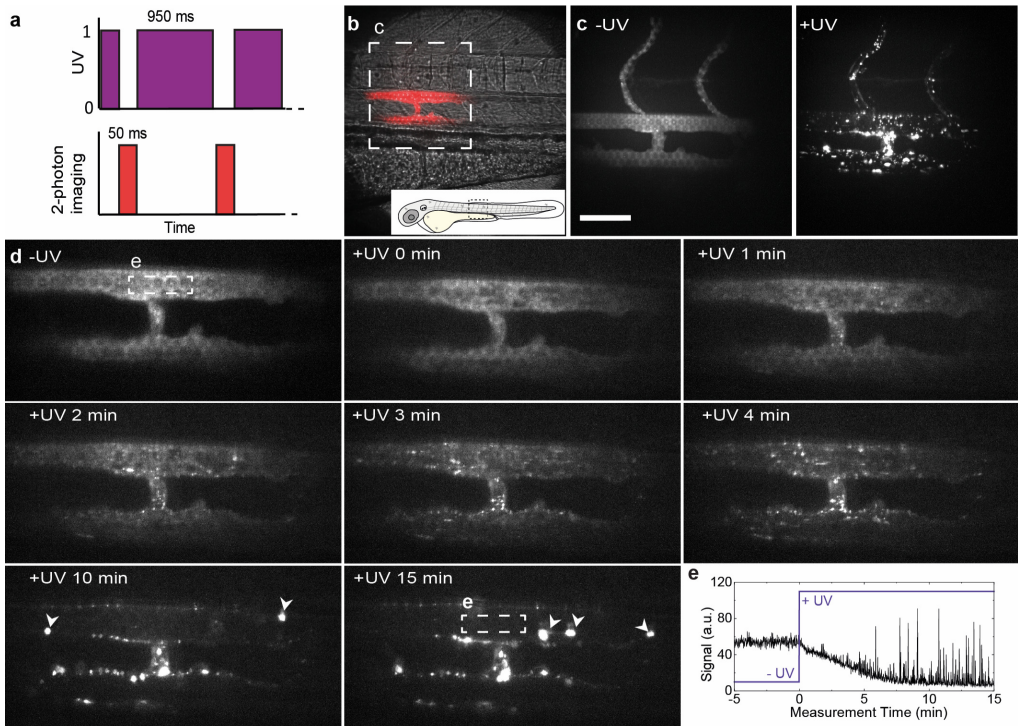
Figure 5.5. Real time multi-photon imaging of liposome surface charge switching *in situ* and *in vivo*. (a) The zebrafish embryo was exposed to UV light between the acquisitions of the camera, resulting in a 95% duty cycle of UV illumination per frame. (b) Transmission image of the imaging location, emission image overlaid in red. (c) Maximum intensity projections of two-photon z-stacks (spanning the full width of the embryo) showing DOPC:**4** liposome distribution, before and after UV exposure. These images confirm the vessel connected to, and extending dorsally from the PCV, is an ISV. (d) Time-lapse images of DOPC:**4(→3)** liposome distribution before and during UV irradiation. In later timeframes, large clusters of liposomes (indicated with white arrowheads) were observed passing through the plane of view in circulation. (e) Mean fluorescence intensity within the ROI (lumen of the DA, white square in **(c**, 15 min). Liposome fluorescence intensity immediately decreased upon UV irradiation. High intensity spikes of fluorescence, due to large circulating liposome aggregates passing through the ROI, registered from 5 minutes after UV irradiation start. Liposomes contained 1 mol% fluorescent lipid probe, DOPE-LR, for visualisation. Scale bars: 50 μm.

Having shown photoswitching of liposome surface charge occurs within seconds (Figure 5.4b), we next investigated the tissue level fate of *i.v.* administered DOPC:**4** liposomes, within the embryonic zebrafish, in real time (imaging rate: 1 frame per second, fps), before and during light-triggered surface charge switching. For this, a custom built, two-photon microscope was equipped with a 370 ± 7 nm LED, enabling alternating UV irradiation (95% UV duty cycle, Figure 5.5a) and two-photon fluorescence imaging. For these experiments, we focused on a single plane (200 μm x 200 μm) of view which included both the dorsal aorta (DA) and posterior cardinal vein (PCV) to ensure potential liposome selectivity (venous *vs.* arterial endothelium) could be observed (Figure 5.5b). From the acquired movie, two fundamental and competing

interactions of cationic nanoparticles could be simultaneously observed, namely non-specific adsorption of liposomes to endothelial cells (ECs) and liposome aggregation in circulation (Figure 5.5d for selected individual frames). Non-specific adsorption of liposomes to ECs was observed less than a minute after light activation, evident as emerging punctae of immobile fluorescence adhered to all blood vessel walls within the plane of view. The number of immobile punctae increased over time, and while there was no apparent selectivity for arterial or venous blood vessels, the largest number of liposomes were associated with the walls of the intersegmental vessel (ISV) connected to, and extending dorsally from, the PCV (Figure 5.5d). ISVs are narrower blood vessels than both DA or caudal vein (CV) and the blood flow velocity within this vessel is reduced.[52] As a result, circulating cationic liposomes will spend an increased residence time within this vessel, compared to larger DA or CV blood vessels, under reduced shear stress.[53,54] This, in turn, presumably increases the propensity of cationic liposomes to adhere to the anionic, heparan sulfated endothelium of the ISV through direct electrostatic interactions.

Competing with the non-specific adsorption to the blood vessel walls, cationic liposome aggregation in circulation was also observed following light activation. This could be directly visualized as increasingly large and bright fluorescent particles passing through the plane of view in circulation (Figures 5.5d,e). Aggregation of cationic liposomes is caused by the adsorption of anionic serum proteins/macromolecules to the newly revealed cationic nanoparticle surface,[55,56] and we have recently shown cationic liposomes adsorb significantly more serum proteins than anionic or neutral liposomes *in vitro*.[57] Adsorption of this protein corona will not only mask underlying cationic surface charge (preventing direct electrostatic interaction with blood vessel walls) but will induce liposome aggregation and concomitant uptake in blood resident macrophages. Indeed, over the course of this research and in the absence of light activation, we have observed variable, low level uptake of DOPC:**4** liposomes within blood resident macrophages, predominantly within the CHT of the embryo. This may be due to incidental light exposure during experimental and microscopy procedures, partial photolysis and subsequent aggregation of liposomes in circulation, followed by irreversible recognition and clearance *via* the RES.

These simultaneous and competing interactions of cationic liposomes *in vivo* can be explained by the contrasting fates of DOPC:**4**→**3** liposomes as they transition through various intermediate charged states, from (near) neutral to cationic surface charge. In particular, during the light triggered transition of DOPC:**4** liposome surface charge, an intermediate physicochemical state, highly prone to blood-resident macrophage uptake (*i.e.* compositionally similar to DOPC liposomes containing 10 mol% **3**), is, at least momentarily, inevitable (Figure 5.6a). The extent of macrophage uptake versus non-specific adsorption to ECs, should, therefore, be dependent on the residence time of partially activated DOPC:**4**→**3** liposomes in
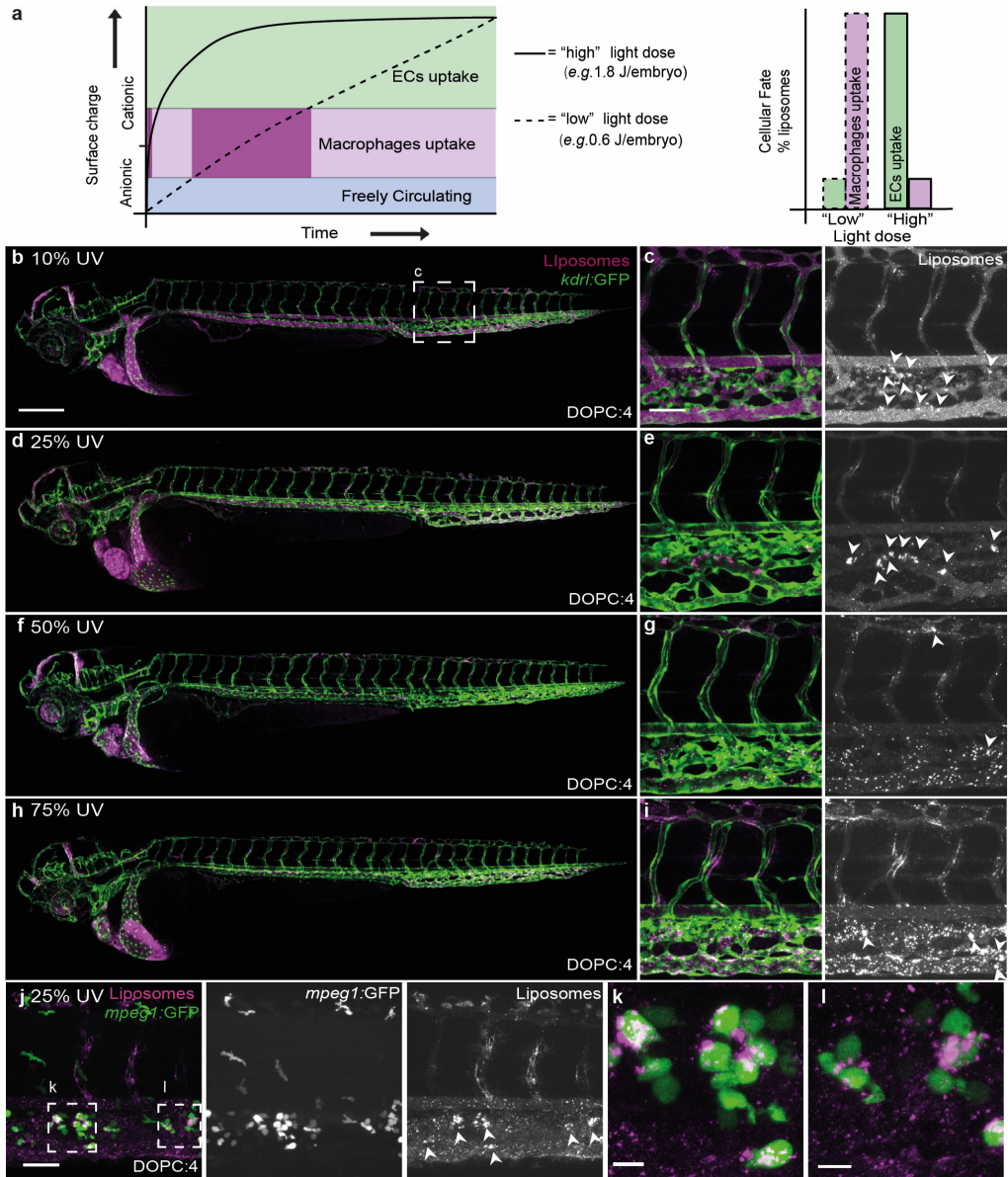
Figure 5.6. Effect of light dose on the *in vivo* fate of DOPC:4 liposomes. (a) Reducing the UV light dose applied to the embryo increases the time taken for DOPC:**4** liposomes to transition to DOPC:**3** liposomes. This, in turn, increases the resident time spent by DOPC:**4→3** liposomes at an intermediate cationic surface charge density leading to irreversible clearance of liposomes by blood resident macrophages. (b-i) Whole embryo and tissue level views of DOPC:**4** liposome biodistribution in *kdrl:GFP* embryos following embryo irradiation with variable light doses (15 min, 370 ± 7 nm, ~90 mW cm^{-2}, UV duty cycle stated for each image). Apparent liposome uptake in blood resident macrophages highlighted with white arrowheads. (j-l) Tissue level and zoomed views of DOPC:**4→3** liposome biodistribution in *mpeg1:GFP* embryos following embryo irradiation at 25% UV duty cycle (15 min, 370 ± 7 nm, 0.6 J

per embryo). Liposomes contained 1 mol% fluorescent lipid probe, DOPE-LR, for visualization. Scale bars: 200 μm (whole embryo); 50 μm (tissue level), 10 μm (zoomed).

circulation. To test this hypothesis, we systematically reduced the applied UV light dose (from 75% to 10% UV duty cycle; 1.8 to 0.24 J per embryo respectively) to extend the time taken for DOPC:**4** liposomes to transition from a (near) neutral to cationic surface charge *in situ* and *in vivo* (Figures 6b-i). In this way, the biodistribution of DOPC:**3** liposomes, containing varying mol% **3** (Figures 5.3b-i), could be replicated. Most striking, at 25% applied light (0.6 J per embryo), DOPC:**4→3** liposomes were predominantly taken up by blood resident macrophages within the CHT of the embryonic zebrafish, analogous to (near) neutral DOPC:**3** liposomes (10 mol% **3**) (Figures 5.6d, e, j-l). This result confirmed that an extended residence time of only partially activated DOPC:**4→3** liposomes leads to irreversible clearance of liposomes by the RES.

5.5.3 LIGHT-TRIGGERED LIPOSOMAL CELL UPTAKE AND PAYLOAD DELIVERY

Next, we investigated the intracellular fate of DOPC:**4** liposomes following *in situ* and *in vivo* surface charge switching. To verify endocytosis of DOPC:**4→3** liposomes, a pH-sensitive fluorescent lipid probe (DOPE-pHrodo, 1 mol%) was incorporated within the DOPC:**4** liposome membrane. The fluorescence intensity of pHrodo increases >100-fold in mildly acidic environments (*e.g.* late endosomes/lysosomes, pH <6). To accurately assess evolving pHrodo fluorescence, wild type (AB/TL) embryos were used to avoid potential fluorescence bleed through from transgenic fluorescent markers. Following *i.v.* injection and in the absence of light, pHrodo-associated fluorescence was observed in a small number of cells within the CHT of the embryonic fish (Figures 5.7a, b). While the absence of cell specific (transgenic) fluorescent markers does not allow for definitive identification of this cell type, its location within the CHT and rounded morphology (delineated by pHrodo fluorescence), is characteristic of low-level phagocytic uptake of DOPC:**4(→3)** liposomes within blood resident macrophages, as previously mentioned. Following *in situ* light irradiation, however, increasing pHrodo fluorescence, primarily associated with SECs, was observed over time (up to 5 hpi) (Figure 5.7c). This timeframe suggests a significant fraction of DOPC:**4→3** liposomes are not only endocytosed by SECs but remain within endosomes during trafficking and maturation to late endosomes/lysosomes. This would be consistent with the very high lysosomal activity of SECs, whose primary physiological role in the body is to recognize, clear and breakdown endogenous and pathogenic waste from the blood.[58] It is also possible that a fraction of endocytosed, cationic DOPC:**4→3** liposomes, within SECs, macrophages or other ECs, manage to successfully escape endosomes prior to the first imaging time point. Within the cytosol and beyond the acidic

endosome microenvironment, potential intracellular fluorescence associated with pHrodo probes would not be visible.
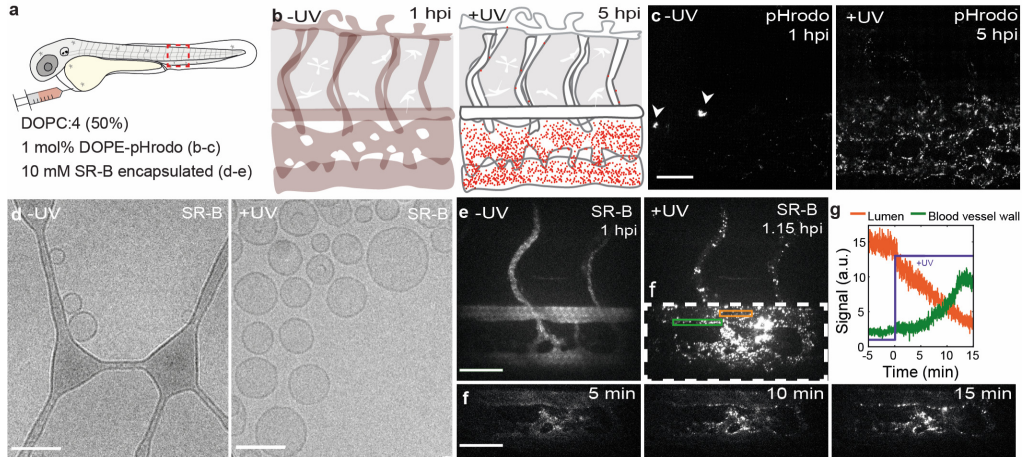

Figure 5.7. Cellular fate of DOPC:4→3 liposomes and their encapsulated payloads. (a,b) Schematics showing the site of microinjection within a 2 dpf embryo and the evolving fluorescence of pHrodo-containing DOPC:**4→3** liposomes within the tail region of a wildtype (AB/TL) embryonic zebrafish, over time. The fluorescence intensity of pHrodo increases >100-fold in mildly acidic environments (*e.g.* late endosomes/lysosomes, pH <6) and is, therefore, particularly apparent within SECs – cells with exceptionally high lysosomal activity. (c) Tissue level views of evolving pHrodo-associated fluorescence over time either in the absence of UV irradiation and following *in situ* UV irradiation (15 min, 370 ± 7 nm, 2.4 Jcm^{-2}). In the absence of UV irradiation, pHrodo-associated fluorescence is observed within a small number of cells within the CHT of the embryo (white arrowheads). Liposomes contained 1 mol% DOPE-pHrodo for visualization. Scale bar: 50 μm. (d) CryoTEM images of SR-B filled, DOPC:**4** liposomes before and after *in situ* irradiation (15 min, 370 ± 7 nm, 202 mW cm^{-2}). Scale bars: 100 nm. (e) Maximum intensity projections of two-photon z-stacks (spanning the full width of the embryo) showing SR-B filled DOPC:**4** liposome distribution, before and after UV irradiation. Scale bar: 50 μm. (f) Time-lapse images of SR-B filled DOPC: **4→3** liposome distribution during UV irradiation. Scale bar: 50 μm. (g) Mean SR-B fluorescence intensity within ROIs (lumen of the DA, orange line; DA vessel wall, green line, shown in **(e)**), before and during UV irradiation. SR-B fluorescence intensity in circulation decreases upon UV irradiation with a concomitant increase in SR-B fluorescence intensity associated with the DA blood vessel wall. Liposomes (e-g) containing encapsulated SR-B (10 mM) and otherwise unlabeled.

Having confirmed endocytosis of light-activated DOPC:**4→3** liposomes *in vivo*, we finally investigated the *in vivo* fate of liposome encapsulated and membrane impermeable payloads, following light triggered surface charge switching. For this, self-quenching concentrations of water soluble, sulforhodamine B (SR-B, 10 mM) were passively encapsulated within DOPC:**4** liposomes. As for empty liposomes, the morphology and size of the SR-B filled DOPC:**4** liposomes did not significantly change following irradiation (Figure 7d). To monitor the fate of liposome encapsulated SR-B *in vivo*, we again performed alternating UV irradiation and two-photon fluorescence imaging (1fps) within live embryos (Figures 5.7e-g). In this case, we focused on a single plane (200 μm x 200 μm) of view to include the DA, CHT and CV. This

region of the embryo includes a significant population of SECs, as well as blood resident macrophages, within which DOPC:**4**→**3** liposomes extensively accumulate. From the acquired movies, SR-B filled DOPC:**4** liposomes, prior to light activation, appeared freely circulating, evident as homogenous, low level (quenched) SR-B fluorescence, confined within the zebrafish vasculature. Upon light triggered activation (95% UV duty cycle, 2.3 J per embryo) and surface charge switching, however, localized and de-quenched SR-B could be seen as increasingly bright, fluorescent punctae, associated with all blood vessel walls but most prevalent throughout the sinusoid-like network of CHT blood vessels. Again, it is likely that DOPC: **4**→**3** liposome association and uptake within the CHT is enhanced due to the reduced blood flow velocities and sheer stresses experienced by liposomes within this sinusoidal-like tissue. Likewise, the co-existence of immobile as well as highly mobile SR-B fluorescent punctae is again indicative of intracellular SR-B delivery to both ECs (immobile) and blood resident macrophages (mobile).

As a representative membrane impermeable, small molecule cargo, the successful intracellular delivery of liposome-encapsulated SR-B serves as promising evidence that this proof-of-concept technology will likely be transferable to other, therapeutically relevant (and membrane impermeable) payloads.

5.6 DISCUSSION

The discovery of simple and effective targeted drug delivery systems should be preceded by a thorough understanding of the nano-bio interactions involved.[59] Here, we exploit the well characterized and contrasting fates of differently charged nanoparticles *in vivo*, however, our ability to rationally design a system that is both simple and effective has relied on comprehensive *in vivo* interrogation of all aspects of this technology (*i.e.* different light dosages, surface charge densities, interactions with the RES). To this end, the embryonic zebrafish has provided an invaluable pre-clinical *in vivo* screening platform, offering unprecedented opportunities to assess, analyze and optimize nanoparticle behavior over an entire live organism (*i.e.* visualizing total injected doses), at cellular resolution and in real time.[42,60,61] Furthermore, the presence and conserved function of key RES cell types enables predictive assessment of fundamentally important *in vivo* clearance mechanisms of nanoparticles.[25,43] It is important to stress here, however, that these predictions are strictly qualitative. Given the significant differences in relative numbers of RES cells (*i.e.* SECs *vs* blood resident macrophages), RES tissue size and organization, quantitative predictions (based on observations in the embryonic zebrafish) of nanoparticle clearance by the mammalian RES are not yet possible. As such, the embryonic zebrafish should not replace experiments in larger (mammalian) models but, instead, should be used to guide and optimize nanoparticle design prior to first injections in higher vertebrates.

At a fundamental level, the ability to visualize the formation of a cationic nanoparticle *in situ* has revealed, for the first time, the co-existence of two competing interactions of cationic nanoparticles occurring simultaneously *in vivo*, namely non-specific adsorption to blood vessel walls and opsonisation in circulation. This observation not only highlights the importance of considering the fate of *all* intermediate physicochemical states of stimuli-responsive nanoparticles as they transition from A to B, but, more generally, suggests that the fate of any given cationic nanoparticle is dependent on its surface charge density. Our data indicates that above a certain cationic surface charge threshold, *i.v.* administered nanoparticles will predominantly stick to (and be internalized by) endothelial cells, particularly in blood vessels with reduced blood flow velocity, while below this charge threshold, nanoparticles will tend to aggregate in circulation and be subsequently cleared by the RES. In our experience, *i.v.* administered liposomes with a measured surface charge >20 mV will tend to stick to endothelial cells, whereas those with a surface charge between +5 to +20 mV will tend to aggregate in circulation. Importantly, while we believe a threshold value will apply to all nanoparticle classes, this will likely vary depending on the surface chemistry and self-assembly of any individual nanoparticle and should be determined on a case-by-case basis.

In terms of targeting, the exclusive use of light as trigger forgoes any requirement for exploitable differences between target and non-target tissues (*e.g.* passive targeting of solid tumors *via* the EPR effect). As such, this liposome technology has the potential to be transferable to any light accessible tissue. Given the poor tissue penetration and significant potential cytotoxicity of using short wavelength UV-A light,[62,63] however, we would aim future efforts at replacing *o*-nitrobenzyl chemistries with photocages sensitive to longer wavelength light or two-photon activation. In this vein, a family of zwitterionic BODIPY-derived photocages have recently been reported that can be efficiently cleaved using single photon visible or NIR light.[39] In theory, these photocages, connected to a cholesterylamine lipid anchor and incorporated within DOPC liposomes should not affect the surface charge and, therefore, the biodistribution of photoactive liposomes. In addition, light can be focused with precise spatial resolution. This has been exemplified by the clinical application of Visudyne® - a liposome-photosensitizer (verteprofin) formulation, administered intravenously and indicated for the photodynamic therapy of age-related macular degeneration (AMD).[64] In this case, non-thermal, red light (689 nm) is applied to the eye of a patient to trigger localised therapy. Unfortunately, given the small size (2-3 mm in length) of the zebrafish embryo and the practical difficulties in ensuring no incident or scattered UV-A light reached the dark side of the agar embedded embryo, we have been unable to demonstrate localized liposome surface charge switching and intracellular uptake within the embryonic fish in this study.

In conclusion, we describe a liposome technology that successfully couples complete external control of *in vivo* liposome targeting together with the transport of encapsulated and membrane impermeable cargos across cell membranes. While these combined features are unique in the context of stimuli-responsive drug delivery systems (reviewed in refs 65,66), including those for which charge switching is central to function (reviewed in ref 67), the stand out feature of these liposomes is undoubtedly their compositional simplicity. The last decades have seen the empirical design of increasingly more complex nanomedicine designs, but it is now generally acknowledged that this approach has impeded rather than promoted the clinical translation of new nanomedicines.[59,68–70] In contrast, clinically approved and targeted nanomedicines tend to be compositionally simple,[49] with designs based on robust physicochemical principles (*e.g.* PEGylation to improve circulation lifetimes)[71] and well characterized and exploitable, albeit now clinically questionable,[72,73] biological phenomena (*e.g.* the EPR effect of select solid tumors).[74] Following these principles, we have designed a simple and effective proof-of-concept liposome technology, composed of just two lipids, based on, and preceded by, a thorough understanding of both the physicochemical and *in vivo* nano-bio interactions involved. As such, it is our hope that this study, and in particular the tools and methods employed, will expedite a transition from the empirical design of increasingly complex nanomedicines to the rational design of new, simple and effective nanomedicines.[75]
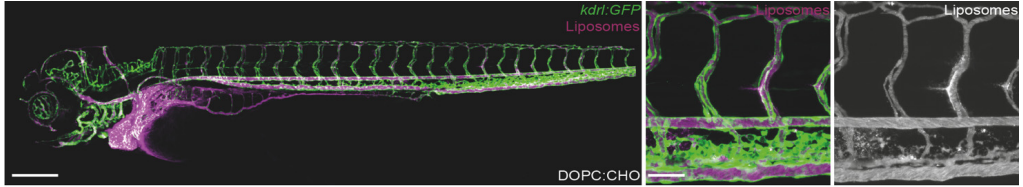
5.7 SUPPLEMENTARY FIGURES

Figure S5.1: Biodistribution of DOPC:cholesterol liposomes. Whole embryo and tissue level views of DOPC:cholesterol (1:1) liposome distribution in kdrl:GFP transgenic embryos (2 dpf), 1 hpi. DOPC:cholesterol liposomes freely circulate throughout the vasculature of the embryonic zebrafish and do not appreciably interact with blood-resident macrophages, SECs, or any other endothelial cell types of the embryo. Liposomes contained 1 mol% fluorescent lipid probe, DOPE-LR, for visualization. Scale bars: 200 μm (whole embryo); 50 μm (tissue level).

Figure S5.2: Biodistribution of cationic liposomes. Whole embryo and tissue level views of liposome distribution in kdrl:GFP transgenic embryos (2 dpf), 1 hpi of a.DOPC:DOTAP (1:1), b.DOPC:1(1:1) and c.DOPC:2(1:1) liposomes. All three cationic liposome formulations are visible as immobile fluorescent punctae associated with blood vessel walls throughout the vasculature of the zebrafish embryo and are largely removed from circulation. Liposomes contained 1 mol% fluorescent lipid probe, DOPE-LR, for visualization. Scale bars: 200 μm(whole embryo); 50 μm (tissue level).
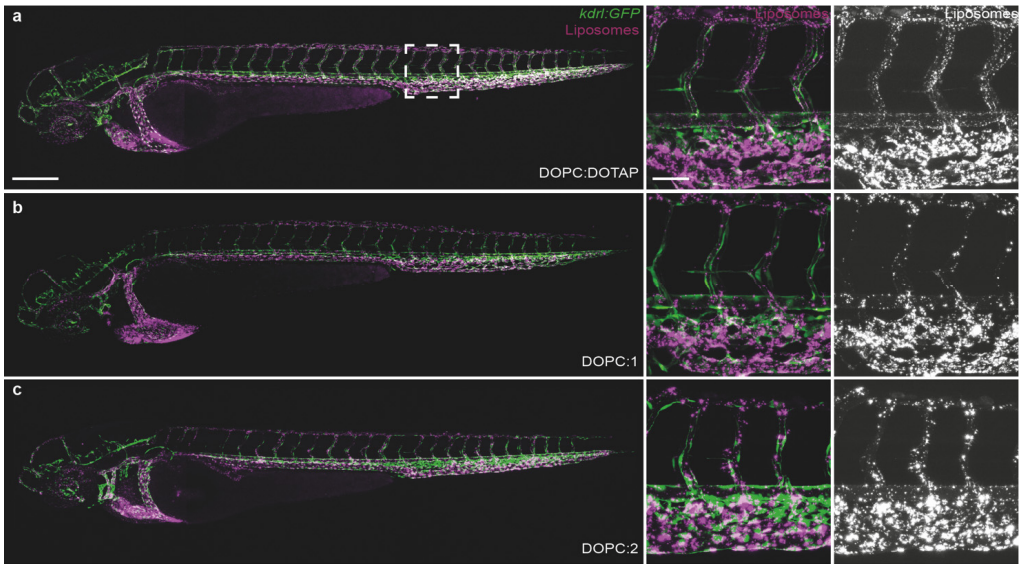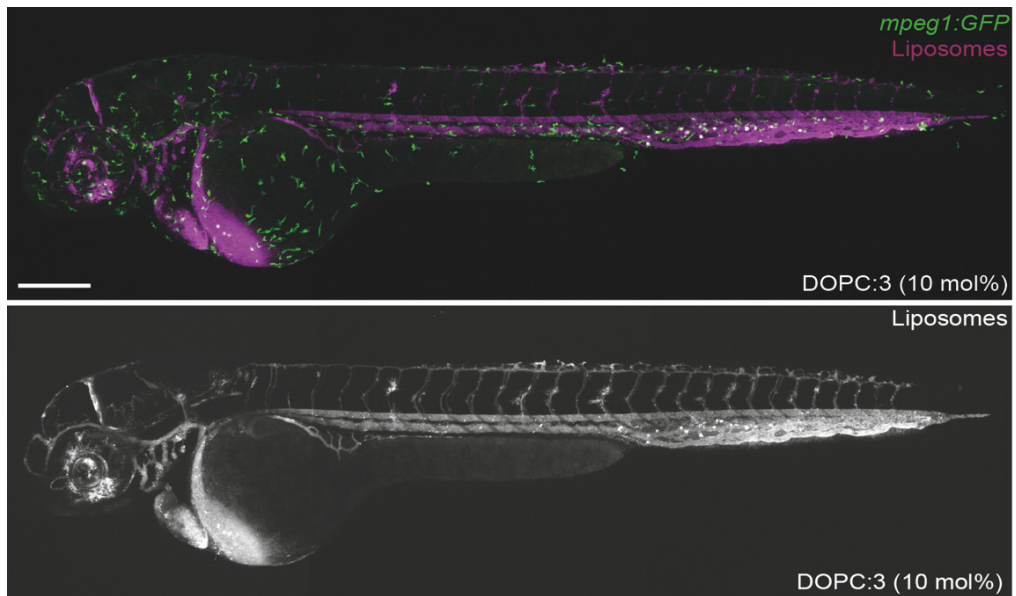
Figure S5.3. Uptake of DOPC:3 (9:1) liposomes within blood resident macrophages. Whole embryo views of DOPC:3 (9:1) liposome distribution in mpeg1:GFP transgenic embryos (2 dpf), 1 hpi. Extensive fluorescence co-localization of liposomes and blood resident macrophages can be observed primarily within the CHT of the embryonic fish. In addition, a significant fraction of liposomes remains in circulation. Liposomes contained 1 mol% fluorescent lipid probe, DOPE-LR, for visualization. Scale bar: 200 μm (whole embryo).
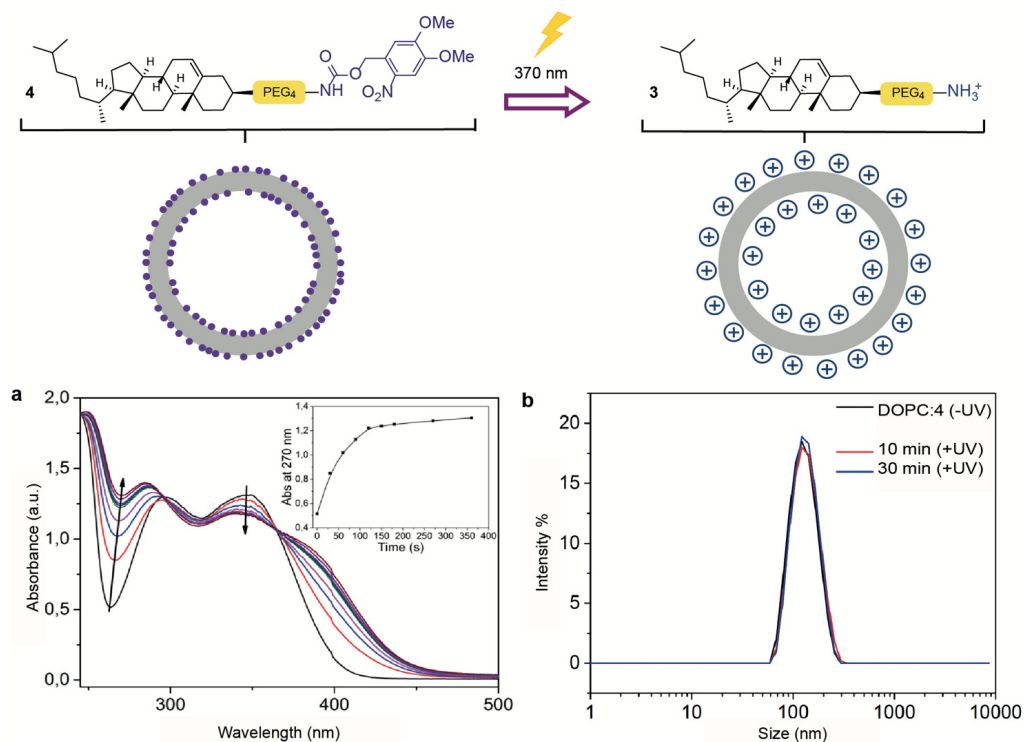
Figure S5.4. Photolysis of 4. a. Time evolution of the UV/Vis spectra of a solution of **4** (200 μM; H2O/MeCN/tBuOH, 1:1:1) during UV irradiation (370 ±7 nm, 202 mW cm-2). Inset: Time evolution of the UV absorbance at 270 nm. b. DLS spectra of DOPC:4(1:1) liposomes before and after light activation (10 and 30 min, 370 ±7 nm, 202 mW cm^{-2}) and surface charge switching.
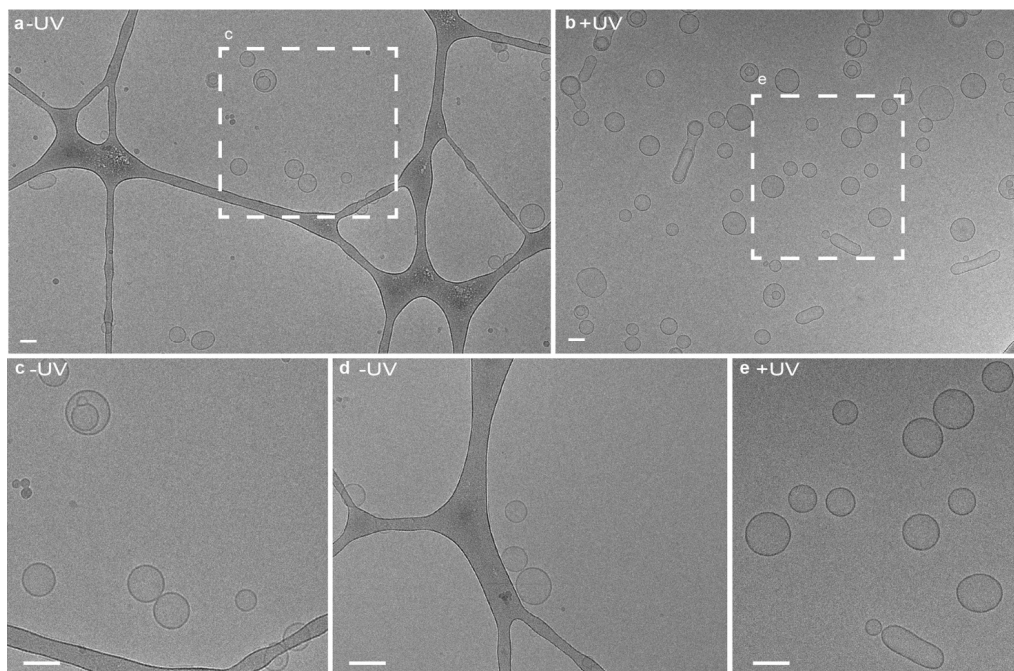
Figure S5.5. Low magnification cryoTEM images of DOPC:4 liposomes before and after UV. CryoTEM images of (empty) DOPC:4 liposomes (a,c,d)before and (b,e)after in situ irradiation (15 min, 370 ±7 nm, 202 mWcm-2). Note: Two individual cryoTEM panels of the same liposome sample are shown for the –UV sample as observed populations of DOPC:4liposomes, prior to UV irradiation, were consistently less than those after UV irradiation despite identical liposome concentrations.Scale bars: 100 nm.
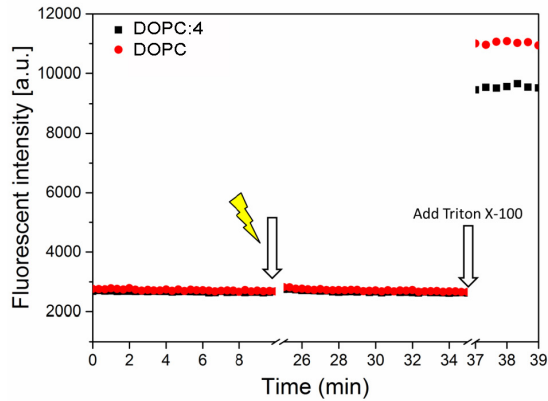
Supplementary Figure S5.6. Contents (SR-B) leakage. SR-B leakage (and dye de-quenching) from DOPC:4liposomes before and after UV irradiation. Fluorescence emission (excitation: 520 nm; emission: 580 nm) was measured every 20 s for 600 s, the sample was then irradiated (20 mins, 370 ±7 nm, 202 mW cm^{-2}) in a quartz cuvette and fluorescence re-measured for a further 600 s. Triton X-100 (10 μL, 1% w/v) was added to solubilize liposomes and release encapsulated SR-B. DOPC (100% DOPC content) was used as a control to demonstrate contents leakage was not dependent on UV irradiation alone.
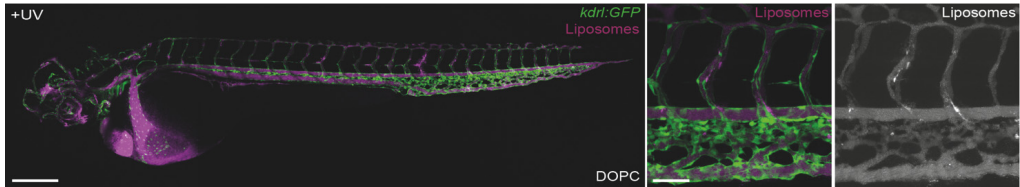
Supplementary Figure S5.7. Biodistribution of freely circulating DOPC liposomes following UV irradiation. Whole embryo and tissue level views of DOPC (100% DOPC content) liposome distribution in kdrl:GFPtransgenic embryos (2 dpf), 1 hpi. following UV in situirradiation (15 min, 370 ±7 nm, ~90 mW cm-2, ~2.4 J per embryo). The biodistribution of DOPC liposomes was unaffected by UV irradiation and liposomes remained in circulation.Liposomes contained 1 mol% fluorescent lipid probe, DOPE-LR, for visualization.Scale bars: 200 μm (whole embryo); 50 μm (tissue level).

| Composition | mol% | Buffer | Size | | Zeta potential (mV) |
			D_h (nm)	PDI	
	95:5	water	116.9	0.108	-7.70
	90:10	water	117.7	0.082	-1.05
DOPC:1	75:25	water	109.5	0.139	24.40
	50:50	water	119.7	0.068	30.13
	95:5	water	113.4	0.098	-9.25
	90:10	water	114.4	0.085	-4.15
DOPC:2	75:25	water	117.8	0.100	13.84
	50:50	water	117.4	0.101	38.10
	95:5	water	112.5	0.058	-8.25
	90:10	water	102.8	0.074	-4.94
DOPC:3	75:25	water	110.8	0.134	15.07
	50:50	water	122.7	0.156	48.53
DOPC:DOTAP	50:50	water	123.9	0.050	44.83
DOPC:4 (before UV)	50:50	HEPES	105.2	0.085	-8.07
DOPC:4 (after UV)	50:50	HEPES	115.2	0.101	25.93

Supplementary Table T5.1. Composition, size and measured zeta potentials of liposomes. All reported DLS measurements and zeta potentials are the average of three measurements. For measurements monitoring changes following light activation, liposomes were irradiated (20 mins, 370 nm± 7 nm, 202 mWcm-2) in quartz cuvettes, with the LED mounted at a distance of 1cm from the sample. Reported sizes and zeta potentials are for individual liposome samples but representative over multiple sample preparations. The number of individual liposome preparations varied depending on liposome formulation. In the case of DOPC:4 liposomes(prior to UV irradiation), sizes and zeta potentials did not significantly deviate across >5independent formulations. This included variations in DOPC supplier, CHCl3 lipid stock solutions and synthesized batches of 4. Batch-to-batch variation in the measured zeta potential of DOPC:4→3liposomes (i.e. after UV irradiation) resulted in a liposome surface charges ranging from +20 to +35 mV z-potential. The same liposome sample was measured before and after UV irradiation.

5.8 Bibliography

1. Zhao, Z., Ukidve, A., Krishnan, V. & Mitragotri, S. Effect of physicochemical and surface properties on in vivo fate of drug nanocarriers. *Adv. Drug Deliv. Rev.* **143**, 3–21 (2019).

2. Honary, S. & Zahir, F. Effect of zeta potential on the properties of nano-drug delivery systems - A review (Part 1). *Trop. J. Pharm. Res.* **12**, 265–273 (2013).

3. Elci, S. G. *et al.* Surface Charge Controls the Suborgan Biodistributions of Gold Nanoparticles. *ACS Nano* **10**, 5536–5542 (2016).

4. Xiao, K. *et al.* The effect of surface charge on in vivo biodistribution of PEG-oligocholic acid based micellar nanoparticles. *Biomaterials* **32**, 3435–3436 (2011).

5. He, C., Hu, Y., Yin, L., Tang, C. & Yin, C. Effects of particle size and surface charge on cellular uptake and biodistribution of polymeric nanoparticles. *Biomaterials* **31**, 3657–3666 (2010).

6. Zhang, Y. N., Poon, W., Tavares, A. J., McGilvray, I. D. & Chan, W. C. Nanoparticle-liver interactions: Cellular uptake and hepatobiliary elimination. *J. Control. Release* **240**, 332–348 (2016).

7. Gessner, A., Lieske, A., Paulke, B. R. & Müller, R. H. Functional groups on polystyrene model nanoparticles: Influence on protein adsorption. *J. Biomed. Mater. Res. - Part A* **65**, 319–326 (2003).

8. Gessner, A., Lieske, A., Paulke, B. R. & Müller, R. H. Influence of surface charge density on protein adsorption on polymeric nanoparticles: Analysis by two-dimensional electrophoresis. *Eur. J. Pharm. Biopharm.* **54**, 165–170 (2002).

9. Devine, D. V., Wong, K., Serrano, K., Chonn, A. & Cullis, P. R. Liposome-complement interactions in rat serum: implications for liposome survival studies. *BBA - Biomembr.* **1191**, 43–51 (1994).

10. Lundqvist, M. *et al.* Nanoparticle size and surface properties determine the protein corona with possible implications for biological impacts. *Proc. Natl. Acad. Sci. U. S. A.* **105**, 14265–14270 (2008).

11. Walkey, C. D. & Chan, W. C. W. Understanding and controlling the interaction of nanomaterials with proteins in a physiological environment. *Chem. Soc. Rev.* **41**, 2780–2799 (2012).

12. Lazarovits, J., Chen, Y. Y., Sykes, E. A. & Chan, W. C. W. Nanoparticle-blood interactions: The implications on solid tumour targeting. *Chem. Commun.* **51**, 2756–2767 (2015).

13. Aggarwal, P., Hall, J. B., McLeland, C. B., Dobrovolskaia, M. A. & McNeil, S. E. Nanoparticle interaction with plasma proteins as it relates to particle biodistribution, biocompatibility and therapeutic efficacy. *Adv. Drug Deliv. Rev.* **61**, 428–437 (2009).

14. Alexis, F., Pridgen, E., Molnar, L. K. & Farokhzad, O. C. Factors affecting the clearance and biodistribution of polymeric nanoparticles. *Mol. Pharm.* **5**, 505–515 (2008).

15. Semple, S. C., Chonn, A. & Cullis, P. R. Interactions of liposomes and lipid-based carrier systems with blood proteins: Relation to clearance behaviour in vivo. *Adv. Drug Deliv. Rev.* **32**, 3–17 (1998).

16. Cho, E. C., Xie, J. W., Wurm, P. A. & Xia, Y. N. Understanding the Role of Surface Charges in Cellular Adsorption versus Internalization by Selectively Removing Gold Nanoparticles on the Cell Surface with a I-2/KI Etchant. *Nano Lett.* **9**, 1080–1084 (2009).

17. Arvizo, R. R. *et al.* Effect of nanoparticle surface charge at the plasma membrane and beyond. *Nano Lett.* **10**, 2543–2548 (2010).

18. Verma, A. & Stellacci, F. Effect of surface properties on nanoparticle-cell interactions. *Small* **6**, 12–21 (2010).

19. Yue, Z. G. *et al.* Surface charge affects cellular uptake and intracellular trafficking of chitosan-based nanoparticles. *Biomacromolecules* **12**, 2440–2446 (2011).

20. Nazarenus, M. *et al.* In vitro interaction of colloidal nanoparticles with mammalian cells: What have we learned thus far? *Beilstein J. Nanotechnol.* **8**, 1477–1490 (2014).

21. Fröhlich, E. The role of surface charge in cellular uptake and cytotoxicity of medical nanoparticles. *Int. J. Nanomedicine* **7**, 5577–5591 (2012).

22. Kim, S. T., Saha, K., Kim, C. & Rotello, V. M. The role of surface functionality in determining nanoparticle cytotoxicity. *Acc. Chem. Res.* **46**, 681–691 (2013).

23. Goodman, C. M., McCusker, C. D., Yilmaz, T. & Rotello, V. M. Toxicity of gold nanoparticles functionalized with cationic and anionic side chains. *Bioconjug. Chem.* **15**, 897–900 (2004).

24. Bobo, D., Robinson, K. J., Islam, J., Thurecht, K. J. & Corrie, S. R. Nanoparticle-Based Medicines: A Review of FDA-Approved Materials and Clinical Trials to Date. *Pharm. Res.* **33**, 2373–2387 (2016).

25. Campbell, F. *et al.* Directing Nanoparticle Biodistribution through Evasion and Exploitation of Stab2-Dependent Nanoparticle Uptake. *ACS Nano* **12**, 2138–2150 (2018).

26. Hayashi, Y. *et al.* Differential Nanoparticle Sequestration by Macrophages and Scavenger Endothelial Cells Visualized in Vivo in Real-Time and at Ultrastructural Resolution. *ACS Nano* **14**, 1665–1681 (2020).

27. Yin, H. *et al.* Non-viral vectors for gene-based therapy. *Nat. Rev. Genet.* **15**, 541–555 (2014).

28. Friend, D. S., Papahadjopoulos, D. & Debs, R. J. Endocytosis and intracellular processing accompanying transfection mediated by cationic liposomes. *Biochim. Biophys. Acta - Biomembr.* **1278**, 41–50 (1996).

29. Zhao, Y. & Huang, L. Lipid nanoparticles for gene delivery. *Adv. Genet.* **88**, 13–36

(2014).

30.   Gao, X. & Huang, L. A novel cationic liposome reagent for efficient transfection of mammalian cells. *Biochem. Biophys. Res. Commun.* **179**, 280–285 (1991).

31.   Song, W. *et al.* The autophagic response to polystyrene nanoparticles is mediated by transcription factor EB and depends on surface charge. *J. Nanobiotechnology* **13**, 87–98 (2015).

32.   Klán, P. *et al.* Photoremovable protecting groups in chemistry and biology: Reaction mechanisms and efficacy. *Chem. Rev.* **113**, 119–191 (2013).

33.   Yun, S. H. & Kwok, S. J. J. Light in diagnosis, therapy and surgery. *Nat. Biomed. Eng.* **1**, 8 (2017).

34.   Moore, C. M., Pendse, D. & Emberton, M. Photodynamic therapy for prostate cancer - A review of current status and future promise. *Nat. Clin. Pract. Urol.* **6**, 18–30 (2009).

35.   Ibsen, S. *et al.* Localized in vivo activation of a photoactivatable doxorubicin prodrug in deep tumor tissue. *Photochem. Photobiol.* **89**, 698–708 (2013).

36.   Kim, T. Il *et al.* Injectable, cellular-scale optoelectronics with applications for wireless optogenetics. *Science (80-.).* **340**, 211–216 (2013).

37.   Rubinstein, N., Liu, P., Miller, E. W. & Weinstain, R. Meso-Methylhydroxy BODIPY: A scaffold for photo-labile protecting groups. *Chem. Commun.* **51**, 6369–6372 (2015).

38.   Goswami, P. P. *et al.* BODIPY-Derived Photoremovable Protecting Groups Unmasked with Green Light. *J. Am. Chem. Soc.* **137**, 3783–3786 (2015).

39.   Peterson, J. A. *et al.* Family of BODIPY Photocages Cleaved by Single Photons of Visible/Near-Infrared Light. *J. Am. Chem. Soc.* **140**, 7343–7346 (2018).

40.   Smith, A. M., Mancini, M. C. & Nie, S. Bioimaging: Second window for in vivo i maging. *Nat. Nanotechnol.* **4**, 710–711 (2009).

41.   Brittijn, S. A. *et al.* Zebrafish development and regeneration: New tools for biomedical research. *Int. J. Dev. Biol.* **53**, 835–850 (2009).

42.   Sieber, S. *et al.* Zebrafish as a preclinical in vivo screening model for nanomedicines. *Adv. Drug Deliv. Rev.* **151**, 152–168 (2019).

43.   Sieber, S. *et al.* Zebrafish as a predictive screening model to assess macrophage clearance of liposomes in vivo. *Nanomedicine Nanotechnology, Biol. Med.* **17**, 82–93 (2019).

44.   Kirby, C., Clarke, J. & Gregoriadis, G. Effect of the cholesterol content of small unilamellar liposomes on their stability in vivo and in vitro. *Biochem. J.* **186**, 591–598 (1980).

45.   Briuglia, M. L., Rotella, C., McFarlane, A. & Lamprou, D. A. Influence of cholesterol on liposome stability and on in vitro drug release. *Drug Deliv. Transl. Res.* **5**, 231–242 (2015).

46.   Fantini, J. & Barrantes, F. J. How cholesterol interacts with membrane proteins: An exploration of cholesterol-binding sites including CRAC, CARC, and tilted domains.

Front. Physiol. **4**, 31 (2013).

47. Olzmann, J. A. & Carvalho, P. Dynamics and functions of lipid droplets. *Nat. Rev. Mol. Cell Biol.* **20**, 137–155 (2019).

48. Batist, G., Barton, J., Chaikin, P., Swenson, C. & Welles, L. Myocet (liposome-encapsulated doxorubicin citrate): a new approach in breast cancer therapy. *Expert Opin Pharmacother* **3**, 1739–1751 (2002).

49. Chang, H. I. & Yeh, M. K. Clinical development of liposome-based drugs: Formulation, characterization, and therapeutic efficacy. *Int. J. Nanomedicine* **7**, 49–60 (2012).

50. Dong, Q., Svoboda, K., Tiersch, T. R. & Todd Monroe, W. Photobiological effects of UVA and UVB light in zebrafish embryos: Evidence for a competent photorepair system. *J. Photochem. Photobiol. B Biol.* **88**, 137–146 (2007).

51. Wang, R., Zhang, H., Du, J. & Xu, J. Heat resilience in embryonic zebrafish revealed using an in vivo stress granule reporter. *J. Cell Sci.* **132**, jcs234807 (2019).

52. Fieramonti, L. *et al.* Quantitative measurement of blood velocity in zebrafish with optical vector field tomography. *J. Biophotonics* **8**, 52–59 (2015).

53. Jiang, X. Y. *et al.* Quantum dot interactions and flow effects in angiogenic zebrafish (Danio rerio) vessels and human endothelial cells. *Nanomedicine* **13**, 999–1010 (2016).

54. Gomez-Garcia, M. J. *et al.* Nanoparticle localization in blood vessels: dependence on fluid shear stress, flow disturbances, and flow-induced changes in endothelial physiology. *Nanoscale* **10**, 15249–15261 (2018).

55. Rausch, K., Reuter, A., Fischer, K. & Schmidt, M. Evaluation of nanoparticle aggregation in human blood serum. *Biomacromolecules* **11**, 2836–2839 (2010).

56. Zhao, W., Zhuang, S. & Qi, X. R. Comparative study of the in vitro and in vivo characteristics of cationic and neutral liposomes. *Int. J. Nanomedicine* **6**, 3087–3098 (2011).

57. Pattipeiluhu, R. *et al.* Unbiased Identification of the Liposome Protein Corona using Photoaffinity-based Chemoproteomics. *ACS Cent. Sci.* **6**, 535–545 (2020).

58. Smedsrød, B. Clearance function of scavenger endothelial cells. *Comp. Hepatol.* **14**, s22 (2004).

59. Witzigmann, D., Hak, S. & van der Meel, R. Translating nanomedicines: Thinking beyond materials? A young investigator's reply to 'The Novelty Bubble'. *J. Control. Release* **290**, 138–140 (2018).

60. Sieber, S. *et al.* Zebrafish as an early stage screening tool to study the systemic circulation of nanoparticulate drug delivery systems in vivo. *J. Control. Release* **264**, 180–191 (2017).

61. Witzigmann, D. *et al.* Optimization-by-design of hepatotropic lipid nanoparticles targeting the sodium-taurocholate cotransporting polypeptide. *Elife* **8**, e42276 (2019).

62. McMillan, T. J. *et al.* Cellular effects of long wavelength UV light (UVA) in mammalian cells. *J. Pharm. Pharmacol.* **60**, 969–76 (2008).

63.   Narayanan, D. L., Saladi, R. N. & Fox, J. L. Ultraviolet radiation and skin cancer. *Int. J. Dermatol.* **49**, 978–986 (2010).

64.   Fenton, C. & Perry, C. M. Verteporfin: A review of its use in the management of subfoveal choroidal neovascularisation. *Drugs and Aging* **23**, 421–445 (2006).

65.   Blum, A. P. *et al.* Stimuli-responsive nanomaterials for biomedical applications. *J. Am. Chem. Soc.* **137**, 2140–2154 (2015).

66.   Mura, S., Nicolas, J. & Couvreur, P. Stimuli-responsive nanocarriers for drug delivery. *Nat. Mater.* **12**, 991–1003 (2013).

67.   Chen, X., Liu, L. & Jiang, C. Charge-reversal nanoparticles: novel targeted drug delivery carriers. *Acta Pharm. Sin. B* **6**, 261–267 (2016).

68.   Editorial. Time to deliver. *Nat. Biotechnol.* **32**, 961 (2014).

69.   Wicki, A., Witzigmann, D., Balasubramanian, V. & Huwyler, J. Nanomedicine in cancer therapy: Challenges, opportunities, and clinical applications. *J. Control. Release* **200**, 138–157 (2015).

70.   Venditto, V. J. & Szoka Jr., F. C. Cancer nanomedicines: so many papers and so few drugs! *Adv Drug Deliv Rev* **65**, 80–88 (2013).

71.   Immordino, M. L., Dosio, F. & Cattel, L. Stealth liposomes: review of the basic science, rationale, and clinical applications, existing and potential. *Int. J. Nanomedicine* **1**, 297–315 (2006).

72.   Wilhelm, S. *et al.* Analysis of nanoparticle delivery to tumours. *Nat. Rev. Mater.* **1**, 16014 (2016).

73.   Sindhwani, S. *et al.* The entry of nanoparticles into solid tumours. *Nat. Mater.* **19**, 566–575 (2020).

74.   Maeda, H., Nakamura, H. & Fang, J. The EPR effect for macromolecular drug delivery to solid tumors: Improvement of tumor uptake, lowering of systemic toxicity, and distinct tumor imaging in vivo. *Adv. Drug Deliv. Rev.* **65**, 71–79 (2013).

75.   Hua, S., de Matos, M. B. C., Metselaar, J. M. & Storm, G. Current trends and challenges in the clinical translation of nanoparticulate nanomedicines: Pathways for translational development and commercialization. *Front. Pharmacol.* **9**, 790 (2018).

76.   Kemmer, G. C. *et al.* Lipid-conjugated fluorescent pH sensors for monitoring pH changes in reconstituted membrane systems. *Analyst* **140**, 6313–6320 (2015).

77.   de Belder, A. N. & Wik, K. O. Preparation and properties of fluorescein-labelled hyaluronate. *Carbohydr. Res.* **44**, 251–257 (1975).

78.   Aleström, P. *et al.* Zebrafish: Housing and husbandry recommendations. *Lab. Anim.* **0**, 1–12 (2019).

79.   Jin, S. W. S.-W., Beis, D., Mitchell, T., Chen, J. N. & Stainier, D. Y. R. Cellular and molecular analyses of vascular tube and lumen formation in zebrafish. *Development* **132**, 5199–5209 (2005).

80.   Ellett, F., Pase, L., Hayman, J. W., Andrianopoulos, A. & Lieschke, G. J. mpeg1

promoter transgenes direct macrophage-lineage expression in zebrafish. *Blood* **117**, 49–56 (2011).

81.   Weinstein, B. M., Stemple, D. L., Driever, W. & Fishman, M. C. Gridlock, a localized heritable vascular patterning defect in the zebrafish. *Nat. Med.* **1**, 1143–1147 (1995).

82.   Schindelin, J. *et al.* Fiji: an open-source platform for biological-image analysis. *Nat. Methods* **9**, 676–82 (2012).

83.   Schneider, C. A., Rasband, W. S. & Eliceiri, K. W. NIH Image to ImageJ: 25 years of image analysis. *Nat. Methods* **9**, 671–675 (2012).

84.   Van den Broek, B., Oosterkamp, T. H. & van Noort, J. A Multifocal Two-Photon Microscopy Setup for Parallel 3D Tracking of Gold Nanorods. *Biophys. J.* **98**, 178a (2010).

Chapter 6

The biodistribution and immuno-responses of differently shaped non-modified gold particles in zebrafish embryos

Chapter 6 highlights a study which demonstrates the capabilities of our TPMM in a real-case scenario. The study was performed in zebrafish embryos, where to two-photon excitation and the high temporal resolution enabled imaging of particle distribution in real-time.

Author contributions:
M.V. conceived the research
M.v.P, M.P, R.V designed the experiments
M.v.P, M. P., R.V. carried out the experiments
M.v.P, M. P., R.V. analyzed the data.
R.V and S.J.T.v.N designed and build the microscope
M.v.P. wrote the manuscript with feedback from all authors
M.V. and J.v.N. supervised the research

6.1 PREFACE

For another application of the novel two-photon microscope technique we focus on the bio-distribution and immune-response of differently shaped gold nanoparticles (AuNPs) in zebra fish embryos. The unique properties of AuNPs make them interesting materials to work with, however their effects on the environment and on the health of organisms has yet to be fully understood. Imaging of AuNPs in live samples is difficult however by their weak one-photon luminescence brightness which impairs visibility in confocal microscopy. Confocal microscopy was used first to image fluorescently tagged macrophages, which are indicators of the immuno-response. However, to directly resolve where AuNPs are located in the zebrafish embryo, and whether they are being taken up by macrophages, a different imaging modality was required.

As gold nanoparticles feature impressive brightness upon two-photon excitation, as can also been seen in chapter 2 of this thesis, our two-photon multifocal microscope (TPMM) was especially well suited for measuring their distribution. Imaging the tail of the embryo we could discern individual spots, likely originating from single AuNPs, in real-time. Moreover, the high temporal resolution allowed us to image a macrophage which had taken up numerous NPs as it travelled along an artery wall. Direct imaging of AuNP macrophage uptake corroborated the confocal images, visualizing the first response of the immune system of the embryo reacts to the AuNPs and actively tries to dispose them.

These results illustrate how real-time imaging combined with two-photon excitation can provide insight in fast (biological) processes which would normally be eluded from detection. Moreover, it further shows how NPs are excellent contrast agents in two-photon microscopy. Overall, TPMM is an excellent imaging modality to obtain a more detailed understanding of the pathological effects of nanoparticles, like AuNPs, in live organisms.

6.2   INTRODUCTION

A central paradigm of toxicology is that toxic effects induced by a xenobiotic are due to a cascade of processes including Adsorption at sites of uptake, Distribution to target organs where the toxicant potentially induces a response, and ultimate storage in either the target organ or in any other organ, followed by Metabolization and Excretion (ADME)[1]. To make the chain of events even more complicated, it is to be acknowledged that different chemicals commonly follow different pathways, although they might end up in the same storage organ or tissue[2]. The myriad of processes may lead to various adverse effects, which makes it important to understand the mechanistic pathways and the main parameters affecting toxicity. While *in vitro* assays provide only limited information about the ADME of compounds, *in vivo* studies such as with zebrafish embryos provide more in depth insights[3] because cells in living organisms communicate and are specialized to perform specific essential functions. Using either *in vitro* or *in vivo* methods, it is key to understand the factors influencing (parts of) the ADME of xenobiotic compounds.

In the case of nanoparticles (NPs), uptake across epithelial membranes is dictated (among other factors) by size, shape and surface charge [4]. Just as for size [4], both the shape of particles as well as the accessory surface area influence how particles behave in exposure media [5]. Particle aggregation and dissolution for those particles that can dissolve (which is not the case for gold nanoparticles (AuNPs)) are in general the most important fate-determining processes. While size has been shown to influence uptake and biodistribution in zebrafish embryos [6,7] the impact of different nano-shapes on biodistribution is less investigated. Particle shape can be an important factor for cellular uptake, circulation time within the organism, and subsequently the biodistribution of nanoparticles [5]. In general, small, elongated nanoparticles are more easily taken up by cells than large and flat individual, non-aggregated particles [8]. This same tendency was found for the endpoint of biodistribution, as nanorods distributed throughout tumor tissues, whereas gold spheres and discs were located only at the surface of the tumor [9]. Moreover, the aspect ratio of rods was found to determine uptake and internal distribution: short rods were taken up faster and were trapped in the liver, while longer rods with a smaller aspect ratio showed lower uptake efficiency and were trapped in the spleen of mice [10–12]. Additionally, sharp gold nanostars can pierce the membranes of endosomes and escape to the cytoplasm regardless of their surface chemistry, size or composition [11,13].

As a noble metal with low toxicity, gold has been an ideal material in nanomedicine for diagnostic and therapeutic purposes such as imaging agents and drug-delivery systems [11,14,15]. Specifically coating/labeling the gold nanoparticles enables researchers to guide the particles to the desired target [9]. What happens to the gold nanoparticle when the coating or labeling is released is hardly studied, although some studies found that the coating can change [16] and even separate from the particles [17] under *in vivo* conditions. Gold is found to be biocompatible [15,18],

and its nanoform is categorized as an active and insoluble material which promotes cellular effects and/or mobility in organisms [19]. Therefore, it can be used as a platform for delivery in nanomedicine and for *in vivo* imaging experiments without major adverse effects. Due to their distinctive plasmonic resonances [20], high Rayleigh scattering [18], and resistance against photo-bleaching and photo-blinking [20], are gold particles very suitable for a variety of imaging techniques. Additionally, gold particles can be synthesized relatively easily, with control of their size and shape [20]. The fact that gold nanoparticles are synthesized in different shapes, combined with their inert properties makes gold the perfect material for testing the effect of shape on particle toxicity.

In this study, we aimed to determine the biodistribution and subsequent adverse responses to differently shaped, non-modified gold particles in zebrafish embryos. We used the word trafficking for active movement across the body of the organism, and the word biodistribution for where the AuNPs are located in the ZF embryo at a given time (static measurement 48 hours after exposure). The underlying research questions were:

1. Do differently shaped AuNPs induce different biodistribution patterns and hence do they accumulate in different target organs?

To answer this research question, the biodistribution of AuNPs was measured after 2 days of NP exposure. Our assumption is that once particles are accumulated in organs, due to agglomeration they are no longer available for biodistribution since biodistribution is limited to particles and agglomerates smaller than 250 nm [21]. By imaging after 2 day of exposure the AuNPs can be visualized in the target organs as sufficient uptake of AuNPs is expected to have taken place after this exposure duration without experiencing any morphological malformation [14,20].

2. What type of trafficking can we identify for AuNPs?

In general, nanoparticle clearance can occur via the hepatobiliary pathway or via the kidneys [22]. For the first pathway, uptake by macrophages is essential, whereas clearance via the urine occurs without intervention of macrophages. By tracking the movement of particles directly after internalization (simulated by microinjection), the initial clearance mechanism of the organism can be visualized.

3. Is the difference in biodistribution patterns also reflected in different response patterns?

   As shown by previous research [23], immune responses, both local and systemic, are valuable endpoints for monitoring biodistribution. We therefore investigated the extent of recognition of the particles by neutrophils and macrophages.

4. Is the exposure to AuNPs also translated into effects on the behaviour of hatched zebrafish embryos?

   In ecotoxicology, assessment of the behavioral response of hatched zebrafish embryos after exposure is a commonly used sub-lethal and sensitive apical endpoint [24]. By investigating sensitive sub-lethal endpoints, early signs of toxicity can be detected.

6.3 MATERIALS AND METHODS

Preparation of particle suspensions. Gold nanospheres and nano-urchins with nominal sizes of 60 nm were purchased from Sigma Aldrich (Zwijndrecht, The Netherlands). The particles were suspended in 0.1 mM phosphate buffered saline. Gold nanorods with a nominal size of 40 x 60 nm, stabilized with polyvinylpyrrolidone and suspended in water, were purchased from Nanopartz Inc. (Loveland, USA). Gold nano-bipyramids with a nominal size of 45 x 140 nm were purchased from Nanoseedz, ltd. (Hong Kong, China). The bipyramids were stabilized with polyethylene glycol in water and rinsed before use with demineralized water. Exposure suspensions were prepared by adding the purchased stock suspensions to egg water (60 µg/ml Instant Ocean Sea Salt, Sera GmbH, Heinsberg, Germany). All dilutions were freshly prepared and sonicated for 10 minutes in an ultrasonic water bath (USC200T, VWR, Amsterdam, The Netherlands), after which the embryos were immediately exposed.

Physicochemical characterization. The size and morphology of the suspended AuNPs were characterized using transmission electron microscopy (TEM; JEOL 1010, JEOL Ltd., Tokyo, Japan) after 1 hour of incubation in egg water. Dynamic light scattering assessments were performed on a Zetasizer Nano-ZS instrument (Malvern Instruments Ltd, Malvern, UK) to detect the size distribution and zeta-potential of Au NP suspensions in egg water at 0 h, 1 h and 24 h.

Zebrafish husbandry. Zebrafish were handled as described by animal welfare regulations and maintained according to standard protocols (http://ZFIN.org). Adult zebrafish were maintained at 25 ± 5 ˚C in a 14 h: 10 h light-dark cycle. Fertilized zebrafish eggs were obtained from Caspar zebrafish (*Danio rerio*), MPEG1.4:mCherry/MPX:GFP zebrafish and KDRL:GFP zebrafish, dependent on the analysis.

Waterborne exposure of zebrafish embryos to AuNPs. The OECD guideline 157 for the standard ZebraFish Embryo Test-protocol [25] was modified as described by Van Pomeren, et al[7]. We used the exposure window from 3 days post fertilization (dpf) till 5 dpf, since this exposure window was found to be associated with the highest amount of uptake[7]. Embryos were exposed to nominal concentrations of 5 mg/L. At this concentration, we expect to obtain sufficient signal for imaging while not observing any morphological malformations [14,20,27]. As a result, the concentration applied is expected to be too low to observe any sub-lethal effects as well.

Confocal microscopy. During the exposure period, Casper zebrafish embryos were examined daily to check fitness (malformations and mortality) using a dissecting microscope. During the final examination, embryos were rinsed three times with egg water, kept under anesthesia

(0.02% Tricaine, Sigma) in egg water and embedded with low melting agarose (CAS 39346-81-1, Sigma Aldrich, Zwijndrecht). Fitness was not affected during this inspection. Final examination was performed using the reflection of Au NPs according to the method described by Kim et al.[28] using a confocal microscope (Zeiss LSM5 Exciter).

Stereo fluorescence microscopy. Biodistribution and subsequent identification of target organs can be visualized by examination of the immune responses that are locally induced by the particles [23]. Similar to the analysis described above and applying the same exposure period, transgenic MPEG1.4:mCherry/MPX:GFP zebrafish embryos were examined daily. During the final examination, embryos were rinsed three times with egg water, kept under anesthesia (0.02% Tricaine, Sigma) in egg water and imaged in an agarose (CAS 9012-36-6**,** Sigma Aldrich, Zwijndrecht) covered Petri dish. Final examination was performed using the fluorescent signal of the fluorescent-labeled neutrophils (GFP) and the macrophages (mCherry) with a fluorescence stereo microscope (MZ 205 FA, Leica). Doing so, each image contains three channels: bright field, fluorescent green (GFPgreen/neutrophils), and fluorescent red (DRSred/macrophages). Using ImageJ software [29], images were assessed for fluorescence intensity and a corrected total cell fluorescence (CTCF) value was calculated [30].

Two photon multifocal laser microscopy. In order to investigate the clearance mechanism of the organism, the time dynamics of nanoparticles was tracked in order to follow the clearance. The time dynamics of particle trafficking was visualized with a two photon multifocal laser microscope [31]. For this, the particle with the most optimal optical properties was chosen, as this method is only suited for particles with a plasma resonance close to 830 nm. For our selection of particles, the nano-bipyramids showed to be best suited since their plasma resonance was 850 nm. A high, non-environmental relevant concentration (19 mg/L) was selected to guarantee good visibility. To assure particle presence in the organism, 3 day old transgenic KDRL:GFP zebrafish embryos were injected in the duct of Cuvier with 2nL nano-bipyramid gold NPs using a Femtojet injector (Eppendorf), half an hour prior to scanning. During the scanning, embryos were kept under anesthesia (0.02% Tricaine) in egg water while they were embedded in 0.4% low melting agarose. The success of the injections was assessed by looking at the absence of leakage to the yolk and the displacement of blood cells by injection-fluid.

Behavioral analysis. Since gold rarely induces lethal effects at the tested concentration, behavioral analysis was chosen as a more sensitive toxicity endpoint, as commonly used in neurotoxicity [24]. Before behavioral analysis, all living embryos (120 hpf) were evaluated in terms of normal development, morphological defects and vitality using a stereo dissecting microscope. The behavioral analysis was performed by subjecting the embryos to the light–dark challenge test as modified according to Hua et al.[23]. Low locomotor activity of zebrafish embryos occurred under light exposure (basal phase). A sharp spike of fast swimming activity

was induced by a sudden transition to dark, lasting less than 2 s (challenge phase)[23]. A total of 22 min of recording was used: 10 minutes acclimatization, 4 minutes basal phase, 4 minutes challenge phase and 4 minutes recovery phase. The total distance moved and the velocity of each zebrafish embryo was tracked using the Zebrabox (Viewpoint, Lyon, France) and analyzed using EthoVision software (Noldus Information Technology, Wageningen, The Netherlands).

Statistical analysis. Data of the behavioral test and the immune responses (represented as CTCF) were presented as mean ± standard error of the mean (SEM). The homogeneity of variance was checked using the SPSS 23 software package. The significance level for all calculations was set at $p < 0.05$. Significant differences between the different exposures within each phase were tested using a one-way analyses of variance (ANOVA) with Tukey's multiple comparison post-test.

6.3 RESULTS

6.3.1 PHYSICOCHEMICAL CHARACTERIZATION

Using TEM images (Figure 6.1), size and shape of the particles were verified. According to the pictures, no large size deviations nor impurities were observed. This was in agreement with the information received from the producers.

Hydrodynamic size measurements obtained by means of DLS showed little variation over time (Table 6.1). This was with the exception of the nano-Au bipyramids as these particles did not follow this general pattern and formed aggregates immediately after preparation of the test suspension, which became even larger over time. This observation is probably related to the observation of the zeta potential being close to zero, which is indicative of lack of repulsive forces.
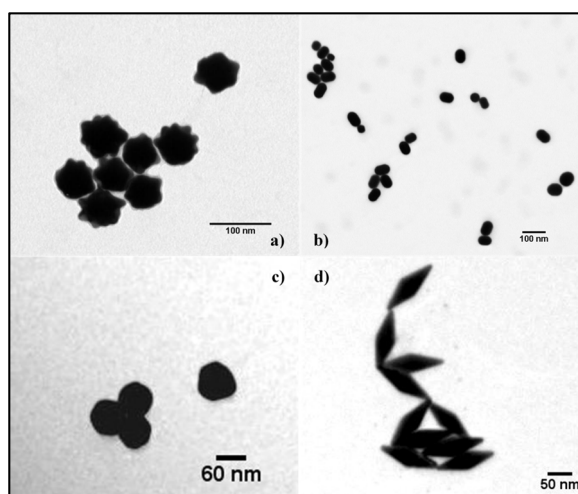

Figure 6.1: TEM images of the four tested nanogold particles. (a) nano-urchins (b) nanorods (c) nanospheres and (d) nano-bipyramids.

	Zeta potential (mV ± SD)				Size distribution (nm ± SD)		
	0h	1h	24h		0h	1h	24h
Nanosphere	-24 ± 2	-28 ± 4	-18 ± 5		74 ± 0	76 ± 2	79 ± 0
Nanorod	-27 ± 1	-28 ± 0	-11 ± 1		71 ± 0	73 ± 0	79 ± 3
Nano-urchin	-8 ± 1	-9 ± 0	-30 ± 1		88 ± 6	98 ± 6	72 ± 1
Nano-bipyramid	9 ± 1	3 ± 1	-4 ± 1		501 ± 45	1158 ± 151	5014 ± 2138

Table 6.1: Zeta potential and size distribution as measured by DLS of the different gold nanoparticles over time.

6.3.2 BIODISTRIBUTION OF AuNPs

Using a confocal laser-scanning microscope, clusters of nanoparticles could be visualized in exposed zebrafish embryos. Independent of the shape, every type of particle was observed to be present in the intestinal tract (examples of confocal images of particles in the intestinal tract can be found in the supplementary materials). Nanorods were found to efficiently distribute to other digestive organs of the embryo as well, such as the liver/gallbladder (Figure S6.1). For most of the particle shapes, clusters were also found in most probably a blood vessel near the eye (Figure 6.2).
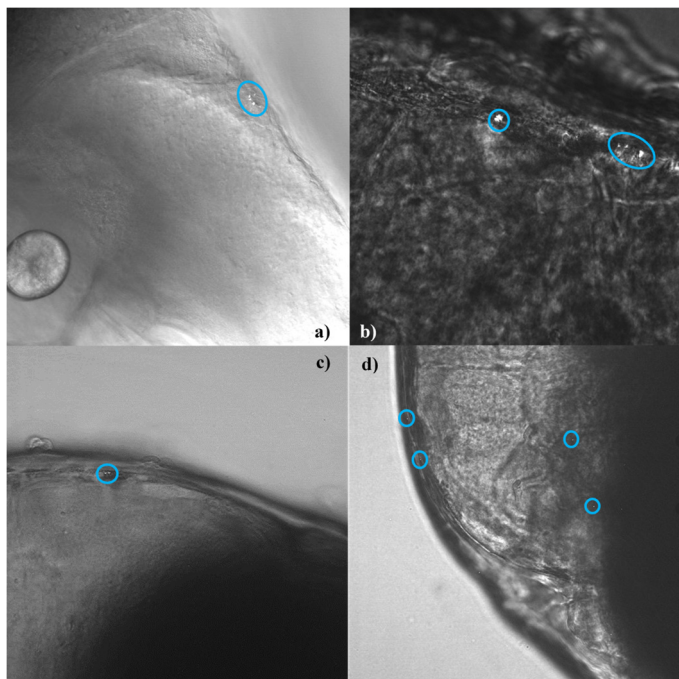

Figure 6.2: Confocal images showing particle clusters in blood vessels near the eye of the zebrafish embryo (5 dpf) for different nanogold particles. a) nanorods b) nano-urchins c) nanospheres and d) nano-bipyramids.

6.3.3 TRAFFICKING OF AUNPS

For the optical most optimal nanoparticles, the nano-bipyramids, the time dynamics of biodistribution were examined. After intravenous injection, the particles were found to be distributed throughout the tail of the embryo (Figure 6.3). As can be observed from Figure 6.3, free particles and clusters distributed through the bloodstream. Particles are thereafter phagocytosed by macrophages. A macrophage loaded with particles can be observed in the tissue (confirmed by the fluorescent signal), which moved over the tissue to the vein (Figure 6.3). From there, it will go to the liver or spleen to be cleared from the organism [33].
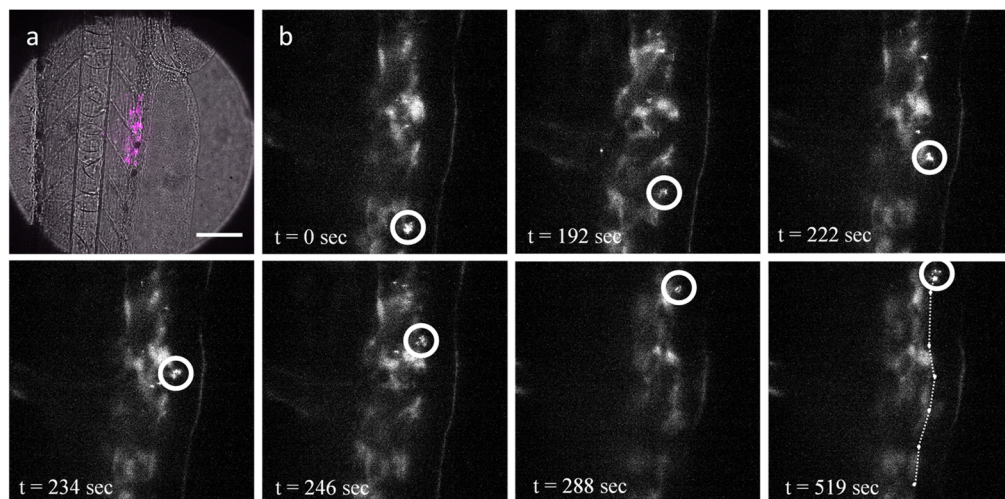

Figure 6.3: Macrophage filled with gold bipyramids moves along the artery wall after which it is released into the bloodstream. a) Transmission image with emission overlay (magenta) of the imaged region (scale bar 2 μm). b) Macrophage (white circle) moves along the artery wall, at t = 519 seconds the macrophage releases from the artery wall into the bloodstream.

6.3.4 IMMUNO-RESPONSES

Upon inspection of the response of the immune system of the whole organism and of responses in specific regions (Figure 6.4 and Figure S6.2), different response patterns were observed. In case of the neutrophils (Figure 6.4; a, c, e), the nano-urchins, nanorods and nano-bipyramids did not induce any visible effect on the immune system at the whole organismal scale (Figure 6.4a) and in the tail (Figure 6.4c).
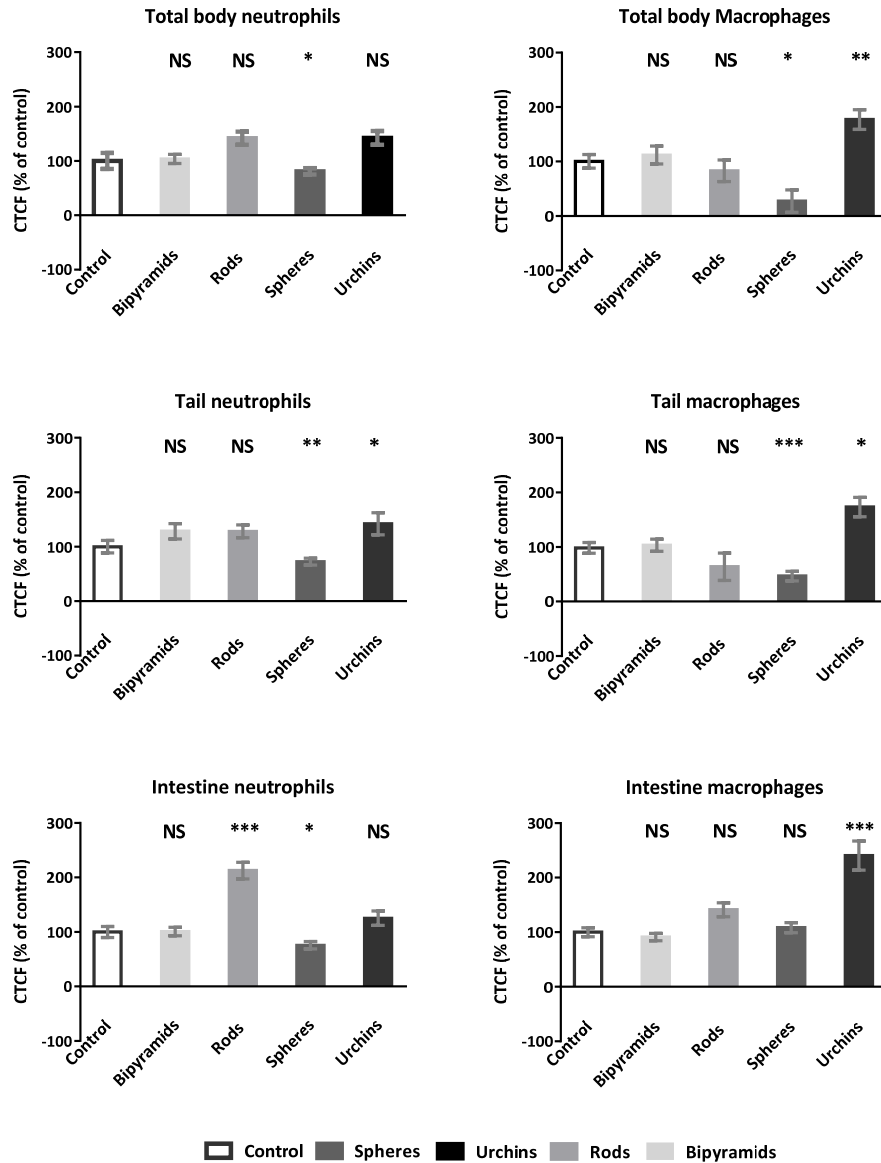
Figure 6.4: Abundance (relative to control) of neutrophils (a, c and e) and macrophages (b, d and f) in 5 dpf zebrafish embryos after exposure to differently shaped nanogold particles. The abundance in three different sections is provided: Whole organism (a and b), tail section (c and d) and intestine region (e and f). Asterisks indicate statistically significant differences to controls (*p < 0.05, **p < 0.01, and ***p < 0.001). Data are provided as mean and standard error of the mean (n=20).

However, embryos exposed to spherically shaped gold particles induced a reduced amount of neutrophils at the whole organism scale and in the tail region. Examination of the intestine (Figure 6.4e) learned that more neutrophils were present in embryos that were exposed to rods (compared to the control), whereas the embryos exposed to nanospheres again reduced the amount of neutrophils.

For the macrophages (Figure 6.4; b, d, f) at each examination level (whole body (b), tail (d) and intestine (f)) the embryos exposed to urchin shaped nanogold were observed to have a higher level of macrophages. For the embryos that were exposed to spherical nanogold particles, the overall abundance of macrophages was decreased for both the whole body and the tail region, whereas the intestine region had macrophages abundances that were comparable to the control.

The differently shaped particles showed different distribution patterns into the main digestive organs: gall bladder, pancreas and liver (Table 6.2). Embryos that had a high expression of either neutrophils or macrophages in the intestinal region, generally showed high abundance of immune cells in the gallbladder (Figure 6.5a), pancreas and / or liver (Figure 6; different combinations have been observed). The majority of the particles were transported to the pancreas, except for the nanospheres. Nanospheres were predominantly found within the liver. Nanospheres and nano-urchins were thereafter mostly found in the gall bladder, whereas nanorods and nano-bipyramids distributed mostly to the liver.
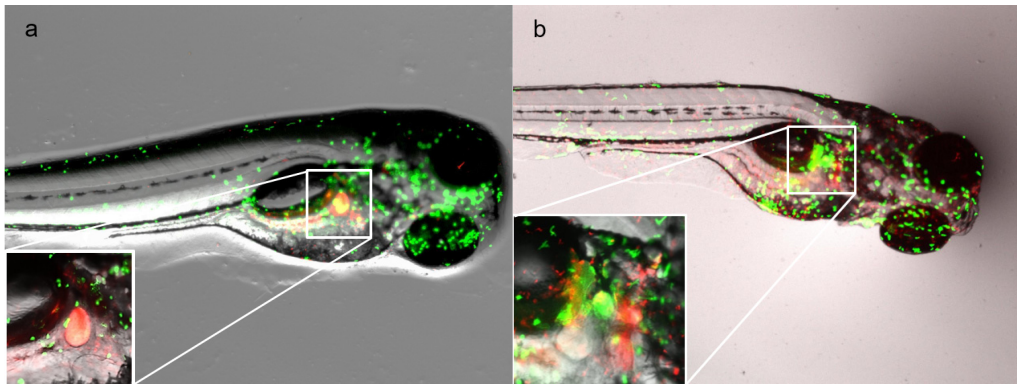
Figure 6.5: Images of fluorescent neutrophils (green) and macrophages (red) in zebrafish embryos after exposure to gold nano-bipyramids. The insets are providing further details using 2 times (*a*) and 6 times (*b*) magnification.

The observed distribution patterns (Table 6.2) were consistent with the observed abundance of immune cells (expressed as CTCF value) in the embryos (Figure 6.4): the nanorods and nano-urchins showed a high increase of the CTCF value in the intestine region and both shapes showed high abundancy of immune cells in the pancreas. In some cases, the immune cells accumulated more at the top of the pancreas, at the islets of Langerhans, rather

than accumulating in the whole pancreas (Figure 6.5b) For the nano-bipyramids, no obvious relation between the total amount of immune cells and the presence of immune cells in specific organs was observed. Exposure to nanospheres induced a reduction in the total amount of immune cells in the body as well as a strong reduction in fluorescent signal in the tail. However, no difference compared to the control was observed in fluorescent signal in the intestine region. This suggests that there was an overall reduction in the amount of immune cells and that the majority of the immune cells were translocated from the tail to the digestive organs and intestine.

	Gall bladder	Pancreas	Liver
Nanospheres	41 %	35 %	71 %
Nanorods	32 %	74 %	37 %
Nano-urchins	20 %	80 %	5 %
Nano-bipyramids	16 %	79 %	57 %

Table 6.2: Percentage of fish that showed high numbers of immune cells in the specified organs (n=19±1). Note that one single fish might be scored for multiple organs.

6.3.5 BEHAVIORAL RESPONSE

In order to investigate induced toxic effects related to the shape dependent biodistribution, a behavioral test was performed. The results of the behavior test showed that in the base phase a slight difference was observable with regard to the total distance that the hatched embryo moved (Figure 6.6). For embryos exposed to urchin shaped particles, the total distance moved was increased in the base phase whereas the other exposed groups did not show large differences, not even for the nano-bipyramids that also were predominantly found in the pancreas. In addition, accumulation of spherical particles in a high-energy demanding organ as the liver did not reduce the activity of the embryos. In the challenge phase, when stress was induced, embryos exposed to nano-bipyramids showed a reduced movement distance (Figure 6.6) and subsequent velocity (data not shown). On the other hand, the embryos exposed to nanorods traveled a longer distance per time interval and in total (Figure 6.6). In the recovery phase, the same tendency for the embryos exposed to nano-urchins as in the base phase was observed, although the effect is not so profound.
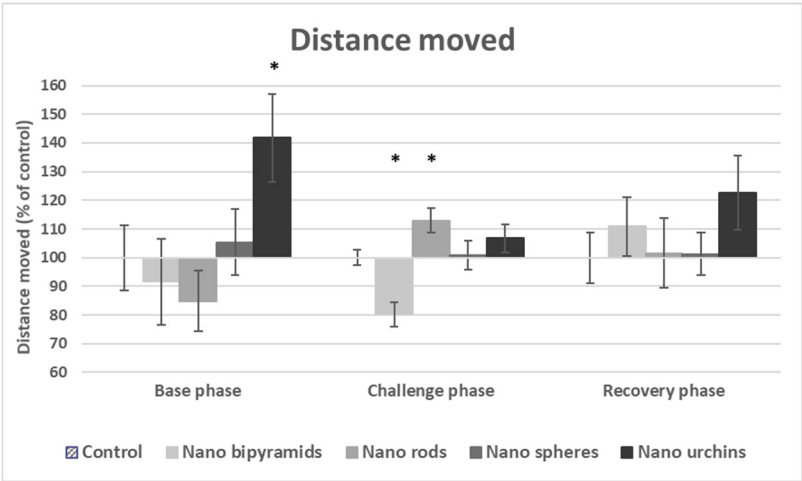
Figure 6.6: Total distance moved of 5dpf embryos exposed to different nanogold particles. Results are provided per stage of the behavior test (mean and standard error of the mean). Asterisks indicate significant differences to controls (*p < 0.05, **p < 0.01, and ***p < 0.001).

6.4 DISCUSSION AND CONCLUSION

The first question we aimed to answer is whether differently shaped Au-NPs are differently distributed within zebrafish embryos and whether the NPs reach different target organs. All shapes were found to accumulate on the intestinal mucosa. Yet adsorption to the intestinal mucosa is still not to be considered as either uptake or biodistribution. Evidence of the particles actually crossing the intestinal mucosa is provided by their presence in other digestive organs (such as the liver and gall bladder) as proven by confocal imaging. It should be noted that all differently shaped gold particles were found to be present in a blood vessel near the eye of the embryo. This is in line with our previous study[7], using fluorescent polystyrene (PS) particles with comparable size as the AuNPs tested in this study. Exposure to smaller (1.3 nm) AuNPs resulted in disruption of the growth and pigmentation of the eye of the embryos [34]. Due to high auto-fluorescence levels in the eye in our study, it was not feasible to examine the accumulation of gold in the eye. However, the presence and the mobility of the gold NPs in the blood veins, as shown by both our confocal imaging techniques, indicates a possibility of distribution throughout the organism and thus translocation to the eye.

Typically, xenobiotic particles that are taken up in the blood system are distributed throughout the organism and inflict harm to their host. To reduce or prevent harm, organisms evolved mechanisms to remove these particles from their body. For our second research question, we aimed to identify the clearance mechanism of the particles. As we saw in the time dynamic recording of the nano-bipyramids (Movie S1, SM), particles are taken up by macrophages and thereafter trafficking via the mononuclear phagocytic system (MPS). In general, spherical shaped particles show the fastest clearance rate compared to rod shaped particles [11], thereby favoring the hepatobiliary pathway over clearance via the kidneys [22,27]. Moreover, the clearance rate is further reduced when the particles are disk- or lamella-shaped [11], become more elongated [35], or develop sharp structures [13]. Once particles are taken up in macrophages, clearance via the MPS continues via the spleen, liver and eventually via bile trough the gallbladder into the digestive tract and feces [33]. In 5 dpf zebrafish embryos, the function of the spleen – which is not yet developed – is taken over by the pancreas [36]. Indeed, the pancreas, liver, gall bladder and digestive tract were found to contain nanoparticles. Just as for PSNPs [23], gold particles induced intestinal inflammation. Even more, induced activity of the innate immune system in the digestive organs was observed, which confirms the presence of the particles in these organs.

By using the immune response of the embryos, we aimed to answer our third research question: is the biodistribution reflected in different response patterns. Actually, a shape dependent pattern can be observed. Specifically focusing on the gall bladder, liver and pancreas, the distribution of the particles over these organs depends on particle shape. The differences across the distribution patterns indicate that the particles behave slightly different, although they

eventually reach the same target organs – yet in different ratios. In *in vitro* studies, the shape of the particle was shown to influence the rate of uptake and the circulation time, and subsequently the target organ [11]. Spherically shaped particles are most efficiently taken up compared to their rod and elliptical counterparts [11], whereas particles with sharp edges are capable of escaping the endosome and therewith prolonging their retention time [13]. Having a higher circulation time results in a larger probability to reach other target organs rather than the most prominent clearing organ – the liver [11]. As a matter of fact, the shape that was found to accumulate the most in the liver was the nanosphere.

The fourth question we aimed to answer is whether the biodistribution is reflected in the organismal behavior responses. The observed differences in the behavior test were only marginally significant and not always repeatable. As stated earlier by Browning et al. (2009), random internal distribution of individual gold nanoparticles into vital organs of the zebrafish can result in effects on the individual level while this is not a concentration dependent effect. After long-term exposure to PS NPs, particles were found to distribute into the brain where they modified brain tissue and subsequently changed behavior [37]. For that reason, exposure for a longer period might result in the presence of gold NPs in the brain of zebrafish, resulting in abnormal behavior patterns. Additionally, gold particles affecting the eye in early development induced behavioral effects [34]. With our exposure concentration, we were not able to observe any strong effects on the behavior, indicating that for this exposure period the concentration is too low to induce any behavioral effects. However, the nano-bipyramids reduced the total distance moved in the challenge phase, indicating that the embryos lack the energy to produce the full energy burst as seen in the control group. At the same time, no visible in- or decreases in immune levels were observed. This combination of observations suggests that the total energy budget of the organism is decreased, where the organisms allocates most of their energy to the immune response leaving less energy for locomotive responses. Reduction in locomotive responses is detrimental for the survival of an individual and it might even indicate a possible reduced fecundity due to a lack in energy. So, although we did not find strong effects of any of the gold nanoparticles on the behavior in zebrafish embryos after short exposure time, such effects might occur at higher concentrations, after long-term exposure or after exposure from the fertilization onwards.

Although some minor effects were observed, the different distribution patterns per particle shape did not induce significant sub-lethal effects. Since most studies report no cytotoxicity [38] nor toxicity [39] of gold particles, the absence of significant effects is not surprising. Often within drug delivery systems in which gold nanoparticles are used, surface modifications of the nanoparticles or protein labels are used to assist delivering the particle to the target organ. Over time, it might be likely that those surface modifications become unstable, and fractions of bare particles appear. The absence of sub-lethal effects due to bare and differently shaped gold nanoparticles strengthens the justification for utilizing gold nanomaterials as tracing agents in biodistribution studies and nanomedicine. We echo the suggestion made by Truong et al. (2015),

who stated on the basis of studying the biodistribution behavior more closely, that it will become possible to design particles that reach the desired target organ by choosing the appropriate particle shape. In this contribution, we showed that the biodistribution for all differently shaped gold NPs occurs rapidly via the circulatory system. However, harm remains limited, since the particles are distributed via the MPS towards the clearance organs where they are stored before elimination.

Internalized AuNPs were found to traffic throughout the blood system and reach via this medium most probably the whole organism. We observed presence of the particles in and trafficking via macrophages, indicating that the majority of the particles is removed via the MPS. Clearance via the MPS will result in biodistribution of particles in the digestive organs. In our study, exposure to differently shaped gold particles induced shape dependent biodistribution patterns. For each differently shaped particle, we found a different ratio in which they were distributed over the three assessed target organs: liver, gall bladder and pancreas. Although the particles were distributed differently over the examined digestive organs, in none of the cases major sub-lethal effects were observed. The biodistribution patterns indicated that long-term exposure might induce sub-lethal effects being shape-dependent. Finally, for nanosafety assessment, it is eminent that shape-features should be taken into account as a possible toxicity modifying factor as it affects the biodistribution patterns.
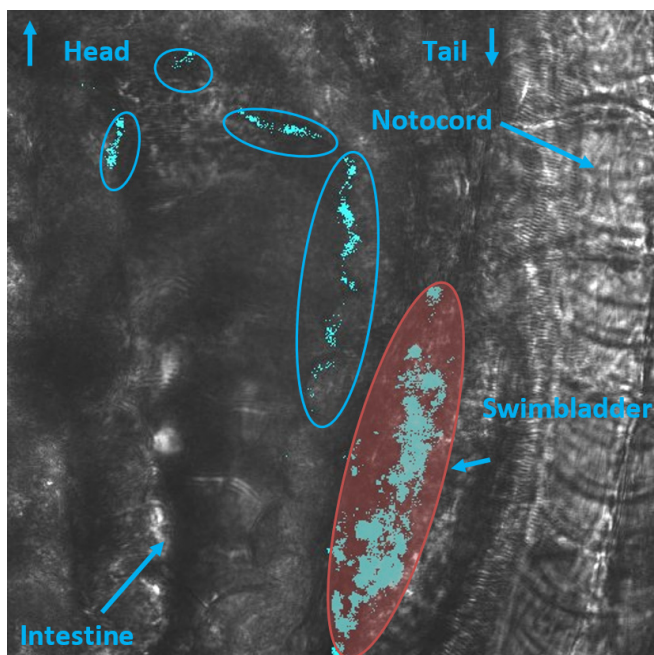
6.5 SUPPLEMENTARY FIGURES

Figure S6.1: Confocal image of gold nano-urchin in different digestive organs. Autofluorescence in the swim bladder is marked red.
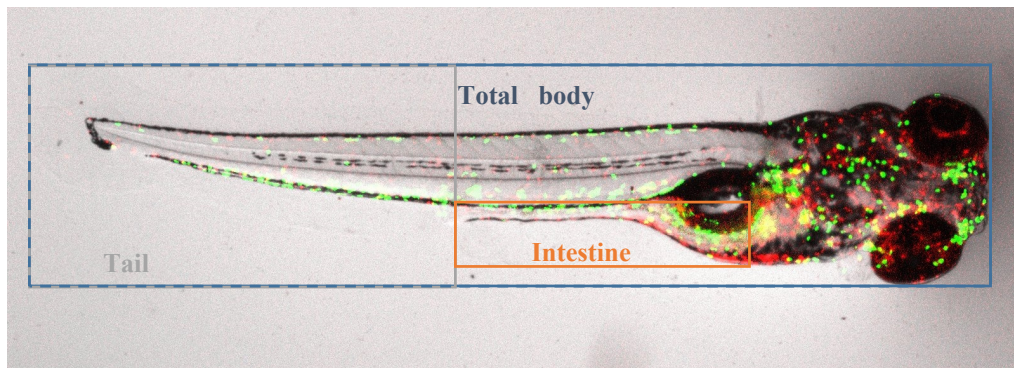
Figure S6.2 Image of a control fish with the different measurements areas used for the immune response assessment indicated: total body (blue), tail (green) and intestine (red).

6.6 BIBLIOGRAPHY

1.   Handy, R. D., Henry, T. B., Scown, T. M., Johnston, B. D. & Tyler, C. R. Manufactured nanoparticles: their uptake and effects on fish--a mechanistic analysis. *Ecotoxicology* 17, 396–409 (2008).

2.   Vijver, M. G. *et al.* Kinetics of Zn and Cd accumulation in the isopod Porcellio scaber exposed to contaminated soil and/or food. *Soil Biol. Biochem.* 38, 1554–1563 (2006).

3.   Macrae, C. A. & Peterson, R. T. Zebrafish as tools for drug discovery. *Nat. Publ. Gr.* 14, 721–731 (2015).

4.   Carnovale, C., Bryant, G., Shukla, R. & Bansal, V. Size, shape and surface chemistry of nano-gold dictate its cellular interactions, uptake and toxicity. *Prog. Mater. Sci.* 83, 152–190 (2016).

5.   Gatoo, M. A. *et al.* Physicochemical properties of nanomaterials: implication in associated toxic manifestations. *Biomed Res. Int.* 2014, 498420 (2014).

6.   Skjolding, L. M. *et al.* An assessment of the importance of exposure routes to the uptake and internal localisation of fluorescent nanoparticles in zebrafish (Danio rerio), using light sheet microscopy. *Nanotoxicology* 11, 351–359 (2017).

7.   van Pomeren, M., Brun, N. R., Peijnenburg, W. J. G. M. & Vijver, M. G. Exploring uptake and biodistribution of polystyrene (nano) particles in zebrafish embryos at different developmental stages. *Aquat. Toxicol.* 190, 40–45 (2017).

8.   Nazarenus, M. *et al.* In vitro interaction of colloidal nanoparticles with mammalian cells: What have we learned thus far? *Beilstein J. Nanotechnol.* 5, 1477–1490 (2014).

9.   Black, K. C. L. *et al.* Radioactive 198Au-doped nanostructures with different shapes for in vivo analyses of their biodistribution, tumor uptake, and intratumoral distribution. *ACS Nano* 8, 4385–4394 (2014).

10. Huang, X. *et al.* The shape effect of mesoporous silica nanoparticles on biodistribution, clearance, and biocompatibility in vivo. in *ACS Nano* 5, 5390–5399 (2011).

11. Truong, N. P., Whittaker, M. R., Mak, C. W. & Davis, T. P. The importance of nanoparticle shape in cancer drug delivery. *Expert Opin. Drug Deliv.* 12, 1–14 (2015).

12. Qiu, Y. *et al.* Surface chemistry and aspect ratio mediated cellular uptake of Au nanorods. *Biomaterials* 31, 7606–7619 (2010).

13. Chu, Z. *et al.* Unambiguous observation of shape effects on cellular fate of nanoparticles. *Sci. Rep.* 4, 4495 (2014).

14. Khlebtsov, N. & Dykman, L. Biodistribution and toxicity of engineered gold nanoparticles: a review of in vitro and in vivo studies. *Chem. Soc. Rev.* 40, 1647–1671 (2011).

15. Takeuchi, I., Nobata, S., Oiri, N., Tomoda, K. & Makino, K. Biodistribution and excretion of colloidal gold nanoparticles after intravenous injection: Effects of particle size. *Biomed. Mater. Eng.* 28, 315–323 (2017).

16. Simpson, C. A., Huffman, B. J., Gerdon, A. E. & Cliffel, D. E. Unexpected toxicity of monolayer protected gold clusters eliminated by PEG-thiol place exchange reactions. *Chem. Res. Toxicol.* 23, 1608–1616 (2010).

17. Bogdanov, A. a *et al.* Gold Nanoparticles Stabilized with MPEG-Grafted Poly(l - lysine): in Vitro and in Vivo Evaluation of a Potential Theranostic Agent. *Bioconjug. Chem.* 26, 39–50 (2015).

18. Browning, L. M. *et al.* Random walk of single gold nanoparticles in zebrafish embryos leading to stochastic toxic effects on embryonic developments. *Nanoscale* 1, 138 (2009).

19. Arts, J. H. *et al.* A decision-making framework for the grouping and testing of nanomaterials (DF4nanoGrouping). *Regul. Toxicol. Pharm.* 71, S1–S27 (2015).

20. Mesquita, B. *et al.* Gold nanorods induce early embryonic developmental delay and lethality in zebrafish (Danio rerio). *J. Toxicol. Environ. Heal. - Part A Curr. Issues* 80, 672–687 (2017).

21. Bruinink, A., Wang, J. & Wick, P. Effect of particle agglomeration in nanotoxicology. *Arch. Toxicol.* 89, 659–675 (2015).

22. Kumar, R. *et al.* In vivo biodistribution and clearance studies using multimodal organically modified silica nanoparticles. *ACS Nano* 4, 699–708 (2010).

23. Brun, N. R. *et al.* Nanoparticles induce dermal and intestinal innate immune system responses in zebrafish embryos. *Environ. Sci. Nano* 5, 904–916 (2018).

24. Legradi, J., el Abdellaoui, N., van Pomeren, M. & Legler, J. Comparability of behavioural assays using zebrafish larvae to assess neurotoxicity. *Environ. Sci. Pollut. Res.* 22, 16277–16289 (2015).

25. OECD. *Validation report (phase 1) for the zebrafish embryo toxicity test, part I. Series on Testing and Assessment No. 157. ENV/JM/MONO(2011) 37. Paris, France* (2011).

26. van Pomeren, M., Peijnenburg, W., Brun, N. & Vijver, M. A novel experimental and modelling strategy for nanoparticle toxicity testing enabling the use of small quantities. *Int. J. Environ. Res. Public Health* 14, 1348 (2017).

27. Pan, Y. *et al.* High-sensitivity real-time analysis of nanoparticle toxicity in green fluorescent protein-expressing zebrafish. *Small* 9, 863–869 (2013).

28. Kim, C. S. *et al.* Cellular imaging of endosome entrapped small gold nanoparticles. *MethodsX* 2, 306–315 (2015).

29. Schindelin, J. *et al.* Fiji: an open-source platform for biological-image analysis. *Nat. Methods* 9, 676–82 (2012).

30. Balasubramanian, V., Srinivasan, R., Miskimins, R. & Sykes, A. G. A simple aza-crown ether containing an anthraquinone fluorophore for the selective detection of Mg(II) in living cells. *Tetrahedron* 72, 205–209 (2016).

31.   van den Broek, B., Ashcroft, B., Oosterkamp, T. H. & van Noort, J. Parallel nanometric 3D tracking of intracellular gold nanorods using multifocal two-photon microscopy. *Nano Lett.* 13, 980–6 (2013)

32.   Hua, J., Vijver, M. G., Ahmad, F., Richardson, M. K. & Peijnenburg, W. J. G. M. Toxicity of different-sized copper nano- and submicron particles and their shed copper ions to zebrafish embryos. *Environ. Toxicol. Chem.* 33, 1774–82 (2014).

33.   Huwyler, J., Kettiger, H., Schipanski, A. & Wick, P. Engineered nanomaterial uptake and tissue distribution: from cell to organism. *Int. J. Nanomedicine* 8, 3255 (2013).

34.   Kim, K. T., Zaikova, T., Hutchison, J. E. & Tanguay, R. L. Gold nanoparticles disrupt zebrafish eye development and pigmentation. *Toxicol. Sci.* 133, 275–288 (2013).

35.   Sun, L. *et al.* Cytotoxicity and mitochondrial damage caused by silica nanoparticles. *Toxicol. Vitr.* 25, 1619–1629 (2011).

36.   Danilova, N. & Steiner, L. A. B cells develop in the zebrafish pancreas. *Proc. Natl. Acad. Sci.* 99, 13711–13716 (2002).

37.   Mattsson, K. *et al.* Altered behavior, physiology, and metabolism in fish exposed to polystyrene nanoparticles. *Environ. Sci. Technol.* 49, 553–561 (2015).

38.   Chen, Y. *et al.* Gold nanoparticles coated with polysarcosine brushes to enhance their colloidal stability and circulation time in vivo. *J. Colloid Interface Sci.* 483, 201–210 (2016).

39.   Asharani, P. V, Lianwu, Y., Gong, Z. & Valiyaveettil, S. Comparison of the toxicity of silver, gold and platinum nanoparticles in developing zebrafish embryos. *Nanotoxicology* 5, 43–54 (2011).

Summary

One of the great accomplishments of modern society is our more thorough understanding on how organisms function. A plethora of applications has emerged from this knowledge to revolutionize medicine – and many other industries. As our insight in complex biological systems grew, research became more specific and aiming at an understanding our cells and bodies on the molecular scale. Research on this smallest biological scale was propelled by recent developments in microscopy techniques. A prominent example was awarded the Nobel prize in 2014, demonstrating the importance of new super-resolution microscopy techniques for biology and physics research.

Here we developed a novel approach for single particle and single molecule tracking using two-photon microscopy (TPM). TPM is generally associated with slow, deep-tissue imaging using high laser power, a low background and negligible out-of-focus photobleaching. This would make TPM highly suitable for imaging weak signals of single molecules. However, the high laser powers required for two-photon excitation (TPE) causes enhanced in-focus bleaching and the slow imaging speeds impede tracking of fast, dynamic processes. TPM is therefore generally used for static, deep-tissue imaging.

In this thesis we splitted the TPE beam into multiple weaker beamlets for fast and gentle two-photon imaging. By simultaneously scanning several 100 beamlets, we achieved limited bleaching and fast imaging, while retaining the useful TPE properties of low background and thin optical sectioning. With abovementioned advantages, we demonstrated for the first time that two photon microscopy can readily be used to capture single particles and even single molecules in living samples.

In **Chapter 2** we first explored the possibility of single-molecule sensing by utilizing gold nanorods (GNRs). Plasmonic metallic nanoparticles are used in (bio-)sensing applications because their localized surface plasmon resonance (SPR) is highly sensitive to changes in environment. Although optical detection of scattered light from single particles provides a straight-forward means of detection, the two-photon luminescence (TPL) of single gold nanorods (GNRs) has the potential to
increase the sensitivity due to the large anti-Stokes shift and the non-linear excitation mechanism. However, two-photon microscopy and spectroscopy are restricted in bandwidth and have been limited by the thermal stability of GNRs. We used two-photon multifocal microscopy (TPMM) to simultaneously measure the two-photon excitation spectra of hundreds of individual GNRs with sub-nanometer accuracy. By keeping the excitation power under the melting threshold, we showed that GNRs were stable in intensity and spectrum for more than 30 minutes, demonstrating absence of thermal reshaping. Spectra featured a signal-to-noise ratio > 10 and a reduced the plasmon peak width to typically 30 nm. Changes in the refractive index of the

medium of less than 0.04, corresponding to a change in surface plasmon resonance of 8 nm, could be readily measured and over longer periods. We used this enhanced spectral sensitivity to measure the presence of neutravidin, demonstrating the potential of TPL spectroscopy of single GNRs for enhanced plasmonic sensing.

In **Chapter 3** we changed to *in vivo* applications to see how the confined excitation and high frame rates could contribute to tracking of single particles. Nano-scopic tracking of single particles by fluorescence microscopy is a powerful technique to study life processes at the molecular scale. Single-particle, and even single-molecule, tracking in individual cultured cells has been used widely and yielded spectacular results. However, nanometric imaging and tracking in larger multicellular samples remains challenging, due to the increased scattering of light, increased out-of-focus fluorescence and reduced resolution in the third dimension. Using two-photon – rather than one photon – excitation relieves these constraints and we explored the possibilities of TPMM for *in vivo* single particle tracking. We showed that the combination of a modern scientific CMOS camera, which features a higher sensitivity and very low dark signal, with a reduced power per focus and a reduced duty cycle for excitation yields extraordinary low bleaching rates, framerates larger than 10 Hz and a field of view of 100's of microns while maintaining the advantages of two photon excitation. We demonstrated the use of this novel microscopy modality in zebrafish embryos and rapeseed pollen, and show that it allows for multicolor imaging, using spectral selection in either excitation or emission. Furthermore, we showed that single GNRs in the veins of zebra fish embryos could be tracked with nanometric accuracy, resolving temporal fluctuations in bloodstream velocity. The unprecedented photostability in combination with the reduced background suggested that it should be possible to resolve single fluorescent proteins *in vivo* with TPMM.

In **Chapter 4** we investigated the ability of TPMM to image single fluorescent proteins. Single molecule microscopy is often hampered by autofluorescence and *in vivo* inelastic scattering impairs the visibility of the weak signal from single fluorophores. The lower background that TPE provides, is an excellent basis for high signal-to-noise ratio imaging. However, the low two-photon absorption cross-section of most fluorophores requires a high light intensity. This is usually implemented by confocal scanning and yields lower frame rates and increases photobleaching. We used TPMM to increase the image speed, and compared two scanning modes that both yielded a wide-field light-sheet-like excitation. In live zebrafish embryos background fluorescence and photobleaching were further reduced, enabling tracking of single fluorophores for more than 30 seconds. Furthermore, we showed that multifocal excitation with structured light-sheet illumination (SLIM) suppressed background in highly scattering environments. Finally, we used single-molecule tracking to quantify diffusive behavior of single eGFP-HRas molecules and observed longer and less confined tracks, that suggested that the mobility of those proteins differs in different regions of the same cell. The experiments demonstrated for the first time that two-photon microscopy can readily be used for

in vivo single-molecule tracking and, contrary to previous reports, it is shown to reduce photobleaching, while achieving significantly improved signal to noise ratios and z-resolution.

In **Chapter 5** we highlighted a collaboration study where we image the transition of photo-switchable liposomes to a cationic surface charge inside live zebrafish embryos in real time. Surface charge plays a fundamental role in determining the fate of a nanoparticle, and any encapsulated content, *in vivo*. Prior to light activation, intravenously administered liposomes, composed of only two lipid reagents, freely circulated and successfully evaded innate immune cells present in the fish. Upon *in situ* irradiation and surface charge switching, however, liposomes rapidly adsorbed to, and were taken up by, endothelial cells and/or were phagocytosed by blood resident macrophages. Made possible by the high temporal resolution of TPMM, this transition could be captured by interlacing irradiation and image acquisition. Coupling complete external control of nanoparticle targeting together with the intracellular delivery of encapsulated (and membrane impermeable) cargos, the compositionally simple liposomes were proof that advanced nanoparticle function *in vivo* does not require increased design complexity but rather a thorough understanding of the fundamental nano-bio interactions involved. The TPMM measurements revealed dynamics of the cationic transition of the liposome to which would normally be obscured by slower scanning confocal microscopes. The study illustrates how TPMM can contribute to a more thorough understanding of chemical and biological processes which take place inside living organisms, and showcases the potential of TPMM for future similar studies.

Chapter 6 features another single particle collaboration study which illustrated the capabilities of TPMM for real-case scenarios. The study focused on the bio-distribution and immune-response of differently shaped gold nanoparticles (AuNPs) in zebrafish embryos. The unique properties of AuNPs make them interesting materials to work with, however their effects on the environment and on the health of organisms has yet to be fully understood. Imaging of AuNPs in live samples is difficult by their weak one-photon luminescence brightness which impairs visibility in confocal microscopy. Confocal microscopy was used first to image fluorescently tagged macrophages, which are indicators of the immuno-response. However, to directly resolve where AuNPs are located in the zebrafish embryo, and whether they are being taken up by macrophages, a different imaging modality was required.

Gold nanoparticles feature impressive brightness upon TPE, as described chapter 2 of this thesis and our TPMM was especially well suited for measuring their distribution. Imaging the tail of the embryo we could discern individual spots, likely originating from single AuNPs, in real-time. Moreover, the high temporal resolution allowed us to image a macrophage which had taken up numerous NPs as it travelled along an artery wall. Direct imaging of AuNP macrophage uptake corroborated the confocal images, visualizing the first response of the immune system of the embryo as it reacts to the AuNPs and actively tries to dispose them.

These results illustrate how real-time imaging combined with two-photon excitation can provide insight in fast (biological) processes which would normally be eluded from detection.

Moreover, it further shows how AuNPs are excellent contrast agents in two-photon microscopy. Overall, TPMM is an excellent imaging modality to obtain a more detailed understanding of the pathological effects of nanoparticles, like AuNPs, in live organisms.

In conclusion, the novel two-photon method has demonstrated its ability of high-resolution, fast, low-background and gentle *in vivo* imaging. Imaging particle distributions in real-time in live organisms is readily achieved in TPMM and can be further exploited by looking at the particle-fate over longer terms by extending the measurement time. The ability to resolve even single fluorophores *in vivo* for prolonged periods, open up many possibilities to investigate a wide variety of cellular processes. TPMM could bring new insights in the inner workings of cells and help to progress our fundamental understanding of biological processes. Overall, our novel TPMM method offers an attractive method to study single-particles and single-molecules in living organisms and forms a new step in single-molecule biophysics. .

Samenvatting

Een van de grote prestaties van de moderne beschaving is ons beter begrip van hoe organismes functioneren. De overvloed aan toepassingen die hieruit zijn voortgekomen heeft een revolutie in de gezondheidszorg – en in menig andere industrie – teweeggebracht. Met het groeiende inzicht in complexe biologische systemen is het onderzoek zich gaan richten op hoe onze cellen en ons lichaam functioneren op een moleculaire schaal. Onderzoek op deze kleinste biologische schaal werd voortgestuwd door recente ontwikkelingen in de microscopie. De toekenning van de Nobelprijs in de natuurkunde in 2014, benadrukte het belang van nieuwe super-resolutie microscopen voor biologisch en natuurkundig onderzoek.

In dit proefschrift hebben we een nieuwe benadering ontwikkeld voor het volgen van individuele deeltjes en moleculen met twee-foton microscopie. Deze techniek wordt normaal geassocieerd met het langzaam maken van afbeeldingen diep in het weefsel, met zeer lage achtergrondfluorescentie en verwaarloosbare verbleking van fluoroforen buiten het brandpunt. De lage achtergrond zou twee-foton microscopie zeer geschikt moeten maken voor het afbeelden van de zwakke signalen afkomstig van individuele moleculen. Echter, het hoge vermogen van de laser dat nodig is voor twee-foton excitatie zorgt ervoor dat fluoroforen zeer snel verbleken, en het langzame scannen van de laserbundel belemmert het volgen van snelle dynamische processen. Twee-foton microscopie wordt daarom over het algemeen gebruikt voor het afbeelden van grote en statische weefsels.

In dit proefschrift splitsten we de laserbundel in meerdere, zwakkere bundeltjes voor snel en zachtaardige excitatie. Het simultaan scannen van enkele honderden laserbundels zorgt voor beperkte fluorofoor-verbleking en hoge scansnelheden, terwijl de nuttige twee-foton eigenschappen van een lage achtergrond fluorescentie en een hoge axiale resolutie behouden blijven. Met deze voordelen, demonstreren we voor de eerste keer dat twee-foton microscopie gebruikt kan worden voor het afbeelden van individuele deeltjes en zelfs individuele moleculen in levende organismen.

In **Hoofdstuk 2** onderzochten we de mogelijkheid om individuele moleculen te detecteren door gebruik te maken van gouden nanostaafjes. Deze metalen nanodeeltjes worden gebruikt voor het detecteren van (bio)moleculen omdat de gelokaliseerde oppervlakte-plasmon-resonantie zeer gevoelig is voor veranderingen in de omgeving. Het door individuele nanodeeltjes verstrooide licht is voldoende om veranderingen van de plasmon resonantie optisch te kunnen detecteren. De twee-foton luminescentie van individuele gouden nanostaafjes heeft de potentie om de gevoeligheid nog hoger te maken door de grote anti-Stokes verschuiving en het niet-lineaire excitatie mechanisme. Echter, reguliere twee-foton -microscopie en -spectroscopie hebben beperkte bandbreedte en worden gelimiteerd door de geringe thermische stabiliteit van de nanostaafjes. We hebben twee-foton multifocale microscopie gebruikt voor het

gelijktijdig meten van de excitatie spectra van honderden individuele gouden nanostaafjes met sub-nanometer nauwkeurigheid van de golflengtes. Door het excitatievermogen onder de smelt temperatuur te houden, hebben we laten zien dat nanostaafjes stabiel bleven voor meer dan 30 minuten. De spectra hadden een signaal-ruis-verhouding van boven de 10 en de plasmonpiek had een typische breedte van 30 nm. Veranderingen in de brekingsindex van het immersie medium van minder dan 0.04, wat een plasmonverschuiving van 8 nm veroorzaakte, konden gemakkelijk gemeten worden en over lange tijd. We gebruikten de door twee-foton excitatie verbeterde spectrale gevoeligheid om de aanwezigheid van neutravidine te meten, en daarmee de potentie van twee-photon spectroscopie op individuele gouden nanostaafjes voor verbeterde plasmonische sensoren aan te tonen.

In **Hoofdstuk 3** stapten we over naar *in vivo* toepassingen om te zien hoe de lokale excitatie en hoge beeldfrequentie kunnen bijdragen aan het volgen van individuele deeltjes in levend weefsel. Het volgen van deeltjes op de nanoschaal is een krachtige techniek voor het bestuderen van biologische processen op moleculaire schaal. In gecultiveerde cellen heeft het volgen van individuele moleculen spectaculaire resultaten opgeleverd. Echter, hetzelfde verrichten in grotere organismen blijft zeer uitdagend door de toename in verstrooid licht en achtergrondfluorescentie, en door de relatief lage resolutie in de derde dimensie. Door gebruik te maken van twee-foton – in plaats van één-foton – excitatie worden deze problemen verminderd. We hebben laten zien dat de combinatie van een moderne wetenschappelijke CMOS-camera, die een hoge gevoeligheid heeft en lage ruis, een verlaagd excitatievermogen per focus en een verlaagde belichting *duty cycle*, resulteert in uitzonderlijke lange fluorofoor-verblekingstijden, beeldfrequenties van 10 Hz, en een gezichtsveld van honderden micrometers, terwijl de voordelen van twee-foton excitatie behouden blijven. We hebben deze nieuwe microscopie modaliteit toegepast in zebravis embryo's en koolzaad pollen, en waren in staat om afbeeldingen te maken met meerdere kleuren door het spectraal selecteren van fluoroforen in excitatie of emissie. Bovendien hebben we laten zien dat individuele gouden nanostaafjes in de aderen van zebravis embryo's gevolgd kunnen worden met nanometer nauwkeurigheid, en daarmee ook fluctuaties van de bloedstroom in kaart gebracht.

De uitzonderlijke fotostabiliteit in combinatie met de lage achtergrondruis suggereert dat het mogelijk zou moeten zijn om individuele fluorescerende eiwitten af te kunnen beelden *in vivo* met twee-foton multifocale microscopie. In **Hoofstuk 4** hebben we dit onderzocht. Microscopie op individuele moleculen wordt vaak belemmerd door autofluorescentie terwijl *in vivo* in-elastische verstrooiing van licht de zichtbaarheid van het zwakke signaal verder bemoeilijkt. De lagere achtergrond die twee-foton excitatie bewerkstelligt, zorgt voor afbeeldingen met een hoge signaal-ruis-verhouding. Echter, de lage twee-foton absorptiediameter van de meeste fluoroforen vereist een hoge lichtintensiteit. Dit wordt meestal geïmplementeerd door middel van confocaal scannen en resulteert in lage beeldfrequenties en snelle verbleking van fluoroforen. Wij gebruiken twee-foton multifocale microscopie om de opnames te versnellen, en vergelijken twee scan-modi die beide een dunne excitatie-plak

realiseren. Achtergrond fluorescentie en het verbleken van fluoroforen is aanzienlijk verlaagd in levende zebravis embryo's. Dit was voldoende om individuele fluoroforen meer dan 30 seconden te volgen. Bovendien hebben we laten zien dat multifocale excitatie met gestructureerde belichting het achtergrond signaal nog verder kan verlagen in zeer licht-verstrooiende omgevingen. Als laatste hebben we algoritmes geïmplementeerd om het diffuse gedrag van individuele eGFP-HRas moleculen, eiwitten die externe signalen door de cel membraam doorgeven, te kwantificeren. Een verschil in begrenzing van de beweging van deze moleculen suggereerde dat de mobiliteit van HRas varieert tussen verschillende regio's van dezelfde cel. De experimenten hebben voor de eerste keer laten zien dat twee-foton microscopie gebruikt kan worden voor het volgen van individuele moleculen in levende cellen en laten, in tegenstelling tot eerdere bevindingen, een vermindering in het verbleken van fluoroforen zien, terwijl de signaal-ruis-verhouding en axiale resolutie significant verbetert.

Hoofdstuk 5 is een studie die we samen hebben gedaan met wetenschappers uit de chemie en moleculaire biologie. We hebben de transitie van foto-gevoelige liposomen naar een kationische oppervlaktespanning in de aderen van levende zebravis embryo's gemeten. Oppervlaktespanning speelt een belangrijke rol in het lot van liposomen *in vivo*. Voorafgaand aan licht-activatie circuleerden intraveneuze toegediende liposomen vrij door het bloedvatenstelsel en wisten deze de immuno cellen in de vis te ontlopen. Na *in situ* belichting, en de daaropvolgende verandering in oppervlaktespanning, werden de liposomen echter snel geadsorbeerd aan en geëndocyteerd door endotheelcellen. Ook werden ze gefagocyteerd door macrofagen in het bloed. Deze transitie kon worden afgebeeld dankzij de hoge tijdsresolutie van de twee-foton multifocale microscoop, waarbij *in situ* belichting snel kon worden gewisseld met het maken van een microscopie-plaatje. De transitie naar kationische toestand van de liposomen zou normaal verborgen blijven met langzamere confocale microscopen. De externe optische controle maakt het mogelijk om nanodeeltjes met ingekapselde (en membraam-permeabele) farmaceutische stoffen gericht te bezorgen op gewenste locaties in het lichaam van de zebravis embryo. Deze geavanceerde functies konden gerealiseerd worden met eenvoudige liposomen, en de microscopie geeft een beter begrip van interacties tussen nanodeeltjes en biologisch weefsel. Deze studie illustreert hoe twee-foto multifocale microscopie kan bijdragen aan een beter begrip van chemische en biologische processen die plaatsvinden in levende organismen.

In **Hoofdstuk 6** gebruiken we twee-foton multifocale microscopie om de distributie en immunorespons van verschillende groottes en vormen van gouden nanodeeltjes in zebravis embryo's in kaart te brengen. De unieke eigenschappen van gouden nanodeetjes maken ze interessant om mee te werken, maar hun effecten op het milieu en op de gezondheid van organismen zijn nog niet goed begrepen. Confocale microscopie werd eerst gebruikt om fluorescerend-gelabelde macrofagen af te beelden, die een indicatie zijn voor het immuunrespons van het embryo. Echter, om gouden nanodeeltjes direct te kunnen lokaliseren in zebravis embryo's en om vast te stellen of ze worden opgenomen door macrofagen, hebben we twee-foton multifocale microscopie gebruikt. In de staart van een embryo konden we

individuele gouden nanodeeltjes zien. De hoge temporele resolutie maakte het bovendien mogelijk om een macrofaag af te beelden die meerdere nanodeeltjes had gefagocyteerd terwijl deze langs een aderwand bewoog. Deze resultaten illustreren hoe twee-foton multifocale microscopie een inzicht kan verschaffen in snelle (biologische) processen die normaal verborgen zijn voor detectie. Bovendien laat het zien dat gouden nanodeeltjes uitstekende labels zijn om contrast te verschaffen in twee-foton microscopie.

Samenvattend hebben we laten zien dat deze nieuwe twee-foton methode in staat is om snel plaatjes te kunnen maken met hoge-resolutie, minimale achtergrond en lage -fototoxiciteit en -fotobleking. Het afbeelden van de distributie van enkele deeltjes in levende organismen gaat gemakkelijk in twee-foton multifocale microscopie en kan verder gebruikt worden om het lot van deeltjes te volgen over een langere tijdsperiode. De eigenschap om zelfs individuele fluoroforen te kunnen meten *in vivo* en gedurende lange periodes opent talrijke mogelijkheden om verschillende cellulaire processen te bestuderen. Onze nieuwe microscoop is dus een aantrekkelijke methode voor het bestuderen van individuele moleculen en deeltjes in levende organismen en vormt een nieuwe stap in *single-molecule* biofysica. Twee-foton multifocale microscopie zou nieuwe inzichten kunnen brengen in hoe cellen werken en meehelpen aan het vergroten van ons fundamenteel begrip van biologische processen.

List of publications

Van Pomeren, M., Peijnenburg, W. J. G. M., Vlieg, R. C., van Noort, J. & Vijver, M. G. The biodistribution and immuno-responses of differently shaped non-modified gold particles in zebrafish embryos. *Nanotoxicology* **13**, 558–571 (2019).

Arias-Alpizar, G., Kong, L., Vlieg, R. C., Rabe, A., Papadopoulou, P., Meijer, M. S., Bonnet, S., Vogel, S., van Noort, J., Kros A., Campbell, F., Light-triggered switching of liposome surface charge directs delivery of membrane impermeable payloads in vivo. *Nat. Commun.* **11**, 1–14 (2020).

Brinkmann, B. W., Beijk, W.F., Vlieg, R.C., Mejia, J., Lamers, G., van Noort, J., Peijnenburg, W. J. G. M., and Vijver, M. G. Adsorption of titanium dioxide nanoparticles onto zebrafish eggs affects colonizing microbiota. *Aquatic Toxicology*, (submitted).

Vlieg, R.C., Pham, C., van Noort, J., Multiplexed two-photon excitation spectroscopy of single gold nanorods for single molecule biosensing. (In preparation).

Vlieg, R. C., Siemons, C., Arias-Alpizar, G., Papadopoulou, P., Boutilier, K., van Noort, J., Two-photon multifocal microscopy for *in vivo* single particle tracking. (In preparation).

Curriculum vitae

Redmar Cornelis Vlieg was born on 9 April 1992 in Blaricum, The Netherlands. After receiving his VWO diploma from the Nijmeegse Scholengemeenschap Groenewoud in 2010, he went to the University of Twente to study biomedical engineering. In 2013 he obtained the Bachelor of Science and continued at the University of Twente for a Msc. degree in biomedical engineering. During this time, he spent five months at AOM-labs at the Australia National University in Canberra under supervision of Dr. Steve Lee, where he chemically cleared mouse tissue and imaged the results using two-photon microscopy. For his final internship, Redmar worked on a photo-acoustic setup for early detection of rheumatoid arthritis at the biomedical photonic imaging group, Twente University, under supervision of Prof. Srirang Manohar.

After obtaining his Msc. degree in 2016 and being interested in research and the development of new imaging modalities, Redmar started his PhD at the group of Prof. John van Noort at Leiden University. His PhD research revolved around the development of a two-photon multifocal microscope, and how that could be used for single-molecule and single-particle tracking in live samples. During his time in Leiden, Redmar also joined the board of the 'Leids Promovendi Overleg', where, as an external affairs officer and secretary, he was involved in representing PhDs of Leiden in local and national matters, and the organization of events for the social well-being of PhDs.

Upon completing his PhD in 2020, Redmar started at MILabs in Utrecht, The Netherlands, where he works on the development of an optical module for the imaging of mice for pre-clinical research.